Schottky Contact Formation to Bulk Zinc Oxide

by

Martin Ward Allen

B.Sc. (Bris)

M.Sc. (Oxon)

A thesis presented for the degree of

Doctor of Philosophy

in

Electrical and Electronic Engineering

at the

University of Canterbury,

Christchurch, New Zealand.

5th of June, 2008

Abstract

Zinc oxide is a II–VI semiconductor with considerable potential for optoelectronic and power–electronic applications in the UV spectrum, due to its wide direct band gap (3.35 eV at 300 K), high exciton binding energy (60 meV), high melting point, and excellent radiation hardness. A key requirement for many device applications is the consistent production of high performance Schottky contacts. Schottky contact formation to *n*-type ZnO was investigated via systematic studies into the relative performance of different metal and metal oxide Schottky contacts to hydrothermal and melt grown, bulk ZnO. The results of these studies can be explained by the dominating influence of two key mechanisms in the formation of high quality contacts:

(a) the removal of the natural hydroxide termination of ZnO and the associated surface accumulation layer, and

(b) the minimisation of process induced oxygen vacancies which tend to pin the barrier height of ZnO Schottky contacts in the 0.6 – 0.8 eV range.

These investigations also led to the discovery of a new technique for the consistent production of high quality ZnO Schottky contacts, using the deposition of metal oxide films in reactive oxygen ambients. Specifically, silver oxide, iridium oxide, and platinum oxide films were used to consistently produce highly rectifying, very low ideality factor Schottky contacts to bulk ZnO, with figures of merit significantly better than those published in the literature.

In addition, a number of previously unreported, surface polarity related effects were discovered in the electrical and optical properties of ZnO, which increase in magnitude with decreasing carrier concentration of the ZnO material. For example, metal oxide Schottky contacts fabricated on the Zn-polar surface of hydrothermal ZnO have significantly higher barrier heights than those on the O-polar surface, and low temperature (4 K) photoluminescence emission, from free excitons and excitons bound to ionised donors, is also significantly stronger from the Zn-polar face of the same material. These effects are thought to be related to the large spontaneous polarisation ($-0.057\ Cm^{-2}$) of ZnO, and indicate that surface polarity is an important variable when comparing experiment results with theoretical models, and in the future design of ZnO based devices.

Acknowledgments

1) PERSONAL

This doctoral thesis marks the end of a three year odyssey which began in April 2005. Most journeys are seldom undertaken alone. The help, encouragement and companionship of others is required along the way. This thesis is no exception. I am principally indebted to the support, sacrifice and patience of my wife Barb, who so often took on the role of a solo parent during those long hours spent in laboratory.

All journeys into unknown territory require a knowledgeable guide, and in this I have been extremely fortunate with regard to my principal supervisor, Assoc. Prof. Steven Durbin. Steve has provided amazing daily support and encouragement; providing a constant stream of ideas (most of which have been feasible), resources, and the many links to international collaborators which have been such an enjoyable part of this work. I was equally fortunate in my co-supervisors Assoc. Prof. Maan Alkaisi, who actively supported my enrolment as a doctoral student, and Assoc. Prof. Roger Reeves whose collaboration led to new discoveries in ZnO optical phenomena. I also greatly appreciated the advice and encouragement of Prof. Richard Blaikie at various points along the way.

I am very grateful to the Royal Society of New Zealand for the teacher fellowship I was awarded in 2003; this provided a twelve month break from the frenetic world of secondary school teaching and enabled me to become a researcher once again, in the development of erythemal UV monitoring dosimeters. I am particularly grateful for the interest and encouragement from many people in the Department of Electrical and Computer Engineering during that time, particularly Richard Duke, Simon Round, Maan Alkaisi, Richard Blaikie, Ron Battersby, Dermot Sallis, Scott Lloyd, and Nick Smith. This rewarding experience ultimately led to my successful application for a University of Canterbury Doctoral Scholarship in 2005.

As a laboratory rookie, I was grateful to the training and advice provided by Gary Turner and Helen Devereux. The long hours in the close confines of the laboratory were made enjoyable by the eclectic mix of nationalities who shared and competed for equipment; Euan Boyd (Scotland) and I had lots of fun in the early days of growing silver oxide films, Volker Nock proved on a daily basis that Germans do have a sense of humour, Leo Schuler (Switzerland) readily shared his laboratory expertise, and Florian L'Hostis (France) provided the gaulic flourish. I was also fortunate to work along side the other members of Steve's research group; Chito Kendrick, William Lee, Jessica Chai, and Dr. Craig Swartz.

Many of the optical and metal oxide growth discoveries in this thesis have resulted from the spectroscopic and pulsed laser deposition skills of Paul Miller, Martin Henseler, and Reuben Mendelsberg from Roger Reeves' research group in the Department of Physics and Astronomy. I am also grateful for the help of Dr. Colin Doyle and Prof. James Metson from the Department of Chemistry at the University of Auckland, N.Z. in the surface characterisation of bulk ZnO using x-ray photoemission spectroscopy.

I am also indebted to my mother-in-law Jos Kelly for helping to run the family during my trips overseas and who always provided a perspective to the meaning of hard work. Also, to my parents Jean and Eddie for their constant encouragement and support.

Most of my working days have started and ended with an 8 km cycle ride to the University campus in Ilam; more than 10,000 cycle–kms in total, which may have offset the amount of paper I have used over the three years and the air travel to overseas conferences, making this thesis 'carbon neutral' – something my mother-in-law would appreciate.

As is often the case, as one journey ends, another one begins, but hopefully this time with a little more balance between work and play.

2) LIST OF INTERNATIONAL COLLABORATORS

Holger von Wenckstern and Marius Grundmann,
Institut für Experimentelle Physik II, Universität Leipzig, Linnestraße 5, 04103, Germany.

Stuart Hatfield, Paul Jefferson, Philip King, Timothy Veal, and Christopher McConville,
Department of Physics, University of Warwick, Coventry, CV4 7AL, United Kingdom.

Xiaojun Weng and Joan Redwing,
Department of Materials Science and Engineering, and Materials Research Institute, The Pennsylvania, State University, University Park, Pennsylvania 16802, USA.

Ori Avayu and Yossi Rosenwaks,
School of Electrical Engineering, Tel Aviv University, Tel Aviv 69978, Israel.

Masakazu Kobayashi,
Waseda University, 1-104 Totsukamachi, Shinjuku-ku, Tokyo, 169-8050, Japan.

Tom Myers
Department of Physics, West Virginia University, Morgantown, West Virginia, USA.

Contents

Preface

This thesis describes research undertaken in the Department of Electrical and Computer Engineering at the University of Canterbury, Christchurch, New Zealand from April 2005 to March 2008 into the formation of Schottky contacts to bulk zinc oxide. The work presented in this thesis has been published in the following articles and presentations:

Publications in Peer Reviewed Journals:

M.W. Allen and S.M. Durbin, "Influence of oxygen vacancies on Schottky contacts to ZnO," Applied Physics Letters **92**, 1 (2008).

M.W. Allen, S.M. Durbin and J.B. Metson, "Silver oxide Schottky contacts on n-type ZnO," Applied Physics Letters **91**, 053512 (2007).

H. von Wenckstern, H. Schmidt, M. Grundmann, M.W. Allen, P. Miller, R.J. Reeves and S.M. Durbin, "Defects in hydrothermal bulk ZnO," Applied Physics Letters **91**, 022913 (2007).

M.W. Allen, P. Miller, R.J. Reeves and S.M. Durbin, "Influence of spontaneous polarization on the electrical and optical properties of bulk, single crystal ZnO," Applied Physics Letters **90**, 062104 (2007). [Selected for the 19 February 2007 issue of the Virtual Journal of Nanoscale Science and Technology **15** (7) 2007].

M.W. Allen, M.M. Alkaisi and S.M. Durbin, "Metal Schottky diodes on Zn-polar and O-polar bulk ZnO," Applied Physics Letters **89**, 103520 (2006). [Selected for the 18 September 2006 issue of the Virtual Journal of Nanoscale Science and Technology **14** (12) 2006].

Peer Reviewed Conference Proceedings:

M.W. Allen, H. von Wenckstern, M. Grundmann, P. D. C. King, S. A. Hatfield, P. H. Jefferson, T. D. Veal, C. F. McConville, and S.M. Durbin, “Mechanisms in the Formation of High Quality Schottky Contacts to n-type ZnO,” Proceedings of the Fall 2007 Meeting of the Materials Research Society (26 - 30 November 2007, Boston, MA, USA) Symposium L, **1035**, L10-06.

M.W. Allen, P. Miller, J. Chai, J.B. Metson, R.J. Reeves, M. Alkaisi and S.M. Durbin, "Schottky contact behaviour as a function of metal and ZnO surface polarity," Proceedings of the Fall 2006 Meeting of the Materials Research Society (27 November - 1 December 2006, Boston, MA, USA) Symposium K, **957**, K09-03.

Oral Conference Presentations (contributing author in bold):

M.W. Allen, P. Miller, R.J. Reeves, O. Avayu, Y. Rosenwaks, and S.M. Durbin, “Spontaneous Polarisation Effects in ZnO,” 2008 International Conference On Nanoscience and Nanotechnology (25-29 February 2008, Melbourne, Victoria, Australia).

M.W. Allen, C.H. Swartz, M. Henseler, R.J. Reeves, J.B. Metson, H. Von Wenckstern, M. Grundmann, S.A. Hafield, P.H. Jefferson, P.D.C. King, T.D. Veal, C. McConville, M. Kobayashi and S.M. Durbin, "Mechanisms in the formation of high quality Schottky contacts to n-type ZnO," Symposium L of the 2007 Fall Meeting of the Materials Research Society (26 -30 November 2007, Boston, MA, USA).

C.H. Swartz, **S.M. Durbin**, M.W. Allen, and T.H. Myers, “Separation of Surface and Bulk Conduction in Hydrothermally grown ZnO Using Variable Magnetic Field Hall Effect Measurements,” Symposium L of the 2007 Fall Meeting of the Materials Research Society (26 -30 November 2007, Boston, MA, USA).

C.H. Swartz, M.W. Allen, S.M. Durbin and T.H. Myers, "Separation of surface and bulk conduction in ZnO using variable magnetic field Hall effect measurements," 54th American Vacuum Society Symposium (14-19 October 2007, Seattle, Washington, USA).

M.W. Allen, C.H. Swartz, P. Miller, R.J. Reeves, and S.M. Durbin, "Influence of surface polarity on the electrical and optical properties of bulk ZnO," 2007 Electronic Materials Conference (20-22 June 2007, Notre Dame, Indiana, USA)..

M.W. Allen, C.H. Swartz, P. Miller, R.J. Reeves, J.B. Metson, M.M. Alkaisi, and S.M. Durbin, "High quality silver oxide Schottky devices on polar and non-polar zinc oxide," AMN-3, 3rd International Conference on Advanced Materials and Nanotechnology (11-17 February 2007, Wellington, New Zealand).

M.W. Allen, P. Miller, J. Chai, J.B. Metson, R.J. Reeves, M.M. Alkaisi and **S.M. Durbin**, "Schottky Contact Behaviour as a Function of Metal and ZnO Surface Polarity," Symposium K of the 2006 Fall Meeting of the Materials Research Society (27 November - 1 December 2006, Boston, USA).

M.W. Allen, P. Miller, R.J. Reeves, J.B. Metson, M.M. Alkaisi, and S.M. Durbin, "ZnO Schottky diode performance as a function of surface polarity," 4th International Workshop on ZnO (3-6 October 2006, Giessen, Germany).

M.W. Allen, W.C.T. Lee, P. Miller, R.J. Reeves, M.M. Alkaisi and **S.M. Durbin**, "ZnO Schottky diode performance as a function of Schottky metal and surface polarity," 2006 Electronic Materials Conference (28-30 June 2006, State College, PA, USA).

List of Figures

List of Tables

Acronyms / Abbreviations

AFM	Atomic Force Microscopy
DB	Defect Band
CBM	Conduction Band Minimum
CBP	Chemical Bond Polarisation
CNL	Charge Neutrality Level
CL	Cathodoluminescence
FL	Fermi Level
FWHM	Full Width at Half Maximum
HYD	Hydrothermal
MBE	Molecular Beam Epitaxy
MCF	Multi-Carrier Fitting
MESFET	Metal Epitaxial Semiconductor Field Effect Transistor
MIGS	Metal Induced Gap States
MOCVD	Metal Organic Chemical Vapour Deposition
LEED	Low Energy Electron Diffraction
NBE	Near Band Edge
PL	Photoluminescence
PLD	Pulsed Laser Deposition
QMSA	Quantitative Mobility Spectrum Analysis
RF	Radio Frequency
RR	Rectifying Ratio
RT	Room Temperature
SCCM	Standard Cubic Centimeter per Minute
SCVT	Seeded Chemical Vapour Transport
SEM	Scanning Electron Microscopy
SKPM	Scanning Kelvin Probe Microscopy
STP	Standard Temperature and Pressure
TCO	Transparent Conducting Oxide
TE	Thermionic Emission
TEM	Transmission Electron Microscopy
TFE	Thermionic Field Emission

TMAH	Tetramethyl Ammonium Hydroxide
UPS	Ultra-violet Photoelectron Spectroscopy
VBM	Valence Band Maximum
VBXPS	Valence Band X-ray Photoemission Spectroscopy
XEDS	X-ray Energy Dispersive Spectroscopy
XRD	X-Ray Diffraction
XPS	X-ray Photoemission Spectroscopy

Chapter 1

Zinc Oxide

1.1 INTRODUCTION

Zinc oxide (ZnO), known by the synonyms chinese white, zinc white, flowers of zinc, and philosopher's wool, is a versatile, non-toxic compound that plays an important role in a wide range of industrial processes and commercial products. In 2004, worldwide usage of ZnO was approximately 1 million tonnes; the largest consumers were the glass and ceramics industries where it is used as a fluxing agent [1]. ZnO is also an important chemical in rubber production due to its efficient activation of the vulcanization process and for imparting improved heat conductivity and anti-aging properties to finished products.

ZnO has a very low toxicity, combined with antibacterial and fungi static properties. Topical ZnO ointments and creams are used to treat minor skin irritations such as nappy rash, burns and abrasions. Calamine lotion is made from a mixture of ZnO with approximately 0.5% iron (III) oxide. In chinese herbal medicine, ZnO is referred to as “Lu-Gan-Stone” in the famous 52 volume medical compendium *Ben Cao Gang Mu* written by Song Ying Xing in the Ming Dynasty (1378 - 1644) [2]. In powder form, it is a powerful whitening agent in pharmaceuticals, cosmetics, and paints. It is found in many types of sunscreen due to its high refractive index and its ability to absorb broad spectrum UVA and UVB radiation. ZnO is added to breakfast cereals, dietary supplements and agricultural feeds as a source for the essential nutrient zinc.

ZnO occurs naturally as the mineral zincite which can be quarry mined or manufactured synthetically. Most of the world's ZnO is manufactured via the French process whereby metallic zinc vapor is burned in a combustion chamber, producing agglomerated ZnO particles with an average size of greater than 100 nm. Recently, this process has been modified to produce micron length, needle shaped nanostructures with average diameters of 30 – 40 nm which enhances their chemical activity and antibacterial properties [1]. This nanoscale ZnO also develops an efficient deodorant action, thought to be due to its ability to react rapidly with ammonia molecules in the body or environment [2].

ZnO was first used as a semiconductor in the early days of radio detection at the beginning of the 20th century with zincite crystals providing a rectifying junction with either a thin metal wire in a cat's whisker (point contact) arrangement, or with the mineral chalcopyrite in a combination known as a Perikon detector. The green luminescence properties of ZnO phosphors have been known for over 100 years and have recently regained renewed interest for use in low voltage field emission displays. In the past 30 years, ZnO ceramic varistors with Bi_2O_3 additives have been widely used to protect electronic circuits and power distribution lines from destructive voltage levels induced by lightning impulses or switching surges. The highly nonlinear current-voltage characteristics (similar to back-to-back Zener diodes) of these devices is due to the cumulative effect of many potential barriers at the grain boundaries of the polycrystalline ZnO material.

Zinc oxide has a unique set of semiconductor properties: a wide band gap (3.35 eV at 300 K), a high free exciton binding energy (60 meV), excellent radiation hardness, and high spontaneous and piezoelectric polarizations. It has a low toxicity and is relatively cheap. As a result, it is currently the subject of an intense worldwide research effort towards high performance semiconductor devices such as:

1) high efficiency UV light emitting diodes and laser diodes for the lighting and communications industries,
2) high temperature power diodes and field effect transistors for harsh enviro-nents and space applications,
3) UV detectors for imaging and medical research,
4) nanoscale electrical generators, and
5) transparent conducting electrodes for flat panel displays and solar cells.

This has resulted in a dramatic increase in ZnO related research publications (Figure 1.1) and funding, whose sustainability largely depends on a breakthrough in the p-type doping of ZnO. Like many wide band gap semiconductors, ZnO exhibits a potentially serious doping asymmetry [1, 4]. As grown, ZnO is intrinsically *n*-type and can be extrinsically *n*-doped to the point of becoming a transparent conducting oxide (TCO), whereas *p*-type ZnO with sufficient hole mobility for device production has yet to be realised. The problem appears to be that *p*-type dopants in ZnO form deep acceptor levels while encouraging the formation of compensating defects. In the worst case of high quality *p*-type ZnO being unattainable, recent advances in Schottky contact formation, including those described in this thesis, should allow the development of devices 2 – 4 from the above list, while the development of TCOs can also

be achieved without the need for *p*-type material. In the more optimistic case, the same advances in high quality Schottky contacts to *n*-ZnO will be important in the design of device grade, ohmic contacts to *p*-type material.

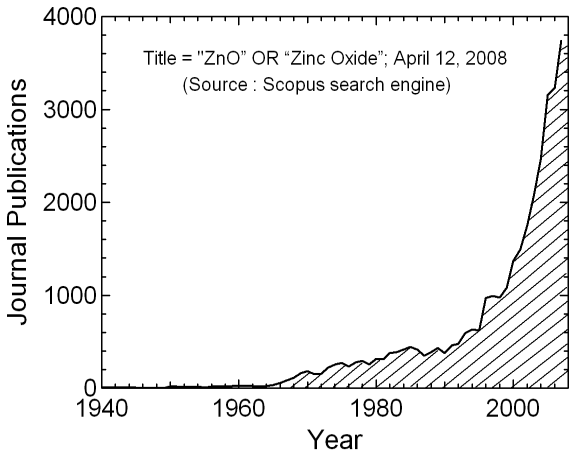

Figure 1.1: ZnO publications per year since 1940 (Source: Scopus™ search engine, search parameters "ZnO" OR "Zinc Oxide" in article title; April 12, 2008).

1.2 ZINC OXIDE AS A SEMICONDUCTOR

Zinc oxide is a highly functional wide band gap semiconductor with a direct band gap of 3.35 eV at room temperature, with photons emitted from band to band transitions having energies in the UVA spectrum (Figure 1.2).

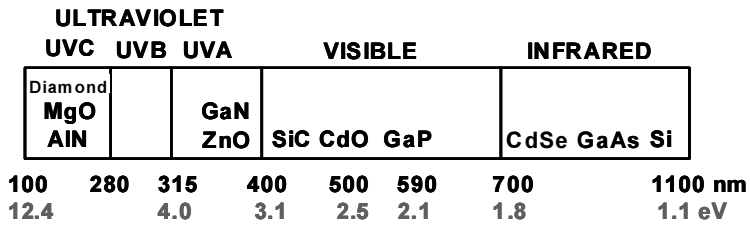

Figure 1.2: Band gaps of selected semiconductors and associated photon wavelengths for band-to-band transitions.

There many excellent reviews of the semiconductor properties of ZnO [5-10] which describe its electronic band structure, lattice parameters, bulk carrier transport, optical properties, defects, doping, band gap engineering, and the progress towards device fabrication. Table 1.1 gives a comparison of the basic semiconductor properties of ZnO compared to those

of GaN, the most successful wide band gap semiconductor in terms of commercial device applications.

Table 1.1: Comparison of semiconductor properties of ZnO with those of GaN, its principal competitor as a wide band semiconductor [5-10].

Semiconductor	ZnO	GaN
band gap (300 K)	3.35 eV	3.39 eV
crystal structure	wurtzite	wurtzite
lattice constants (300 K)	a = 0.3250 nm c = 0.5205 nm	a = 0.3189 nm c = 0.5185 nm
melting point	2250 ^{o}C	2770 ^{o}C
dislocation density	< 10^4 cm^{-2}	> 10^6 cm^{-2}
electron mobility (300 K)	200 $cm^2V^{-1}s^{-1}$	1000 $cm^2V^{-1}s^{-1}$
exciton binding energy	60 meV	25 meV
spontaneous polarisation	-0.057 Cm^{-2}	-0.029 Cm^{-2}
breakdown voltage	5.0 x 10^6 Vcm^{-1}	5.0 x 10^6 Vcm^{-1}

ZnO has similar properties to GaN, a multi-billion dollar technology in the lighting industry for the production of blue, ultraviolet and white light emitting devices. ZnO has several potential cost advantages over GaN, such as the availability of wet chemical etching, the ability to grow high quality bulk single crystal substrates, and the simpler, lower temperature growth of thin films. Most significantly ZnO has a much larger exciton binding energy, which should lead to brighter light emission and exciton-recombination UV lasing at room temperature. However, breakthroughs in the production of *p*-type GaN using Mg doping were achieved in 1990s while high quality *p*-type ZnO has yet to be realised.

1.2.1 Unresolved Issues

Despite the exponential increase in ZnO based research over the past 20 years, there are still a number of fundamental issues that have yet to be satisfactorily resolved:

1) Intrinsic *n*-type conductivity of ZnO – specifically the relative importance of intrinsic defects (such as zinc interstitial and oxygen vacancies) and unintentionally introduced impurities (in particular H, Al, Ga, In, and Fe) in determining the electrical properties of “undoped” ZnO.

2) Green defect-band luminescence of undoped ZnO – candidates include donor – acceptor pair transitions involving oxygen and zinc vacancies, and copper impurities; however no conclusive evidence has yet been found which would enable a definite assignment.

3) Surface conductivity – ZnO has a highly active chemical and electrical surface, which has been widely used in gas sensing and catalytic processes. Since the 1960s it has been known that the presence of adsorbates such as oxygen, hydrogen, and water vapour can significantly change the band bending and electrical properties near the surface [11]. However, the adhesion chemistry and charge transfer behind these changes is not fully understood.

4) Schottky contact formation – due to its wide band gap, the formation of Schottky contacts to ZnO should be relatively straightforward. However, despite more than 50 years of effort, an agreed methodology (and a theoretical description) for the consistent fabrication of high quality Schottky contacts to ZnO is lacking.

The principal aim of this thesis is to progress the understanding of Schottky contact formation to ZnO, however this has necessarily involved a consideration of the other three unresolved issues.

1.2.2 Crystal Structure

Zinc oxide crystallizes in the hexagonal wurtzite structure (Figure 1.3a), defined by the *a* and *c* axes. This structure consists of two interpenetrating hexagonal close packed (hcp) sublattices, one for each type of atom, which are offset with respect to each other along the c-axis by the parameter *u*, which is defined as the length of the Zn–O bond along the c-axis in units of c. From Figure 1.3(a), $u = 1.992/5.206 = 0.382$ which represents a relaxation of the Zn and O atoms from the ideal wurtzite value of $u = 3/8 = 0.375$ [12]. Each oxygen atom is tetrahedrally co-ordinated to four zinc atoms and visa versa, which is typical of sp^3 covalent bonding, but each Zn–O bond also has a substantial ionic character. This creates a permanent electric dipole in each elementary tetrahedral unit, which results in a large macroscopic spontaneous polarisation of -0.057 Cm^{-2} [13].

ZnO is at the borderline between ionic and covalent classification with an ionicity of 39% [14] and is treated as an ionic oxide by catalytic chemists. The ZnO structure [Figure 1.3(b)] can be considered as a series of alternating planes of Zn and O atoms with the stacking sequence AaBbAa along the c-axis. Cleaving the crystal perpendicular to the c-axis results in two structurally different surfaces with three fold co-ordination: the Zn-polar (0001) surface

which consists of an entire outer plane of Zn atoms and an O-polar $(000\bar{1})$ surface with an outer plane of O atoms. The non-polar m-plane $(1\bar{1}00)$ and a-plane $(11\bar{2}0)$ surfaces are energetically more favourable, consisting of a mixed termination of an equal number of Zn and O atoms arranged in rows of Zn–O dimers.

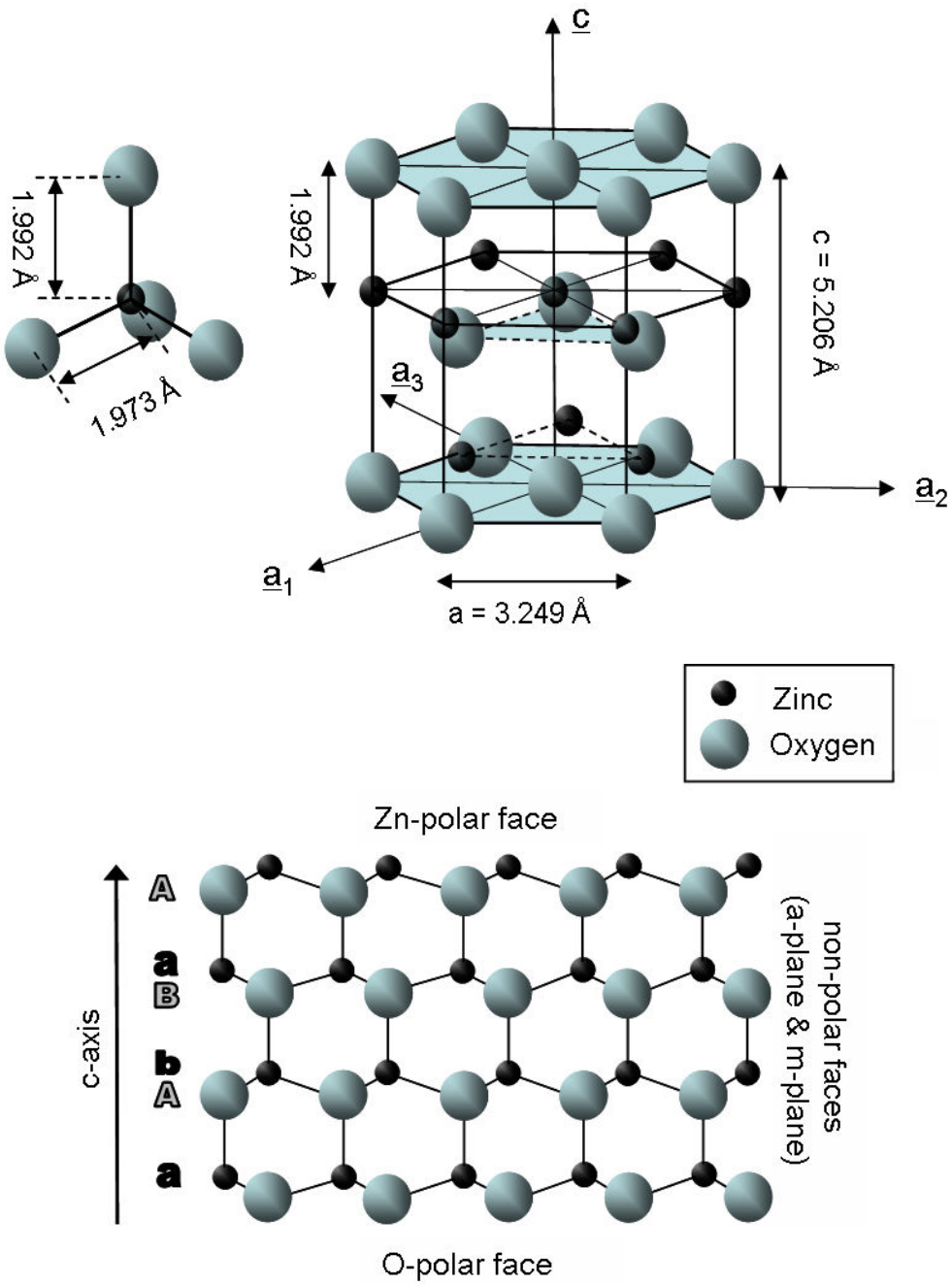

Figure 1.3: ZnO Wurtzite structure: (a) 3 dimensional view and (b) 2 dimensional projection along the$[11\bar{2}0]$ direction.

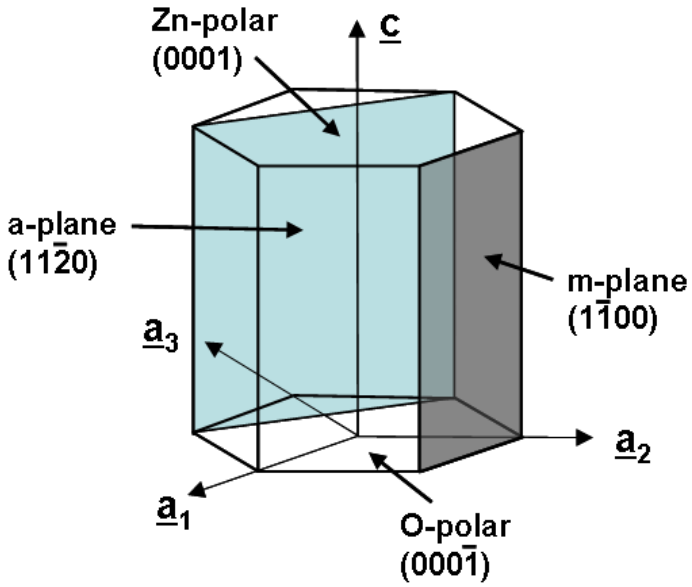

Figure 1.4: The non-polar a-plane (11$\bar{2}$0) and m-plane (1$\bar{1}$00) faces of wurtzite ZnO.

1.2.3 Bulk Crystal Growth

ZnO oxide has the outstanding advantage of the commercial availability of the bulk grown single crystal wafers, which have significantly lower dislocation densities than the best GaN or SiC material. These wafers are produced by the following methods:

1) Seeded Chemical Vapour Growth [15] — sublimation of polycrystalline ZnO precursor material and deposition onto a seed crystal.

2) Melt Growth [16] — radio frequency induction melting and subsequent cooling of the ZnO precursor material in a cold wall crucible with an over-pressure of oxygen [Figure 1.5(a)].

3) Hydrothermal Growth [17] — ZnO precursor material dissolved in an aqueous solution of LiOH and KOH mineralisers and placed in a platinum lined, steel autoclave. Crystallisation takes place at approximately 300^{o}C and a pressure of 80 MPa onto a seed crystal [Figure 1.5(b)].

In most semiconductor systems, such as Si and GaAs, bulk grown wafers are used as templates for the lattice matched growth of higher quality thin films by techniques such as molecular beam epitaxy, pulsed laser deposition, and chemical vapor deposition. However, at the present time, bulk grown wafers provide the best available ZnO material in terms of

crystallinity, surface morphology, and electron mobility. Due to the very low thermal gradients present during growth, hydrothermal ZnO has the highest crystallinity and lowest dislocation density. It also tends to have a higher extrinsic impurity concentration, from the incorporation of Li and Na from the LiOH and NaOH mineralisers used to dissolve the ZnO precursor material. These group I impurities are acceptors which suppress the carrier concentration of hydrothermally grown ZnO by 2 – 3 orders of magnitude. The availability of a range of high quality, bulk ZnO material with similar mobilities but large differences in carrier concentration is very useful, as it allows the effect of carrier concentration on the electrical and optical properties of ZnO to be investigated.

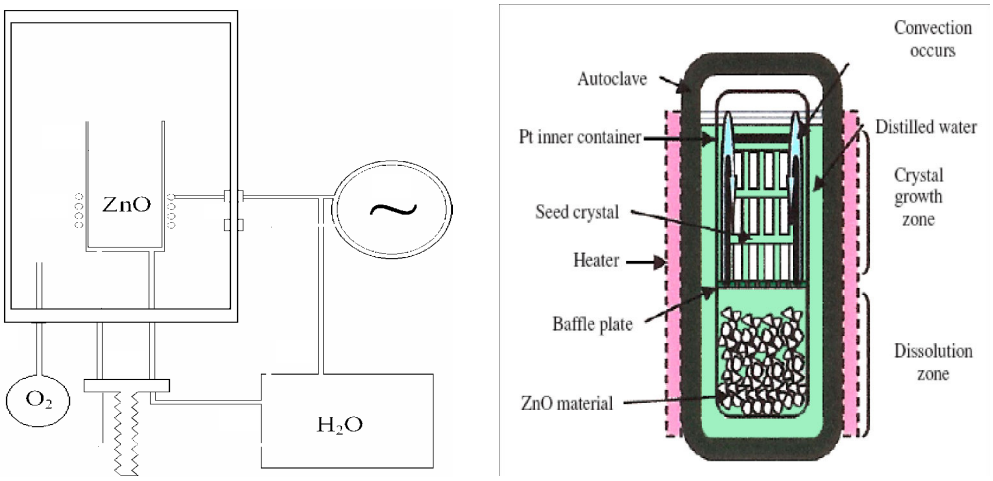

Figure 1.5: Schematic illustration of (a) melt, and (b) hydrothermal growth of bulk ZnO crystal boules [16,17].

1.3 THESIS OUTLINE

In this thesis, single crystal, bulk wafers, grown using the hydrothermal and melt techniques were used to investigate the formation of Schottky contacts to ZnO and to develop a new technology for the consistent production of high quality rectifying devices. Melt grown wafers were obtained from Cermet Inc., Atlanta, Georgia, (USA), and the hydrothermally grown material was purchased from Tokyo Denpa Co. Ltd., Tokyo, (Japan). A comparison of their properties is given in Table 1.2. Both these types of bulk ZnO provide consistent, high quality, baseline material allowing systematic studies of Schottky contact formation to be carried out.

Table 1.2: Comparison of single crystal, bulk ZnO grown using the hydrothermal [Tokyo Denpa Co. Ltd (Japan)] and melt [Cermet Inc. (USA)] techniques [16,17].

	Hydrothermal ZnO	Melt ZnO
growth temperature	300 – 400 ^{o}C	> 1975 ^{o}C
growth rate	1 mm/day	1-5 mm/hr
X-ray rocking curve	8 arcsec FWHM	30 arcsec FWHM
free electron concentration (300 K)	$10^{13} – 10^{14}$ cm^{-3}	$10^{16} – 10^{17}$ cm^{-3}
electron mobility (300 K)	200 cm^{2}V^{-1}s^{-1}	200 cm^{2}V^{-1}s^{-1}
resistivity (300 K)	3000 – 300 Ωcm	3 – 0.3 Ωcm
etch pit density	~ 300 cm^{-2}	~ 10^4 cm^{-2}

Chapter 2 provides the theoretical background to Schottky contact formation and a comparison of the competing theoretical descriptions: the Schottky–Mott, Metal Induced Gap States, Chemical Bond Polarisation, and Induced Defect models. Schottky contact formation takes place on the semiconductor surface, which is complex in nature, containing electronic states which are often significantly different from those in the semiconductor bulk. Chapter 3 investigates the nature of the ZnO surface, using atomic force microscopy, x-ray photoemission microscopy, photoluminescence microscopy, and variable magnetic field Hall effect measurements. The dependence of surface properties on crystallographic orientation is also established.

Historically, the most effective way to investigate Schottky contact formation to other semiconductors has been to compare the properties of contacts fabricated using different metals with a range of work functions. This is done for ZnO in Chapter 4, via a number of systematic experiments into the variation of ZnO Schottky contact performance over a range of Schottky metals. These experimental results are compared against the predictions of the theoretical models introduced in Chapter 2. The most significant finding of Chapter 4 was the improved performance of oxidised silver Schottky contacts. A detailed investigation of this effect is carried out in Chapter 5, in which the discovery of the superior rectifying performance of metal oxide Schottky contacts fabricated in reactive oxygen ambients is presented.

During the course of the investigations into Schottky contact formation, a number of previously unreported, surface polarity related effects were observed. These are described in Chapter 6 and compared with two contrasting theoretical descriptions: the spontaneous polarisation and ionic models. Chapter 7 presents a new theoretical description of Schottky

contact formation to ZnO, in which the density of interfacial oxygen vacancies determines the degree of Fermi level pinning of the resulting Schottky contact. The ability of this model to explain the results contained in this thesis and those in the literature is discussed.

Finally Chapter 8 is a review of the main conclusions of this thesis and an outline of the future work needed.

Chapter 2

Schottky Contact Models

This chapter introduces the concept of Schottky contacts between metals and semiconductors, explains the 'figures of merit' of contact performance, describes how these can be determined, and how different current transport processes can be identified. Various models of Schottky contact behaviour are introduced which make different assumptions concerning the nature of the interaction between the metal and the semiconductor.

2.1 INTRODUCTION

Schottky diodes are essentially the most simple of devices consisting of two types of metal contact to a given semiconductor: a rectifying (Schottky) contact and a non-rectifying (Ohmic) contact. However, despite more than half a century of concerted effort, the fundamental mechanisms governing Schottky contact formation are still not fully defined and remain the subject of ongoing debate. This is largely due to the complex nature of semiconductor surfaces, which have reconstructed features and a higher density of unsatisfied (dangling) bonds compared to the semiconductor bulk. Semiconductor surfaces are also prone to contamination by either the physisorption or chemisorption of external adsorbates such as carbon, water vapour, and oxygen molecules.

2.2 SCHOTTKY CONTACT FORMATION

The rectifying effect of metal – semiconductor contacts was first discovered by Braun [18] in 1874, who observed one-way conduction in a galena (lead sulfide) crystal when contacted by a thin metal wire. This arrangement is known as a point rectifier and found widespread use in early crystal radio receivers. Point rectifiers have a low capacitance, which is important for radio detection, but have poor rectification and early reverse breakdown due to electric field crowding near the sharp contact. Most modern Schottky diodes use larger area (10 μm - 1 mm diameter) contacts fabricated using a variety of techniques, such as thermal evaporation, electron beam evaporation, sputtering, and pulsed laser deposition, usually in high vacuum conditions to avoid oxidation of the metal.

2.2.1 The Schottky-Mott Model

Schottky barrier formation was explained by Schottky [19] and Mott [20] in 1938 in terms of a space charge region on the semiconductor side of the contact which is depleted of majority charge carriers. The Schottky – Mott model assumes no interaction of any kind between the metal and the semiconductor. Since the respective Fermi levels of any two solids in contact must be the same in thermal equilibrium, the Schottky barrier is created by the redistribution of electric charge between the metal and semiconductor as their respective Fermi levels equalise. This process is shown in Figure 2.1 for a metal of work function ϕ_M immediately before and after contact with an *n*-type semiconductor of electron affinity χ_S.

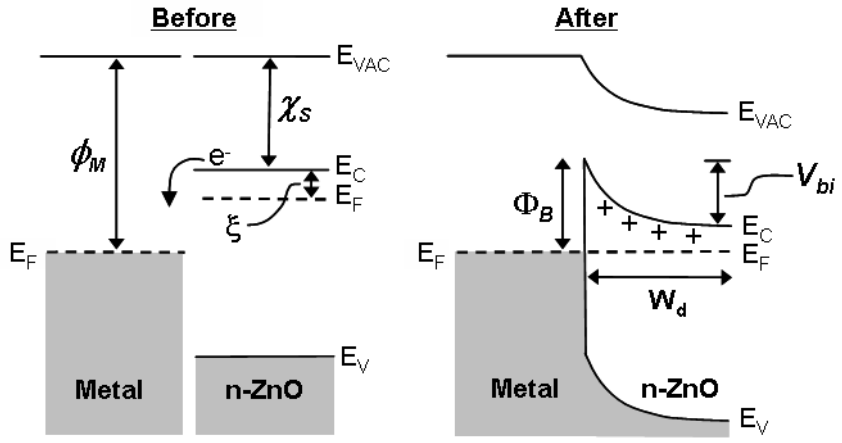

Figure 2.1. Schottky contact formation for an *n*-type semiconductor.

Before contact, the Fermi levels of the metal and semiconductor, referenced to the vacuum level, are ϕ_M and $\chi_S + \xi$ respectively, where ξ is the energy difference between the bottom of the conduction band (E_C) and the Fermi level (E_F). On contact, electrons flow from the semiconductor to the metal until the Fermi levels line up, leaving behind a depletion region of positive space charge in the semiconductor. The density of states at the metal Fermi level is so high that the transfer of charge from the semiconductor causes negligible change in its position. Hence, the depletion region lies in the semiconductor only.

In the absence of interface states, the Schottky barrier height is simply the difference between the work function of the metal and the electron affinity of the semiconductor,

$$\Phi_B = \phi_M - \chi_S \ . \tag{2.1}$$

The width of the depletion region W_d can be determined by applying the Poisson equation to the positive charge density created in the semiconductor. This is done using the "*abrupt*" or "*full depletion*" approximation [21, 22] in which:

1) the semiconductor is assumed to be fully depleted throughout W_d, i.e. all donors are completely ionised between the Schottky interface and W_d; and
2) outside the depletion region the semiconductor is neutral and the electric field is zero.

Using this approximation, the charge density in the depletion region is a step function, as shown in Figure 2.2(a),

$$\rho(x) = \begin{cases} qN_D & 0 < x < W_d \\ 0 & x \geq W_d \end{cases} \tag{2.2}$$

where N_D is the effective doping density of the semiconductor. The positive charge in the semiconductor ($Q_S = qN_DW_d$) is exactly balanced by the negative charge in the metal ($Q_M = -Q_S$) so that the electric field is zero outside the depletion region. The one-dimensional Poisson equation can be solved to find the electric field distribution $E(x)$,

$$\frac{dE}{dx} = -\frac{d^2V}{dx^2} = \frac{\rho(x)}{\varepsilon_S\varepsilon_0} . \tag{2.3}$$

Using the boundary condition $E(W_d) = 0$, the electric field [Figure 2.2(b)] in the depletion region is,

$$E(x) = \begin{cases} -\dfrac{qN_D}{\varepsilon_S\varepsilon_0}(W_d - x) & 0 < x < W_d \\ 0 & x \geq W_d \end{cases} \tag{2.4}$$

where the maximum electric field, $E_{max} = -qN_DW_d/\varepsilon_S\varepsilon_0$, occurs at the Schottky interface. Equation (2.4) can be integrated to give the potential distribution [Figure 2.2(c)] in the semiconductor, where the potential drop across the depletion region is known as the built-in voltage V_{bi},

$$V(x) = \begin{cases} -V_{bi}\left(1 - \dfrac{x}{W_d}\right)^2 & 0 < x < W_d \\ 0 & x \geq W_d \end{cases} \tag{2.5}$$

where the width of the depletion region (W_d) and the built in voltage (V_{bi}) are related by,

$$W_d = \sqrt{\frac{2\varepsilon_s\varepsilon_0 V_{bi}}{qN_D}} \; . \tag{2.6}$$

The built in voltage (V_{bi}) is related to the barrier height (Φ_B) of the Schottky contact by $\Phi_B = V_{bi} + \xi$. In practice, the thermal energy distribution of the majority carriers must be taken into account and this causes a reduction in the potential drop across the depletion region of kT/q. As a result, the width of the depletion region W_d and the maximum electric field E_{max} now becomes,

$$W_d = \sqrt{\frac{2\varepsilon_s\varepsilon_0}{qN_D}\left(V_{bi} - \frac{kT}{q}\right)} \tag{2.7}$$

and

$$E_{max} = -\sqrt{\frac{2qN_D}{\varepsilon_s\varepsilon_0}\left(V_{bi} - \frac{kT}{q}\right)} \; . \tag{2.8}$$

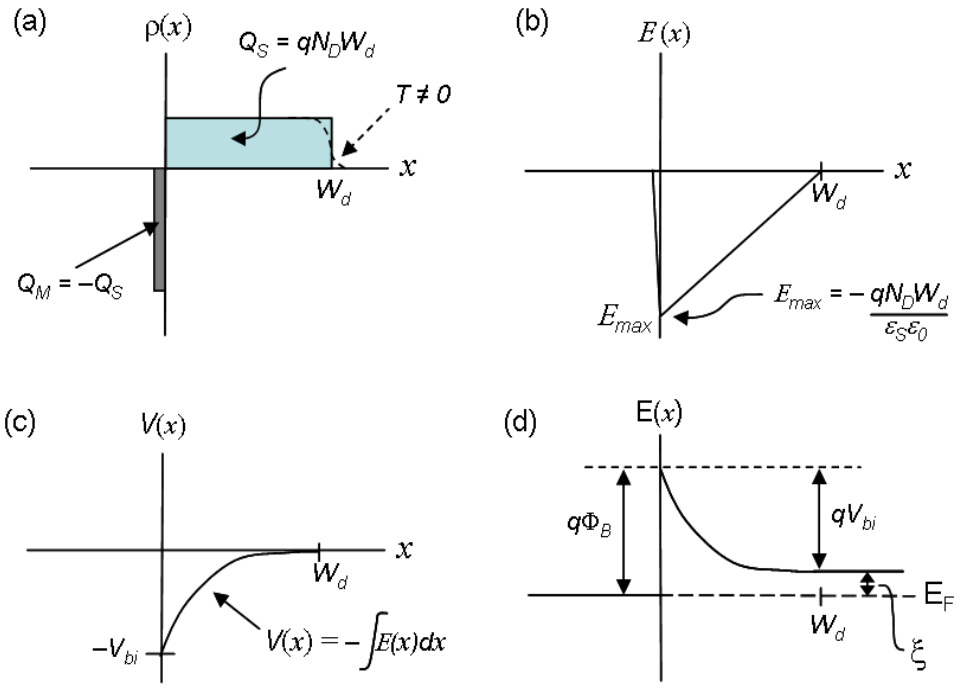

Figure 2.2. Analysis of the Schottky contact depletion region using the Poisson equation and the "*full depletion"* approximation: (a) charge density, (b) electric field, (c) potential, and (d) energy variations.

2.3 MEASURING SCHOTTKY BARRIER HEIGHTS

2.3.1 Current–Voltage (*I–V*) Characteristics

The most widely used method to determine the barrier height of a Schottky contact is to measure its current–voltage (*I–V*) characteristics [23]. The accepted theory of current transport across a Schottky contact was developed by Hans Bethe while working on microwave radar during World War II, and reported in a M.I.T. Radiation Laboratory Report dated November 23, 1942 [24]. In Bethe's theory, the current is determined by the thermionic emission of electrons (for *n*-type semiconductors) over the Schottky barrier. This is valid provided the electrons approaching the barrier are in thermal equilibrium and the emission probability is low enough that the resulting current flow does not disturb this thermal equilibrium. In practice these conditions are met provided $\Phi_B >> kT/q$.

The thermionic emission (TE) of electrons in either direction over a potential barrier of height Φ_B is [22],

$$J_{TE} = A^* T^2 exp\left(-\frac{q\Phi_B}{kT}\right) \tag{2.9}$$

where J_{TE} is the current density, A^* the Richardson constant, k the Boltzmann constant, and T the semiconductor temperature. When the Schottky contact is forward biased [Figure 2.3(a)] by an external voltage V, the barrier potential is lowered to $\Phi_B - qV$. The electron flow from the semiconductor to the metal increases and the forward current density is now,

$$J_{fwd} = A^* T^2 exp\left[-\frac{q(\Phi_B - V)}{kT}\right] . \tag{2.10}$$

The current density flowing in the reverse direction (electron flow from the metal to the semiconductor) is independent of the applied bias voltage and is known as the saturation current density J_0 where,

$$J_0 = A^* T^2 exp\left(-\frac{q\Phi_B}{kT}\right) . \tag{2.11}$$

The net current flowing across the Schottky contact is therefore,

$$J = J_{fwd} - J_0 = J_0\left[exp\left(\frac{qV}{kT}\right) - 1\right] . \tag{2.12}$$

For applied bias voltages $V >> kT/q$ the -1 term in equation (2.12) is negligible and the current density should increase exponentially with V.

When the Schottky contact is reversed biased [Figure 2.3(b)], the barrier potential increases to $\Phi_B + qV$ which makes $J_{fwd} << J_0$ and the net current density is equal to the saturation current density J_0 which is independent of V.

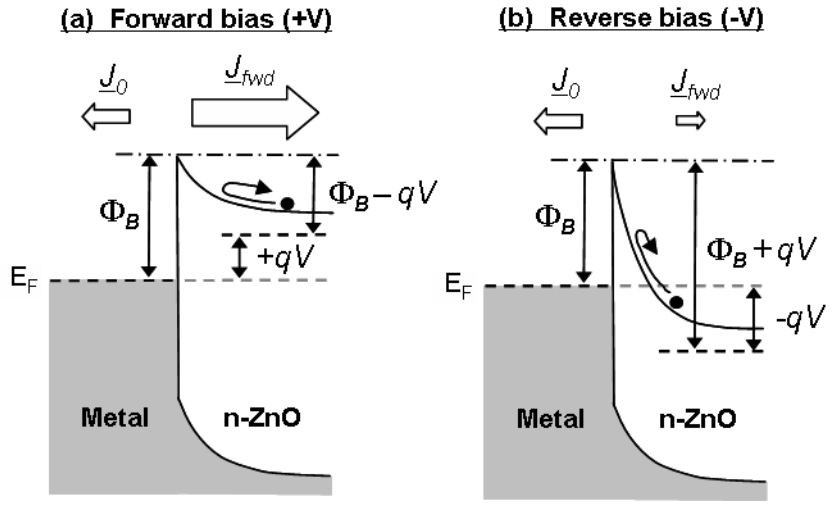

Figure 2.3. Band diagram of a Schottky contact to an n-type semiconductor under (a) forward and (b) reverse bias conditions.

Equation (2.12) represents the ideal case of pure thermionic emission over a homogeneous, defect free, Schottky barrier with no interface states. For the analysis of real I–V characteristics an ideality factor η is introduced into (2.12) giving,

$$J = J_0\left[exp\left(\frac{qV}{\eta kT}\right) - 1\right] \tag{2.13}$$

provided the contact area is known, I–V characteristics are usually plotted as lnJ versus V from which η can be obtained from the slope of the linear region of the forward bias region. Provided $V >> kT/q$,

$$\eta = \frac{q}{kT} ln\left(\frac{d\,lnJ}{dV}\right)^{-1} . \tag{2.14}$$

The effective barrier height Φ_B can be obtained by extrapolating the same linear region to V = 0 V to find the saturation current density J_0 from which,

$$\Phi_B = -\frac{kT}{q} ln\left(\frac{J_0}{A^* T^2}\right) . \tag{2.15}$$

Values of η greater than unity are caused by non-ideal behaviour which cause the Schottky contact to deviate from pure thermionic transport. The most common types of non-ideal

behaviour are image force lowering, field emission, and lateral contact inhomogeneity which are described in Section 2.4.

2.3.2 Capacitance–Voltage (*C–V*) Characteristics

The capacitance–voltage (*C–V*) technique provides an alternative method of measuring the barrier height that does require the dimensions of the contact. It can also be used to obtain a depth profile of the effective donor concentration of the semiconductor [23].

The depletion region of the Schottky contact is a natural dielectric. It lies entirely within the semiconductor and consists of space charge from ionised donors which are largely unscreened by mobile carriers. The depletion region thus forms a "parallel plate" capacitor with the metal and the undepleted bulk of the semiconductor. When an external voltage is applied, the width of the depletion region (W_d) changes, increasing under reverse bias as more unscreened ionised donors are exposed. The width of the depletion region at zero bias was derived in Section 2.2.1 using the Poisson equation and the "*full depletion*" approximation. Under a small applied bias V, Equation (2.7) is simply modified by a change of the boundary condition from $V(W_d) = 0$ to $V(W_d) = V$ to give,

$$W_d = \sqrt{\frac{2\varepsilon_s\varepsilon_0}{qN_D}\left(V_{bi} - \frac{kT}{q} - V\right)} \ . \tag{2.16}$$

The total space charge Q_{SC} in the depletion region is,

$$Q_{sc} = qN_D W_d A \tag{2.17}$$

where A is the area of the contact and N_D is the effective donor density. The small-signal capacitance of the Schottky junction $C = dQ/dV$ is then,

$$C = A\sqrt{\frac{q\varepsilon_s\varepsilon_0 N_D}{2(V_{bi} - kT/q - V)}} \quad so \quad \frac{A^2}{C^2} = \left(\frac{2}{q\varepsilon_s\varepsilon_0 N_D}\right)\left(V_{bi} - \frac{kT}{q} - V\right). \tag{2.18}$$

In *C–V* characterisation, $1/C^2$ is measured as a function of the applied bias voltage V by applying a small a.c. signal (typical frequency 10 kHz - 1 MHz). The effective donor concentration (depth profile) can be obtained from the slope of the $1/C^2$ *vs* V plot,

$$N_D = -\frac{2}{A^2 q\varepsilon_s\varepsilon_0}\left[\frac{d}{dV}(1/C^2)\right]^{-1} \tag{2.19}$$

while V_{bi} is obtained from the intercept of the slope with the $1/C^2$ axis. If the Schottky contact is inhomogeneous then the *C–V* technique will give the average V_{bi}.

2.4 SOURCES OF NON-IDEAL BEHAVIOUR

The common sources of non-ideal current transport through a Schottky contact are illustrated in Figure 2.4. The other major cause of non-ideal behaviour is barrier height inhomogeneity in which there is a spatial distribution of the barrier height across the contact.

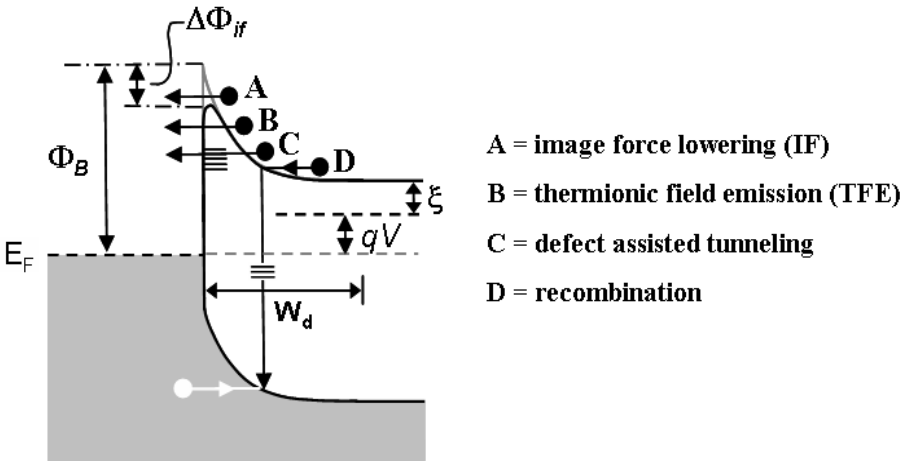

Figure 2.4. Non-ideal current transport processes across a Schottky diode under a forward bias of V.

2.4.1 Image Force Lowering

The effective barrier height of all Schottky junctions, even for perfectly homogeneous contacts with no interface states, is slightly reduced due to image force (IF) lowering, also known as the Schottky effect. As an electron approaches the barrier, it experiences a small attractive force with the positive "image" charge that is induced in the metal [25, 26]. This effect lowers the height of the barrier by an amount $\Delta\Phi_{if}$ given by,

$$\Delta\Phi_{if} = \left[\left(\frac{q^3 N_D}{8\pi^2 \varepsilon_\infty^2 \varepsilon_s \varepsilon_0^3}\right)\left(\Phi_B - V - \xi - \frac{kT}{q}\right)\right]^{\frac{1}{4}} . \qquad (2.20)$$

Since $\Delta\Phi_{if}$ increases with increasing reverse bias, image force lowering causes Φ_B to be a function of V. For a given semiconductor, $\Delta\Phi_{if}$ also depends on the effective doping concentration N_D, and although $\Delta\Phi_{if}$ is small for moderately doped semiconductors, it does lead to a voltage dependence of the reverse current which would otherwise be constant at J_o [Equation (2.11)]. Since barrier lowering is only experienced by electrons approaching the interface, it only affects I–V and not C–V measurements. The increased ideality factor (η_{if}) of a Schottky diode due to image force lowering is given by,

$$\frac{1}{\eta_{if}} = 1 - \frac{\Delta\Phi_{if}}{4}\left(\Phi_B - V - \xi - \frac{kT}{q}\right)^{-1} . \tag{2.21}$$

2.4.2 Thermionic Field Emission

The width of the depletion region W_d is proportional to $N_D^{-1/2}$ [Equation (2.16)]. Therefore, in heavily doped semiconductors the barrier may be thin enough for electrons to tunnel directly through it. A more likely process for moderately doped semiconductors is thermionic field emission (TFE), in which carriers are thermally excited to a position on the barrier which is sufficiently thin for tunneling to occur. A comparison of the tunneling parameter E_{00} with the thermal energy kT determines the relative probability of these processes [22, 25],

$$E_{00} = \frac{qh}{4\pi}\left(\frac{N_D}{m^*\varepsilon_s\varepsilon_0}\right)^{\frac{1}{2}} \tag{2.22}$$

where m^* is the effective electron mass. When $E_{00} << kT$ the dominant current transport process is thermionic emission, whereas when $E_{00} >> kT$ field emission (tunneling) becomes important. For $E_{00} \sim kT$, current transport will be significantly affected by TFE which causes a lowering $\Delta\Phi_{TFE}$ of the effective barrier height given by,

$$\Delta\Phi_{TFE} = \left(\frac{3E_{00}}{2}\right)^{\frac{2}{3}}\left(\Phi_B - \xi - \frac{kT}{q}\right)^{\frac{1}{3}} \tag{2.23}$$

and an increased ideality factor of,

$$\eta_{TFE} = \frac{qE_{00}}{kT}\coth\left(\frac{qE_{00}}{kT}\right) . \tag{2.24}$$

For Schottky contacts to semiconductors with $N_D < 10^{18}$ cm^{-3} the probability of TFE is very small, except possibly at very low temperatures. This situation can change with the presence of defect states or traps in the depletion region of the semiconductor which increase the tunneling probability and consequently η_{TFE}, as electrons can first tunnel into these defect states and then through the barrier.

2.4.3 Recombination

Recombination currents can occur in the depletion region of a Schottky contact due to the simultaneous capture of electrons and holes by defect states in the semiconductor. The recombination current is given by,

$$J_{rc} = \frac{qN_i W_d}{2\tau}\left[exp\left(\frac{qV}{\eta_{rc}kT}\right)\right] \tag{2.25}$$

where η_{rc} is the ideality factor for this process (which is typically close to 2), N_i is the minority carrier concentration, and τ is the minority carrier lifetime within the depletion region. For wide band gap semiconductors such as ZnO, N_i and therefore J_{rc} are very small. For these materials, hopping current transport may be more effective, with electrons tunneling between successive defect states.

2.4.4 Schottky Barrier Inhomogeneity

Real Schottky contacts are likely to contain inhomogeneities that cause a spatial variation in barrier height. These fluctuations may be caused by:

- structural defects (e.g. dislocations, pits, grain boundaries, polishing damage, roughness) at the semiconductor surface;
- surface contamination (e.g. adsorbates such as hydrocarbons, water vapour, and oxygen);
- intrinsic point defects or intrinsic defect clusters (e.g. vacancies, vacancy clusters, interstitials); or
- extrinsic surface defects (e.g. metal interdiffusion spikes or doping inhomogeneity).

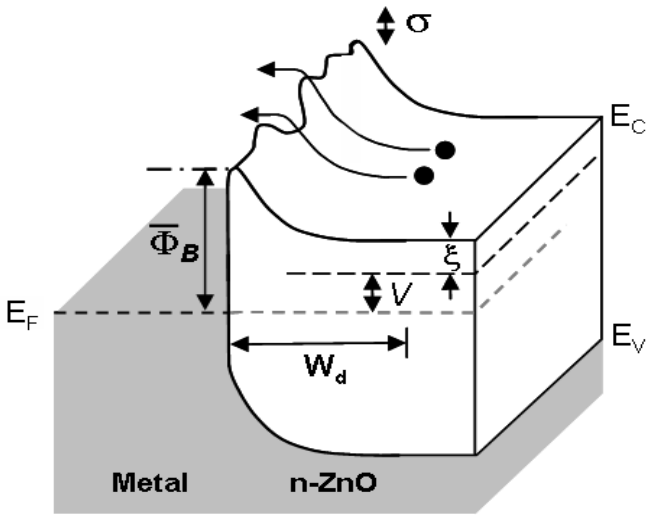

Figure 2.5. Band diagram (in two dimensions) of an inhomogeneous Schottky contact under an applied forward bias *V*.

Henisch [27] proposed that barrier height fluctuations are unavoidable and occur even in the most carefully fabricated Schottky contacts. Werner and Guttler [28] developed a widely used model for Schottky barrier fluctuations caused by spatial inhomogeneities of a length scale less than the depletion region width W_d. They assumed a Gaussian distribution $P(\Phi_B)$ of barrier heights with a mean value $\overline{\Phi}_B$ and a standard deviation σ. By integrating the current flow over $P(\Phi_B)$ they found the following relation for the apparent, effective barrier height of an inhomogeneous contact from *I–V* measurements:

$$\Phi_B^{inh} = \overline{\Phi}_B - \frac{q\sigma^2}{2kT} . \tag{2.26}$$

Equation (2.26) reflects the fact that d.c. current will tend to flow preferentially through the low barrier height regions especially at low temperatures. The apparent ideality factor is given by,

$$\frac{1}{n_{imh}} - 1 = -\rho_2 + \frac{q\rho_3}{2kT} \tag{2.27}$$

where ρ_2 and ρ_3 are coefficients which quantify the change in the barrier height distribution $P(\Phi_B)$ with bias voltage V.

The same authors also argued that capacitance measurements are insensitive to potential fluctuations of a length scale less than W_d and therefore the barrier height determined by the *C–V* technique represents the mean value $\overline{\Phi}_B$.

2.5 INTERACTING SCHOTTKY CONTACT MODELS

Over the past 50 years, the Schottky – Mott model, which assumes no interaction between the metal and semiconductor, has been extensively tested for a wide range of semiconductors by investigating the dependence of the Schottky barrier height on the metal work function to find the interface behaviour parameter,

$$S_\Phi = \frac{d\Phi_B}{d\phi_M} \tag{2.28}$$

where $S_\Phi = 1$ for the Schottky - Mott model [from Equation (2.1)]. Figure 2.6 shows experimental values of S_Φ for a range of common semiconductors [29].

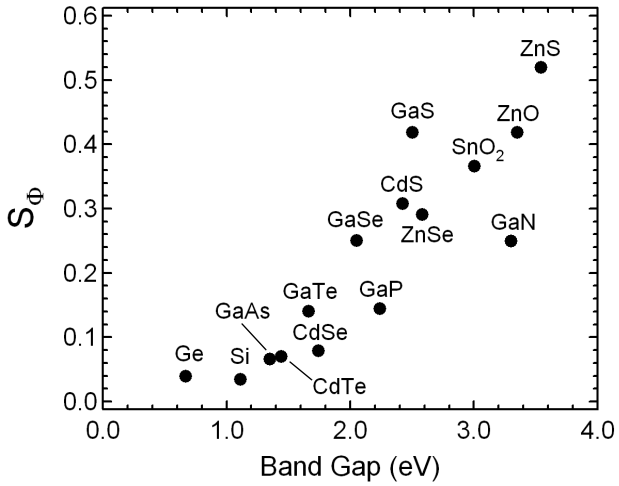

Figure 2.6. Experimentally determined interface behaviour parameter S_Φ versus semiconductor band gap [29].

In general, metals with larger work function systematically produce higher Schottky barriers, however the experimentally determined S_Φ for most semiconductors are much lower than unity, and in some cases (e.g. Si and Ge) the measured barrier height is almost independent of the Schottky metal. This phenomenon is known as Fermi level pinning and is usually attributed to the presence of charged interface states near the Schottky interface which form an electric dipole lowering the effective barrier height [30],

$$\Phi_B = \phi_M - \chi_S + qV_{int} \tag{2.29}$$

where V_{int} is the potential due to the interface dipole.

The poor predictive ability of the Schottky – Mott model has led to the introduction of subsequent models which assume some kind of interaction at the Schottky interface, such as the overlap of electron wave functions, chemical bonding, or the creation of defects. These interactions provide the source of the interface dipole term in Equation (2.29) provided they create an interface charge in the semiconductor with a small physical separation δ (~ a few Angstroms) from the metal. Consequently, models of this type are often referred to as fixed separation models [25]; three competing versions will now be described.

2.5.1 Metal Induced Gap States (MIGS) Model

In 1947, Bardeen [31] proposed that a high density of charged surface states on the semiconductor could cause pinning of the Fermi level at the Schottky interface. In 1965, Heine [32] showed that the wave functions of the metal electrons can tail or tunnel into the

semiconductor in the energy range where the metal conduction band overlaps the semiconductor band gap. The contemporary extension of Heine's work is now referred to as the Metal Induced Gap States or MIGS model [33] in which the distribution of MIGS, $D_{GS}(E)$, (number of gap states per unit area per eV) is assumed to be determined only by the semiconductor. This distribution contains an energy level called the charge neutrality level, at a potential ϕ_{CNL}, below which the MIGS are donor-like (neutral when filled, positively charged when empty) and above which the MIGS are acceptor-like (negatively charged when filled, neutral when empty). This charge neutrality level is also referred to in the literature as the branch point energy.

The MIGS model still assumes an ideal (i.e. purely thermionic), defect free, and laterally homogeneous Schottky interface in which the only interaction is from the decay of electron wave functions from the metal into the semiconductor, which changes the charge distribution near the interface. This model provides an explanation for the observed weak dependence of barrier height on metal work function and gives a better agreement with actual observations [33].

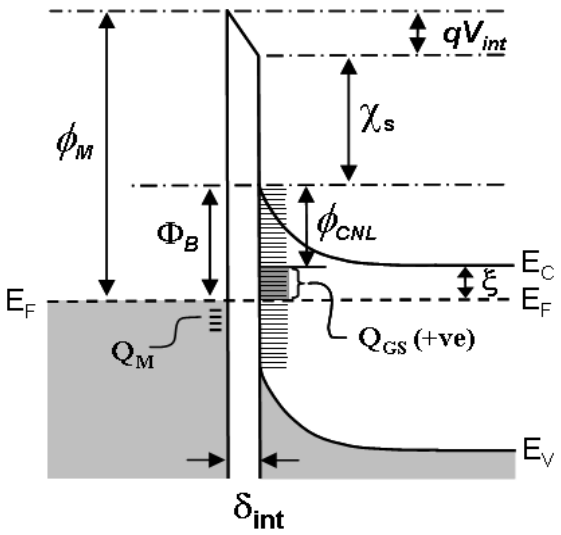

Figure 2.7. Schottky barrier formation using the metal induced gap states (MIGS) model [25].

On Schottky contact formation, the MIGS are filled up to the interface Fermi level (E_F). For the situation shown in Figure 2.7, the Fermi energy lies below the charge neutrality level and so the interface states have a net positive charge Q_{GS} per unit area,

$$Q_{GS} = qD_{GS}(\Phi_B - \phi_{CNL}) \tag{2.30}$$

where the density of gap states, $D_{GS}(E)$, is assumed to be constant near ϕ_{CNL}. When $E_F > \phi_{CNL}$ the interface states have a net negative charge, while for $E_F = \phi_{CNL}$ the net interface charge is zero.

Schottky interfaces must be electrically neutral in thermal equilibrium. The charge per unit area on the semiconductor side of the interface is the sum of Q_{GS} and the space charge due to unscreened ionised donors Q_{SC}. This must be balanced by an equal charge density Q_M of opposite sign on the metal so that,

$$Q_M + Q_{GS} + Q_{SC} = 0 \ . \tag{2.31}$$

Gauss's law can be applied to the metal surface of the interface layer to calculate the electric field which is assumed to be uniform,

$$E = -\frac{V_{int}}{\delta_{int}} = -\frac{Q_M}{\varepsilon_{int}\varepsilon_0} \tag{2.32}$$

where ε_{int} is the dielectric constant of the interface region (which can be approximated by $2\varepsilon_\infty$ where ε_∞ is the optical dielectric constant of the semiconductor [30]) and δ_{int} is the separation between the MIGS and the metal (assumed to be approximately the decay length of the MIGS).

For most Schottky contacts it can be shown that $Q_{SC} << Q_{GS}$ in which case Equations (2.30), (2.31), and (2.32) can be combined to give the voltage drop V_{int} due to the interface dipole,

$$V_{int} = \frac{q\delta_{int}D_{GS}(\Phi_B - \phi_{CNL})}{\varepsilon_{int}\varepsilon_0} \ . \tag{2.33}$$

This can used in equation (2.29) to give,

$$\Phi_B = \phi_M - \chi_S + \frac{q^2\delta_{int}D_{GS}(\Phi_B - \phi_{CNL})}{\varepsilon_{int}\varepsilon_0} \tag{2.34}$$

which can be further rearranged to,

$$\Phi_B = \gamma_{GS}(\phi_M - \chi_S) + (1 - \gamma_{GS})\phi_{CNL} \tag{2.35}$$

where γ_{GS} is the gap states parameter,

$$\gamma_{GS} = \left(1 + \frac{q^2\delta_{int}D_{GS}}{\varepsilon_{int}\varepsilon_0}\right)^{-1} \ . \tag{2.36}$$

In the MIGS model, the Schottky barrier height is essentially determined by the charge neutrality level (ϕ_{CNL}) of the semiconductor and the density of MIGS (D_{GS}). When the density of MIGS is high, $\gamma_{GS} << 1$ and Φ_B is pinned close to the ϕ_{CNL}, while if the density of MIGS is low, $\gamma_{GS} \sim 1$ and the Schottky - Mott relationship is regained. The interface behavior parameter $S_\Phi = d\Phi_B/d\phi_M$, defined earlier, is actually equal to γ_{GS} for the MIGS model, and is determined by the density of states (D_{GS}) and the decay length (δ_{int}) of the MIGS. The CNL potential (ϕ_{CNL}) is also referred to as the zero charge transfer barrier height Φ_{bp} [26] and the energy level of the CNL relative the vacuum level is known as the branch point energy W_{bp}.

Mönch [26, 33] proposed that the branch point energies of semiconductors $W_{bp} = q(\chi_s + \phi_{CNL})$ vary linearly with their electronegativities (X_S) with the same constant of proportionality A_X (A_X = 0.86 eV per Miedema electronegativity unit or 1.79 eV per Pauling unit) as the relationship between metal work functions and their electronegativities (X_M). In this case, equation (2.35) can be rewritten to give,

$$\Phi_B = \Phi_{bp} + S_X(X_M - X_S) \quad where \quad S_X = \gamma_{GS} A_X \,. \tag{2.37}$$

$S_X = d\Phi_B/dX_M$ is a new interface behaviour parameter. Mönch determined the branch point energies of a number of semiconductors from band gap calculations using the empirical tight binding approach [33, 34]. He also deduced a simple approximation for calculating γ_{GS} and S_X from the optical dielectric constant ε_∞ which is known for most semiconductors,

$$\gamma_{GS} = [1 + 0.1(\varepsilon_\infty - 1)^2]^{-1} \,. \tag{2.38}$$

Therefore the interface behaviour parameters $S_\Phi = d\Phi_B/d\phi_M$ and $S_X = d\Phi_B/dX_M$ can be approximated by,

$$S_\Phi = [1 + 0.1(\varepsilon_\infty - 1)^2]^{-1} \quad and \quad S_X = A_X[1 + 0.1(\varepsilon_\infty - 1)^2]^{-1} \,. \tag{2.39}$$

The MIGS model can be tested by comparing the experimentally determined S_Φ or S_X for a number of semiconductors against the prediction of equation (2.39). This is usually done by constructing plots of $(S_\Phi^{-1} - 1)$ against $(\varepsilon_\infty - 1)^2$. However, care must be taken because the MIGS model is only strictly valid for the image-force-corrected barrier heights Φ_B^{hom*} of ideal, laterally homogeneous Schottky contacts [26]. Real contacts nearly always have some form of non-ideality, often due to inhomogeneities in the Schottky interface. Mönch suggested that Φ_B^{hom*} can be determined for a given metal – semiconductor combination by plotting the experimentally determined effective barrier heights (Φ_B) and ideality factors (η) for multiple Schottky diodes, extrapolating the relationship to find the barrier height (Φ_B^{if}) corresponding to the image force controlled limit (η_{if}), and then adding the image force lowering correction

$\Delta\Phi_{if}$. A reasonable correlation between $(S_{\Phi}^{-1} - 1)$ and $(\varepsilon_{\infty} - 1)^2$ has been found (Figure 2.8) providing support for the MIGS fixed separation model, as have the demonstrations of the existence of MIGS using scanning tunneling spectroscopy [36, 37].

The width of the interface region δ_{int} over which the charge separation and interface dipole occurs is related to the exponential decay length of the MIGS, which is shorter for ionic semiconductors compared to covalent semiconductors due to greater screening. As a result, $\gamma_{GS,covalent} < \gamma_{GS,ionic}$, and Fermi level pinning due to MIGS is expected to be more dominant for covalent semiconductors, such as Si, Ge and GeAs, than for more ionic semiconductors such as ZnO.

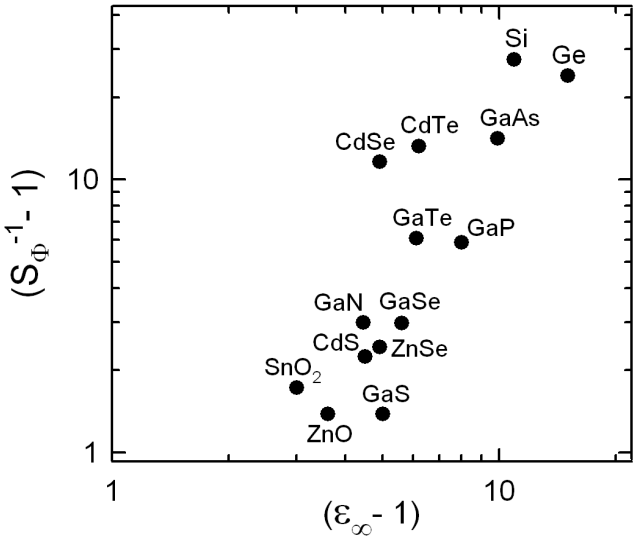

Figure 2.8. Interface parameters S_{Φ} as a function of optical dielectric constant ε_{∞} for a range of semiconductors [25, 33].

2.5.2 Chemical Bond Polarisation (CBP) Model

The chemical bond polarisation (CBP) model still assumes an ideal (i.e. purely thermionic), defect free Schottky interface but with the creation of MIGS replaced by the creation of chemical bonds between the metal and semiconductor. In quantum mechanical terms, the interface states are created by the overlap of wave functions from both the semiconductor and the metal, and therefore are a property of both not just the semiconductor as in MIGS.

In 2001, Tung [30, 35] proposed that chemical bonding at the metal – semiconductor interface plays an important role in Schottky barrier formation. He argued that when a metal forms an intimate contact with a semiconductor, chemical bonds have to form. The polarisation

associated with this bonding causes a charge rearrangement at the interface. This creates an interface dipole that weakens the dependence of the barrier height on the metal work function, reducing $S_\Phi = d\Phi_B/d\phi_M$.

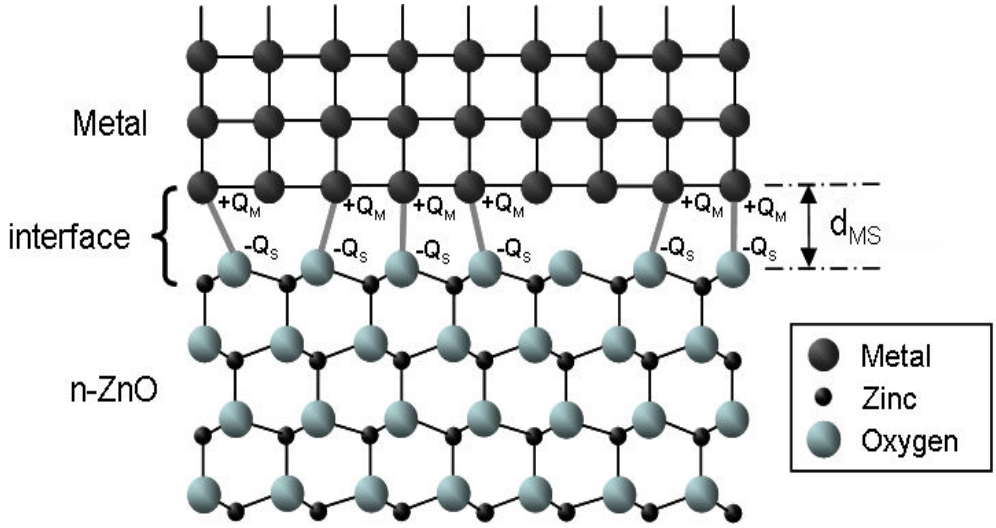

Figure 2.9. Random interface bonding at a Schottky interface on the O-polar face of *n*-ZnO.

The crystal structure of the metal at the Schottky interface is typically polycrystalline in nature with the bonding geometry having a non-periodic, random nature. Because of this randomness, the interface dipole is expected to reflect the macroscopic properties of the chemical bonding rather than the microscopic structure of the interface which would otherwise be different for each metal–semiconductor combination. Tung modelled this chemical bonding by treating the metal–semiconductor interface as a giant molecule consisting of an abrupt interface plane containing a density N_B of chemical bonds. Bonding is assumed to only occur between atoms situated on the actual interface plane with N_B less than the number of interfacial semiconductor or metal atoms per unit area due to lattice mismatch, misaligned bond geometry, and polycrystalline grain boundaries. The chemical potential equalisation method (the chemical potential of all interface atoms must be the same) is used to estimate the charge rearrangement and electric dipole at the interface. Each pair of metal–semiconductor atoms taking part in the interface bonding acquires an equal and opposite bond polarisation charge given by [29],

$$Q_M = -Q_S = \frac{\phi_M - \chi_S - E_g/2}{E_g - \kappa} \tag{2.40}$$

where κ is a constant which is usually small compared E_g. This charge transfer creates an interface dipole with a voltage drop,

$$V_{int} = \frac{qQ_M N_B d_{MS}}{\varepsilon_{int}\varepsilon_0} = \frac{qN_B d_{MS}(\phi_M - \chi_S - E_g/2)}{\varepsilon_{int}\varepsilon_0(E_g - \kappa)} . \quad (2.41)$$

Using V_{int} in Equation (2.29) gives,

$$\Phi_B = \gamma_{CB}(\phi_M - \chi_S) + (1 - \gamma_{CB})\frac{E_g}{2} \quad (2.42)$$

where γ_{CB} is the chemical bond polarisation parameter,

$$\gamma_{CB} = 1 - \frac{q^2 N_B d_{MS}}{\varepsilon_{int}\varepsilon_0(E_g + \kappa)} \quad (2.43)$$

and where d_{MS} is the separation between the metal and semiconductor atoms at the interface plane which is of the order of 0.25 nm, and N_B is the density of chemical bonds at the interface. Like MIGS, the chemical bond polarisation (CBP) model predicts a much weaker dependence of Φ_B on metal work function than the Schottky–Mott model. However, unlike MIGS, there is a natural tendency for Φ_B to converge towards half the band gap of the semiconductor, instead of converging towards the charge neutrality level.

The interface behavior parameter, $S_\Phi = d\Phi_B/d\phi_M$, is equal to γ_{CB} in the CBP model. As before, the interface dielectric constant ε_{int} can be approximated by $2\varepsilon_\infty$, and due to the dielectric screening at the interface $E_g + \kappa \approx E_g$. Therefore Equation (2.43) can be expressed as,

$$[\varepsilon_\infty(1 - S_\Phi)]^{-1} \approx \frac{2\varepsilon_0 E_g}{q^2 N_B d_{MS}} . \quad (2.44)$$

Tung used experimentally determined data for S_Φ and ε_∞ to construct a plot (shown in Figure 2.10) of $[\varepsilon_\infty(1 - S_\Phi)]^{-1}$ versus E_g which shows the predicted linear relationship. This suggests that the product of N_B and d_{MS} is reasonably constant for the semiconductors in the plot. Assuming d_{MS} to be ~ 0.25 nm, this gives a value of N_B of ~ 10^{14} cm^{-2} suggesting that chemical bonding (or some form of overlap of both the metal and semiconductor wave functions) is ubiquitous and that the degree of polarisation of these bonds determines the size of the interface dipole.

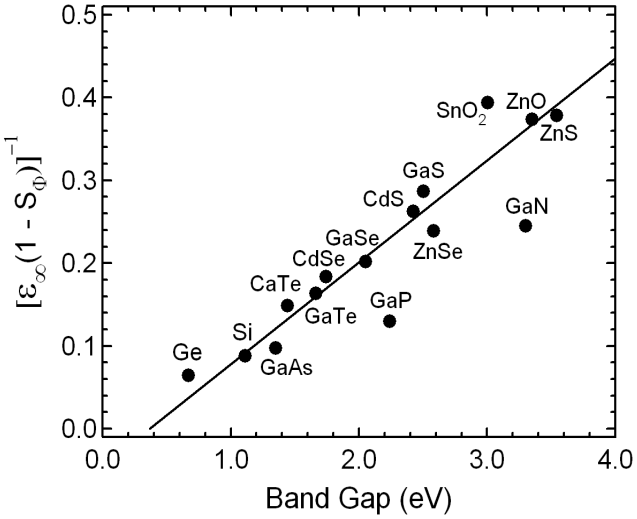

Figure 2.10. Experimentally determined interface behaviour parameter S_Φ plotted as $[\varepsilon_\infty(1-S_\Phi)]^{-1}$ versus semiconductor band gap E_g to test the validity of CBP model [29].

2.5.3 Induced Defect Model

In the induced defect model, the interaction between the metal and semiconductor is the metal-induced formation of native point defects in the semiconductor near the Schottky interface. The charge associated with these defects creates an interface dipole which in turn influences the barrier height according to Equation (2.29). The analysis is similar but more complex than that used in the MIGS model, because the density of MIGS is assumed to be constant throughout the semiconductor band gap, while in the induced defect model the distribution of defect states is more narrowly centred on a particular defect energy level. Figure 2.11 shows the situation for a donor-like defect (neutral when filled, positively charged when empty) with a narrow energy level distribution centred at E_{DS}. The net positive charge residing in the defect states of the donor is given by,

$$Q_{DS} = q \int_{\Phi_B}^{E_C} D_{DS}(E)\,dE \ . \tag{2.45}$$

As before, charge neutrality must be observed between the metal and semiconductor,

$$Q_M + Q_{DS} + Q_{SC} = 0 \ . \tag{2.46}$$

Assuming $Q_{DS} >> Q_{SC}$, Equation (2.32) can again be used to find V_{int} ,

$$V_{int} = \frac{q\delta_{int}}{\varepsilon_S\varepsilon_0}\int_{\Phi_B}^{E_C} D_{DS}(E)dE \quad . \tag{2.47}$$

(Note: the semiconductor dielectric constant ε_S is used in equation (2.47) instead of ε_{int} because the material separating the defects from the metal is the semiconductor itself and not a material with the average dielectric properties of the metal and the semiconductor as in the MIGS and CBP models). Using V_{int} in Equation (2.29) gives,

$$\Phi_B = \phi_M - \chi_S + \frac{q^2\delta_{int}}{\varepsilon_S\varepsilon_0}\int_{\Phi_B}^{E_C} D_{DS}(E)dE \tag{2.48}$$

which can be solved numerically to find Φ_B.

If the defect density is sufficiently high, the interface Fermi level is pinned close to the energy level of the defect, ($E_F \sim E_{DS}$) as shown in Figure 2.11(a). Figure 2.11(b) shows the situation where the defect density is insufficient to completely pin the Fermi level, in which case $E_{DS} > E_F$ and Equation (2.47) can be approximated by,

$$\Phi_B = \phi_M - \chi_S - \frac{q\delta_{int}N_{DS}}{\varepsilon_s\varepsilon_0} \tag{2.49}$$

where N_{DS} is the sheet density of defects (number of defects per unit area) which are assumed to be completely charged. The third term in equation (2.49) is the potential due to the interface dipole V_{int} . For ZnO, assuming an interface gap of 1 Angstrom, a charged defect density of 1 x 10^{14} cm^{-2} would cause a V_{int} of ~ 200 meV.

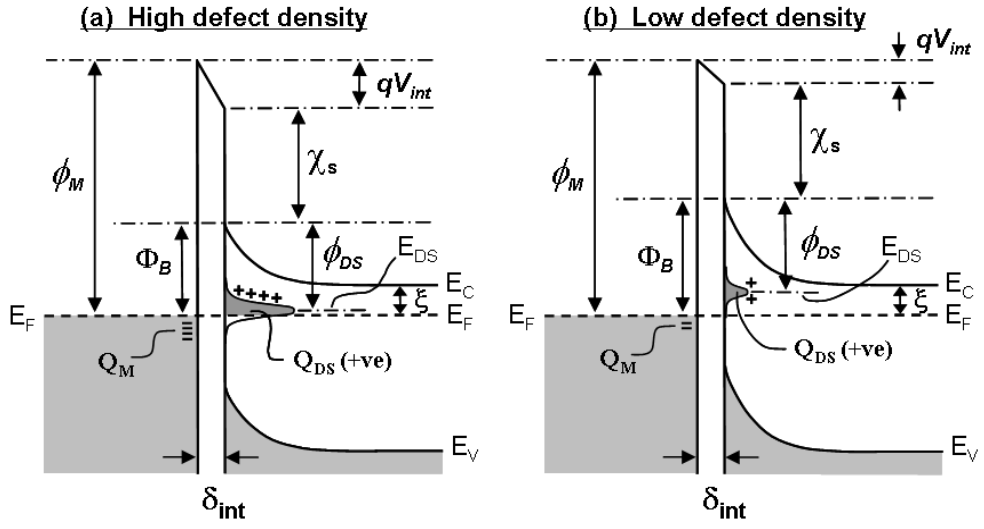

Figure 2.11. Band diagrams showing the influence of (a) a high density, and (b) a moderate density of a donor-like defect on Schottky contact formation to a *n*-type semiconductor.

The most publicised application of the metal induced defect model has been to explain the Fermi level pinning of metal and non-metal contacts to GaAs (E_g = 1.42 eV) and other III – V semiconductors. This model, originally called the Unified Defect Model [38], became the Advanced Unified Defect Model (AUDM) after the As_{Ga} antisite (an As atom on the Ga site in the GaAs lattice) was identified as the main defect responsible for the Fermi level pinning in Schottky contacts to both n-type and p-type GaAs [39]. For example, as-deposited Schottky contacts to n-type GaAs are strongly pinned with a barrier height of ~ 0.8 eV which is almost independent of metal work function (S_Φ ~ 0.07 from Figure 2.6). This is close to the energy level of the As_{Ga} (+1,0) transition,

$$As_{Ga}^{X} \rightarrow As_{Ga}^{\bullet} + e' \quad for\ which \quad E[As_{Ga}(+1,\ 0)] \ = \ E_{VBM} + 0.75eV\ . \qquad (2.50)$$

GaAs bulk crystals are grown under As- rich conditions, favouring the formation of As_{Ga} antisites which tend to pin the free GaAs surface near the middle of the band gap. The AUDM successfully predicts changes in barrier height on annealing by considering the effect of the resulting chemical reactions on the As_{Ga} defect density. For Au contacts, annealing creates additional As_{Ga} defects which cause a reduction in barrier height. In contrast, the annealing of Al contacts decreases the As_{Ga} defect density, weakening the Fermi level pinning and increasing the barrier height.

2.5.4 Comparison of the MIGS, CBP, and Induced Defect Models

The MIGS, CBP, and Induced Defect models provide different explanations for the source of the interface states created when a metal and semiconductor are brought into intimate contact. Therefore, any attempt to understand Schottky contact formation to a given semiconductor requires an assessment of the relative contribution of quantum mechanical gap states, chemical bonding, and point defect creation. If none of these are by themselves dominant, then some form of hybrid approach may need to be employed such as ‘MIGS plus CBP’ or ‘CBP plus Induced Defects’ etc. Fortunately, the formation of reasonable quality Schottky contacts allows the use of a range of techniques such as thermal admittance spectroscopy and deep level transient spectroscopy [23] which can be used to study the semiconductor defects which have an important influence on their fabrication.

Finally, Table 2.1 gives a summary of the MIGS, CBP, and Induced Defect models and their predictions for ZnO.

Table 2.1: Comparison of the predictions of the Metal Induced Gap States (MIGS), Chemical Bond Polarisation (CBP), and Induced Defect models.

	MIGS	CBP	Induced Defect
Barrier height given by:	$\Phi_B = \Phi_{bp} + S_X(X_M - X_S)$	$\Phi_B = S_\Phi(\phi_M - \chi_S) + (1 - S_\Phi)\frac{E_g}{2}$	Numerical solution of: $\frac{\varepsilon_s(\Phi_B - \phi_M + \chi_S)}{\delta_{int}} = -q\int_{\Phi_B}^{E_C} D_{DS}(E)dE$
Interface parameter: ($S_X = 2.27 S_\Phi$)	$S_X = \left(1 + \frac{q^2\delta_{int}D_{gs}}{2\varepsilon_\infty\varepsilon_0}\right)^{-1}$ or $S_X = A_X[1 + 0.1(\varepsilon_\infty - 1)^2]^{-1}$	$S_\Phi = 1 - \frac{q^2 N_B d_{MS}}{2\varepsilon_\infty\varepsilon_0(E_g + \kappa)}$	
Interface states created by:	exponential decay of electron wave functions from the metal into the band gap of the semiconductor.	polarised chemical bonding between metal and semiconductor atoms at the interface.	metal-induced creation of charged point defects in the semiconductor near the interface.
Conclusions:	high density of MIGS states causes the interface Fermi level (FL) to be pinned near the CNL. FL pinning stronger for covalent semiconductors.	density of interface states similar between semiconductors. FL pinning near the middle of the band gap stronger for narrow band gap semiconductors with low optical dielectric constants.	high defect densities cause the FL to be pinned close to the defect's energy position in the band gap.
Predictions for n-type ZnO:	ε_∞ = 4.6 [29] S_Φ = 0. 435 S_X = 0. 375 / 0.78 for Miedema/Pauling units. $\Phi_B = 0.3 + 0.375(X_M - X_S)$	S_Φ = 0. 419/E_g = 3.2 eV[29] $\Phi_B = 0.419(\phi_M - \chi_S) + 0.93$	not available

Chapter 3

The Zinc Oxide Surface

Since Schottky contact formation involves the creation of an intimate contact between a metal and a semiconductor, an understanding of the structural, chemical, and electrical nature of the zinc oxide surface is important for any attempt to control the properties of the resulting contacts. In this chapter, atomic force microscopy, x-ray photoemission spectroscopy, photoluminescence spectroscopy, and variable magnetic field Hall effect measurements are used to investigate the morphology, chemical termination, band bending, and defect nature of the ZnO surface.

3.1 ATOMIC FORCE MICROSCOPY (AFM)

AFM uses a miniature silicon (or silicon nitride) cantilever, with a probe tip of nanometer scale radius of curvature, to topographically scan the surface of a sample. The images presented here were obtained by tapping mode AFM in ambient air. In tapping mode, a piezoelectric crystal is used to oscillate the cantilever near its resonant frequency while a feedback loop measures the oscillation amplitude and adjusts the tip–sample separation to maintain constant amplitude and force on the sample. The scanned tip–sample separation then provides an image of the surface.

Figure 3.1 shows AFM images of the Zn-polar, O-polar, and m-plane faces of hydrothermally grown bulk ZnO, cleaned using the simple organic solvents acetone, methanol, and iso-propyl-alcohol, and dried using N_2 gas. These three surfaces show distinct differences in structure; most strikingly the Zn-polar face is covered in triangular islands and pits similar to those observed by Dulub *et al.* [40, 41] by scanning tunneling microscopy. These are thought to be the result of the electrostatic stabilisation of the Zn-polar surface by the removal of surface atoms [40] as discussed in more detail in Chapter 6. The O-polar surface has a more disordered morphology with an irregular distribution of holes. The m-plane surface has a corrugated morphology along the [0001] direction [42, 43].

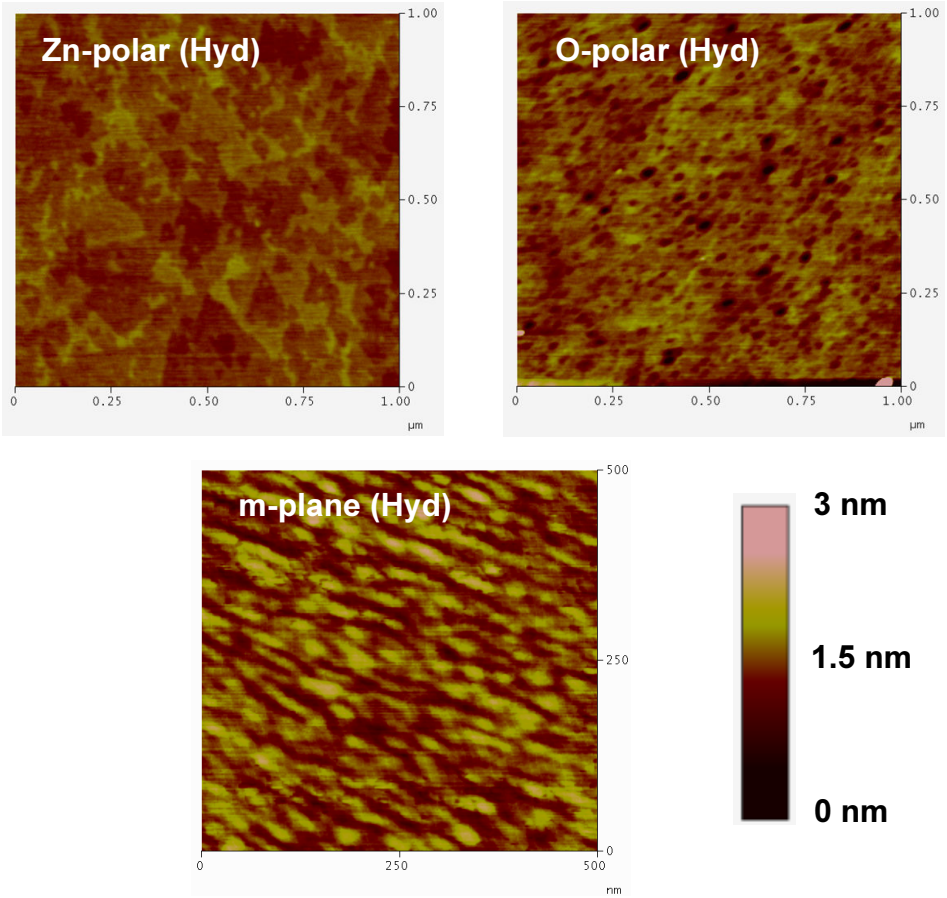

Figure 3.1: Tapping mode AFM images of the Zn-polar, O-polar, and m-plane surfaces of hydrothermally grown bulk ZnO (from Tokyo Denpa Co. Ltd).

3.2 X-RAY PHOTOEMISSION SPECTROSCOPY (XPS)

X-ray photoemission spectroscopy (XPS) is a high energy application of the photoelectric effect discovered by Hertz in 1887 and explained by Einstein in 1905 [44]. Monochromatic soft x-rays are used to illuminate a region of the sample being analysed. The kinetic energy of the photoelectrons leaving the sample, usually with a 90^{o} takeoff angle, is measured using a spectrometer to give a spectrum which contains a series of photoemission peaks. The binding energy of the electrons is equal to the difference between their kinetic energy and the photon energy of the X-rays. The binding energy position of the peaks are specific to each element in the sample while the peak area can be used (with appropriate sensitivity factors) to determine the chemical composition of the sample surface. XPS can also provide information of the type

of bonding, as the shape of each peak and its binding energy can be slightly altered by the chemical surroundings of the emitting atom. Although the x-rays can excite electrons up to a depth of ~ 1 μm into the sample, only those from approximately 0.5 – 5 nm below the surface can escape, making XPS a surface sensitive tool. Even greater surface sensitivity can be obtained by tilting the sample and analysing electrons with shallower take-off angles. In-situ sample cleaning and depth profiling can be carried out using argon ion beam sputtering.

3.2.1 XPS of the Zn-polar and O-polar Surfaces of Bulk ZnO

XPS of hydrothermal and melt grown bulk ZnO surfaces were carried out (unless otherwise stated) using a Kratos XSAM800 instrument at the Research Centre for Surface and Materials Science, University of Auckland, with the assistance of Dr. C. Doyle and Prof. J.B. Metson. Data was collected using a 1486.6 eV monochromatic Al Kα x-ray source, a hemispherical electron energy analyser operated in the fixed analyser transmission mode, and an ultra-high vacuum chamber with a base pressure ~ 10^{-8} mbar. Samples were also sent to collaborators at the University of Warwick, U.K, and Purdue University, U.S.A., for analysis using similar XPS equipment. Three different types of spectra were collected:

1) Survey spectra (pass energy 160 eV, 1.0 eV step size) – in which relative peak areas are used to quantify the concentration of each element in the near surface region. The peak areas are first corrected using relative sensitivity factors based on instrument modified Schofield cross-sections (18.92, 2.93, and 1.00 for Zn 2p 3/2, O 1s, and C 1s peaks respectively);

2) Core level spectra (pass energy 20 eV, 0.1 eV step size) – these are high resolution scans of individual emission peaks used to determine the chemical bonding and oxidation level of individual types of atom;

3) Valence band spectra (pass energy 20 eV, 0.1 eV step size) – these are high resolution scans of the highest energy photoelectrons which can be used to measure the valence band density of states and determine the near-surface band bending.

Since high resistivity samples are prone to charging during x-ray irradiation, and this can affect the position and shape of the XPS spectra, the ZnO samples were carefully grounded on a stainless steel holder using either carbon tape or silver paste. For the valence band spectra, samples were backside coated with a layer of indium to improve the electrical connection

between the sample and the machine. Unless otherwise stated, low energy electron flood charge compensation was used during data acquisition.

Figure 3.2 shows survey spectra, taken consecutively from Zn-polar and O-polar face samples cut from the same double-sided polished, hydrothermal, c-axis, bulk ZnO wafer. Both faces show the same Zn and O core level emissions, plus a signal due to adventitious carbon contamination at 285.0 eV. No iron was detected confirming that the sample holder was not being sampled. Surprisingly, the ratio of O:Zn was higher on the Zn-polar face. This was investigated on several other hydrothermal and melt wafers, and was found to be a consistent feature.

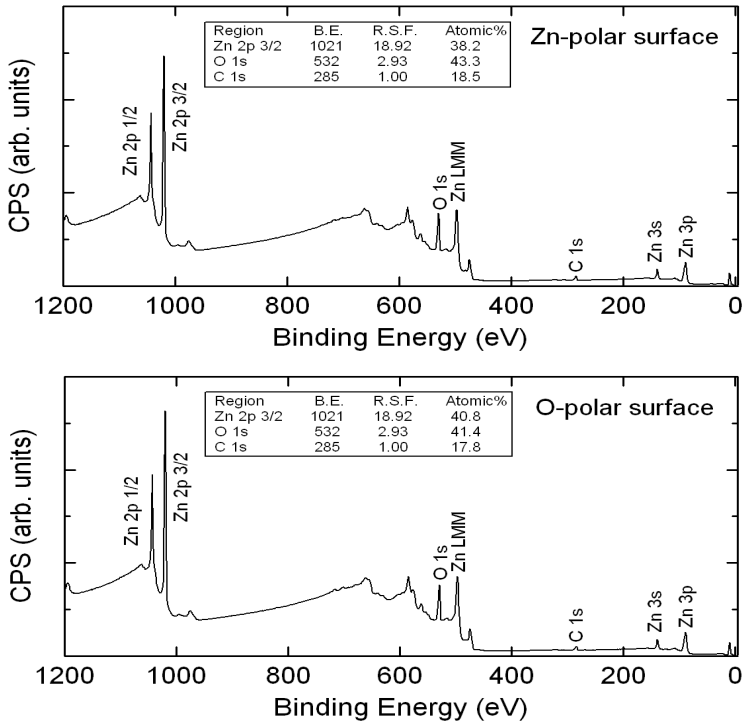

Figure 3.2: XPS survey spectra collected from the Zn-polar and O-polar faces of hydrothermal bulk ZnO with a quantification analysis based on the peak areas of the Zn 2p 3/2, O 1s, and C 1s core level emissions, with relative sensitivity factors of 18.92, 2.93, and 1.00 respectively.

Figures 3.3(a) and (b) show the core O 1s level spectra from the same hydrothermal samples. The dominant emission is from the well-defined O 1s line at 531.0 eV, due to lattice oxygen. On both faces, there is a pronounced shoulder at higher binding energies which has been unambiguously related to hydroxide bonding [42, 45, 46]. The O 1s spectra were fitted using three Voigt functions with a Gaussian:Lorentzian ratio of 70:30. The two main peaks at 531.0 and 532.8 eV are due to the lattice oxygen bonding and OH bonding respectively, while a third, much smaller, unknown peak is required to exactly fit the shape of the shoulder. This

third peak is significantly larger on the O-polar face, which also has a slightly more pronounced shoulder compared to the Zn-polar face.

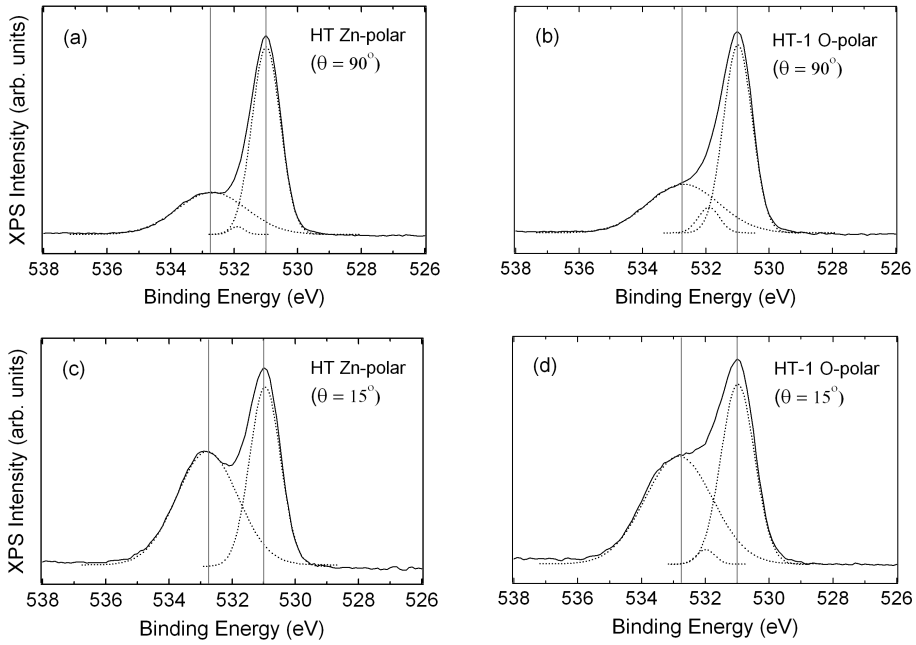

Figure 3.3: Variable angle XPS of the O 1s core level on the Zn-polar and O-polar faces of hydrothermally grown bulk ZnO, for takeoff angles of 90° and 15°.

Figures 3.3(c) and (d) show the O 1s spectra re-measured using a photoelectron take-off angle of 15° from the surface. The increase in the intensity of the OH peak indicates that the hydroxide bonding is located at or close to the surface. The O 1s spectra were monitored for a further 24 hours at a chamber pressure of 10^{-8} mbar and remained unchanged, indicating that the hydroxide layer is persistent and probably chemisorbed.

3.2.2 Graphical Layer Depth Profiling using Angle Resolved XPS

Spruytte *et al.* [47] have developed a graphical method to estimate the composition, thickness, and depth of different near surface layers using angle resolved XPS. This method involves calculating the relative atomic concentrations (referred to as reduced area fractions $F_i(\theta)$ in [47]) of each chemical species, *i*, at two different take-off angles, in this case 15° and 90°. This provides sufficient information to determine the depth (d_j) and thickness (t_j) of each layer *j*, provided they are uniform and contain chemical species that are present in one layer only. The parameters *R* and *S* are first calculated from,

$$R = \frac{F_i(15^o)}{F_i(90^o)} \tag{3.1}$$

and

$$S = \sum_i F_i(90^o) = e^{d_j/\lambda}(1 - e^{-t_j/\lambda}) \ . \tag{3.2}$$

Provided that each chemical species *i* is present in only one layer *j* then,

$$F_i(\theta) = n_i e^{d_j/\lambda \sin\theta}(1 - e^{-t_j/\lambda \sin\theta}) \tag{3.3}$$

where n_i is the concentration of chemical species *i* , and λ is the inelastic mean free path of the photoelectrons which is ~ 2.0 nm. *R* is the ratio of the reduced area fractions measured at 15° and 90° calculated for each chemical species, and *S* is the sum of the reduced area fractions at 90° of all the chemical species present in a given layer. The higher the value of *R*, the shallower the chemical species relative to the surface. The values of *R* and *S* determined from the 15° and 90° XPS spectra are given in Table 3.1.

Table 3.1: Reduced area fractions $F_i(15^o)$ and $F_i(90^o)$ measured at take-off angles of 15° and 90° from (a) the Zn-polar face; and (b) the O-polar face of hydrothermal bulk ZnO.

(a) Chemical Species	$F(15^o)$	$F(90^o)$	R [= $F(15^o)$ / $F(90^o)$]
Zn	20.3	46.7	0.43
lattice O	15.9	25.0	0.64
hydroxide O	19.5	12.3	1.6
C	44.3	16.1	2.8

(b) Chemical Species	$F(15^o)$	$F(90^o)$	R [= $F(15^o)$ / $F(90^o)$]
Zn	26.8	49.7	0.54
lattice O	15.1	21.1	0.72
hydroxide O	19.0	13.9	1.4
C	39.1	15.3	2.6

The values of *R* in Table 3.1 indicate that both polar faces contain a carbon contamination layer ($R \sim 2.7 \pm 0.1$) at the surface, above a hydroxide layer ($R \sim 1.4 \pm 0.1$) which in turn lies on top of the lattice ZnO. The thickness and depth of each layer is determined by plotting *R* and *S* on a graphical solution of Equations (3.1) – (3.3) as shown in Figure 3.4 This shows that the

thickness of both the C and OH layers on each polar face is ~ 0.4 nm, at depths of ~ 0.1 nm and ~ 0.5 nm respectively.

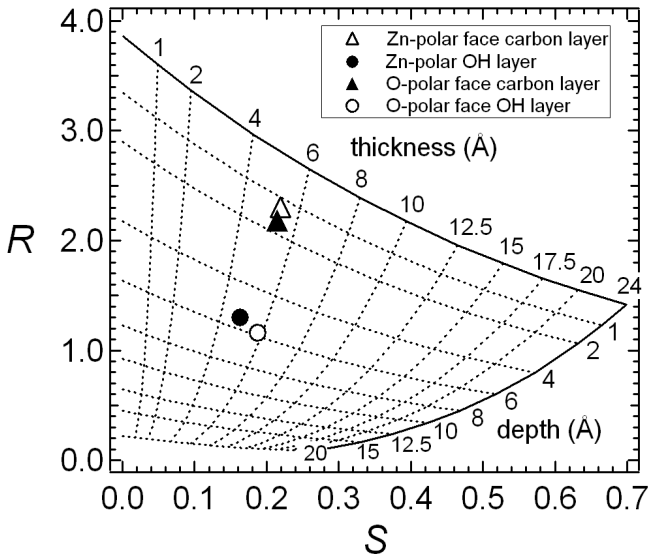

Figure 3.4: Graphical solution (assuming λ = 2.0 nm) for the thickness and depth of carbon and hydroxide layers on the Zn-polar and O-polar faces of hydrothermal bulk ZnO using the method of Spruytte *et al*. [47].

XPS spectra taken from the Zn-polar and O-polar faces of additional hydrothermal wafers and a melt grown wafer (Figure 3.5) showed almost identical O 1s spectra, with the ubiquitous presence of a high binding energy shoulder and an underlying hydroxide peak. Further angle resolved spectra taken on the m-plane face of hydrothermal ZnO also indicated the presence of a hydroxide layer. Coppa *et al.* [45] used XPS to determine the presence of a 1.6–2.0 [0.7-2.6] monolayer hydroxide coverage on the Zn-polar [O-polar] surfaces of doubled-sided bulk ZnO wafers grown using the seeded chemical vapor transport method. A number of other authors have reported the presence of unreconstructed (1 x 1) hydroxyl saturation on the Zn-polar and O-polar faces of bulk ZnO crystals [46, 48, 49]. Valtiner *et al.* [46] also showed that the Zn-polar surface is stabilised by the adsorption of OH. Kunat *et al.* [48, 49] reported that H_2O is readily dissociated (at oxygen vacancies) on the clean, hydrogen free, O-polar surface forming a hydrogenated OH terminated surface with an O-H binding energy of 130 kJ/mol. They also showed that a clean and hydrogen free, O-polar surface can be obtained by heating the substrate at 600 K and that it is characterised by a (1 x 3) reconstruction with a large number of oxygen vacancies–one vacancy per (1 x 3) unit cell.

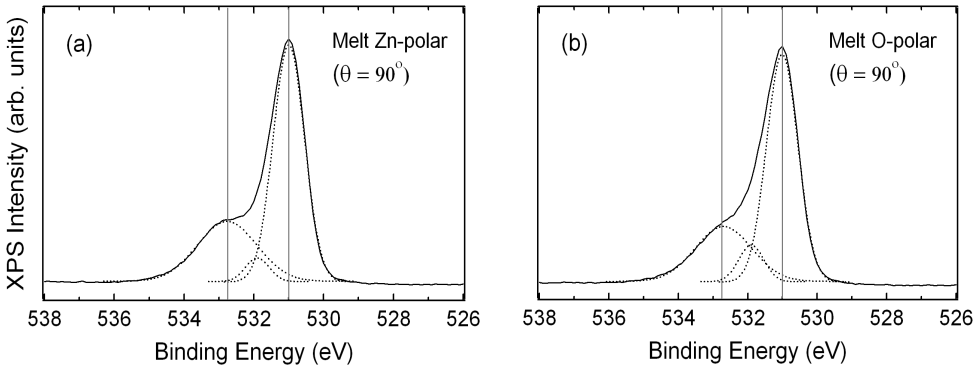

Figure 3.5: XPS of the O 1s core level on the Zn-polar and O-polar faces of melt grown bulk ZnO, for a fixed takeoff angle of 90^{o} after similar sample preparation.

In light of these reports and the angle resolved XPS measurements presented here, it seems reasonable to propose that the ZnO surface is naturally terminated by OH groups as shown in Figure 3.6. Each surface Zn atom on the Zn-polar face is threefold co-ordinated to lattice oxygen with the remaining tetrahedral position occupied by the oxygen atom of a surface hydroxyl. This would also explain the higher O:Zn ratio observed on the Zn-polar face, since the OH termination provides an additional plane of O atoms. The OH termination on the O-polar face is achieved by the addition of a layer of H atoms. In atmospheric conditions, it is likely that there will be additional physisorbed species, such as water vapour and oxygen molecules, which are attracted to the hydroxide layer. Oxygen species are known to be electron acceptors when adsorbed onto ZnO [11], and can significantly lower the surface conductivity.

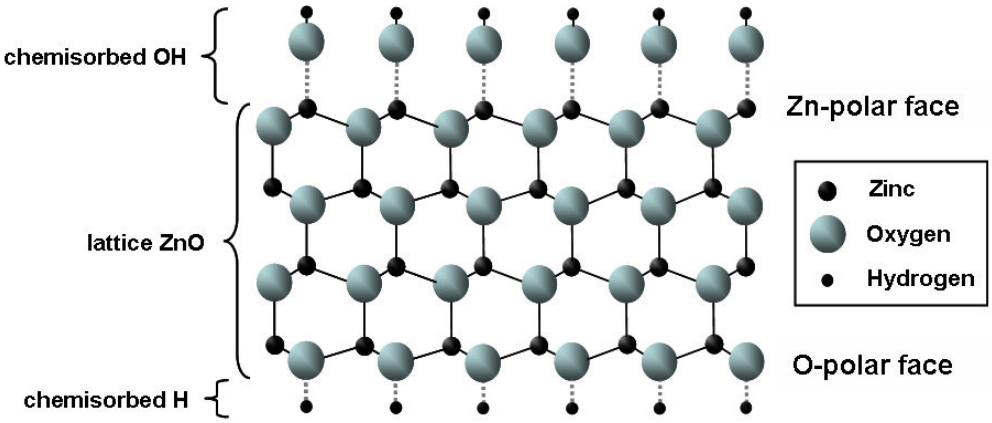

Figure 3.6: (1 x 1) hydroxide terminated Zn-polar and O-polar ZnO surfaces.

3.3 VALENCE BAND X-RAY PHOTOEMISSION SPECTROSCOPY

XPS is a particularly useful tool for investigating the valence band structure of semiconductors and for determining the position of the surface Fermi level with respect to the valence band minimum [50 – 53].

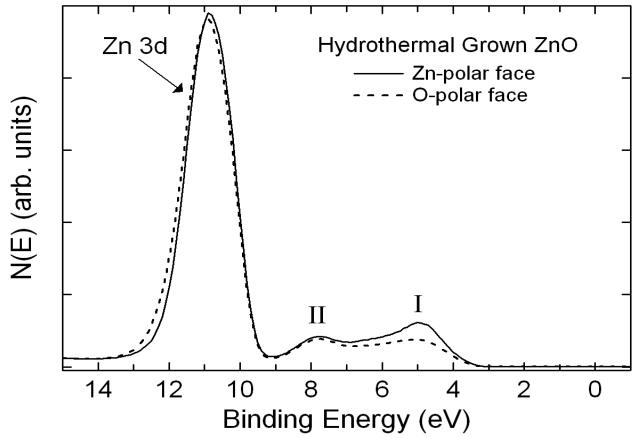

Figure 3.7: Valence band XPS spectra taken from the Zn-polar and O-polar faces of the same hydrothermal, bulk, c-axis wafer (n = 1 x 10^{14} cm^{-3}).

Figure 3.7 shows the valence band XPS spectra collected from the Zn-polar and O-polar faces of the same double-sided polished, hydrothermal, c-axis, bulk ZnO wafer. All samples were ultrasonically cleaned in organic solvents. The spectra were measured by collaborators at the Department of Physics, University of Warwick, UK using a Scienta ESCA300 spectrometer with a monochromatic Al Kα X-ray source ($h\nu$ = 1486.6 eV), electron energy analyser, and a similar detector to the Kratos XSAM800 instrument at the University of Auckland. The spectra were collected without the use of an electron flood gun. Provided the samples are well grounded to the instrument, the binding energy scale can be referenced to the Fermi level of the sample. The binding energy scale was also calibrated using the Fermi edge of an ion-bombarded silver reference sample. The spectra show the presence of three main peaks at 10.9, 7.8 and 4.9 eV. The highest binding energy peak is mainly due to the Zn 3d core level which is not part of the valence band density of states. The two main peaks in the valence band region have been labelled I (4.9 eV) and II (7.8 eV). Peak II involves the hybridised O 2p and Zn 4s and 4p orbitals, while peak I is attributed mainly to the O 2p orbitals [53,54].There is evidence of a polarity related effect in Figure 3.7, in that peak I is significantly more intense on the Zn-polar face; a similar effect was also observed in other wurtzite semiconductors, e.g. GaN, InN, and CdS.

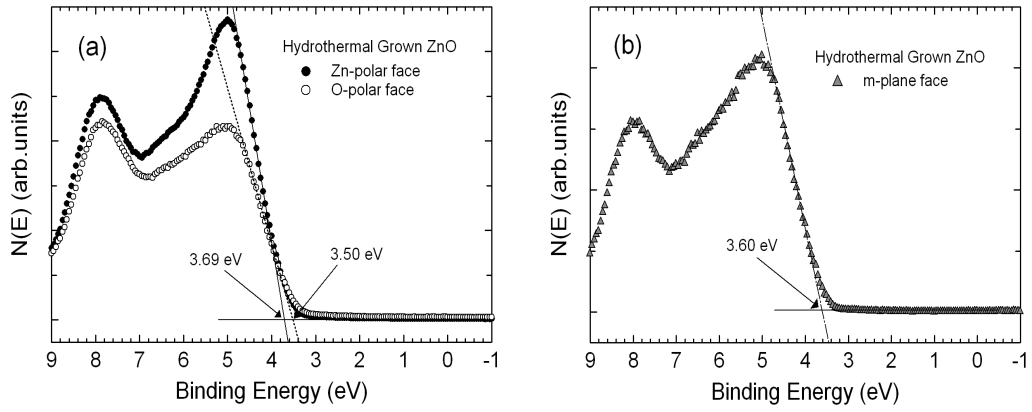

Figure 3.8: VBM to Fermi level separation determined from linear fits to the leading edge of the valence band XPS spectra from (a) the Zn-polar and O-polar faces of the same hydrothermal, c-axis, bulk ZnO wafer; and (b) from a hydrothermal, m-plane, bulk ZnO wafer.

The position of the valence-band maximum (VBM) with respect to the Fermi level (E_F) on each face can be determined by extrapolating a linear fit to the low binding energy edge of the valence band spectrum to a line fitted to the instrument background [50]. This is shown in Figure 3.8(a) for the Zn-polar and O-polar face of the same hydrothermal, c-axis wafer and in Figure 3.8(b) for a separate hydrothermal m-plane wafer. The VBM – E_F values for each face are given in Table 3.2. Since the band gap of ZnO is 3.35 eV (at RT), the Fermi levels at all three surfaces are well into the conduction band. This corresponds to strong downwards band bending and the presence of an electron accumulation layer on each face.

Table 3.2: VBM – Fermi level values determined from valence band XPS spectra and downward near-surface band bending, assuming a ZnO band gap of 3.35 eV (at RT) and a CBM – Fermi level energy difference of 0.27 eV for hydrothermal bulk ZnO.

Hydrothermal ZnO Polarity	VBM – Fermi level (eV)	Downward Band Bending (eV)
Zn -polar	3.69	0.61
O - polar	3.50	0.42
m-plane	3.60	0.52

Table 3.2 also shows the magnitude of the downward band bending, which can be calculated provided the energy of the Fermi level below the conduction band minimum, $\xi = E_C - E_F$, is known. For non-degenerate semiconductors ξ is given by,

$$\xi = kTln\left(\frac{N_C}{n}\right) \tag{3.4}$$

where n is the bulk carrier concentration and N_C is the density of states in the conduction band given by,

$$N_C = 2\left(\frac{2\pi m_e^* kT}{h}\right)^{\frac{3}{2}} . \tag{3.5}$$

$N_C = 2.94 \times 10^{18}$ cm^{-3} using the accepted value of 0.27 m_e for the effective electron mass m_e^* of ZnO [5]. For hydrothermal ZnO, $n \sim 1 \times 10^{14}$ cm^{-3} and $\xi = 0.27$ eV; while for melt ZnO, $n \sim 5 \times 10^{16}$ cm^{-3} and $\xi = 0.11$ eV.

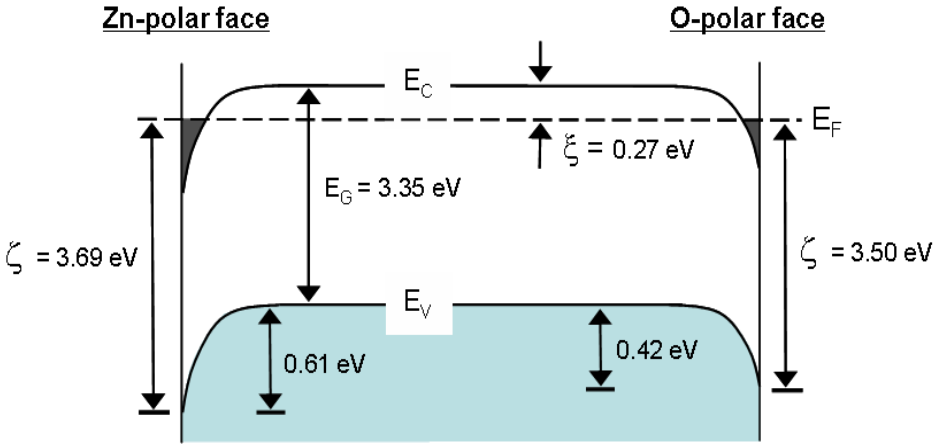

Figure 3.9: Band bending at the Zn-polar and O-polar faces of hydrothermal bulk ZnO showing accumulation layers on both polar faces.

Figure 3.9 illustrates the near surface band bending at the Zn-polar and O-polar hydrothermal bulk ZnO using the values in Table 3.2. The downward band bending is ~ 0.19 eV greater on the Zn-polar face indicating a stronger accumulation layer. Similar results were obtained on additional hydrothermal wafers, using the Kratos XSAM800 instrument at the University of Auckland, indicating that this is a consistent trend.

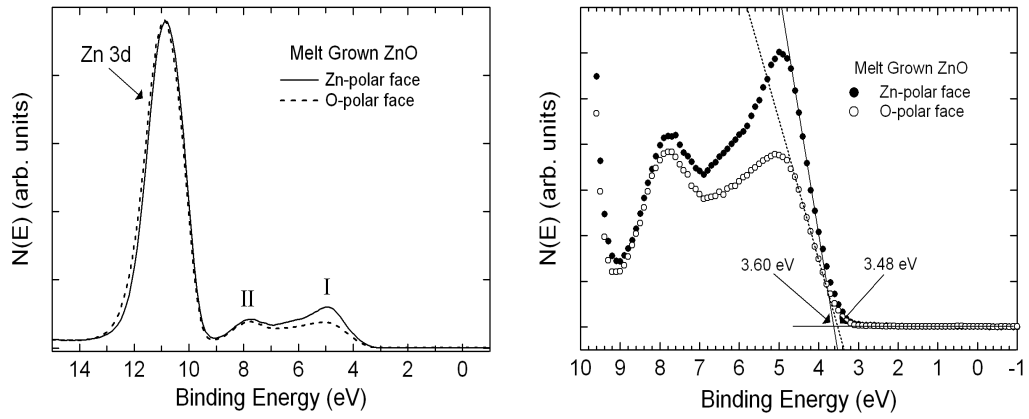

Figure 3.10: (a) Valence band XPS spectra taken from the Zn-polar and O-polar faces of the same melt, bulk, c-axis wafer (n = 5 x 10^{16} cm^{-3}) and (b) VBM to Fermi level separation determined from linear fits to the leading edge of the valence band XPS spectra from (a).

Valance band XPS spectra were also taken on the Zn-polar and O-polar face of an organic solvent cleaned, melt grown, c-axis, bulk ZnO wafer using the Kratos instrument. As an extra precaution the samples were backside coated with indium metal to ensure they were thoroughly grounded to the instrument. The valence band spectra are shown in Figure 3.9 and the VBM – Fermi level results for melt ZnO are summarised in Table 3.3. Both polar surfaces show similar VBM – Fermi level values to those obtained for the hydrothermal ZnO but, due to the 2–3 orders of magnitude higher carrier concentration of the melt material, the calculated downward bending is less. The results still indicate the presence of electron accumulation layers on both faces with a ~0.12 eV stronger downward band bending on the Zn-polar face.

Table 3.3: VBM – Fermi level values determined from valence band XPS spectra and downward (negative) near surface band bending assuming a ZnO band gap of 3.35 eV (at RT) and a CBM – Fermi level energy difference of 0.11 eV for melt bulk ZnO.

Melt ZnO Polarity	VBM – Fermi level (eV)	surface band bending (eV)
Zn -polar	3.60	- 0.36
O - polar	3.48	- 0.24

The XPS measurements in Section 3.2 showed that, under vacuum conditions, the polar and non-polar faces of ZnO are terminated with an hydroxide layer, while the valence band XPS results presented here indicate the presence of an electron accumulation on the same faces. It is reasonable to propose that the two observations are linked. Henrich and Cox [56]

proposed that H atoms donate approximately 0.5 electrons to each surface oxygen ion on the OH terminated Zn-polar and O-polar surfaces of ZnO. Several other groups [11, 57, 58] have reported a hydroxide-induced accumulation layer on both Zn-polar and O-polar surfaces causing a high surface conductivity. Kunat *et al.* [48] proposed that (1 x 1) coverage of hydroxide groups is the most energetically favourable termination of the ZnO surface.

3.4 VARIABLE MAGNETIC FIELD HALL EFFECT MEASUREMENTS

The presence of hydroxide-induced accumulation layers on the ZnO surface clearly has important consequences for its electrical properties. The accumulation layers may also be strong enough to affect bulk electrical measurements, particularly in the case of hydrothermal ZnO which has a very low carrier concentration. Look [60] reported significantly smaller low-temperature mobilities (from variable temperature single field Hall effect measurements) for hydrothermal ZnO compared to melt and SCVT grown ZnO, despite the high crystallinity of the former. Look also suggested that parallel conduction from surface charges may be more dominant in the hydrothermal material due to its lower bulk conductivity and that this should be included in the analysis of Hall effect measurements.

Variable magnetic field Hall effect measurements [61, 62] represent a powerful tool for separating the influences of surface and/or interfacial conducting layers from the bulk properties of a sample. The motion of carriers in the *x*–*y* direction of an isotropic Hall effect sample, perpendicular to an applied magnetic field B in the *z* direction, can be described by the conductivity tensor,

$$\underline{J} = \begin{bmatrix} \sigma_{xx} & -\sigma_{xy} \\ \sigma_{xy} & \sigma_{xx} \end{bmatrix} \underline{E} \ . \tag{3.6}$$

The measured Hall coefficient $R_H(B)$ and conductivity $\sigma(B)$ of the sample are related to the components of the conductivity tensor by,

$$R_H(B) = \frac{\sigma_{xy}/B}{\sigma_{xx}^2 + \sigma_{xy}^2} \tag{3.7}$$

and

$$\sigma(B) = \frac{\sigma_{xx}^2 + \sigma_{xy}^2}{\sigma_{xx}} \ . \tag{3.8}$$

For a sample with multiple carriers in parallel conducting layers, the components of the conductivity tensor can be expressed as the sum over the number of carriers *N*,

$$\sigma_{xx}(B) = \sum_{i=1}^{N} \frac{en_i\mu_i}{1 + (\mu_i B)^2} \tag{3.9}$$

$$\sigma_{xy}(B) = \sum_{i=1}^{N} \frac{en_i\mu_i^2 B}{1 + (\mu_i B)^2} \tag{3.10}$$

where n_i and μ_i and the carrier concentration and mobility of the carrier in layer *i,* which are themselves functions of temperature. As the magnetic field strength increases, the paths of the higher mobility carriers are more heavily deflected and their contribution to σ_{xx} and σ_{xy} changes as they are 'magnetically quenched'.

At a given temperature, the dependences of σ_{xx} and σ_{xy} on the magnetic field are first experimentally determined using Equations (3.7) and (3.8), and then least square fitted using Equations (3.9) and (3.10) with n_i and μ_i as the adjustable parameters. Two fitting procedures are often employed: (i) standard multi-carrier fitting (MCF), in which assumptions have to be made concerning the variety and type of carriers, and (ii) quantitative mobility spectrum analysis (QMSA) [63, 64] in which no *a priori* assumptions are made and through which a continuous spectrum of sheet carrier concentration versus mobility is obtained. The most powerful approach is a hybrid method (QMSA + MCF) in which QMSA is used to provide the starting values for MCF, resulting in a self-consistency check for the dataset.

Hall effect samples, approximately 6 mm x 6 mm x 500 μm, were cut from hydrothermal and melt, c-axis, bulk ZnO wafers. Ohmic Ti/Al/Pt (50 nm/150 nm/30 nm) contacts were fabricated on each corner of the Zn-polar face by e-beam evaporation. Variable magnetic field Hall effect measurements were made using the van der Pauw technique by Dr. C.H. Swartz in collaboration with Prof. Tom Myers at West Virginia University, USA, as a function of temperature over the range 50 – 300 K. At each temperature, measurements were made at 22 logarithmically spaced values of magnetic field from 0 to 12 T. Figure 3.11 shows the QMSA spectrum obtained from the hydrothermal ZnO sample at 150 K. There are two clearly resolved carrier populations: one due to a high mobility bulk electron and the other due to a low mobility electron. The latter is assumed to be from the surface accumulation layer on the Zn-polar face. It was not possible to resolve the mobility of the surface electron because it is below the resolution limit of the technique, which is given by $(\mu_i B)^2 > 0.01$. Subsequent measurements using a 35 T superconducting magnet at the National High Magnetic Field Laboratory, Tallahassee, USA, were still unable to unambiguously resolve its mobility although an upper limit of ~ 30 $cm^2V^{-1}s^{-1}$ can be given.

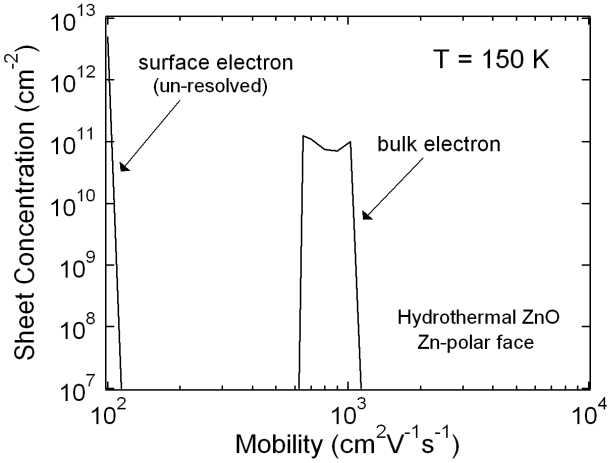

Figure 3.11: QMSA spectrum of hydrothermal bulk ZnO at a temperature of 150 K (van der Pauw contacts fabricated on the Zn-polar face).

Fortunately MCF can be used to remove the effect of the low mobility surface carriers to give accurate values of n_i and μ_i for the high mobility bulk electron. Figures 3.12a & b show the result of this process for the hydrothermal sample with the van der Pauw contacts on the Zn-polar face. Values of n and μ from single field Hall effect measurements at 0.60 T, which inherently include the effect of the surface electron, have been plotted for comparison. Figure 3.12a shows that, at room temperature, the effect of the surface electron is relatively small. However, at temperatures below 200 ^{o}C, when the bulk carriers start to 'freeze out', the surface carriers have a dominant effect on both the carrier concentration and mobility of hydrothermal ZnO. The maximum 'single field' mobility is 400 $cm^2V^{-1}s^{-1}$ at 125 K, but once surface carrier effects are removed the maximum mobility rises to 1100 $cm^2V^{-1}s^{-1}$ at 110 K for the bulk electron only, which is comparable to the maximum single field mobilities reported for melt and SCVP grown ZnO at the same temperature [7, 59].

Figures 3.13a & b show the data obtained for the melt ZnO sample with van der Pauw contacts again on the Zn-polar face. In this case, the room temperature carrier concentration is approximately three orders of magnitude higher. As a result, the surface electron layer has a very small influence on the conductivity at temperatures above 50 K. Below this temperature, most of the bulk carriers freeze out and the degenerate surface carriers become dominant.

In summary, variable magnetic field Hall effect measurements have shown that degenerate, low mobility surface carriers have a significant influence on the bulk electrical properties of hydrothermal ZnO ($n \sim 10^{14}$ cm^{-3}), particularly at temperatures below 200 K. For melt ZnO, surface carriers have little effect on bulk electrical measurements above 50 K due to the higher density of bulk carriers ($n \sim 10^{16} - 10^{17}$ cm^{-3}). However, for both materials, the

surface carriers may provide unwanted conduction paths between the contacts of electrical devices.

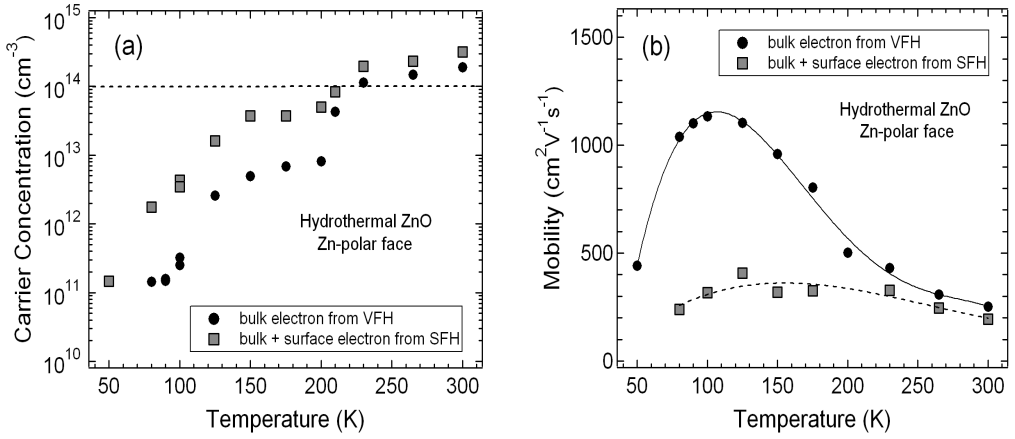

Figure 3.12: Temperature dependence of (a) the carrier concentration, and (b) the mobility for the bulk electron obtained from MCF analysis of variable magnetic field Hall effect measurements (0 - 12 T), compared to the values from single field Hall effect measurements (0.60 T), for van der Pauw contacts on the Zn-polar face of a hydrothermal, bulk, c-axis ZnO wafer (Tokyo Denpa Co. Ltd.).

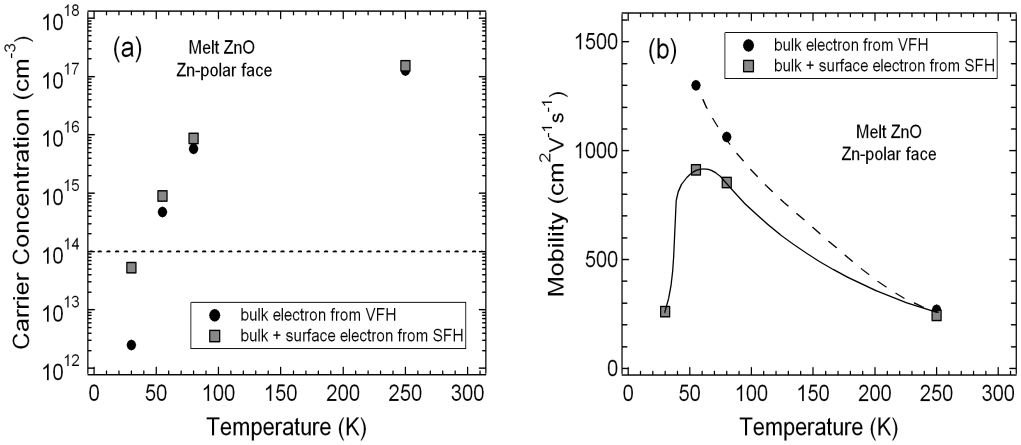

Figure 3.13: Temperature dependence of (a) the carrier concentration and (b) the mobility for the bulk electron obtained from MCF analysis of variable magnetic field Hall effect measurements (0 - 12 T), compared to the values from single field Hall effect measurements (0.60 T), for van der Pauw contacts on the Zn-polar face of a melt, bulk, c-axis ZnO wafer (Cermet Inc.).

3.5 DEFECT BAND PHOTOLUMINESCENCE

Photoluminescence (PL) is a non-destructive technique that is widely used to detect and identify near surface defects in semiconductors [23]. In the case of wide band gap semiconductors such as ZnO, a UV laser is used to create electron hole pairs, up to a depth of approximately 40 nm, which subsequently recombine by radiative and non-radiative transitions (see Figure 3.14). The radiatively emitted photons are collected and analysed using a diffraction grating spectrometer and photomultiplier detector. The PL spectrum provides (i) an indication of the relative optical activity of impurities and defects in the sample, and (ii) radiative transition energies which can be used to determine the electronic energy levels of the associated impurities and defects. The relative intensity of a peak in the PL spectrum is a function of the relative density of the associated impurity or defect and the radiative efficiency of the transition involved.

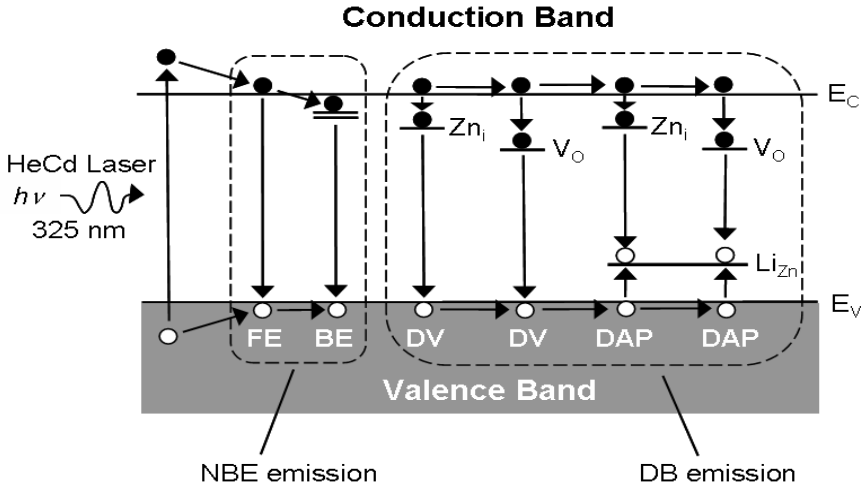

Figure 3.14: Selected near band edge (NBE) and defect band (DB) PL transitions in ZnO [NBE emission from the recombination of free excitons (FE) and excitons bound to extrinsic donors (BE); DB emission from transistions between intrinsic (donor) point defects and either the valence band (DV) or acceptor levels introduced by Group I impurities (DAP)].

Figures 3.15(a) & (b) show (un-normalised) PL spectra taken at (a) room temperature and (b) 4 K by Paul Miller (Department of Physics and Astronomy, University of Canterbury, NZ) from the Zn-polar and O-polar faces of samples cut from the same hydrothermal and melt, double-sided polished, c-axis, bulk ZnO wafers. The samples were excited using 20 mW of the 325 nm line of a HeCd laser with a circular spot diameter of 500 μm and the resulting luminescence was measured using a Spex 1700 spectrometer. The dominant PL emission at room temperature is from near band edge transitions which mainly involve free excitons due to their large binding energy. The broader emission from 2.0 - 2.7 eV is known as the defect

band of ZnO and includes transitions involving intrinsic point defects, such as Zn and O interstitials and vacancies, deep level donors and acceptors, and copper impurities. However, the identity of the dominant transitions in the defect band is still a source of debate. Theoretical studies have indicated that Zn and O vacancies are the most energetically stable point defects, and the defect band has been experimentally observed to change with Zn-rich and O-rich growth conditions, as well as post-annealing in Zn vapour and O_2 ambients [65, 66]. There is some evidence to link the yellow defect band at ~ 2.1 eV with Zn vacancies and the green defect band at ~ 2.5 eV with oxygen vacancies [5]. Brillson *et al*. [67] used this assignment to explain changes induced in the defect band (as measured by depth resolved cathodoluminescence) by the metalisation and subsequent annealing of Au and Ta contacts.

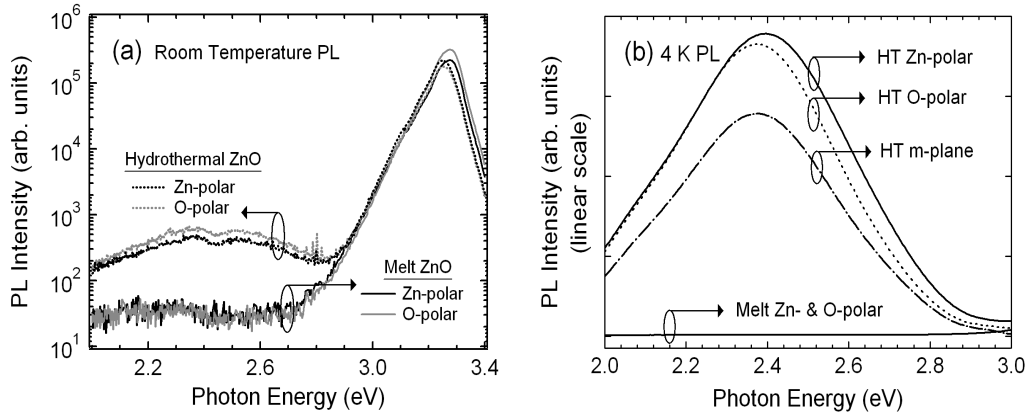

Figure 3.15: (a) Un-normalised, room temperature, near band edge and defect band PL spectra (logarithmic scale) from the Zn-polar and O-polar faces of the same hydrothermal and melt bulk c-axis wafers; and (b) a comparison of un-normalised, 4K, defect band PL spectra.

Significantly, the defect band emission was 1–2 orders of magnitude more intense from the hydrothermal ZnO sample, a finding that was consistently repeated on subsequent wafers. It is tempting to conclude that hydrothermal ZnO has a higher density of near surface defects, especially O vacancies, and in fact Brillson *et al.* [67] have classified hydrothermal and melt bulk crystals as high defect and low defect respectively, based on the relative intensities of their defect band emission. This approach assumes that the radiative efficiency of defect band emission is similar for both hydrothermal and melt ZnO material. However, hydrothermal ZnO has a number of unique chemical and electrical differences. Most significantly, hydrothermal ZnO is heavily compensated by the presence of Li and Na acceptors which are not present in melt ZnO. These introduce deep acceptor states into the band gap of hydrothermal ZnO providing additional radiative recombination paths. Hydrothermal ZnO has a higher degree of crystallinity (from X-ray rocking curve measurements) and forms more ideal Schottky contacts

than melt ZnO (see Chapter 4). This suggests that classifying hydrothermal ZnO as a high surface defect material may not be valid.

3.6 ANNEALING

The post growth annealing of semiconductors is often used to improve their surface morphology and bulk electrical properties. The hydrothermal and melt grown ZnO wafers used in this thesis were all unannealed as-received, so a study was carried out to assess the possible benefits of annealing the wafers before Schottky contact fabrication. A hydrothermal, c-axis wafer (10 mm x 10 mm x 500 μm) was diced into 16 equal sized square samples (approximately 2.5 mm by 2.5 mm) and ultrasonically cleaned in acetone, methanol, and iso-propyl-alcohol. This provided an as-received pair of Zn-polar and O-polar samples, and additional sample pairs which were annealed at 300, 400, 500, 600, and 700 ^{o}C respectively for 90 minutes in a quartz furnace tube. Oxygen gas (99.99% purity) was passed through the tube at a flow rate of 10 sccm (standard cubic centimeters per minute) throughout the annealing process. At each temperature, one sample was annealed with the Zn-polar face upwards and the other with the O-polar face upwards. The opposite face was placed on an alumina sheet which was pre-annealed at 1100 ^{o}C to drive out any surface contamination.

Defect band PL spectra were measured for each pair of annealed samples at a temperature of 4 K using the cold finger of a liquid helium cooled cryostat. All measurements were made during the same experimental run. Following the PL measurements, the samples were recleaned and Ti/Al/Pt ohmic contacts were deposited by e-beam evaporation in each corner providing a square van der Pauw contact geometry. The resistivity and (where possible) carrier concentration and mobility were measured using a single field (0.51 T) Hall effect system.

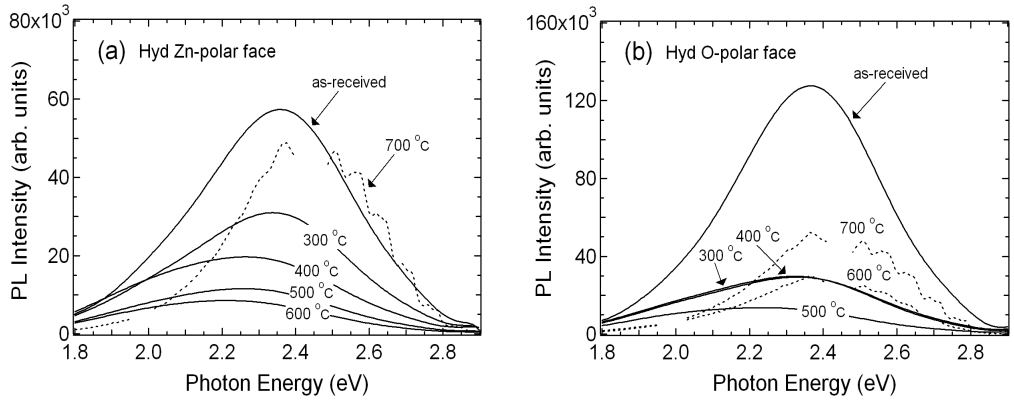

Figure 3.16: Un-normalised defect band PL spectra from the Zn-polar and O-polar faces of the same hydrothermal, bulk c-axis wafer after annealing at various temperatures from 300–700 ^{o}C for 90 minutes in 1 atmosphere O_2.

The un-normalised 4 K defect band PL for each annealing temperature is shown in Figure 3.16. For the unannealed samples, the defect band maximum is at 2.36 eV on both polar faces, with the defect band intensity approximately twice as strong from the O-polar face. The defect band intensity on both polar faces decreases with annealing temperature up to 600 ^{o}C, indicating a possible improvement in near surface material quality. At an annealing temperature of 600 ^{o}C on the O-polar face and 700 ^{o}C on the Zn-polar face, a new, structured, green band with a maximum at 2.42 eV appears, which has been linked to the activation of Cu impurities [68].

Figure 3.17 shows the change in the resistivity with annealing temperature and surface polarity for the hydrothermal, c-axis wafer. The resistivity increased by 5 orders of magnitude on annealing at 300 ^{o}C, and all annealed samples were too resistive for Hall effect measurements. This semi-insulating behaviour makes O_2 annealed hydrothermal ZnO unsuitable for device fabrication.

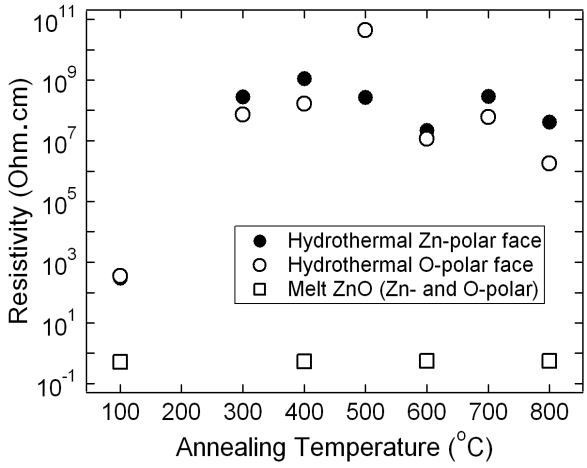

Figure 3.17: Resistivity as a function of annealing temperature (in 1 atmosphere O_2) for hydrothermal and melt bulk ZnO from van der Pauw measurements (conducted at RT).

The effect of annealing on melt ZnO was also investigated using the same methodology. In contrast to the hydrothermal material, the resistivity of melt ZnO showed little change on annealing in 1 atmosphere O_2 from 400–800 ^{o}C (see Figure 3.17). Hall effect measurements were possible on all annealed melt samples; Figure 3.18 shows the change in carrier concentration and mobility with annealing temperature. The carrier concentration of melt ZnO decreased slightly on annealing while the mobility improved by ~ 8% at 600 ^{o}C. The surface morphology of the annealed hydrothermal and melt samples was investigated using AFM. No

significant change in surface roughness was observed until 800 ^{o}C when the first signs of step terracing rearrangement was observed.

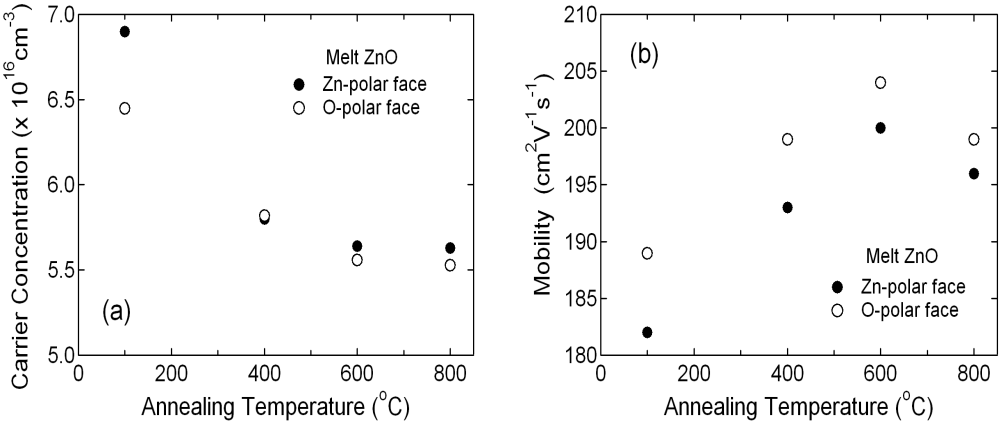

Figure 3.18: Change in (a) the carrier concentration and (b) the mobility of melt bulk ZnO with annealing temperature (for 90 minutes in 1 atmosphere O_2) from single field (0.51 T) Hall effect measurements conducted at RT.

3.7 SUMMARY

The zinc oxide surface is structurally and electrically complex with properties that depend on its crystallographic orientation. The Zn-polar and O-polar faces have attracted considerable attention for their lack of faceting despite being highly unstable from an electrostatic point of view. These polar surfaces are predicted to be stable only if (a) 1/4 of the surface atoms sites are vacant, or (b) they have a 1 x 1 hydroxide termination [40 – 43]. AFM measurements showed some evidence for (a) in the form of triangular surface reconstructions on the Zn-polar face, while XPS measurements indicated that all ZnO surfaces are naturally terminated with a hydroxide layer under vacuum conditions. This hydroxide termination produces an electron accumulation layer which increases the surface conductivity. Valence band XPS measurements were used to quantify the band bending on the polar faces, showing that the accumulation layer was strongest on the Zn-polar face.

It is well known that the surface conductivity of ZnO depends on the ambient atmosphere [11]. Schmidt *et al.* [69] showed that bulk samples that were highly resistive in air could be reversibly transformed to a highly conducting state under vacuum. They also proposed that this was due to an electron conducting surface channel which is passivated in air. This process is illustrated in Figure 3.19. In air or oxygen, the accumulation layer is compensated by acceptor-like adsorbates, O_2 and H_2O, and the surface conductivity is significantly lowered. In

vacuum conditions, the surface conductivity dramatically rises, and it is assumed that some of the O_2 and H_2O adsorbates are removed from the surface, activating the accumulation layer. This surface accumulation layer represents a significant impediment to Schottky contact formation, as the deposition of Schottky metals is done under vacuum conditions.

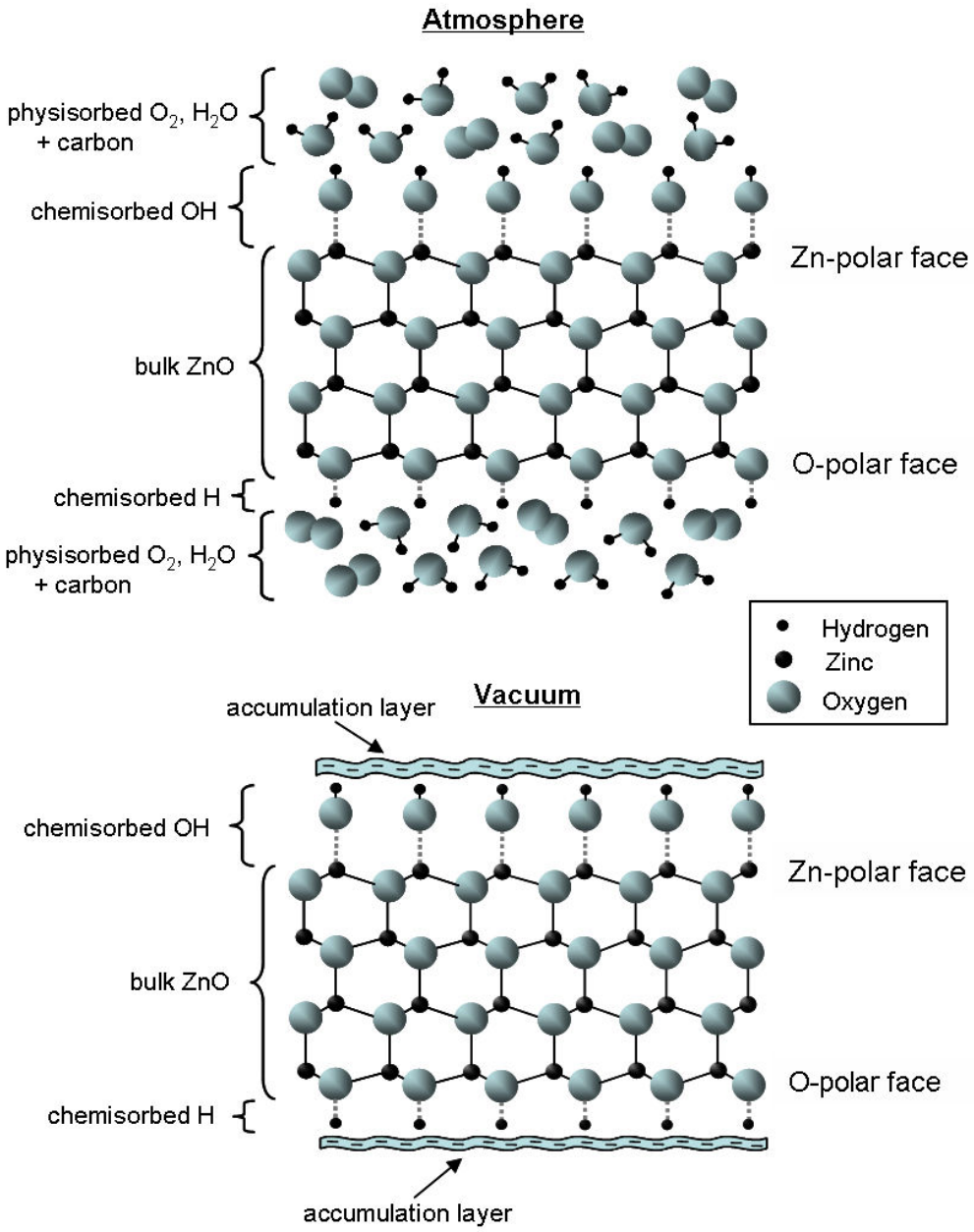

Figure 3.19: Passivation and activation of the surface accumulation layer on the polar surfaces of ZnO, in atmospheric and vacuum conditions.

Chapter 4

Metal Schottky Contacts

4.1 INTRODUCTION

One of the most effective ways to investigate the process of Schottky contact formation to a given semiconductor is to compare the barrier heights obtained for a range of different Schottky metals. However, since the effective barrier height of a Schottky contact usually decreases with increasing ideality factor, care must be taken to only compare the barrier heights of almost ideal, laterally homogeneous contacts [26]. As detailed in several comprehensive reviews of the literature [5, 8], the fabrication of low ideality factor Schottky contacts to ZnO is not a trivial exercise, and it is clear that a methodology for the consistent fabrication of high quality Schottky contacts to this semiconductor has yet to be realised.

4.2 LITERATURE REVIEW

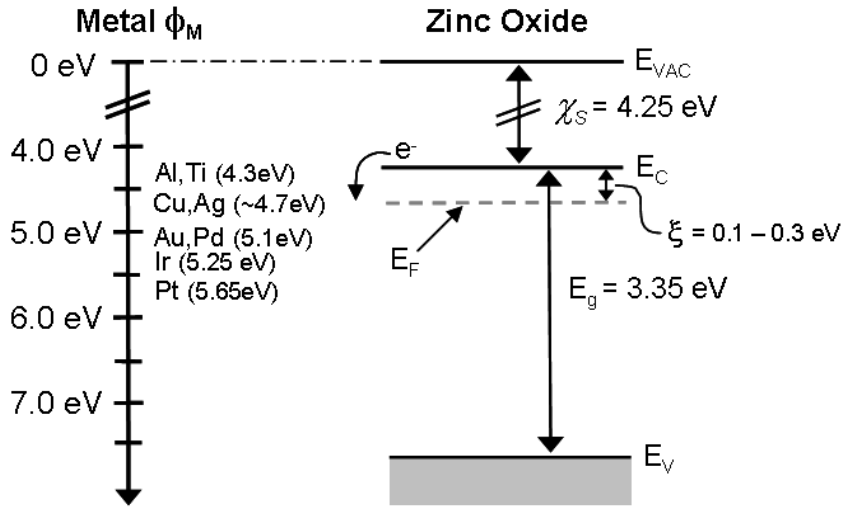

Figure 4.1. Work function of common Schottky metals compared to the band diagram of *n*-type ZnO (ξ is the E_F - E_C separation, which ranges between approximately 0.1 and 0.3 eV depending on the carrier concentration of the as-grown ZnO material).

Figure 4.1 shows the work function of common contact metals compared to the band diagram for *n*-type ZnO. From the Schottky – Mott model, it is apparent that Au, Pd, Ir, and Pt are promising candidates for forming high Schottky barriers to *n*-type ZnO, and indeed most literature reports have involved Au, Pd, and Pt and perhaps more surprisingly Ag. Ir has been ignored until recently [67], probably due to its expense and limited availability. Figure 4.2 shows the barrier height (Φ_B) and ideality factor (η) for Schottky contacts to *n*-type ZnO from the literature with values of $\eta < 1.8$. The surface polarity of the ZnO material, where specified, is also indicated. References are given for the best reports (excluding those published as part of this work which are compared later in this thesis) for each Schottky metal.

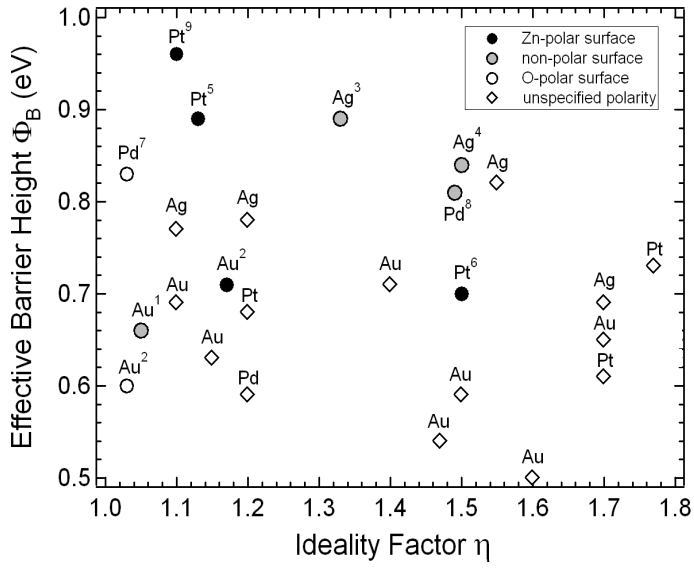

[1]Mead et al., (1965) [70]
[2]Coppa et al., (2005) [73]
[3]Sheng et al., (2002) [74]
[4]Liang et al., (2000) [75]
[5]Kim et al., (2005) [80]
[6]Ip et al., (2004) [85]
[7]Grossner et al., (2004) [92]
[8]von Wenckstern et al., (2004) [93]
[9]Endo et al., (2007) [94]

Figure 4.2. Effective barrier height (Φ_B) versus ideality factor (η) plot for Schottky contacts to *n*-type ZnO as reported in the literature. The polarity of the ZnO material, where specified by the authors, is indicated and references are given for the 'best' reported contacts for each Schottky metal.

Schottky contacts to ZnO were first reported by Mead in 1965 [70,71] on vacuum-cleaved, hexagonal, undoped ZnO crystals ($n \sim 10^{16} - 10^{17}$ cm^{-3}). The barrier heights for Pd (0.65 eV), Ag (0.66 eV), Pt (0.71 eV), and Au (0.71 eV) contacts were determined by the photoresponse method and consequently no values of η were reported. Subsequently Neville and Mead [72] used a two stage acid etch treatment of H_3PO_4 and HCl, followed by a de-ionised H_2O rinse to fabricate Au and Pd Schottky contacts with $\Phi_B = 0.66$ eV and 0.60 eV respectively, and $\eta \sim 1.05$, determined by *I–V, I–V–T, C–V,* and photoresponse methods. However, subsequent attempts to use similar acid-based treatments have produced rather disappointing results. Specifically, Polyakov *et al*. [76] compared the effect of HCl, HNO_3, and organic solvent cleaning on the performance of Au and Ag Schottky contacts on the Zn-polar

face of bulk SCVT grown wafers ($n = 9 \times 10^{16}$ cm^{-3}). For both metals the best results, in terms of lowest reverse leakage current, were achieved with just an organic solvent clean. The barrier heights were 0.65 eV (Au) and 0.69 eV (Ag) with η in the range 1.6–1.8. These results are symptomatic of the literature since 1965 with (a) the majority of barrier heights lying in the 0.6 – 0.8 eV range regardless of the Schottky metal used, (b) relatively high ideality factors (η > 1.3), and (c) the better results achieved using simple organic solvent cleaning. Recently, several authors have reported the success of oxidation treatments in improving Schottky contact performance. These have included remote oxygen plasmas, hydrogen peroxide, UV ozone, and pulsed laser oxygen treatment. This represents a significant development which warrants a detailed review:

4.2.1 Remote Oxygen Plasmas

Coppa *et al*. [45] performed a detailed investigation into the effect of remote plasma cleaning —20 W, 20% O_2 / 80% He plasma, 0.050 Torr, 525 - 550 ^{o}C— on the Zn-polar and O-polar faces of seeded chemical vapour transport (SCVT), bulk ZnO wafers ($n = 1 \pm 5 \times 10^{17}$ cm^{-3}). This combination of annealing and plasma treatment was found to almost completely remove the surface carbon contamination and significantly reduce the thickness of the surface hydroxide layer to ~ 0.4 ± 0.1 monolayers. Without this treatment, Au Schottky contacts on both polar faces showed poor rectifying behavior with η > 2. This was attributed to the presence of a high conductivity surface accumulation layer caused by the hydroxide contamination. The best Au Schottky contacts on both the Zn-polar and [O-polar] surface —Φ_B = 0.71 [0.60] eV, η = 1.17 [1.03]— were achieved using the remote plasma treatment described above, followed by a cooling in the unignited plasma ambient prior to contact deposition. The authors used XPS, UPS, and LEED to propose that this additional step caused the chemisorption of oxygen onto both polar surfaces, resulting in a lowering of the surface conductivity and reduction in near-surface downward band bending. Mosbacker *et al*. [77] observed a conversion from ohmic to rectifying behaviour for Au contacts on the Zn-polar and O-polar faces of SCVT bulk wafers, following room temperature remote 20% O_2 / 80% He plasma pre-treatment, although the barrier heights of the resulting Schottky contacts were only in the 0.42 – 0.50 eV range, with η ~ 2. This pre-treatment was again accompanied by an almost complete removal of carbon and OH contamination from the ZnO surface and also a significant reduction in the defect band emission using depth resolved cathodoluminescence. In addition, 9 K photoluminescence spectra, taken before and after the treatment, showed a dramatic reduction in the I_4 peak at ~ 3.3624 eV from both polar faces, (I_4 is attributed to the neutral hydrogen donor bound exciton) indicating the removal of hydrogen from the near surface region. In subsequent reports, Mosbacker *et al*. extended the use of remote oxygen plasma

treatment to include Au, Pt, Ir, Pd, Ta and Al contacts [78, 79]. They again used depth resolved cathodoluminescence to show that remote oxygen plasma treatment reduces defect band emission and linked this to a reduction in near surface native point defects. They also showed that metal deposition can cause an increase in defect band emission and argued that this was due to the creation of point defects by the metalisation process.

4.2.2 Hydrogen Peroxide

Kim *et al*. [80, 81] first investigated the effect of hydrogen peroxide (H_2O_2) pre-treatment on the Zn-polar face of bulk, single crystal substrates from MAHK Co., Japan. They observed a significant improvement in the rectifying behavior of Pt Schottky contacts, obtaining a barrier height (from *I–V* measurements) of 0.89 eV, a J_{rev} (at -1V) of 6.4×10^{-7} Acm^{-2}, and an ideality factor of 1.15. They also observed a considerable decrease in the defect band PL emission from the Zn-polar surface following H_2O_2 treatment. The same authors also reported the ohmic to Schottky conversion of Pt contacts on the O-polar face of similar wafers [82], using a boiling $(NH_4)_2S_x$ pre-treatment for 30 s. Subsequently, Gu *et al*. [83] reported the ohmic to rectifying conversion of Au contacts to melt grown, bulk ZnO of unspecified surface polarity (from Cermet Inc.) after pre-treatment in boiling H_2O_2 (for 3 minutes). The best Au diodes were η = 1.15, Φ_B = 0.63 V, and a J_{rev} (-1V) = 2×10^{-6} Acm^{-2}. XPS measurements showed that surface carbon contamination was unaffected by this treatment but the concentration of surface OH was significantly reduced. The boiling H_2O_2 treatment also resulted in a significant increase in surface roughness and a loss of Zn in the form of Zn vacancies or vacancy clusters. Similarly Schifano *et al*. [84] obtained an even more dramatic improvement in the rectifying behavior of Pd Schottky contacts by pre-treating the O-polar face of hydrothermally grown, bulk ZnO in H_2O_2 for 15 minutes at room temperature. A rectifying ratio (at ± 2 V) of 10^9 was obtained and a J_{rev} (-2 V) of 4×10^{-9} Acm^{-2} with the contacts stable or improved by annealing at 200°C for 30 minutes in air. However, the ideality factor was high (~ 1.8) indicating that the current transport was not purely thermionic. The H_2O_2 treatment again resulted in a significant increase in r.m.s. surface roughness to approximately 2 ± 0.5 nm with a granular structure clearly evident from AFM.

4.2.3 UV Ozone

Ip *et al*. [85, 87] investigated the use of UV ozone cleaning prior to the deposition of Pt contacts on the Zn-polar face of melt grown, bulk ZnO from Cermet Inc. An ohmic to rectifying conversion was again reported with Φ_B = 0.70 V and η = 1.49. In this case, the r.m.s. surface roughness improved from 0.25 nm to 0.16 nm after ozone treatment which was

attributed to a significant reduction in the surface carbon contamination (from 29.5 to 5.8%) as measured by XPS. XPS measurements also showed only a slight decrease in surface OH, in contrast to the almost complete removal obtained by remote plasma and H_2O_2 treatment. In addition, Nakano *et al*. [88] used the conducting polymer poly(3,4-ethylene,dioxythiphene): poly(styrenesulfonate) or PEDOT:PSS to fabricate Schottky contacts with $\eta = 1.2$ and $\Phi_B = 0.9$ eV on the Zn-polar face of hydrothermally grown, bulk ZnO from Tokyo Denpa Co. Ltd. which was pre-exposed to UV ozone.

4.2.4 Pulsed Laser Excited Oxygen

Oh *et al*. [90] treated the surface of an organic solvent cleaned O-polar, hydrothermally grown, ($n = 2 \times 10^{16}$ cm^{-3}) bulk ZnO substrate from CrysTec GmbH, using a pulsed KrF excimer laser in an 0.1 mtorr oxygen atmosphere. This process resulted in a significant decrease in the intensity of the CL defect band emission from the O-polar surface and an increase in the near band edge emission. In addition, Auger electron spectroscopy (AES) showed a significant reduction in the concentration of carbon (8.4 – 1.3%) and an increase in the atomic oxygen percentage (16.3 – 21.4%) of the treated surface. This was attributed to the KrF laser photon energy being sufficiently high to break the C-H and O-H bonds at the surface while also creating oxygen radicals to reduce the concentration of donor-like surface defects. Pt Schottky contacts fabricated on this surface showed a significant improvement in rectifying performance ($\Phi_{B,I\text{-}V} = 0.73$ V and $\eta = 1.77$) compared with those on untreated surfaces, although the ideality factor was still too high for these to be considered high quality contacts.

4.2.5 Literature Summary

In summary, the following trends have emerged in the literature for Schottky contact formation to n-type ZnO over the past 50 years:

1) Most reported barrier heights have been in the 0.6 – 0.8 eV range, regardless of the Schottky metal used.
2) There are very few reports of “almost ideal” Schottky contacts with ideality factors close to unity as required for comparison with the Schottky – Mott, MIGS, and CBP theories.
3) Pre-contact treatment of the ZnO surface in oxidising conditions can result in improvements in Schottky barrier height, often involving an ohmic – Schottky conversion, but the resulting contacts still tend to have relatively high ideality factors.

4) Φ_B results for the same metal have been difficult to reproduce on a consistent basis, even by the same researchers using the same ZnO material.

5. A methodology for the consistent fabrication of high quality (i.e. high Φ_B, low η) Schottky contacts with reproducible properties is lacking.

4.3 EXPERIMENT I - Ag, Au, Pd, & Pt Contacts on Melt Grown ZnO

The initial experiment was an investigation into the effect of surface polarity on the performance of planar ZnO Schottky diodes, fabricated using all four of the common Schottky metals: Pd, Pt, Au, and Ag. Two melt grown, bulk, c-axis wafers from Cermet Inc. (USA) were used: one polished on the Zn-polar face, and one polished on the O-polar face. Each wafer (10 mm x 10 mm x 500 μm) was cleaved into four approximately equal area samples, one of which was characterised using single field (0.51 T) Hall effect measurements (Table 4.1), and the rest used for diode fabrication.

Table 4.1: Room temperature electrical properties of melt grown wafers from Cermet Inc. characterised by single field (0.51 T) Hall effect measurements using the van der Pauw technique.

Cermet Wafer	n (cm^{-3})	μ ($cm^2V^{-1}s^{-1}$)
Zn-polar	3.5×10^{16}	230
O-polar	3.0×10^{16}	205

4.3.1 Diode Fabrication Method

Each as-received wafer was ultrasonically pre-cleaned for 5 minutes in warm acetone, followed by rinsing in methanol, iso-propyl-alcohol, and drying in N_2. The fabrication technique for both Schottky and ohmic contacts was lift-off photolithography using AZ1518 photoresist, chrome masks, and a Suss MA6 mask-aligner equipped with a 365 nm UV lamp. AZ1518 photoresist was spun onto pre-cleaned samples at 4,000 rpm and then baked in an oven at 96 ^oC for 30 minutes. Samples were then placed in 'soft contact' with a chrome mask, through which rows of 350 μm diameter circular Schottky contacts were patterned onto the resist by a 20 s UV exposure. The circular patterns were then developed using tetramethyl ammonium hydroxide (TMAH) for 20 s, followed by a final rinse in de-ionised H_2O and drying in N_2. A thin film of the appropriate Schottky metal, approximately 50 nm in thickness, was deposited by either thermal evaporation (Au and Ag) or electron beam evaporation (Pd and Pt). Electron beam evaporation was used for Pd and Pt due to their high melting points (1552 and 1772 ^oC) respectively compared to Ag (962 ^oC) and Au (1064 ^oC). The metal film was then

lifted off from the unpatterned areas by removing the underlying unexposed photoresist with ultrasonically agitated acetone. The ohmic contacts consisted of Ti/Al/Pt/Au annular rings of inside diameter 400 μm, outside diameter 600 μm, fabricated using the same lift off technique. All four metals in the ohmic contact were deposited consecutively by electron beam evaporation using a four crucible carousel. The Schottky contact area was 9.62×10^{-3} cm^2 and the radial gap to the ohmic contact was 25 μm. In this way, rows of identical Pd, Ag, Au, and Pt Schottky diodes were fabricated over the same relatively small area of each wafer in an attempt to minimise the effect of variations in surface morphology (see Figure 4.3).

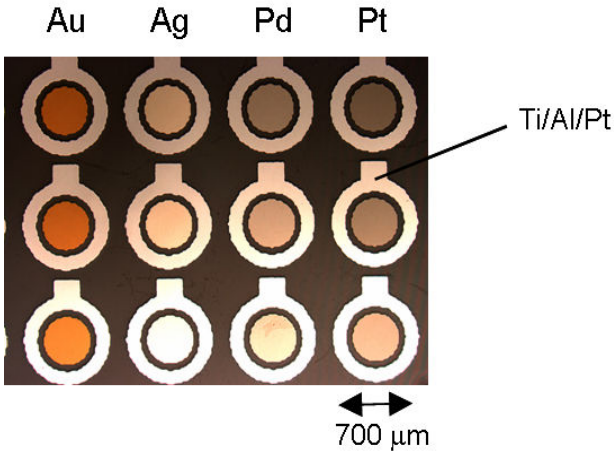

Figure 4.3. Arrays of planar Au, Ag, Pd, and Pt diodes fabricated on the Zn-polar surface of a melt grown, bulk, single crystal wafer from Cermet Inc.

Figure 4.4 shows the typical *I–V* characteristics of the Pd, Pt, Au, and Ag Schottky diodes on both the Zn-polar and O-polar melt grown wafers. All measurements were conducted in dark conditions and at room temperature, using a HP4155A parameter analyser. These *I–V* characteristics showed no significant polarity difference for the Au and Ag diodes; however, the reverse leakage currents for the Pd and Pt diodes were significantly lower on the O-polar surface. Table 4.2 gives a summary of the *I–V* and *C–V* results (taken at 100 kHz using a Philips PM6304 RCL meter) for each Schottky metal and surface polarity. The series resistance R_s of all diodes was approximately 25 Ω. No significant difference in barrier height was evident for the Au and Ag diodes, although the ideality factors were slightly lower on the O-polar surface. A clear polarity effect was observed for the Pd and Pt diodes with significantly higher barrier heights, lower ideality factors, and lower reverse currents on the O-polar surface. The Ag diodes produced the highest Schottky barriers, which is surprising given that Ag has by far the lowest work function (see Figure 4.1) and should, according to the Schottky – Mott model, give the lowest barrier.

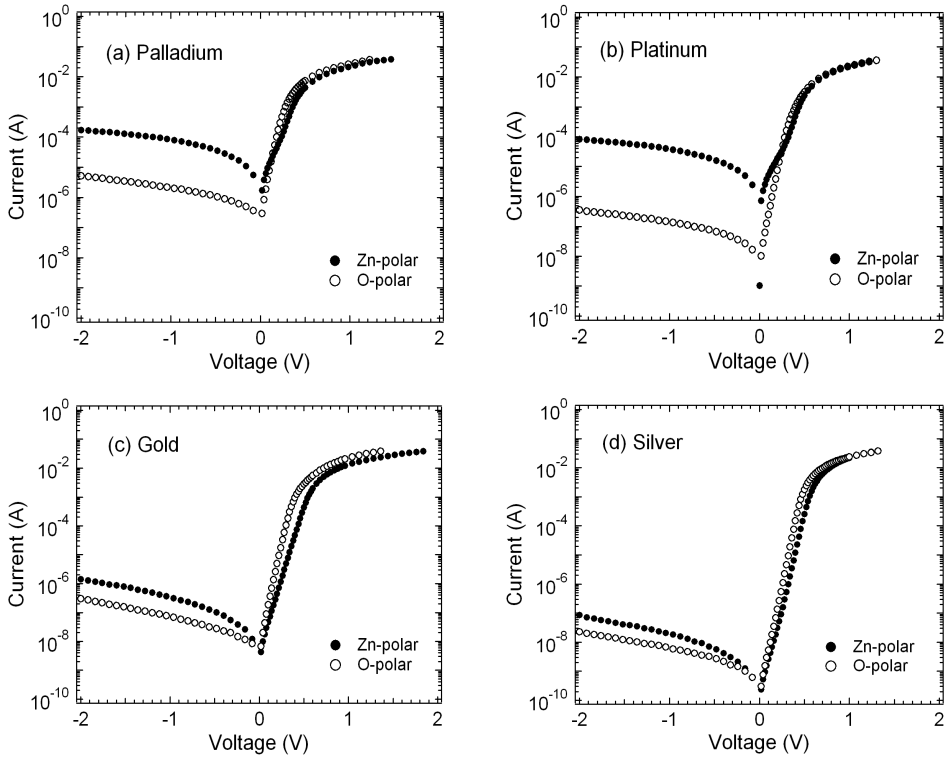

Figure 4.4. Typical room temperature *I–V* characteristics of various planar metal Schottky diodes on single-sided polished Zn-polar and O-polar melt grown, bulk ZnO wafers.

Table 4.2: Planar metal Schottky diode parameters on single-sided polished Zn-polar and O-polar melt grown, bulk ZnO wafers determined from *I–V* and *C–V* measurements. [ideality factor (η), barrier height ($\Phi_{B,I\text{-}V}$), and the rectifying ratio (RR) at ± 1 V from *I–V* measurements and barrier height ($\Phi_{B,C\text{-}V}$) from *C–V* measurements at a frequency of 100 kHz].

Schottky Metal	Surface Polarity	η	$\Phi_{B,I\text{-}V}$ (eV)	RR (± 1 V)	$\Phi_{B,C\text{-}V}$ (eV)
Pd	Zn-polar	2.0	0.55	300	-
	O-polar	1.2	0.59	1.3×10^4	0.59
Pt	Zn-polar	2.0	0.55	600	-
	O-polar	1.2	0.68	1.6×10^5	0.72
Au	Zn-polar	1.4	0.71	3.8×10^4	0.70
	O-polar	1.1	0.69	3.0×10^5	0.70
Ag	Zn-polar	1.2	0.78	1.3×10^6	0.80
	O-polar	1.1	0.77	4.0×10^6	0.80

To investigate the anomalously high barriers for Ag contacts, a further series of Ag diodes were fabricated on additional parts of the same Zn-polar and O-polar wafers. Even more surprisingly, some of these additional Ag contacts showed even better rectifying *I–V* characteristics, with barrier heights varying from 0.77 to 1.02 eV. The *I–V* characteristics of the diodes with the highest barriers are shown in Figure 4.5 and summarised in Table 4.3. Observations using an optical microscope showed that the highest rectifying Ag contacts showed clear signs of oxidation. This, coupled with the observation that the performance of many Ag Schottky diodes tended to 'improve with age', suggests that chemical reactions resulting in the formation of silver oxide may play a role in the Ag contacts.

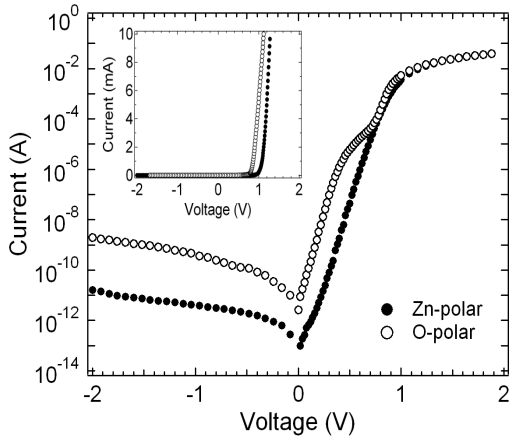

Figure 4.5. Room temperature *I–V* characteristics for the best Ag Schottky contacts on single-sided polished Zn-polar and O-polar melt grown, bulk ZnO wafers.

Table 4.3: Schottky contact parameters for the best Ag Schottky contacts on single-sided polished Zn-polar and O-polar melt grown, bulk ZnO wafers determined from *I–V* and *C–V* measurements.

Surface Polarity	η	$\Phi_{B,I\text{-}V}$ (eV)	RR (± 1 V)	$\Phi_{B,C\text{-}V}$ (eV)
Zn-polar	1.2	1.02	1×10^7	1.00
O-polar	1.1	0.88	1×10^9	0.98

Further evidence for the role of chemical reactions was provided by the dramatic improvement with time in the rectifying properties of certain of the silver contacts on the O-polar wafer as shown in Figures 4.6 and 4.7. Immediately after fabrication these silver contacts has very poor properties, with a rectifying ratio at ± 1V of only ~ 3. However, after storage at room temperature for 6 months, the contacts had changed from a metallic silver appearance to a brown oxidised colour, and the rectifying ratio had increased by approximately 5 orders of magnitude.

The forward current *I–V* characteristics of these 'aged' diodes could not be fitted by a single exponential function, indicating the presence of more than one barrier and suggesting that the oxidation was inhomogeneous and/or incomplete. Approximate values of $\Phi_{B,I\text{-}V}$ and η of 0.70 eV and 1.5 respectively, were obtained from Figure 4.7(a), while a value of $\Phi_{B,C\text{-}V}$ = 0.90 eV (using $\Phi_{B,C\text{-}V} = qV_{bi} + \xi$) was determined from *C–V* characteristics at 20 kHz [see Figure 4.7(b)]. Significantly larger values of $\Phi_{B,C\text{-}V}$ compared $\Phi_{B,I\text{-}V}$ are usually indicative of an inhomogeneous contact [28]. An age-related improvement in Ag and Au Schottky contacts to ZnO has also been observed by other researchers [86].

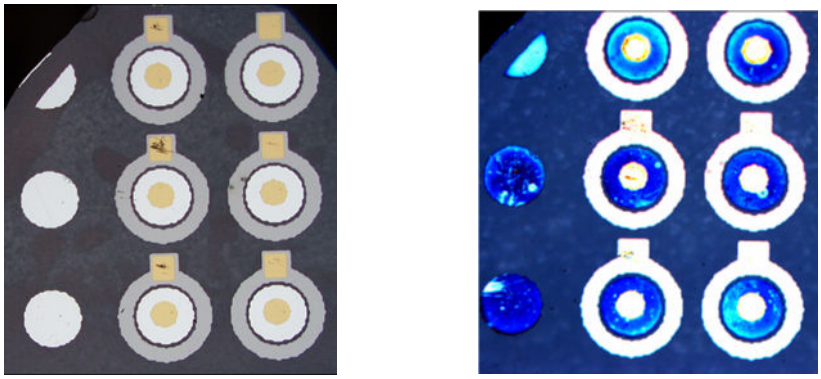

Figure 4.6. Silver Schottky contacts on the O-polar face of melt grown, bulk ZnO, (a) after fabrication and, (b) after 6 months aging.

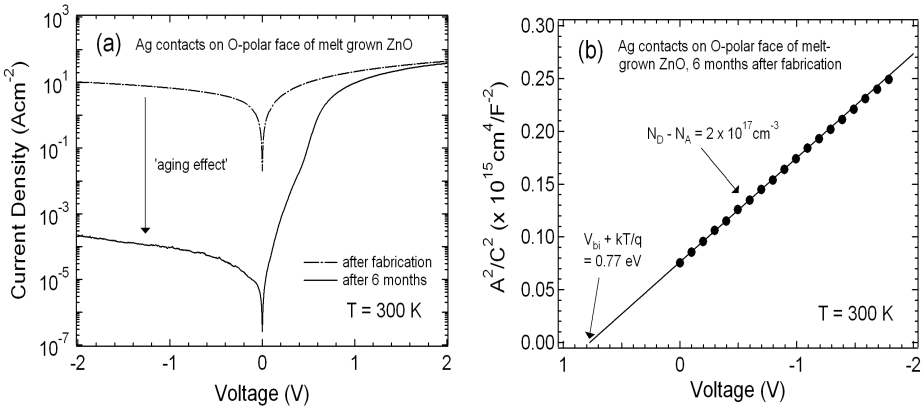

Figure 4.7. (a) typical *I–V* characteristics of certain silver Schottky contacts, after fabrication and after 6 months aging, on the O-polar face of melt grown, bulk ZnO, and (b) typical *C–V* characteristics of the 'aged' silver oxide contacts, measured using a frequency of 20 kHz.

4.3.2 Experiment I Conclusions

The initial experiment involving planar Pd, Pt, Au, and Ag Schottky contacts on single-sided polished Zn-polar and O-polar melt grown, bulk ZnO wafers yielded a number of interesting findings which form the starting point for the rest of the experiments in this chapter. Specifically these were:

1) The polarity of the ZnO surface appears to have a measureable influence on the properties of Schottky contacts;
2) The highest barriers were achieved with Ag as the Schottky metal, which is surprising given that Ag has the lowest work function of the metals used;
3) The barrier height of Ag contacts showed a wide variation (0.77 – 1.02 eV), with the highest barriers on contacts that were visibly oxidised.

4.4 EXPERIMENT II - Au Contacts on Zn-polar Hydrothermal ZnO

The next experiment involved the fabrication of planar Au Schottky diodes on the Zn-polar face of three double-sided polished, hydrothermally grown, bulk, c-axis ZnO wafers from Tokyo Denpa Co. Ltd (Japan), which will be referred to as wafers A1, A2, and A3. The room temperature carrier concentration and mobility of these wafers were $2.5 – 3.0 \times 10^{14}$ cm^{-3} and 190 – 200 $cm^2V^{-1}s^{-1}$. Arrays of Au Schottky diodes were fabricated on each wafer. In each case, the fabrication method was identical to that already described in Section 4.3.1 —a simple organic solvent clean, UV photoresist patterning using TMAH developer, thermal evaporation of Au, and ultrasonically assisted lift off using acetone. As the thickness of the Au Schottky contact was only 20 – 25 nm, an additional 150 μm diameter Au contact pad was added to avoid damage from the probe contacts used in electrical characterisation.

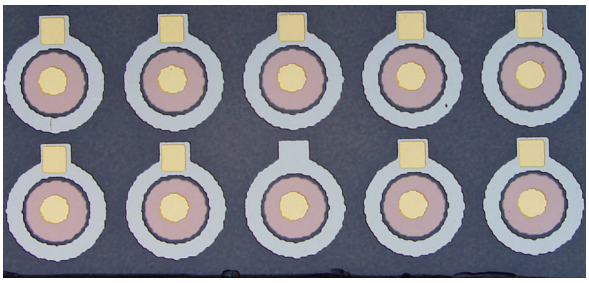

Figure 4.8. Au Schottky diodes on the Zn-polar face of hydrothermal bulk ZnO from Tokyo Denpa Co. Ltd. (Japan).

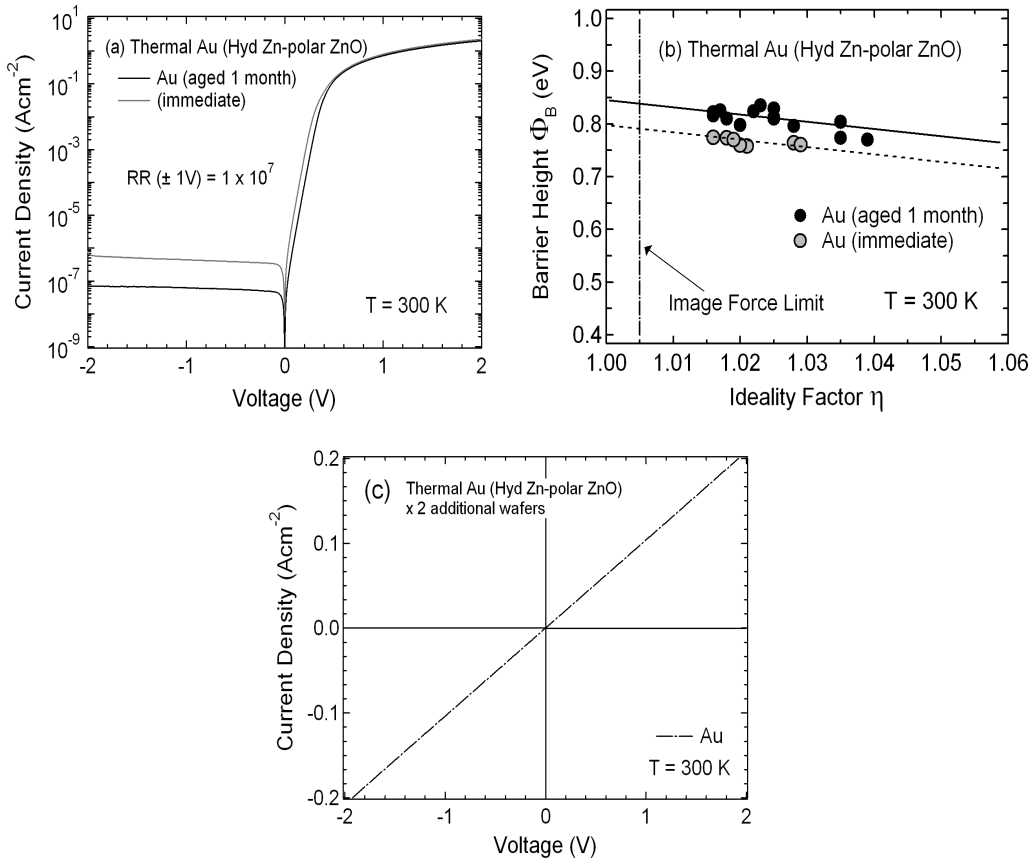

Figure 4.9. (a) Typical *I–V* characteristics of Au Schottky contacts, after fabrication, and after one month, on the Zn-polar face of hydrothermal, bulk ZnO wafer A1; (b) Φ_B versus η plot for multiple Au diodes on wafer A1; and (c) Typical *I–V* characteristics of Au Schottky contacts on the Zn-polar face of hydrothermal, bulk ZnO wafers A2 and A3.

Figure 4.9(a) shows typical *I–V* characteristics of the Au Schottky diodes on the Zn-polar face of wafer A1. An aging effect was again observed, in that the rectifying performance (in terms of Φ_B) of the Au diodes increased slightly on re-testing after 1 month, while subsequent later testing produced no further improvement. Figure 4.9(b) shows an effective barrier height (Φ_B) versus ideality factor plot (η) for multiple Au diodes on wafer A1. The best Au diodes had ideality factors < 1.02, which is close to the image force controlled limit η_{if} of 1.007, calculated using Equations (2.20) and (2.21). Using the method of Mönch [26] described in Section 2.5.1, this Φ_B versus η plot can be extrapolated to η_{if} to give $\Phi_B^{if} = 0.83$ eV which can then be corrected for image force lowering $\delta\Phi_B = 0.02$ eV [Equation (2.20)] to determine a value for the image-force-corrected homogenous barrier height $\Phi_B^{hom*} = 0.85$ eV for Au contacts on the Zn-polar face of hydrothermal ZnO. This value is important as it allows a meaningful comparision with the theoretical models of Schottky

contact formation, whereas the barriers of inhomogenous contacts are lowered by factors such as surface contamination and extrinsic defects which are not included in these models.

In sharp contrast, all the Au diodes fabricated on the Zn-polar face of wafers A2 and A3 were perfectly ohmic in nature. This represents a remarkable difference in performance for Au contacts fabricated in the same way, on the same face, of similar high quality bulk wafers. It is especially surprising that one set of Au contacts gave almost ideal Schottky behavior with ~ 7 orders of magnitude of rectification (at ± 1V), while the others showed no rectifying behavior at all, even after 6 months in storage. To investigate this further, room temperature cathodoluminescence (CL) spectra were measured by collaborators at Waseda University, Tokyo, Japan from the bare surface of wafers A1 and A2 and from underneath the respective Schottky and ohmic Au contacts. The use of depth resolved cathodoluminescence in assessing the defects introduced by Schottky metalisation to ZnO has been developed by Mosbacker *et al.* [78].

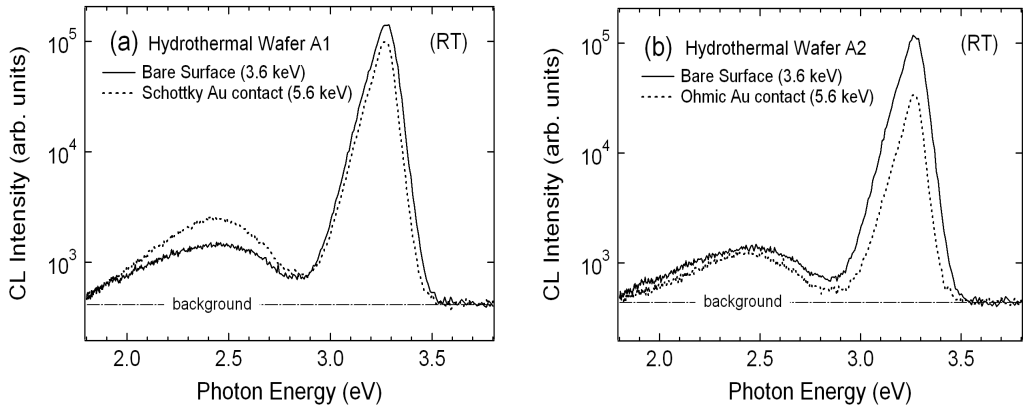

Figure 4.10. Room temperature cathodoluminescence spectra (logarithmic scale) from the bare ZnO surface and underneath (a) Schottky, and (b) ohmic Au contacts on the Zn-polar face of hydrothermally grown, bulk ZnO wafers A1 and A2.

For the CL measurements shown in Figure 4.10, an incident electron beam of energy E_B = 3.6 keV and beam current $I_B = 7 \times 10^{-10}$ A was used to examine the bare Zn-polar ZnO surface, while an electron beam of E_B = 5.6 keV and $I_B = 7 \times 10^{-10}$ A was used to probe underneath the Au contacts. Monte Carlo simulation of the electron cascade generated by the CL beam indicates that for a 3.6 keV beam, peak electron-hole (*e-h*) pair creation occurs at depths of 55 - 85 nm below the ZnO surface [67]. Furthermore, a 5.6 keV electron beam through a 20 – 25 nm Au film, and a 3.6 keV beam directly into the ZnO surface should give comparable peak *e-h* pair creation depths [67]. All spectra were taken at room temperature and are shown without normalisation. The dominant peak with a maximum at ~ 3.3 eV is from near

band edge (NBE) emission while the broader peak with a maximum at ~ 2.45 eV is due to transitions involving defect levels (DL) in the band gap. For each spectrum, the integrated intensity of the NBE and DL emission was calculated and expressed as the fraction I_{DL} / I_{NBE}. The bare surface spectra for both wafer A1 and A2 was very similar with $I_{DL} / I_{NBE} = 0.038$ and 0.040 respectively, indicating similar near-surface defect densities, at least for optically active defects. The CL spectrum through the Schottky Au contact on wafer A1 [Figure 4.10(a)] showed an increase in defect band emission to $I_{DL} / I_{NBE} = 0.10$, which may be due to extra defects created by the Au metalisation. The total intensity of the emission through the Au contact on wafer A2 was less than that for wafer A1, due to a small difference in the relative thickness of the Au contacts. However, the defect band intensity through the ohmic Au contact on wafer A2 was $I_{DL} / I_{NBE} = 0.12$ which is almost identical to that through the Schottky Au contact on wafer A1.

These CL results indicate that the relative intensity of the defect band emission is similar through both the Schottky and ohmic Au contacts. Therefore, it is reasonable to conclude that the dramatic difference in the electrical behaviour of the Au contacts on wafers A1 and A2/A3 must be due to something more fundamental than a small difference in the concentration of metal-induced surface defects, which might be expected to degrade the rectifying performance of the contact rather than cause it to become completely ohmic. Instead, the following explanation is proposed: it was shown in Section 3.3 that, in the vacuum conditions prior to thermal Au deposition, the Zn-polar face of hydrothermally grown, bulk ZnO has a heavy surface accumulation layer due to a hydroxide termination. If either the kinetic energy of the incident Au atoms or collateral radiation from evaporation is sufficient to remove the hydroxide termination, then the accumulation layer will disappear and a high quality Schottky contact will be created. However, if the Au atoms are deposited on top of the hydroxyl groups, then the highly conductive accumulation layer remains in place, allowing electrons to tunnel directly through the Au contact which becomes ohmic in nature. While it is acknowledged that this explanation is speculative, the hydroxide termination / surface accumulation layer is known to exist [45] and the earlier review of oxidation pre-treatments showed that improvement in Schottky contact performance is nearly always accompanied by a significant reduction in surface hydroxide concentration.

This possible explanation will be referred to as the ‘de-hydrogenation model’ and is illustrated in Figure 4.11. Two alternative final Schottky interfaces are shown: the first version corresponds to the replacement of hydroxyl (OH) groups from the Zn-polar ZnO surface and the formation of Au–Zn bonds, while in the second version, the O–H bond of the hydroxyl group is broken, resulting in the removal of just H atoms and the formation of Au–O bonds. Some Au–O bonding may also occur in version 1 as the outermost Zn and O atomic planes are

closely stacked. Dong and Brillson [89] have reported first-principles calculations based on density functional theory for Ag and Au ZnO interfaces. Their results showed that metal–Zn bonding tended to produce ohmic contacts while metal–O bonding gave Schottky-like behaviour. They found that when metal Zn–bonds form, the Schottky barrier height decreases and the Fermi level is pushed towards the conduction band minimum. This theoretical study suggests that version 2 (Figure 4.11) for the Au Schottky interface on the Zn-polar face is more likely.

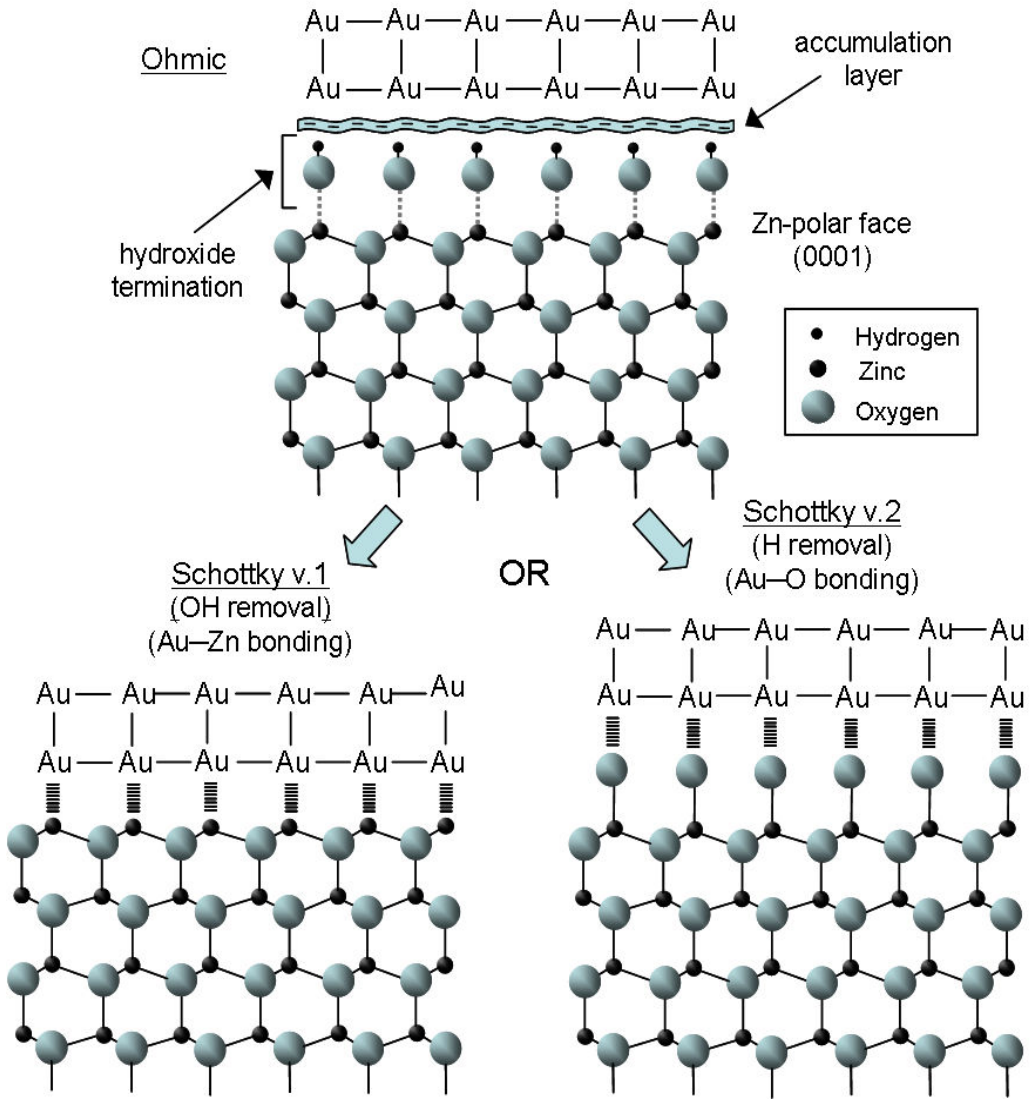

Figure 4.11. 'De-hydrogenation model' – possible explanation of the anomalous formation of ohmic contacts and 'almost ideal' Schottky contacts on similar Zn-polar, hydrothermal bulk ZnO wafers.

It is also possible that a slow "de-hydrogenation" could explain the dramatic age–related rectifying conversion of the 'almost ohmic' Ag Schottky contacts described in Section 4.3. This situation is more complicated, in that the composition of the contacts also changed with time as they oxidised, so in addition to hydroxide/hydrogen removal, there could also be an increase in the work function of the contacts and the diffusion of oxygen to the Schottky interface. Since the O-polar face of ZnO was involved, H rather than OH removal is much more likely, as the latter would involve the breaking of three O–Zn bonds against only a single O–H bond for H removal. Interestingly, Fukutani *et al.* [91] showed that the deposition of Ag atoms onto the hydrogen (1x1) terminated Si(111) surface at 360 K causes H desorption from the surface, and also that H can be desorbed from a cryogenically deposited Si–H–Ag interface by annealing at 300 K. Therefore, it is not difficult to imagine a similar situation for the H terminated O-polar ZnO face (see Figure 4.12) provided the O–Ag bond is energetically more favourable than the O–H bond.

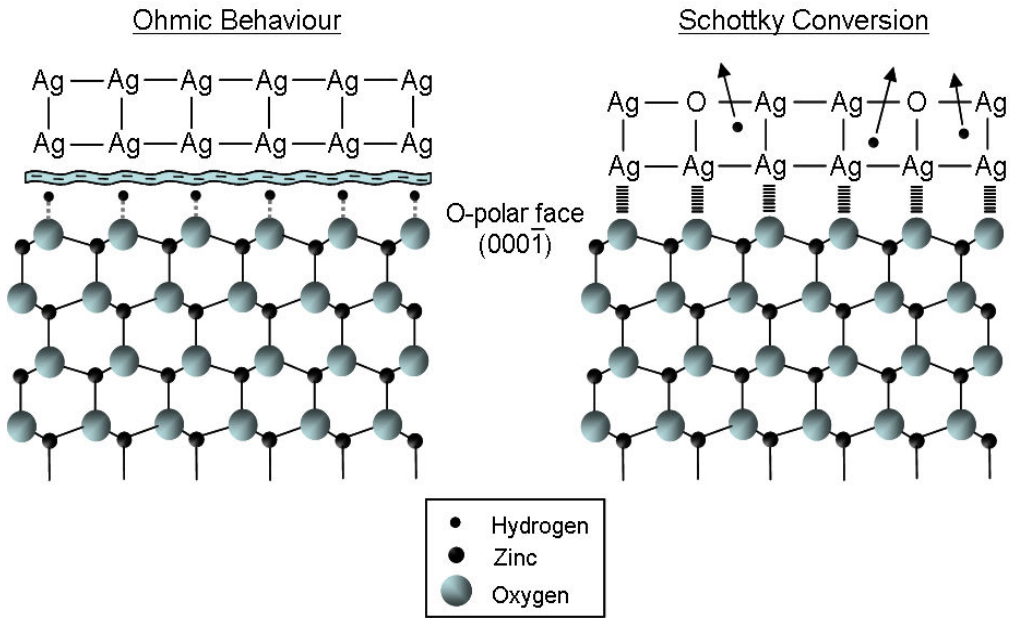

Figure 4.12. Possible age-related conversion from ohmic to Schottky behaviour of Ag contacts, following H desorption from the hydrogen terminated O-polar surface of ZnO.

.

4.5 EXPERIMENT III - Ag Contacts on Zn-polar Hydrothermal ZnO

An array of planar Ag Schottky contacts was also fabricated on wafer A1, using the same organic surface cleaning and photolithographic method as before. The Ag film was deposited by thermal evaporation. Figure 4.13(a) shows the typical *I–V* characteristics of the resulting diodes, while Figure 4.13(b) shows the Φ_B vs η plot for multiple diodes. The best Ag diodes had very low ideality factors, close to the image force limit η_{if} = 1.007. Using the same procedure as before, the Φ_B vs η plot was used to determine the image-force-corrected, homogenous barrier height Φ_B^{hom*} = 0.74 eV for Ag contacts on Zn-polar, hydrothermal ZnO.

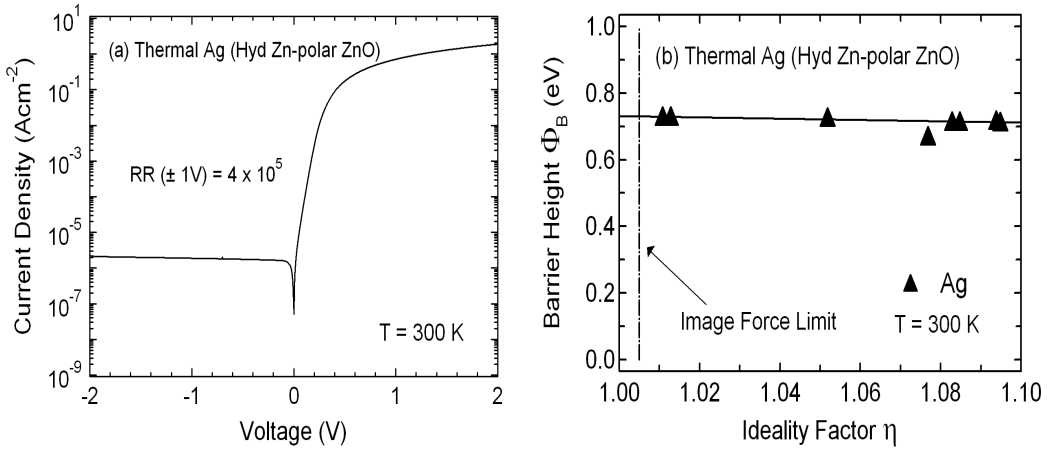

Figure 4.13. Ag Schottky contacts on the Zn-polar face of hydrothermally grown, bulk ZnO wafer A1.

4.6 EXPERIMENT IV - Ir Contacts on Zn-polar Hydrothermal ZnO

Iridium Schottky contacts were photolithographically fabricated on the Zn-polar face of a new hydrothermally grown wafer, wafer A4, from Tokyo Denpa Co. Ltd., which was again given only a simple organic solvent pre-clean. The carrier concentration and mobility of this wafer was 1 x 10^{13} cm^{-3} and 210 $cm^2V^{-1}s^{-1}$ from single field (0.51 T) Hall effect measurements. Due to its very high melting point (2466 ^oC), the Ir contacts were deposited by e-beam evaporation using an amorphous carbon crucible. Figure 4.14(a) shows the typical *I–V* characteristics of the as-deposited Ir contacts, which were poorly rectifying with a rectifying ratio (± 1V) of only ~ 10. These contacts were subsequently post-annealed at 150 ^oC for 90 minutes in oxygen gas. The typical *I–V* characteristics of the annealed Ir diodes [Figure 4.14(a)] showed ~ 5 orders of magnitude improvement in rectifying performance. Figure 4.14(b) shows a Φ_B vs η plot for multiple annealed Ir Schottky contacts. Although the

ideality factors were > 1.1, this plot could still be extrapolated to $\eta_{if} = 1.004$ to determine a homogenous barrier height, $\Phi_B^{hom*} = 1.00$ eV, for Ir contacts on Zn-polar, hydrothermal ZnO. Subsequently, a separate array of Ir Schottky diodes was fabricated by the eclipse pulse laser deposition method, described in Chapter 5, on the Zn-polar face of a separate, organic solvent cleaned, hydrothermal, bulk ZnO wafer from the same manufacturer. Typical *I–V* characteristics and a Φ_B vs η plot for these diodes (as deposited and not annealed) is shown in Figure 4.15. These contacts had extremely low ideality factors and the Φ_B vs η plot was consistent with the value of $\Phi_B^{hom*} = 1.00$ eV determined above.

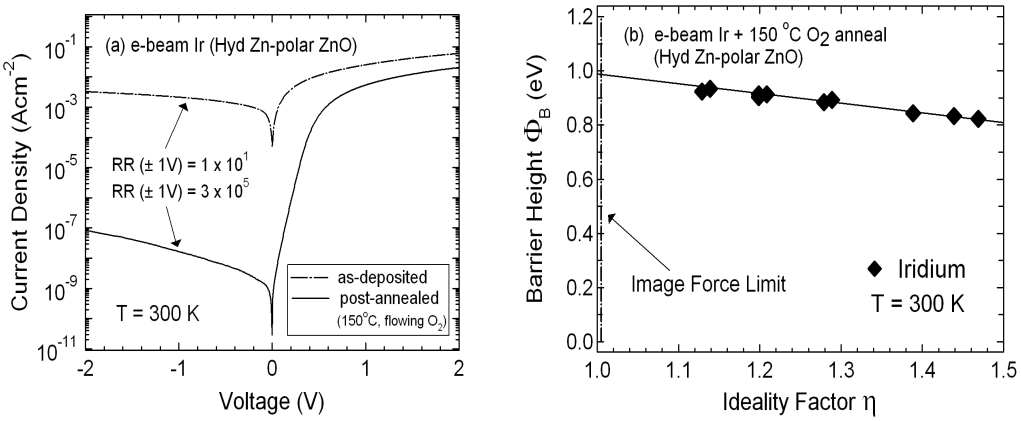

Figure 4.14. (a) Typical *I–V* characteristics of Ir Schottky contacts deposited by electron beam evaporation on the Zn-polar face of hydrothermal bulk ZnO, before and after annealing at 150°C in O_2, and (b) Φ_B vs η plot for multiple annealed Ir Schottky contacts.

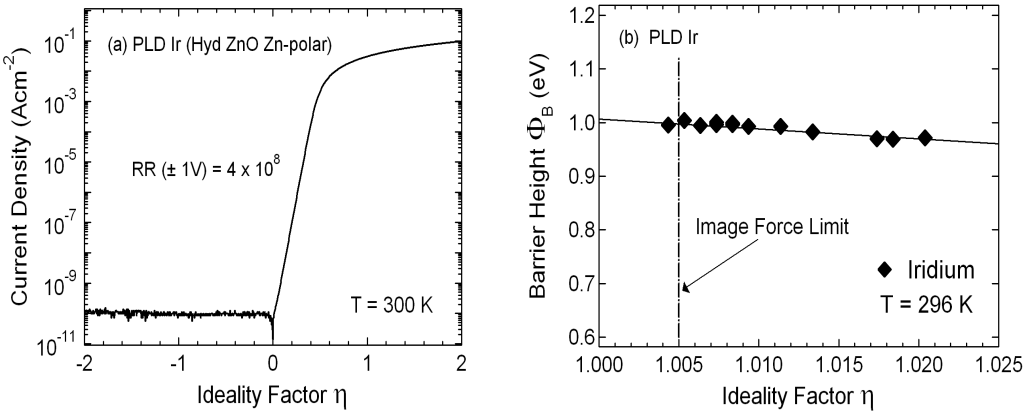

Figure 4.15. (a) Typical *I–V* characteristics of Ir Schottky contacts deposited by eclipse-PLD on the Zn-polar face of hydrothermal bulk ZnO, and (b) Φ_B vs η plot for multiple eclipse-PLD Ir Schottky contacts

4.7 EXPERIMENTS II – IV SUMMARY

4.7.1 Key Findings

Experiments II – IV concerned the fabrication of Au, Ag, and Ir Schottky contacts on the Zn-polar face of hydrothermally grown bulk ZnO from Tokyo Denpa Co. Ltd (Japan). The key findings were:

1) Almost ideal' Au, Ag, and Ir Schottky contacts (ideality factors < 1.02) were fabricated on the Zn-polar face of hydrothermally grown, bulk ZnO with just a simple organic solvent pre-clean and without the need for any special oxidising surface treatments.

2) These are the best reported results for Au, Ag, and Ir Schottky barriers to ZnO (see Figure 4.2). However these 'almost ideal' results could not be consistently reproduced on subsequent hydrothermal wafers, and in fact the majority of subsequent Au contacts were completely ohmic in nature. A comparison of CL spectra taken through both Schottky and ohmic Au contacts showed no significant difference in the CL emission from near surface defects.

3) Φ_B versus η plots from arrays of multiple diodes were used to obtain the image-force-corrected, homogeneous barrier heights, Φ_B^{hom*}, for Au, Ag, and Ir Schottky contacts on the Zn-polar face of hydrothermal, bulk ZnO. These can be meaningfully compared to the predictions of theoretical Schottky models. All previous ZnO Schottky contact reports in the literature have involved single diode results.

4) Au Schottky contacts that were almost ideal (η < 1.02) after fabrication showed a ~ 50 meV (~ 6%) improvement in barrier height after 1 month.

5) Poorly rectifying Ir contacts which were annealed at 150 ^{o}C in O_2 showed a dramatic (5 orders of magnitude) improvement in rectifying properties.

4.7.2 Discussion

Published studies of 'oxidation' pre-treatments on the ZnO surface have emphasized the correlation between improvements in Schottky contact performance and a reduction in surface hydroxide concentration. These improvements have usually involved a conversion from ohmic to rectifying behaviour, although the resulting Schottky contacts often had relatively high

values of η, even on bulk ZnO, suggesting that the oxidation treatment was either incomplete or caused some kind of surface damage. Finding (1) suggests that hydroxide removal can occur on Schottky metal deposition without any oxidation treatment whatsoever, while finding (2) indicates that certain conditions (e.g. metal deposition rate or the kinetic energy of incident metal atoms) may be needed for this to occur.

Finding (4), the ~ 50 meV increase in barrier height of very low ideality factor Au Schottky contacts with time, suggests that chemical reactions at the metal – ZnO interface may provide additional electric dipole contributions to the barrier height. The dramatic improvement of poorly rectifying Schottky contacts with time or annealing in oxygen [finding (5)], suggests that H or O–H bonds at the metal – ZnO interface can be broken by post deposition chemical reactions and/or that defects in the Schottky interface can be passivated by oxygen diffusion.

4.7.3 Comparison with Schottky Contact Models

The experimentally determined, image-force-corrected, homogeneous barrier heights Φ_B^{hom*} for Au, Ag, and Ir Schottky contacts on the Zn-polar face of hydrothermal bulk ZnO, from Experiments II – IV, are summarised in Table 4.4. The remaining literature reports for Schottky contacts to hydrothermally grown, bulk ZnO are shown in Table 4.5. The only metal Schottky contact report to Zn-polar ZnO with a reasonably low ideality factor is that for Pt measured by Endo *et al.* [94]. This is a single diode result, which is not low enough on its own to determine an accurate value of Φ_B^{hom*} for Pt. However, it can be used to provide an indication of the range in which the Φ_B^{hom*} value for Pt might be reasonably expected to occur.

Table 4.4: Image force corrected, homogeneous barrier heights for Ag, Au, and Ir Schottky contacts on the Zn-polar face of hydrothermally grown, bulk ZnO. Pauling and Miedema electronegative values are given for each metal. The electron affinity and Miedema electronegativity for ZnO was assumed to be 4.25 eV and 5.51 respectively.

Schottky Metal	Φ_B^{hom*} (eV)	ϕ_M (eV)	X_M Pauling	X_M Miedema	$\phi_M - \chi_{ZnO}$ (eV)	$X_M - X_{ZnO}$ Miedema
Ag	0.74	4.7	1.93	4.45	0.35	-1.1
Au	0.85	5.1	2.54	5.15	0.85	-0.4
Ir	1.00	5.27	2.20	5.55	1.02	0

Table 4.5: Best literature reports of Schottky contacts to hydrothermally grown ZnO.

Metal	Surface Polarity	Surface Treatment	η	$\Phi_{B,IV}$ (eV)	Ref.
Pt	Zn-polar O-polar	IPA ultrasound	1.1 3.1	0.96 0.6	Endo et al. (2007) [94]
Pt	O-polar	pulsed KrF laser + O_2	1.77	0.73	Oh *et al.* (2007) [90]
Pd	O-polar	organic solvents	1.03	0.83	Grossner *et al.* (2004) [92]
Pd	O-polar	H_2O_2	1.8	-	Schifano *et al.* (2007) [84]
Ir	O-polar	remote O/He plasma	1.58	0.69	Mosbacker *et al.* (2007) [78]
PEDOT:PSS polymer	Zn-polar	dil. HCl + organic solvents + UV ozone	1.2	0.90	Nakano *et al.* (2007) [88]

The data in Table 4.4 was used to construct an image-force-corrected, homogeneous barrier height (Φ_B^{hom*}) versus metal work function (ϕ_M) plot (Figure 4.16) for Ag, Au, and Ir Schottky contacts to Zn-polar hydrothermal ZnO. Figure 4.16 also shows the relationship predicted by (a) the Schottky – Mott model, $\Phi_M = \phi_M - \chi_{ZnO}$, and (b) the chemical bond polarisation (CBP) model, $\Phi_B = S_\Phi(\phi_M - \chi_S) + (1 - S_\Phi)E_g/2$, using the S_Φ value of 0.419 published by Tung [29]. A value of 4.25 eV for the electron affinity (χ_{ZnO}) of ZnO was used in both cases, which is in the middle of the 4.1 – 4.4 eV range quoted in the literature [95, 96]. The Schottky – Mott model appears to be a good fit to this limited data set with the exception of Ag. The work function of Ag is known to vary significantly, between 4.26 and 4.74 eV [97,98], with crystal orientation but would need to be ~ 4.95 eV to fit the Schottky – Mott relationship, which is possible only if the contact was partially oxidised. The predicted value of Φ_B^{hom*} for Pt (work function 5.65 eV) from the Schottky – Mott relationship is indicated in Figure 4.16. This is ~ 1.4 eV, which is very high compared to the Φ_B value of 0.96 eV ($\eta = 1.1$) published by Endo et *al*. [94]. The prediction for Pt is an important test of the Schottky – Mott model as its work function is significantly higher than the other common Schottky metals. Even though the Φ_B value published by Endo et *al*. is for a single diode with $\eta > \eta_{if}$, it seems unlikely (considering the Φ_B versus η relationships for the other metals) that Φ_B^{hom*} for Pt will be close to the value of ~ 1.4 eV predicted by the Schottky – Mott model.

The Φ_B^{hom*} versus ϕ_M relationship predicted by the CBP model significantly overestimates the experimental data for Ag, Au, and Ir. However, this is based on the S_Φ value published by Tung [29] which involves historical results for 'non-ideal' diodes with values of

$\eta > \eta_{if}$. Even taking this into account, the CBP model only gives a good fit to the data in the limit of $S_\Phi \to 1$, for which the CBP model approaches the Schottky – Mott model. The problem with the CBP model is its prediction that any Fermi level pinning at the Schottky interface will be directed towards the middle of the band gap. For wide band gap semiconductors, such as ZnO and GaN, this results in much higher predicted values of Φ_B^{hom*} than experimentally observed [33].

Figure 4.17 shows the Ag, Au, and Ir data in the form of a Φ_B^{hom*} versus metal Miedema electronegativity (X_M) plot, of the type used by Mönch to compare experimental data with the MIGS model [33]. The MIGS model predicts that $\Phi_B = \Phi_{bp} + 0.375(X_M - X_{ZnO})$ where Φ_{bp} is the branch point potential with reference to the conduction band minimum. Mönch published a value for Φ_{bp} of 0.3 eV from an analysis of experimental valence band offsets reported for various ZnO heterostructures [35]. This is surprisingly low compared to other II–VI semiconductors [33] e.g. 1.6 eV [ZnS], 1.2 eV [ZnSe], 1.25 eV [ZnTe] and other wide band gap materials, e.g. 1.0 eV [GaN], 1.6 eV [SiC]. It is also suspiciously close to the E3/E3' defect level which has been shown to dominate the room temperature conductivity of hydrothermal ZnO [99], whereas the MIGS model only applies to defect free interfaces. The electronegativity of ZnO is another adjustable parameter in the MIGS model; the usual approach for binary semiconductors is to use the geometric mean of the atomic electronegativities. In the case of ZnO, $X_{Zn} = 4.05$ and $X_O = 7.51$, which would give $X_{ZnO} = (X_{Zn} \cdot X_O)^{1/2} = 5.51$ (Miedema units). However the Zn-polar [O-polar] faces of ZnO consist of outer atomic planes composed entirely of Zn [O] atoms, and so the electronegativity of ZnO is likely to be different on the two polar faces. The geometric mean is more likely to correspond to the electronegativity of the non-polar, m-plane and a-plane faces, which have an equal number of Zn and O atoms. The electronegativity of the Zn-polar face is likely to be somewhere between the geometric mean, 5.51, and the value for Zn atoms, 4.05.

Figure 4.17 shows three alternatives for the Φ_B^{hom*} versus X_M relationship predicted by the MIGS model, with different values for Φ_{bp} and X_{ZnO}: (a) $\Phi_{bp} = 0.3$ eV, $X_{ZnO} = 5.51$, (b) $\Phi_{bp} = 0.3$ eV, $X_{ZnO} = 4.05$, and (c) $\Phi_{bp} = 1.0$ eV, $X_{ZnO} = 5.51$. Relationships (a) and (b) use the experimental value of Φ_{bp} published by Mönch with X_{ZnO} values corresponding to (a) the geometric mean of Zn and O atoms, and (b) Zn atoms only. Neither of these is a good fit to the experimental data. For a better fit, a larger value of Φ_{bp} is required and prediction (c) shows the MIGS relationship with $\Phi_{bp} = 1.0$ eV. At present, there is no justification for this value apart from the fact that it is more in line with those for other II–VI and wide band gap semiconductors. However, it does give a predicted value for Pt ($X_M = 5.65$) of ~ 1.05 eV which is more in line with the Φ_B value of 0.96 eV ($\eta = 1.1$) published by Endo et *al*. [94]

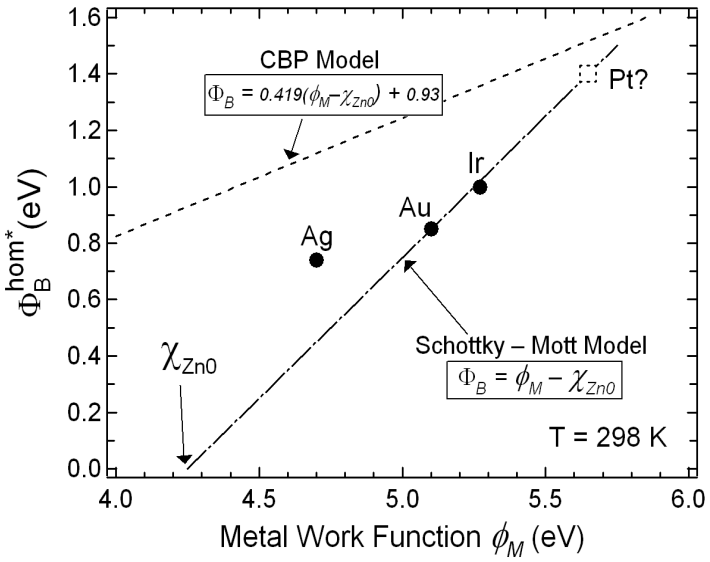

Figure 4.16. Image force corrected, homogeneous barrier height for Ag, Au, and Ir versus metal work function, compared to the predictions of the Schottky – Mott and chemical bond polarisation (CBP) models.

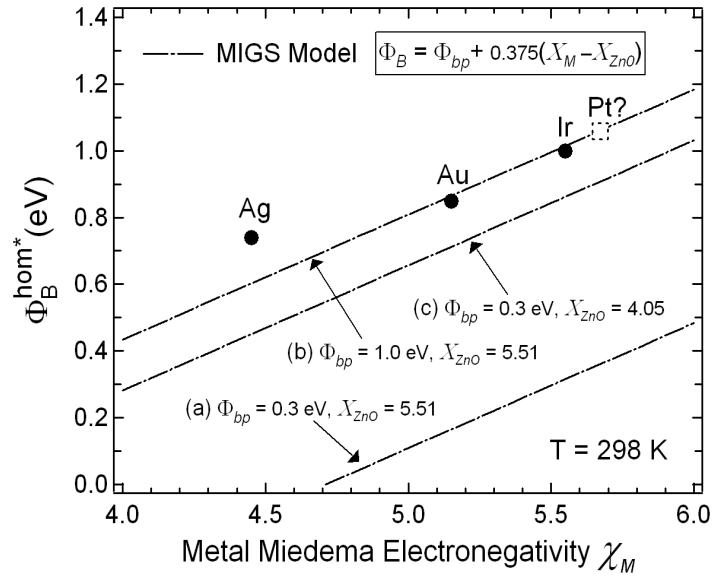

Figure 4.17. Image-force-corrected, homogeneous barrier height for Ag, Au, and Ir versus metal electronegativity (Miedema scale), compared to the predictions of the MIGS model for various values of the parameters Φ_{bp} and X_{ZnO} .

In conclusion, values of Φ_B^{hom*} for Ag, Au, and Ir Schottky contacts to the Zn-polar face of hydrothermal ZnO have been compared to the Schottky – Mott, CBP, and MIGS models. Although this is only a limited data set, it has been derived from 'almost ideal' Schottky contacts with values of $\eta \approx \eta_{if}$ and on the same face, of the same type, of ZnO material. This represents a significant improvement on previous comparisons, with the results suggesting that the MIGS model may provide the best agreement with the experimental Φ_B^{hom*} data for plain metal Schottky contacts to ZnO, provided the branch point energy for ZnO is significantly lower in the band gap than previously published [35].

Chapter 5

Metal Oxide Schottky Contacts

Initial investigations into metal Schottky contacts to *n*-type ZnO revealed that the oxidation of silver contacts could result in significant improvements in their rectifying performance. Further observations of age-related improvements in both silver and gold Schottky contacts suggested that chemical reactions at the metal–ZnO interface may play an important role in Schottky contact formation. In this chapter, reactive oxygen ambients were used to deliberately fabricate metal oxide Schottky contacts on hydrothermal and melt grown bulk ZnO wafers. Schottky contacts involving silver, iridium, and platinum oxides were found to consistently produce very high quality rectifying barriers to *n*-type ZnO and may form the basis of a reliable Schottky contact fabrication technology.

Metal oxide Schottky diodes with both planar and vertical contact geometry were fabricated using the same photolithographic method as described earlier. The only substrate pre-treatment employed was an ultrasonically assisted clean in organic solvents.

5.1 SILVER OXIDE GROWTH

Reactive r.f. sputtering was used to grow a series of 80 nm thick, silver oxide films on organic solvent cleaned, quartz substrates (10 mm x 10 mm x 0.5 mm). Sputtering is a vacuum based vapour deposition technique in which particles (atoms and atomic clusters) are ejected from a target by the bombardment of accelerated inert gas ions (usually argon ions) created in a r.f. or d.c. plasma. Reactive sputtering involves the addition of a second non-inert gas, such as oxygen, which reacts with the ejected particles, either through in-flight collisions or on the substrate itself. A third reaction site is the sputtering target, which can lead to significant changes in its surface composition, known as target poisoning. To avoid this the target was thoroughly pre-sputtered in an argon-only atmosphere before each growth to remove ~ 200 nm of the target surface.

For the silver oxide growth, a 76.2 mm diameter x 6.35 mm thick silver target (purity >99.99%) was used in the r.f. source of a B.O.C. Edwards r.f./d.c. magnetron sputterer. The

vacuum chamber was pumped down to a base pressure of ~ 1 x 10^{-5} mbar before processing. The processing gas consisted of an argon/oxygen gas mixture in which the argon flow was fixed at 10.00 sccm (where sccm denotes cubic centimeter per minute at standard temperature and pressure) and the oxygen flow rate was varied from 0 to 2.40 sccm. Each film was grown for 5 minutes at an r.f. power of 50 W and a processing pressure of ~ 4 x 10^{-3} mbar. The silver oxide films resulting from a compositional sweep with oxygen flow rates from 1.05 to 2.40 sccm are shown in Figure 5.1.

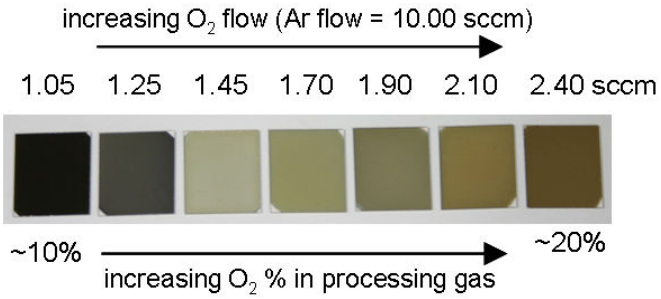

Figure 5.1: Silver oxide films grown by reactive r.f. sputtering with a fixed Ar flow rate of 10.00 sccm and O_2 flow rates from 1.05 – 2.40 sccm on 10 mm x 10 mm x 0.5 mm quartz substrates.

5.1.1 Compositional Analysis

All the silver oxide films were significantly different in appearance to that of a highly reflective, pure metallic silver film of the same thickness. The films grown with low O_2 flow rates were greyish in appearance, while those grown with higher O_2 flow rates were brown. The 1.45 and 1.70 sccm O_2 flow rate films had a yellow/brown appearance and were the most transparent. The composition of these films was investigated by XPS using the Kratos XSAM instrument at the University of Auckland. Figure 5.2 (a) shows a survey scan collected from the as-grown surface of the '1.70 sccm O_2' silver oxide film. The surface of this film was heavily oxidised due to post-growth exposure to air, with an O/Ag atomic fraction of 0.792, close to the value of 0.75 reported for Ag_2O reference powders [110, 111]. Figure 5.2(b) shows a re-measured survey scan taken after the film was *in-situ* sputtered for 4 minutes using a 2.4 keV Ar ion source to remove the heavily oxidised surface layers. No silicon was detected indicating that the quartz substrate was not being sampled. The surface carbon contamination was completely removed and a decrease in the O/Ag fraction to 0.104 was measured, which is more representative of the bulk of the film. Table 5.1 shows the bulk composition for the other silver oxide films in the series, determined in the same way.

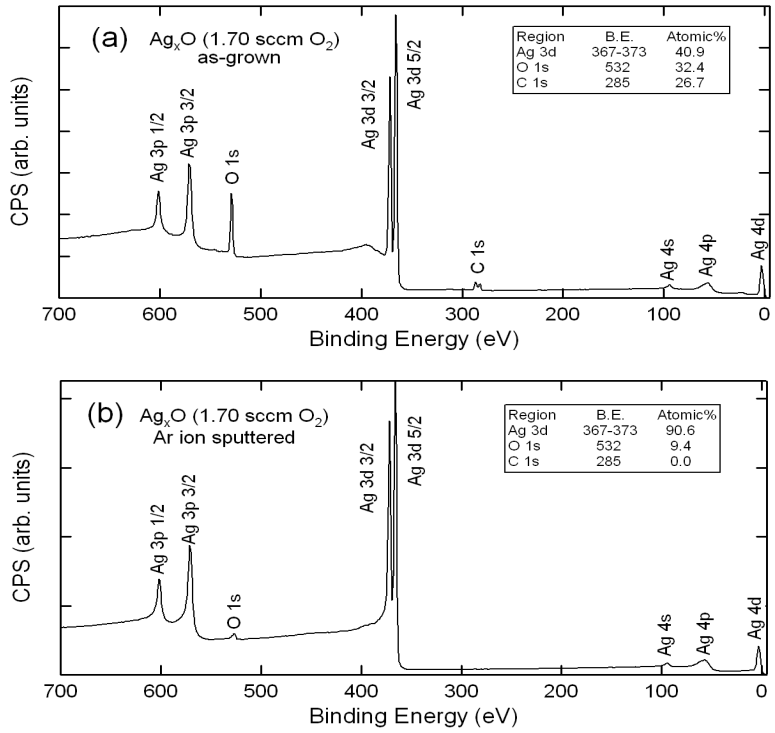

Figure 5.2: XPS survey scan spectra taken from (a) the as-grown surface, and (b) the surface after a 4 minute argon ion sputter to remove the heavily oxidised surface layers of a silver oxide film grown with an O_2 flow rate of 1.70 sccm.

Table 5.1: Composition of silver oxide films grown by reactive r.f. sputtering (50 W) of an Ag target with different Ar/O_2 processing gas compositions. In each case, a fixed argon flow rate of 10.00 sccm was combined with different O_2 flow rates. All films were sputter cleaned for 4 minutes using 2.4 keV Ar ions to remove the more heavily oxidised surface layers.

O_2 flow rate (sccm)	O/Ag fraction
1.05	0.062
1.25	0.065
1.45	0.075
1.70	0.104
1.90	0.125
2.10	0.153

All the films in Table 5.1 were silver rich with O/Ag atomic fractions significantly less than the values of 0.33 and 0.50 expected for stoichiometric Ag_2O and AgO films respectively. However, it is possible that the sputter cleaning may preferentially remove more of the lighter

oxygen atoms from the films, in which case the measured O/Ag fractions in Table 5.1 may represent a lower limit. The 1.25, 1.45, and 1.70 sccm O_2 flow rate silver oxide films were now used to fabricate Schottky contacts on hydrothermal, bulk ZnO.

5.1.2 Initial Silver Oxide Diodes

Planar Schottky diodes consisting of a 300 μm diameter, 80 nm thick silver oxide Schottky contact with a 25 mm annular separation to a Ti/Al/Pt ohmic ring contact were fabricated, using the photolithographic method described in Chapter 4, on the Zn-polar and O-polar faces of the same double-sided polished, hydrothermal, bulk, c-axis ZnO wafer. The carrier concentration and mobility of this wafer were 3 x 10^{14} cm^{-3} and 200 $cm^2V^{-1}s^{-1}$ respectively, from single field (0.51 T) Hall effect measurements using the van der Pauw technique. The silver oxide contacts were fabricated using the reactive r.f. sputtering method described in Section 5.1, with O_2 gas flow rates of 1.25, 1.45, and 1.70 sccm, and with the Ar gas flow fixed at 10.00 sccm. The resulting silver oxide films had low lateral conductivity and consequently a 30 nm platinum capping layer was added using electron beam evaporation. The effective barrier height (Φ_B) and the ideality factor (η) for each diode was determined from its room temperature *I–V* characteristics, in dark conditions.

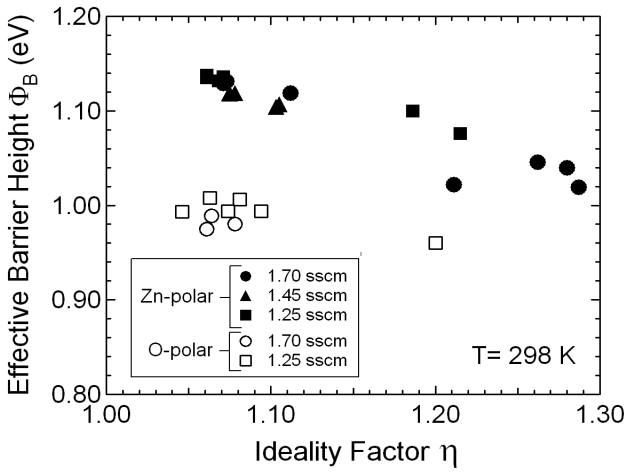

Figure 5.3: Effective barrier height (Φ_B) versus ideality factor (η) plot for silver oxide Schottky diodes on the Zn-polar and O-polar faces of a hydrothermal, bulk, c-axis ZnO wafer (n = 3 x 10^{14} cm^{-3}), fabricated by reactive r.f. sputtering using O_2 flow rates of 1.25, 1.45, and 1.70 sccm.

Figure 5.3 shows a Φ_B versus η plot for the 1.25, 1.45, and 1.70 sccm O_2 flow rate silver oxide Schottky diodes, which were each fabricated simultaneously on the Zn-polar and O-polar faces. On each polar face, the rectifying performance of the different silver oxide films was

very similar, with no significant variation with composition in the 1.25 – 1.70 sccm O_2 flow rate range. The decrease in Φ_B with increasing η is due to the increasing lateral inhomogeneity of the contacts. Most of the silver oxide contacts formed high quality Schottky barriers with ideality factors < 1.10. A distinct surface polarity effect was evident, in that diodes fabricated on the Zn-polar face had significantly higher barrier heights than those on the O-polar face, with the best diodes on both faces having similarly low ideality factors.

Figures 5.4(a) and (b) shows the *I–V* characteristics typical of the best '1.70 sccm O_2' silver oxide diodes on the Zn-polar and O-polar faces. These showed rectifying ratios (at ± 2 V) of more than 9 orders of magnitude, although this is probably an underestimate, especially for the Zn-polar face, as the reverse current had reached the noise level, ~ 50 – 100 fA, of the HP 4155A parameter analyser. Figures 5.4(c) and (d) show that η was independent of bias voltage for significant parts of the forward *I–V* curve, indicating that the silver oxide contacts had good lateral homogeneity. The increase in η at higher forward biases is due to the series resistance of the diodes, while the increase from 0 – 0.2 V on the Zn-polar face is possibly due to a shunt resistance effect or recombination in the depletion region.

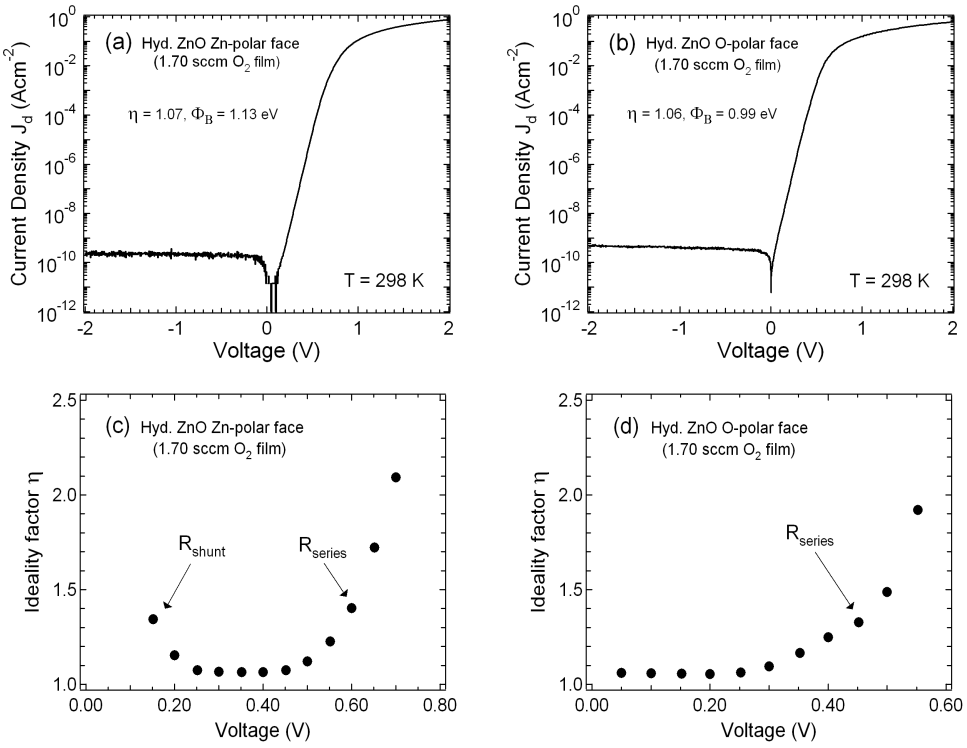

Figure 5.4: Typical *I–V* characteristics of the best silver oxide Schottky diodes fabricated by reactive r.f. sputtering (using a 1.70 sccm O_2 flow rate) on (a) the Zn-polar, and (b) the O-polar face of a hydrothermal, bulk, c-axis ZnO wafer; (c) and (d) are plots of ideality factor (η) versus forward bias for the *I–V* characteristics shown in (a) and (b) respectively.

5.2 SILVER OXIDE SCHOTTKY CONTACTS ON BULK ZINC OXIDE

Following the initial success of silver oxide films in producing highly rectifying, low ideality factor Schottky contacts to hydrothermal bulk ZnO, a subsequent experiment was carried out in which arrays of silver oxide diodes were fabricated on the polar and non-polar faces of additional hydrothermal and melt bulk wafers. The following bulk ZnO wafers were used:

HT-1	double side polished, hydrothermal c-axis wafer, cut to provide Zn-polar and O-polar samples.
HT-2	double sided polished, hydrothermal m-plane wafer, one face of which was processed.
M-1	melt c-axis wafer, single sided polished on the Zn-polar face.
M-2	melt c-axis wafer, single sided polished on the O-polar face.
M-3	melt a-plane wafer, single sided polished.

The electrical characteristics of these wafers, determined from single field (0.51 T) Hall effect measurements, are given in Table 5.2.

Table 5.2: Electrical characterisation of hydrothermal and melt bulk ZnO wafers from single field (0.51 T) Hall effect measurements at room temperature, [carrier concentration (n), mobility (μ), and resistivity (ρ)].

Wafer	n (cm^{-3})	μ ($cm^2V^{-1}s^{-1}$)	ρ (Ωcm)
HT-1 c-axis	1.2×10^{14}	190	300
HT-2 m-plane	2.5×10^{16}	109	2.3
M-1 Zn-polar	1.1×10^{17}	184	0.30
M-2 O-polar	7.4×10^{16}	187	0.45
M-3 a-plane	5.3×10^{16}	187	0.63

Arrays of planar diodes with 300 μm diameter, 80 nm thick silver oxide Schottky contacts (with a 30 nm platinum cap) were fabricated on each of these wafers, using the same reactive r.f. sputtering technique described before, but with a fixed O_2 flow rate of 1.70 sccm. Figures 5.5 (a) and (b) show the *I–V* characteristics of the best silver oxide diodes on the hydrothermal and melt c-axis wafers. These *I–V* characteristics showed that the diodes on the melt ZnO have a much lower series resistance, which is expected due to their 2-3 orders of magnitude lower bulk resistivity. The forward bias *I–V* characteristics of the silver oxide diodes on melt ZnO also showed evidence of a slight 'kink' at ~ 0.65 V which may be due to the influence of more than one barrier.

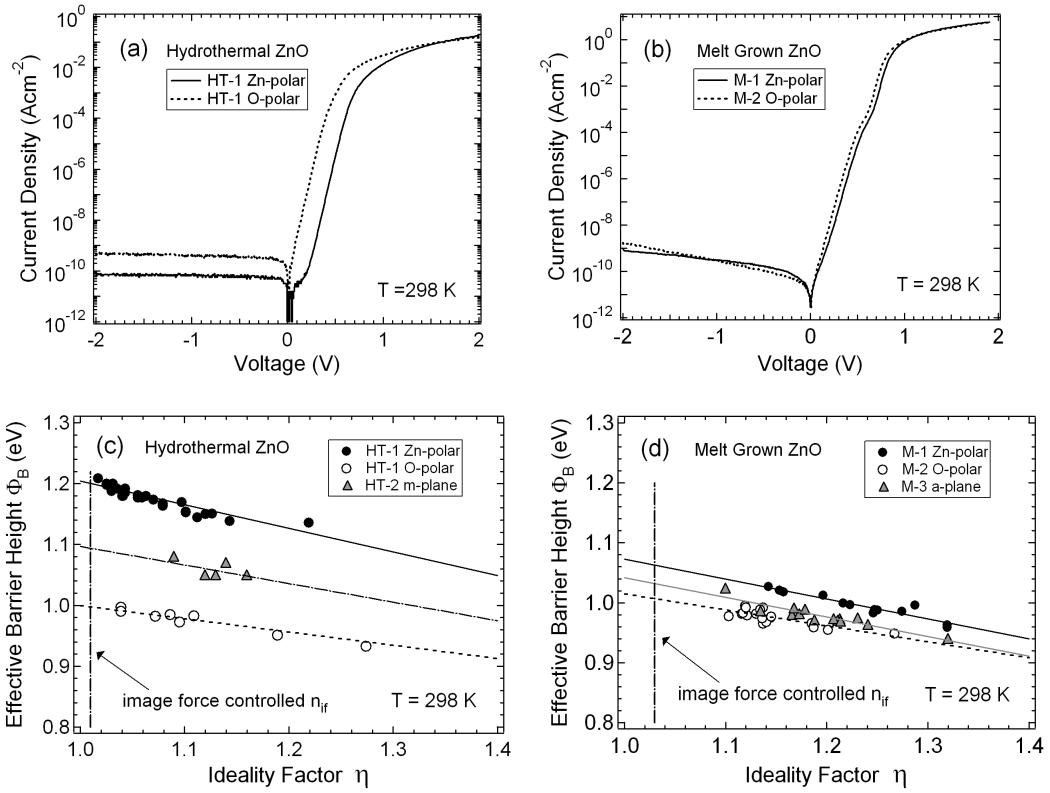

Figure 5.5: Typical *I–V* characteristics of the best silver oxide diodes on (a) the Zn-polar and O-polar face of hydrothermal, c-axis wafer HT-1, and (b) Zn-polar and O-polar melt, c-axis wafers M-1 and M-2. Effective barrier height (Φ_B) versus ideality factor (η) plots for multiple silver oxide diodes on the polar and non-polar faces of (c) hydrothermal, and (d) melt bulk ZnO.

Figures 5.5(c) and (d) show effective barrier height (Φ_B) versus ideality factor (η) plots from the *I–V* characteristics of multiple diodes on each of the ZnO surfaces. The image force controlled ideality factors, η_{if}, for the hydrothermal and melt ZnO wafers have been included in these figures, using Equations (2.20) and (2.21). Significant, ZnO material related, differences can be seen in the Φ_B versus η plots for hydrothermal and melt ZnO, especially for the Zn-polar and non-polar faces. Figure 5.5(c) confirms the previously observed polarity effect for hydrothermal ZnO with silver oxide diodes on the Zn-polar face having significantly higher barriers (by ~ 200 meV) than those on the O-polar face. The diodes on the non-polar, m-plane face had intermediate barrier heights between those on the two polar faces. A much smaller polarity effect was evident for the diodes on melt ZnO with a barrier height difference of ~ 50 meV between the Zn-polar and O-polar faces, with diodes on the non-polar, a-plane face, again having intermediate barrier heights.

Table 5.3: Image force corrections to the effective barrier heights on the polar and non-polar faces of hydrothermal and melt bulk ZnO.

Best Diode	η_{if}	Φ_B^{if} (eV)	$\delta\Phi_B$ (eV)	Φ_B^{hom*} (eV)	E_{00}/kT (at 300 K)	η_{TFE}
HT-1 Zn-polar	1.01	1.20	0.03	1.23	0.005	1.000
HT-1 O-polar	1.01	1.00	0.03	1.03	0.005	1.000
HT-2 m-plane	-	1.09	-	-	-	-
M-1 Zn-polar	1.03	1.07	0.10	1.17	0.16	1.008
M-2 O-polar	1.03	1.01	0.10	1.11	0.13	1.006
M-3 a-plane	1.03	1.04	0.10	1.14	0.11	1.004

For each of the Φ_B versus η plots, there is a clear, linear trend with Φ_B decreasing with increasing η. This is the expected decrease in Φ_B due to increasing lateral inhomegeneity of the contacts. As in Chapter 4, these linear trends can be extrapolated to η_{if} to determine the image force controlled barrier height, Φ_B^{if}, which can in turn be used to obtain the image force corrected, homogeneous barrier height $\Phi_B^{hom*} = \Phi_B^{if} + \delta\Phi_B$, where $\delta\Phi_B$ is the image force lowering correction. The result of such an analysis is shown in Table 5.3 [173], which gives the values of η_{if}, Φ_B^{if} and Φ_B^{hom*} for each of the ZnO faces. The image force correction for the diodes on hydrothermal ZnO is relatively small (~ 0.03 eV) due to its low carrier concentration. However, the correction for melt ZnO (~ 0.10 eV) increases the size of the Φ_B^{hom*} by almost 10%. The values of Φ_B^{hom*} for the different faces of melt ZnO now lie between the values for the polar faces of hydrothermal ZnO. Image force lowering also affects the reverse bias *I–V* characteristics by introducing a voltage dependence in the reverse current. Figures 5.5(a) and (b) show that this dependence is much larger for the melt ZnO diodes, which is consistent with the greater influence of image force lowering.

Figure 5.5 also shows that the ideality factors of the best silver oxide diodes on hydrothermal ZnO, especially on the polar faces, are very close to the image force controlled limit, while the best diodes on melt ZnO have ideality factors which are still significantly larger than η_{if}. It is apparent that some other form of non-ideal behaviour, in addition to image force lowering, is taking place in the melt ZnO diodes. A possible candidate is thermionic field emission (TFE), described in Section 2.4.2. Table 5.3 also gives the tunneling parameter E_{00} and the ideality factor due to TFE, η_{TFE}, for each of the ZnO faces determined using Equations (2.22) and (2.24). TFE is negligible for hydrothermal ZnO since $E_{00}/kT << 1$. TFE is more significant for melt ZnO due to its higher carrier concentration, but is still only expected to cause a modest increase in ideality factor. However the presence of traps, such as those

generated by point defects, in the depletion region can significantly increase the tunneling probability and consequently the ideality factor, as a carrier can first tunnel into these traps and then through the barrier.

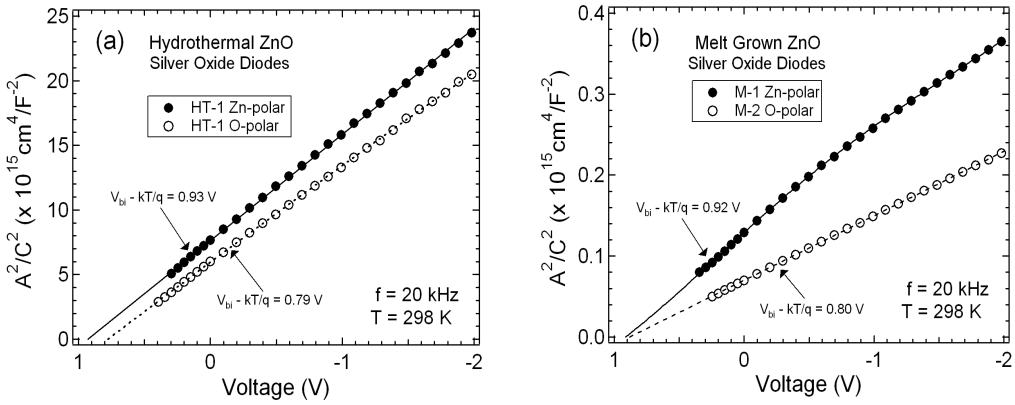

Figure 5.6: Typical C-V characteristics of the best planar silver oxide diodes on hydrothermal and melt c-axis, bulk ZnO wafers and the lines of best fit used to determine the values of V_{bi}.

The *C–V* characteristics of the best diodes on the hydrothermal and melt c-axis wafers are shown in Figure 5.6. These are consistent with the polarity effects observed in the *I–V* characteristics, in that there is a clear difference in the built-in voltage (V_{bi}) for diodes on the Zn-polar and O-polar faces of hydrothermal ZnO, and a much smaller difference for diodes on the polar faces of melt ZnO. The *I–V* and *C–V* characteristics of the best silver oxide diodes on hydrothermal and melt ZnO are summarised in Table 5.4. Good agreement was obtained between the barrier heights determined by *I–V* and *C–V* characterisation.

Table 5.4: Electrical characteristics of the best silver oxide Schottky diodes on hydrothermal and melt, bulk ZnO wafers from room temperature *I–V* and *C–V* measurements, [ideality factor (η) and barrier height ($\Phi_{B,I\text{-}V}$) from I–V measurements; built-in potential ($V_{bi,C\text{-}V}$), barrier height ($\Phi_{B,C\text{-}V}$) and effective donor density ($N_{D,C\text{-}V}$) from C–V measurements].

Best Diode	η	$\Phi_{B,I\text{-}V}$ (eV)	$V_{bi,C\text{-}V}$ (V)	$\Phi_{B,C\text{-}V}$ (eV)	$N_{D,C\text{-}V}$ (cm^{-3})
HT-1 Zn-polar	1.03	1.20	0.93	1.19	2.0×10^{15}
HT-1 O-polar	1.04	0.99	0.78	1.04	2.3×10^{15}
HT-2 m-plane	1.09	1.08	-	-	-
M-1 Zn-polar	1.14	1.03	0.94	1.02	1.5×10^{17}
M-2 O-polar	1.10	0.98	0.89	0.99	2.1×10^{17}
M-3 a-plane	1.10	1.02	-	-	-

5.2.1 Breakdown Voltage

The breakdown voltages of silver oxide diodes on the Zn-polar face of hydrothermal ZnO were determined from their extended reverse bias *I–V* characteristics. These are shown in Figures 5.7(a) and (b) for diodes on the Zn-polar face of two different hydrothermal ZnO wafers. The breakdown voltages were typically in the range of -40 V to -60 V. Similar values were also obtained for vertical geometry (see Section 5.5) silver oxide diodes, with the Schottky contact on the Zn-polar face of hydrothermal ZnO. These compare favourably with the values of 8.5 [7.0] V reported by Coppa *et al.* [45] for Au Schottky diodes on the remote plasma-cleaned, Zn-polar [O-polar] faces of SCVT bulk wafers (n = 1 x 10^{17} cm^{-3}). However, the typical breakdown voltages of the silver oxide diodes are at least an order of magnitude less than those expected for a wide band gap semiconductor. This raises the question of whether the breakdown is occurring in the depletion region or at the Schottky interface.

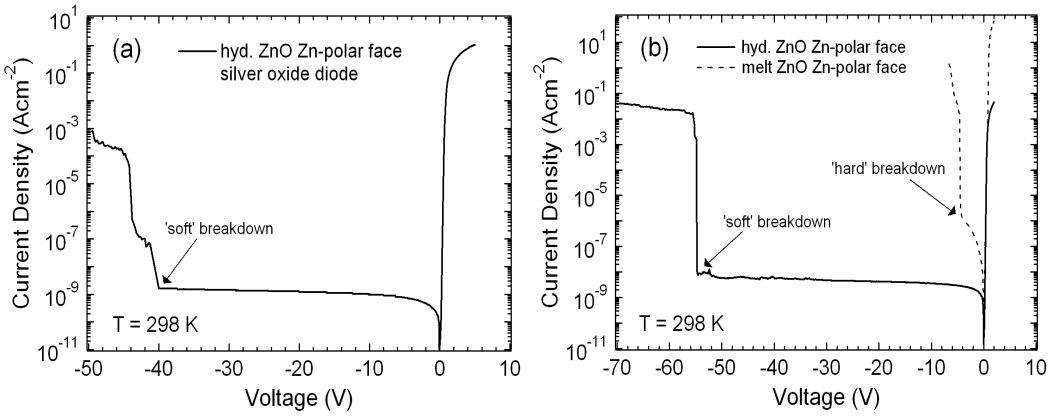

Figure 5.7: (a) *I–V* characteristics showing the reverse breakdown of a planar silver oxide diode on a hydrothermal bulk ZnO wafer, and (b) a comparison of the reverse breakdown of planar silver oxide diodes on an additional hydrothermal bulk ZnO wafer and on a 'melt' bulk ZnO wafer. All diodes in (a) and (b) were fabricated on the Zn-polar face.

The typical breakdown voltage of silver oxide diodes on the Zn-polar face of melt ZnO wafers is shown in Figure 5.7(b). Over several diodes tested, breakdown values were consistently in the -4 V to - 6 V range. The breakdown resulted in a severe, irreversible degradation in diode performance, in contrast to the 'softer' breakdown observed for the diodes on hydrothermal ZnO. This is probably related to the 2 – 3 orders of magnitude lower series resistance for the diodes on melt ZnO which allows much larger breakdown currents to flow. These low breakdown voltages are a little surprising given the excellent rectifying properties of these diodes. However, an explanation may lie in the structural properties of the silver oxide contacts.

5.3 STRUCTURAL PROPERTIES OF SILVER OXIDE CONTACTS

Reactively sputtered silver oxide films have provided a breakthrough in terms of producing high barrier height, low ideality factor Schottky contacts to *n*-type ZnO with high levels of reproducibility and device yield. However, their breakdown voltages were significantly lower than expected. Scanning electron microscopy (SEM), tunneling electron microscopy (TEM), x-ray energy dispersive spectroscopy (XEDS), and x-ray photoemission spectroscopy (XPS) were used to investigate the structural properties of these silver oxide Schottky contacts. These investigations were carried out exclusively on silver oxide films fabricated using oxygen / argon flow rates of 1.70 sccm / 10.00 sccm on the Zn-polar face of hydrothermal bulk ZnO.

5.3.1 Scanning Electron Microscopy (SEM)

Figure 5.8 shows a scanning electron microscope (SEM) image taken using a LEO 1500 series SEM on a silver oxide film, grown on the Zn-polar face of a hydrothermal bulk ZnO substrate, after 30 seconds and then after 5 minutes of growth. The film was polycrystalline with mixed grain sizes ranging from 20 – 40 nm to larger 100 – 200 nm particles.

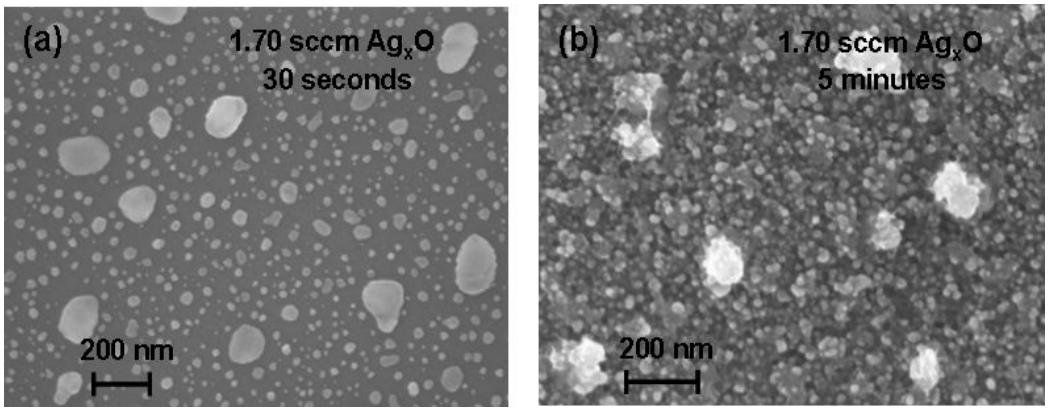

Figure 5.8: SEM images of a reactively r.f. sputtered silver oxide film after (a) 30 seconds, and (b) 5 minutes of growth on the Zn-polar face of a hydrothermal, bulk, c-axis ZnO wafer using an O_2 flow rate of 1.70 sccm (images taken by Jessica Chai, Department of Electrical and Computer Engineering, University of Canterbury, NZ).

5.3.2 Transmission Electron Microscopy (TEM)

Figure 5.9 shows a cross-sectional TEM image of a silver oxide Schottky contact taken along the $(11\bar{2}0)$ axis by collaborators at the Pennsylvania State University, Pennsylvania, U.S.A. The TEM specimen was prepared using conventional mechanical thinning followed by argon ion milling, and the image taken using a JEOL 2010F microscope operated at 200 keV. The TEM image shows a polycrystalline structure containing a number of nanometer-scale voids. The voids were seen everywhere in the film, both in the thin and thick regions of the TEM sample, indicating they are real features and not artefacts. These voids also occur at the Schottky interface and may be a contributing factor in the lower than expected breakdown voltage of the contacts.

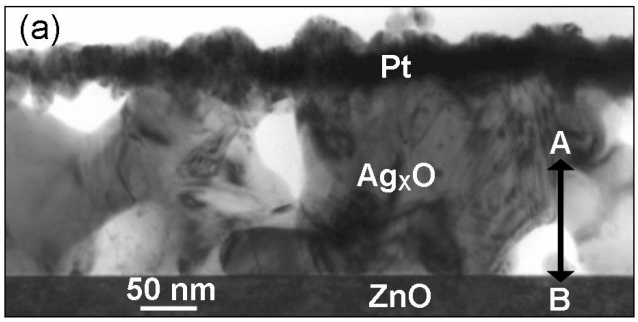

Figure 5.9: Cross-sectional TEM of a platinum capped, silver oxide film on the Zn-polar face of hydrothermal bulk ZnO (note: the film was grown twice the usual thickness for imaging purposes).

5.3.3 X-ray Energy Dispersive Spectroscopy (XEDS)

XEDS is an elemental compositional analysis technique that uses the characteristic energies of x-ray emitted when a sample is bombarded by a beam of energetic electrons, usually from an electron microscope. Figure 5.10 shows an XEDS composition profile along the line marked AB in Figure 5.9. By examining the Zn and O signal from the bulk ZnO (near position B) it is

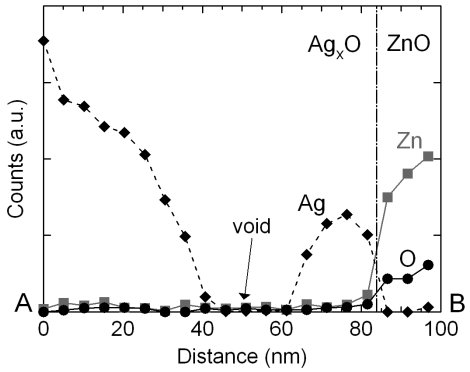

Figure 5.10: XEDS composition profile along the line AB in Figure 5.9.

apparent that the instrument calibration underestimates the oxygen composition. However, taking this into account, it is apparent that little oxygen was detected in the film, indicating that it was highly silver rich.

5.3.4 X-ray Photoemission Spectroscopy (XPS)

In Section 5.1.1, XPS measurements on a sputter cleaned, '1.70 sccm O_2' silver oxide film, fabricated on a quartz substrate using the same growth conditions, gave an O/Ag fraction of ~ 0.10. These measurements were repeated on a '1.70 sccm' silver oxide film grown on the Zn-polar face of a hydrothermal ZnO wafer. This time an O/Ag fraction of ~ 0.04 was estimated from a XPS survey scan (not shown) after 5 minutes of 2.4 keV argon ion sputter cleaning. Figure 5.11 shows a high resolution scan of the core-level O 1s spectrum. Interpretation of this spectrum was made with reference to the XPS study of oxidized silver powders by Waterhouse *et al.* [110]. Three main peaks can be identified at 530.7, 529.2, and 528.3 eV, which are due to subsurface oxygen, Ag_2O and AgO respectively. This suggests that the bulk of the film was highly silver rich but still contained a mixture of oxide phases. However, the key issue is the composition of the silver oxide film, and the nature of the bonding at the Schottky interface, which unfortunately is much more difficult to measure.

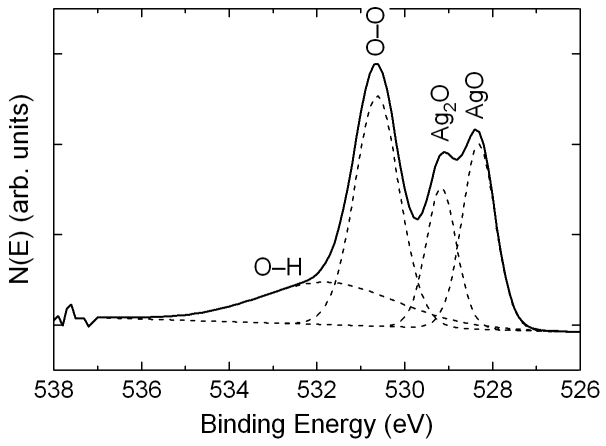

Figure 5.11: O 1s core level spectrum (90^o take off angle) taken from a sputter cleaned '1.70 sccm' silver oxide film grown on the Zn-polar face of a hydrothermal bulk ZnO wafer. The spectrum was fitted using four Voigt functions with a Gaussian:Lorentzian ratio of 70:30.

Figure 5.12(a) shows the valence band XPS spectrum of the sputter-cleaned 'silver oxide' film. Since the film was grounded to the spectrometer, the zero of the binding energy scale represents its Fermi level (E_F). The film has a continuous density of states (DOS) near E_F,

similar to that observed from the sputter-cleaned silver reference sample in Figure 5.12 (b), indicating a metallic-like nature.

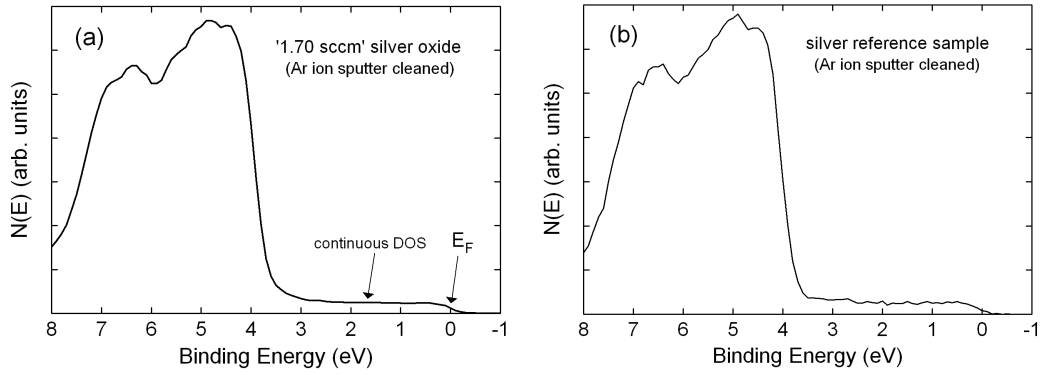

Figure 5.12: Valence band XPS spectrum (90^o take off angle) taken from (a) a sputter cleaned '1.70 sccm' silver oxide film grown on the Zn-polar face of a hydrothermal bulk ZnO wafer, and (b) a sputter cleaned pure silver reference sample, with the zero of the binding energy scale referenced to the Fermi level (E_F) of the sample.

5.4 TEMPERATURE DEPENDENT BEHAVIOUR OF SILVER OXIDE DIODES

There are few literature reports of the temperature dependent behaviour of ZnO Schottky diodes. Sheng *et al.* [74] reported a decrease in η from 1.37 to 1.29 for Ag Schottky contacts fabricated on $(11\bar{2}0)$ *n*-ZnO epilayers over the temperature range 265 – 340 K. A Richardson plot yielded a barrier height of 0.69 eV and an experimental Richardson constant of 0.15 $Acm^{-2}K^{-2}$, significantly lower than the theoretical value of 32 $Acm^{-2}K^{-2}$. However their analysis involved a rather narrow temperature range, which introduces a large uncertainty into their experimental value given the long extrapolation to 1/T = 0. Von Wenckstern *et al.* [93] also reported an experimental Richardson constant orders of magnitude lower than the theoretical value, using *I–V–T* measurements from 210 – 300 K on Pd Schottky contacts to (0001)-oriented ZnO thin films. These contacts had a Φ_B of 0.81 eV and η of 1.49 at 290 K. Most recently, Gur *et al.* [101] performed *I–V–T* measurements over the range 200 – 500 K on Ag Schottky contacts to unspecified bulk ZnO with a Φ_B of 0.82 eV and η of 1.55 at room temperature. An experimental Richardson constant of 0.248 $Acm^{-2}K^{-2}$ was reported but with rather a large uncertainty due to the degree of scatter in their Richardson plot.

All these reports have involved measurements on relatively high ideality factor Schottky contacts which, as a result, may have significant variations in lateral homogeneity and/or be dominated by other current transport processes besides the pure thermionic emission assumed in the Richardson plot analysis. In an attempt to improve on this situation, the current transport

through low ideality factor silver oxide Schottky contacts was investigated over a wide temperature range 40 – 423 K. Silver oxide diodes fabricated on the Zn-polar face of hydrothermal, c-axis, wafer HT-1 were used for these investigations as these have the highest barriers so far reported for ZnO. The *I–V–T* measurements were carried out by collaborators at the University of Leipzig, Germany [99].

5.4.1 Above Room Temperature *I–V–T* Characteristics

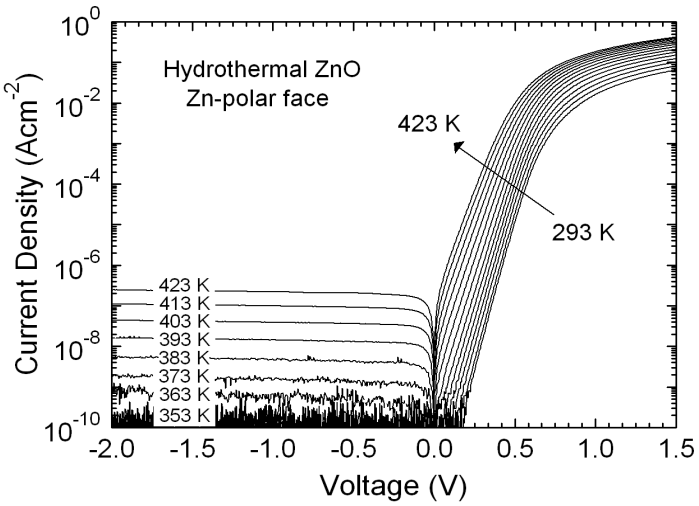

Figure 5.13: Above room temperature *I-V* characteristics of a planar silver oxide Schottky diode on the Zn-polar face of hydrothermal ZnO (c-axis, wafer HT-1) with the diode exposed to air.

Figure 5.13 shows the above room temperature *I–V–T* characteristics measured on a silver oxide diode exposed to atmosphere, from 294 – 423 K at intervals of 10 K; the device temperature was controlled to an accuracy of 0.5% using an Arico P200 temperature controller. The forward bias characteristics show exponential behaviour over many orders of magnitude of current indicating the dominance of thermionic emission. Φ_B and η were determined for each temperature and the results are shown in Figure 5.14(a). Both vary over a relatively small range, in a 'mirror-like' fashion, about mean values of 1.14 eV and 1.10 respectively. Figure 5.14(b) shows a Richardson plot of $\ln(J_0/T^2)$ vs 1000/T (open circles), where J_0 is the saturation current density, obtained by extrapolating the forward bias *I–V* characteristics of Figure 5.13 to zero bias. J_0 is related to the effective barrier height Φ_B and the Richardson constant A* by,

$$J_0 = A^* T^2 exp\left(\frac{-q\Phi_B}{kT}\right) . \qquad (5.1)$$

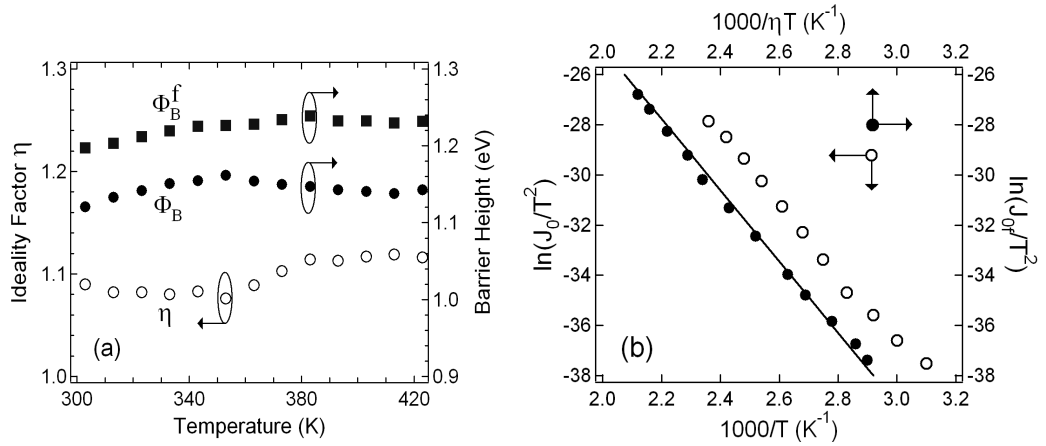

Figure 5.14: (a) Variation of ideality factor η, effective barrier height Φ_B, and flat band barrier height $\Phi_B{}^f$ with temperature for a silver oxide Schottky diode on the Zn-polar face of hydrothermal ZnO; and (b) a Richardson plot (open circles) of $\ln(J_0/T^2)$ vs 1000/T and a modified Richardson plot (solid circles) of $\ln(J_{0f}/T^2)$ vs 1000/ ηT with a linear fit using the theoretical value of A*.

Therefore, Φ_B can also be determined from the slope of the Richardson plot, while A* can be obtained from the intercept. However, the temperature dependence of Φ_B makes fitting a single line to the Richardson plot [open circles of Figure 5.14(b)] problematic.This is often addressed by using the flat band barrier height, Φ_B^f, which is considered to be a fundamental quantity that eliminates the influence of most causes of non-ideal behaviour,

$$\Phi_B^f = \eta\Phi_B - (\eta - 1)\xi \tag{5.2}$$

where $\xi = (kT/q)ln(N_C/n)$ is energy difference between the Fermi level and the bottom of the conduction band. N_C is the conduction band density of states (2.94×10^{18} cm^{-3} for ZnO) and n is the carrier concentration. Substituting Φ_B^f for Φ_B in Equation (5.1) gives,

$$J_{0f} = A^* T^2 exp\left(\frac{-q\Phi_B^f}{\eta kT}\right) \tag{5.3}$$

where J_{0f} is the flat band saturation current density given by,

$$J_{0f} = J_0 exp\left[\left(\frac{\eta - 1}{\eta}\right) ln\left(\frac{N_C}{n}\right)\right] . \tag{5.4}$$

Figure 5.14(a) shows the values of Φ_B^f calculated from the Φ_B and η values (shown in the same figure) using Equation (5.2). As expected Φ_B^f has a smaller temperature dependence than Φ_B, particularly above 340 K. Equation (5.4) was used to generate a modified Richardson plot

of $\ln(J_0/T^2)$ vs $1000/\eta T$ [solid circles of Figure 5.14(b)]. A linear least squares fit was applied to this modified plot using Equation (5.3), the theoretical value of 32 $Acm^{-2}K^{-2}$ for A*, and Φ_B^f as the adjustable parameter. The value of Φ_B^f obtained from the slope of the linear fit was 1.23 eV which is in good agreement with the values shown in Figure 5.14(a) and identical to the value for the image force corrected, homogeneous barrier height, Φ_B^{hom*}, in Table 5.3. This is an important result as it shows agreement between two separate parameters, Φ_B^f and Φ_B^{hom*}, which attempt to eliminate the effects of non-ideal behaviour. It also shows that the experimental data is consistent with the theoretical value of A*.

5.4.2 Reverse Leakage Current

At higher temperatures, the reverse leakage characteristics of the silver oxide Schottky diodes can be more accurately measured as the current rises above the ~ 50 – 100 fA noise level of the HP 4155A parameter analyser (see Figure 5.13). These reverse current characteristics can then be compared to theoretical models for thermionic emission and thermionic field emission to assess the dominant transport mechanism.

For pure thermionic emission (TE), the sole cause of voltage dependency in the reverse current is from the image force lowering of the Schottky barrier. This is known as the 'TE + barrier lowering' model, with the reverse current density, J_R^{if}, given by,

$$J_R^{if} = A^* T^2 \exp\left[-\frac{q(\Phi_B - \Delta\Phi_{if})}{kT}\right] \tag{5.5}$$

where $\Delta\Phi_{if}$ is the barrier lowering due to the image force effect from Equation (2.20). Equations (5.5) and (2.20) can be rearranged to express J_R^{if} as a function of the reverse electric field, E, at the Schottky interface,

$$J_R^{if} = A^* T^2 \exp-\frac{q}{kT}\left[\Phi_B - \left(\frac{qE}{4\pi\varepsilon_s\varepsilon_0}\right)^{\frac{1}{2}}\right] \tag{5.6}$$

and

$$E = \sqrt{\frac{2qN_D}{\varepsilon_s\varepsilon_0}\left(V_R + \Phi_B - \xi - \frac{kT}{q}\right)} \tag{5.7}$$

where N_D is the effective donor density and ε_s is the dielectric constant of ZnO.

For thermionic field emission (TFE), Hatakeyama *et al.* [112] derived a 'compact' expression for the reverse current density expected from the original analysis of Padovani and Stratton [113],

$$J_R^{TFE} = \frac{A^*TqhE}{2\pi kT}\left(\frac{\pi}{2m^*kT}\right)^{\frac{1}{2}} exp\left[-\frac{q}{kT}\left(\Phi_B - \frac{qh^2E^2}{24m^*(2\pi kT)^2}\right)\right] \quad (5.8)$$

where m^* is the effective electron mass (= 0.27 m_e [5]) and the other quantities have their usual meaning.

Figure 5.15(a) shows the reverse leakage current measured at 383 K compared to the predictions of the 'TE + barrier lowering' and TFE models. This shows that the reverse current is a close match to the 'TE + barrier lowering' model with the TFE current being relatively insignificant. Figure 5.15(b) is a comparison of the reverse bias *I–V* characteristics and the 'TE + barrier lowering' model at temperatures from 353 – 423 K, which show excellent agreement. It is therefore reasonable to conclude that the transport process through the silver oxide Schottky contacts, in atmosphere, at room temperature and above is dominated by thermionic emission.

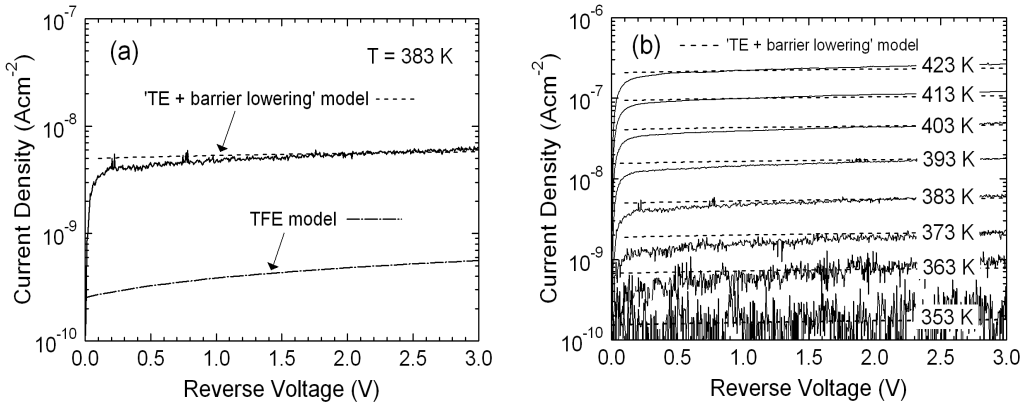

Figure 5.15: (a) Reverse leakage current of a silver oxide Schottky diode on the Zn-polar face of hydrothermal ZnO at 383 K against the predictions of the 'TE + barrier lowering' and TFE models; and (b) measured reverse leakage current and 'TE + barrier lowering' model predictions for temperatures in the 353 – 423 K range.

5.4.3 Below Room Temperature Measurements

For the below room temperature *I–V* characteristics, the same silver oxide diode was mounted on a cold finger, closed cycle cryostat equipped with a LakeShore 330 temperature controller (accuracy ± 0.1 K). The measurements were performed in vacuum at a pressure of 10^{-6} mbar, to avoid condensation of water vapour onto the sample. The diode was held for several hours in the cryostat in dark conditions before the measurements were taken. The results, shown in Figure 5.16, are significantly different from the above room temperature measurements with the diode exposed to air.

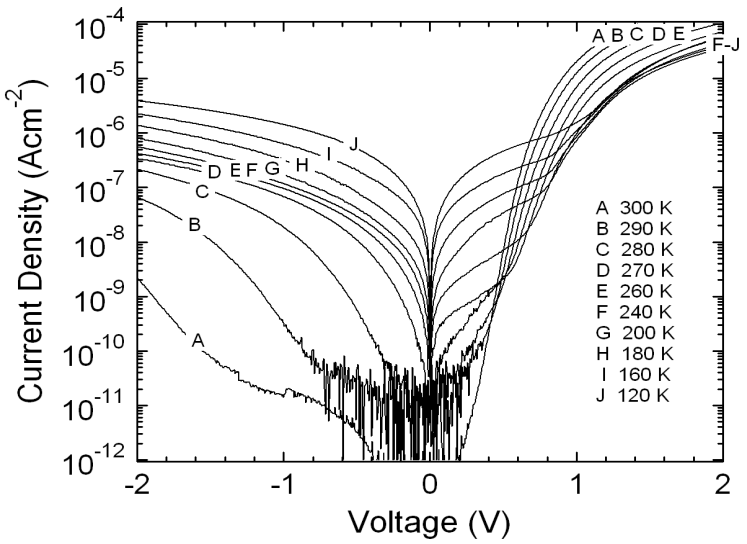

Figure 5.16: Below room temperature *I–V* characteristics of a planar silver oxide Schottky diode on the Zn-polar face of hydrothermal ZnO (wafer HT-1), measured in vacuum at a pressure of 10^{-6} mbar. The Schottky–ohmic contact separation was 25 μm.

Specifically, there is evidence of a vacuum-activated surface conduction path which significantly increases the reverse leakage current. This is equivalent to a shunt resistance between the Schottky and ohmic contacts which decreases with decreasing temperature, and is indicative of degenerate surface carriers experiencing decreased scattering as the temperature is lowered. The surface nature of this shunt resistance was confirmed by re-measuring the *I–V* characteristics (Figure 5.17) with the Schottky to ohmic contact separation increased from 25 μm to 2.5 mm. The reverse leakage current decreased by over four orders of magnitude and the shunt resistance effect was significantly reduced.

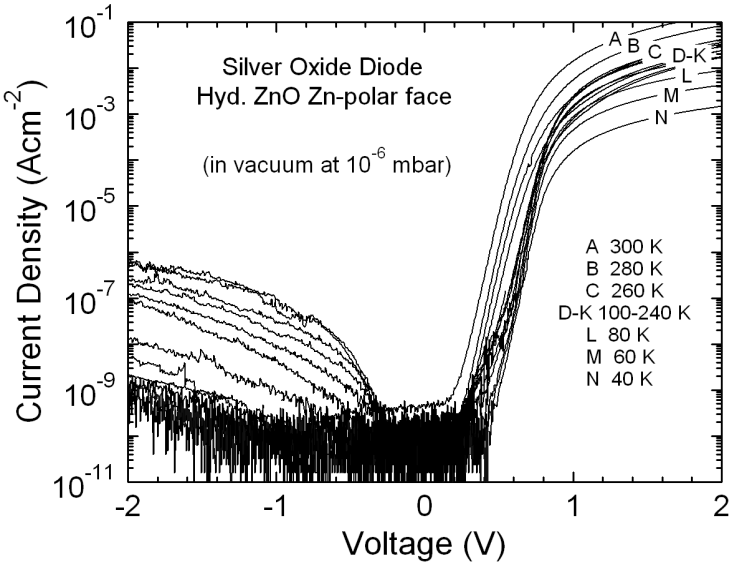

Figure 5.17: Below room temperature *I-V* characteristics of a planar silver oxide Schottky diode on the Zn-polar face of hydrothermal ZnO (c-axis, wafer HT-1) measured in vacuum at a pressure of 10^{-6} mbar. The Schottky–ohmic contact separation was 25 mm..

The below room temperature *I–V* characteristics shown in Figure 5.17 were used to determine Φ_B and η for T < 300 K which are shown, together with the above room temperature values, in Figure 5.18(a).

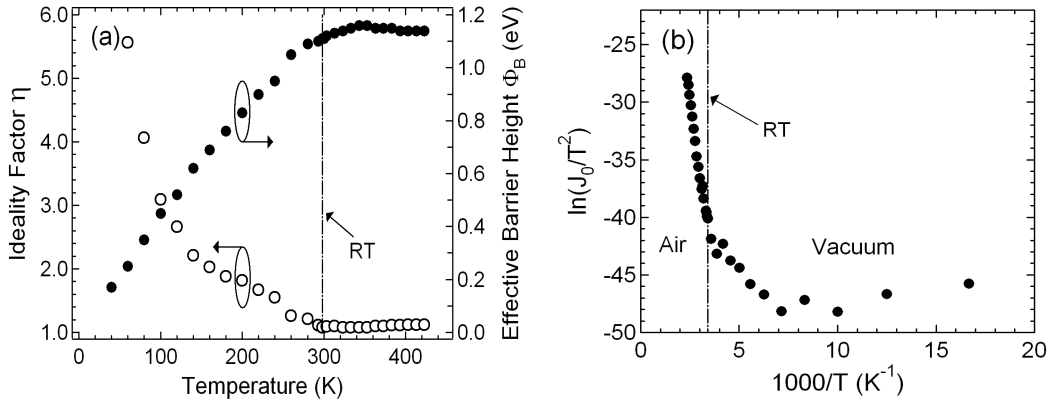

Figure 5.18: (a) Temperature dependence of the effective barrier height (Φ_B) and the ideality factor (η) for a planar silver oxide Schottky diode on the Zn-polar face of hydrothermal ZnO (wafer HT-1): (b) Richardson plot of $\ln(J_0T^2)$ versus 1000/T for the same diode, over the same temperature range.

The decrease in Φ_B and increase of η with decreasing temperature is often attributed to the so called T_o anomaly which can be explained by the inhomogeneity of the Schottky contact [28]. In the present case, it is more likely due to the fact that the bulk (non-degenerate) carriers in hydrothermal ZnO have high activation energies (~ 320 meV) [99] and start to 'freeze out' almost immediately on cooling below room temperature, making current transport from vacuum-activated, degenerate surface carriers increasingly important. The change in conduction mechanism is illustrated in Figure 5.18(b) which shows a combined Richardson plot for the above and below room temperature *I–V* measurements. The deviation from linearity of the below room temperature measurements (in vacuum) indicates a change in transport mechanism. Evidence for presence of a surface conduction layer on the Zn-polar (and O-polar) surface of bulk grown ZnO, under vacuum conditions, was provided by valence band XPS and variable magnetic field Hall effect measurements in Chapter 2.

In the presence of air, the surface conduction layer is passivated by the presence of oxygen and water molecules, which act as acceptors reducing the surface carrier concentration [11]. This process is illustrated in Figure 5.19 shows which the *I–V* characteristics of the planar silver oxide diode (Schottky – ohmic contact separation = 25 μm) exposed to air and vacuum conditions (10^{-6} mbar). There is a significant increase in the reverse leakage current of this planar diode when it is taken from air to vacuum conditions, with the removal of compensating O_2 and H_2O adsorbates activating the surface conduction layer.

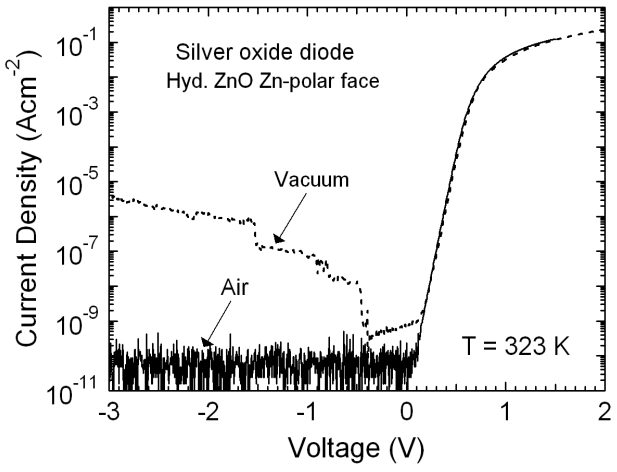

Figure 5.19: *I–V* characteristics of a planar silver oxide Schottky diode on the Zn-polar face of hydrothermal ZnO (wafer HT-1) measured at 323 K in both air and in vacuum conditions (10^{-6} mbar).

5.5 COMPARISON OF PLANAR AND VERTICAL SILVER OXIDE DIODES

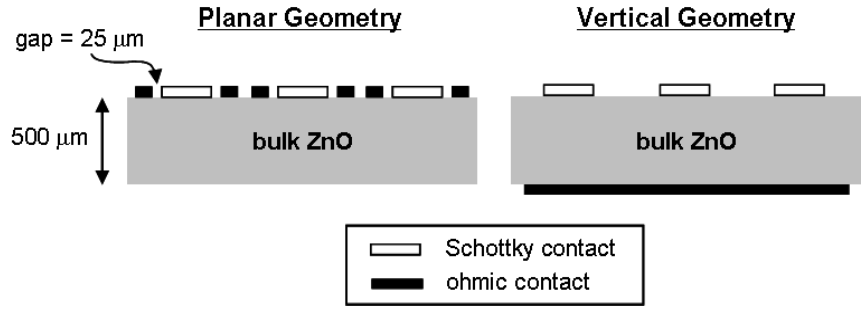

Figure 5.20: Planar versus vertical Schottky diode geometry.

5.5.1 *I–V* Characteristics

All the Schottky diodes presented so far in this thesis have been of the planar geometry type, with the Schottky and ohmic contacts fabricated on the same crystal face (Figure 5.20). To investigate the effect of geometry on diode performance, vertical geometry silver oxide diodes were also fabricated on c-axis and m-plane hydrothermal bulk ZnO wafers (10 mm x 10 mm x 500 μm). As before, the Schottky contacts consisted of arrays of 300 μm diameter, 80 nm thick, silver oxide layers fabricated with an oxygen flow rate of 1.70 sccm and capped with a 30 nm thick platinum film. The ohmic contact consisted of a large area (typically 4 mm x 4 mm) Ti/Al/Pt (40/100/30 nm) layer deposited by electron beam evaporation on the opposite face of the wafer. Figure 5.21(a) shows Φ_B versus η plots determined from the *I–V* characteristics of multiple, vertical geometry silver oxide diodes on the Zn-polar, O-polar, and m-plane faces of hydrothermal bulk ZnO wafers. These Φ_B versus η plots were linearly fitted to determine the image force corrected, homogeneous barrier height, Φ_B^{hom*}, using the method previously described. This gave values for Φ_B^{hom*} of 1.21 and 1.01 for the Zn-polar and O-polar faces respectively, nearly the same as the values of 1.23 and 1.03 (Table 5.3) for planar silver oxide diodes of the same composition.

Figure 5.21(b) shows a direct comparison of the properties of multiple planar and vertical geometry silver oxide diodes. The Φ_B versus η plots for the planar and vertical geometry diodes are very similar, with the barrier heights of the vertical diodes being slightly (~ 20 meV) lower. This small effect may be due to the differences in the effective area of the Schottky contact for the two different geometries, with the effective area likely to be slightly larger for the vertical geometry diodes due to the larger area of the ohmic contact. In general, there appears to be very little difference in the *I–V* characteristics of planar versus vertical geometry silver oxide Schottky diodes.

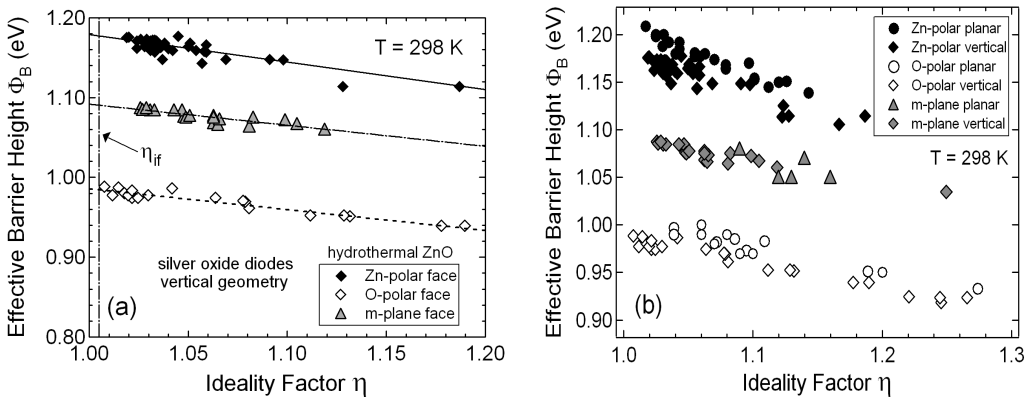

Figure 5.21: (a) Φ_B versus η plots for vertical geometry silver oxide diodes, and (b) a comparison of planar and vertical geometry silver oxide diodes, on the polar and non-polar faces of hydrothermal bulk ZnO.

5.5.2 *C–V* Characteristics

In contrast to the *I–V* characteristics, a significant geometry-related effect was observed for *C-V* measurements. Figure 5.22 shows a comparison of the typical *C–V* characteristics of (a) planar and (b) vertical geometry silver oxide diodes on the different crystal faces of hydrothermal ZnO.

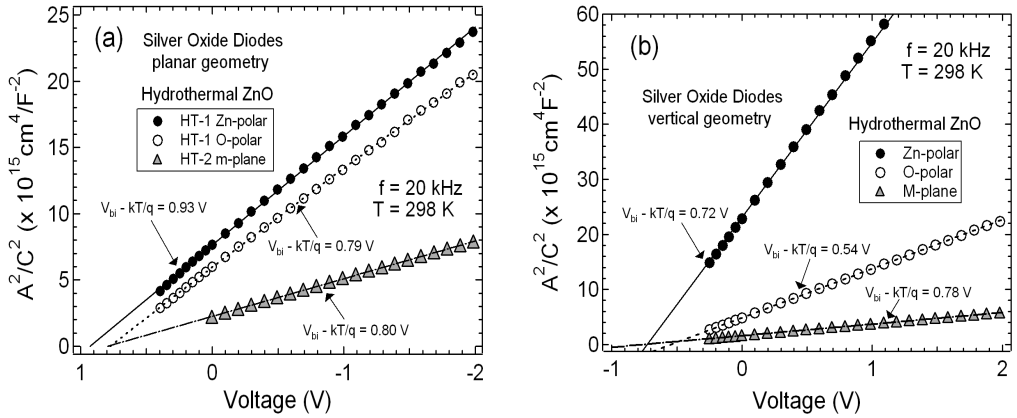

Figure 5.22: Typical *C–V* characteristics of (a) planar geometry and (b) vertical geometry silver oxide diodes on the polar and non-polar faces of hydrothermal ZnO.

The built-in voltage (V_{bi}) obtained from the extrapolation of the corresponding linear fits to $1/C^2 = 0$ are given in Table 5.5. Vertical geometry diodes, with the Schottky contact on the Zn-polar and O-polar faces, have 0.21 – 0.24 eV lower values of V_{bi} compared to planar geometry diodes. The values of $\Phi_{B,C\text{-}V}$ determined from $\Phi_{B,C\text{-}V} = V_{bi} + \xi$, are also shown in

Table 5.5, together with the values of $\Phi_{B,I\text{-}V}$ from the *I–V* characteristics of the same diodes. While the values of $\Phi_{B,C\text{-}V}$ and $\Phi_{B,I\text{-}V}$ are similar for planar geometry diodes, there is a deficit of 0.20 ± 0.02 eV in the values of $\Phi_{B,C\text{-}V}$ for the vertical geometry diodes. Interestingly, in the case of the non-polar m-plane face, there appears to be no 'geometry effect' with the values of $\Phi_{B,C\text{-}V}$ and $\Phi_{B,I\text{-}V}$ almost the same for both planar and vertical geometry diodes. The nature of the polarity and geometry effects are discussed further in Chapter 6.

Table 5.5: Built in voltage (V_{bi}) and barrier height ($\Phi_{B,C\text{-}V}$) determined from the typical *C–V* characteristics of planar and vertical geometry silver oxide diodes on hydrothermal ZnO. The barrier heights ($\Phi_{B,I\text{-}V}$) of the same diodes determined from their *I–V* characteristics are shown for comparison.

Diode Geometry	Polarity	$V_{bi,C\text{-}V}$ (eV)	$\Phi_{B,C\text{-}V}$ (eV)	$\Phi_{B,I\text{-}V}$ (eV)
Planar	Zn-polar	0.93	1.19	1.20
Planar	O-polar	0.78	1.04	1.00
Planar	m-plane	0.80	1.06	1.09
Vertical	Zn-polar	0.72	0.96	1.18
Vertical	O-polar	0.54	0.80	0.98
Vertical	m-plane	0.78	1.04	1.09

5.6 SILVER OXIDE SCHOTTKY CONTACT SUMMARY

The use of reactively sputtered silver oxide films in fabricating Schottky contacts to bulk ZnO resulted in a significant increase in device performance compared to the best reported results in the literature. In addition, this technique appears to have overcome the problems of device yield and reproducibility, which are common for ZnO Schottky contact fabrication using just plain metals. The structural, electrical, and temperature dependent properties of silver oxide Schottky contacts to bulk ZnO have been examined in detail with the following key findings:

1) Reactively sputtered silver oxide films consistently produced low ideality factor Schottky contacts with effective barrier heights between 1.0 – 1.2 eV depending on the bulk ZnO material and surface polarity.
2) The highest barrier heights of 1.2 eV were produced on the Zn-polar face of hydrothermal ZnO.

3) A significant polarity effect occurs for hydrothermal ZnO in that silver oxide contacts fabricated on the Zn-polar face had ~ 200 meV higher barriers than those on the O-polar face, even though the ideality factors on both faces were close to the image force controlled limit.

4) A similar but much smaller polarity effect occurs for silver oxide contacts on melt ZnO. The key difference between melt and hydrothermal ZnO is that the former has 2 – 3 orders of magnitude higher carrier concentration.

5) The silver oxide contacts were highly silver rich (90 – 96% silver by atomic composition) but contained mixed oxide (Ag_2O, AgO) phases. The contacts had poor lateral conductivity and required a 30 nm Pt capping layer for achieve good current flow.

6) The reactively sputtered silver oxide contacts contained a significant density of voids, even at the Schottky interface, indicating there is considerable room for improvement in the structural quality of the contacts.

7) At room temperature and above, with the ZnO surface exposed to air, the current transport between the Schottky and ohmic contact was dominated by pure thermionic emission.

8) When planar silver oxide diodes fabricated on the Zn-polar face of hydrothermal ZnO are placed in vacuum conditions, a surface conduction path is activated which becomes increasingly dominant as the temperature is lowered.

The cause of the interesting polarity effects will be investigated in detail in Chapter 6. The rest of this chapter is focused on investigating whether the success achieved with silver oxide can be extended to other metal oxide films.

5.7 IRIDIUM OXIDE

Following the success of reactively sputtered silver oxide films in producing high quality Schottky contacts to ZnO, the performance of other metal oxides was investigated. Significant improvement in the rectifying performance of certain iridium Schottky contacts on annealing at 150 ^{o}C in an O_2 ambient has already been mentioned in Chapter 4, Section 4.6.

5.7.1 Iridium Oxide Review

Iridium oxide (IrO_2) crystallizes in the tetragonal rutile structure, and has a low resistivity (~ 50 mΩcm) and excellent high temperature electrical and chemical stability [114,115]. Iridium oxide is used in applications such as cathodes for field emission displays [116], electrodes for high density dynamic random access memory (DRAM) and nonvolatile ferroelectric random access memory (NVFRAM), optical switching layers in electrochromic displays, and corrosion resistant electrochemical electrodes [115,117]. Growth methods have included reactive d.c. sputtering [118], pulsed laser deposition [115], chemical vapour deposition [117], and annealing of Ir films in an oxygen atmosphere [114, 116].

Iridium oxide has previously been used in the fabrication of thermally stable Schottky contacts to *n*-GaN and *n*-SiC, by the annealing of Ir contacts in O_2 atmospheres. Kim *et al.* [119, 120] produced IrO_2 Schottky contacts on unintentionally doped, *n*-GaN films (n = 5 x 10^{16} cm^{-3}, μ = 550 cm^{2}V^{-1}s^{-1}) by annealing 10 nm thick Ir contacts at 500 ^{o}C under an O_2 ambient. Schottky diodes with the plain Ir contacts had a Φ_B and η of 1.21 eV and 1.52 respectively, which improved on O_2 annealing to 1.48 eV and 1.09. At the same time, high resolution x-ray diffraction showed the appearance of IrO_2 phases with much higher peak intensities than those from Ir. Similarly, Jeon *et al.* [121] reported an increase in Φ_B from 0.68 to 1.07 eV for 50 nm thick Ir contacts to AlGaN/GaN heterostructures after 500 ^{o}C O_2 annealing. Han *et al.* [114] produced a thermally stable IrO_2 Schottky contact to a *n*-type 4H-SiC epilayer (n = 4 x 10^{15} cm^{-3}) by annealing a 50 nm thick Ir contact at 300 ^{o}C in an O_2 ambient, with an accompanying increase in Φ_B from 1.84 [1.92] eV to 1.95 [2.22] eV from *I–V* [*C–V*] measurements. They also observed an increase in work function of 230 meV as IrO_2 was formed, using synchrotron radiation photoemission spectroscopy.

5.7.2 Growth and Characterisation

For Schottky contact fabrication to bulk ZnO, iridium oxide films were grown by pulsed laser deposition (PLD) via the ablation of a rotating, high purity iridium target by a KrF excimer laser (λ = 248 nm) in an oxygen atmosphere. The growth was carried out in the Department of Physics and Astronomy, University of Canterbury, N.Z., by R. Mendlesberg.

The ZnO substrates were mounted on an unheated stainless steel block in a high vacuum chamber, which was evacuated to a base pressure of 10^{-5} mTorr. An ambient oxygen processing atmosphere was established at pressures of either 50 or 100 mTorr. The KrF laser was focused onto the Ir target, at a 45^{o} angle, with a 2 mm^2 spot size, and a fluence of 15 – 20 Jcm^{-2}. Each film was grown for 1 hour at a pulse rate of 10 Hz. A high fluence was required due to the reflectivity and low vapour pressure of the Ir target which increases the likelihood of superheated explosive droplets being ejected from the target [122]. To limit the incorporation of these droplets into the iridium oxide film, a 10 mm x 10 mm square shadow mask was placed 17 mm in front of the substrate, directly in the line of sight of the target, as shown in Figure 5.23. The target – substrate distance was 50 mm. This technique is usually referred to as eclipse-PLD in which the deposition is ideally limited to the diffusion of atoms, molecules and clusters around the shadow mask.

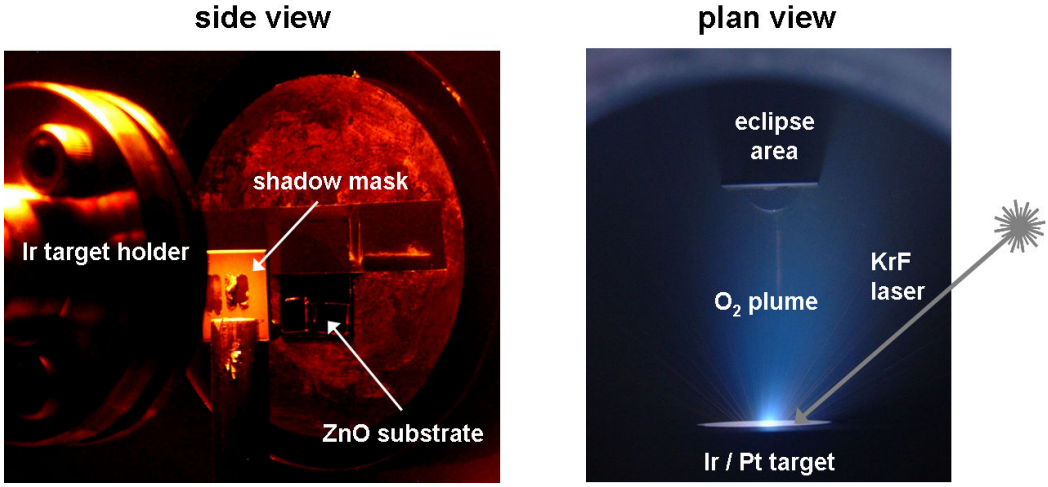

Figure 5.23: eclipse PLD using the ablation of a rotating 2.54 mm diameter, Ir target by a KrF laser in a 100% oxygen ambient.

Two iridium oxide films were grown for 1 hour by eclipse-PLD, one with an ambient oxygen pressure of 50 mTorr and the other 100 mTorr, using the same KrF laser fluence. The thickness of each of the resulting '50 mTorr O_2' and '100 m Torr O_2' films was determined by AFM step-height analysis to be ~ 55 nm and ~ 160 nm respectively, indicating a faster diffusion rate of the ejected particles in the higher O_2 pressure ambient. Figure 5.24 shows an AFM surface plot of the '50 mTorr O_2' film, from which an r.m.s. roughness of ~ 2.5 nm was estimated.

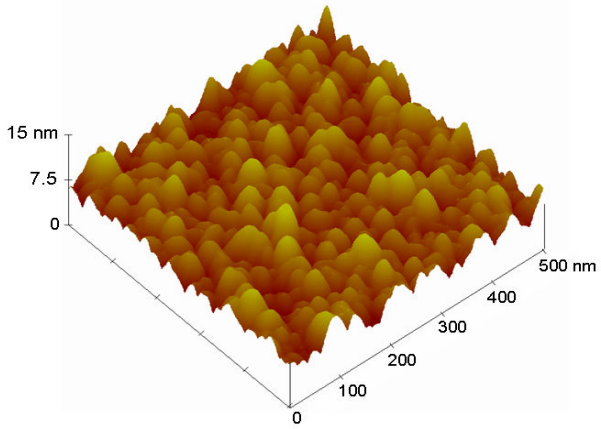

Figure 5.24: Tapping mode AFM image of the surface of a 55 nm thick '50 mTorr O_2' iridium oxide film grown by eclipse PLD on a bulk ZnO substrate.

The composition of the two films was determined from XPS survey scans taken after a 3 – 4 minute sputter clean, using 2.4 keV Ar ions, to remove the more heavily oxidised surface layers. The atomic O/Ir fraction of the 50 mTorr O_2 film was 0.24, compared to 0.11 for the 100 mTorr O_2 film, with the slower growth rate of the former perhaps allowing more opportunity for oxygen incorporation. However, these O/Ir fractions are still significantly less than the stoichiometric value of 0.67 for IrO_2, indicating that the films were both iridium rich. Figure 5.25 shows the valence band XPS spectrum collected from the sputter cleaned 50 mTorr O_2 film (the same spectrum from the 100 mTorr O_2 film was almost identical) indicating metallic like conduction. Unlike the earlier case for silver oxide, these iridium oxide films were found to have good lateral conductivity. Consequently, good electrical contact could be made to these films without the need for a metallic capping layer.

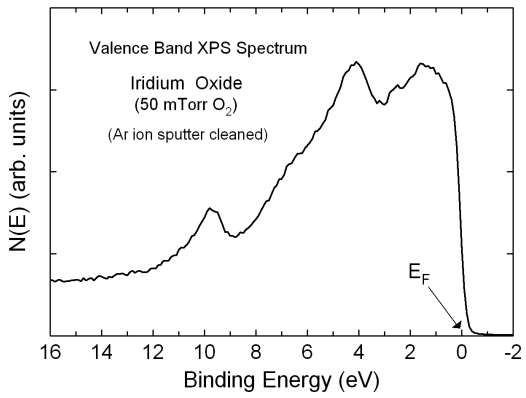

Figure 5.25: Valence band XPS spectrum (90^o take off angle) taken, after a 3 – 4 minute 2.4 keV Ar ion sputter clean, from an iridium oxide film grown, on a bulk ZnO substrate, by eclipse-PLD for 1 hour with an O_2 pressure of 50 mTorr.

5.7.3 Schottky Contact Performance

Separate arrays of vertical geometry diodes, with 300 μm diameter '50 mTorr O_2' and '100 mTorr O_2' iridium oxide Schottky contacts were fabricated on two hydrothermal c-axis ZnO wafers. Figure 5.26 shows typical *I–V* characteristics and Φ_B versus η plots for '50 mTorr O_2' iridium oxide diodes on the Zn-polar and O-polar faces of the same hydrothermal wafer.

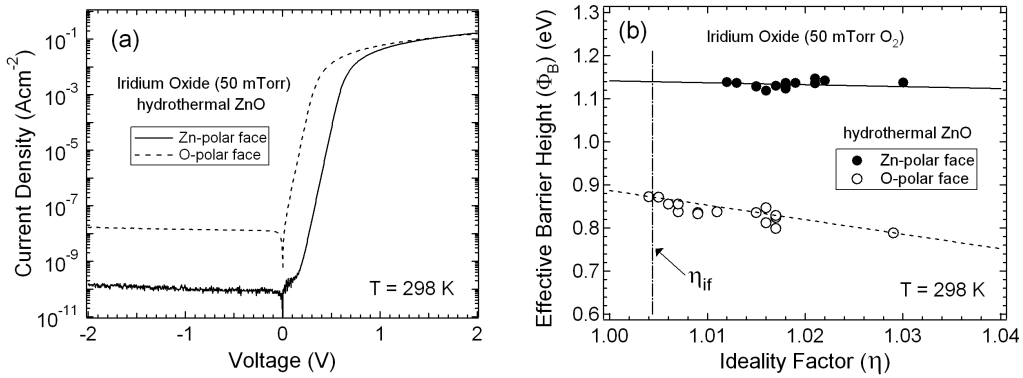

Figure 5.26: (a) Typical *I-V* characteristics and (b) Φ_B versus η plots, for '50 mTorr O_2' iridium oxide diodes on the Zn-polar and O-polar faces of the same hydrothermal c-axis wafer.

These arrays produced a high yield (> 90%) of very low ideality factor Schottky diodes on both polar faces. A dramatic surface polarity related effect was again observed, in that the barrier heights of the diodes on the Zn-polar face were typically 250 meV higher than those on the O-polar face. The ideality factors on both polar faces were very close to the image force controlled limit (η_{if}), indicating that the polarity effect was not due to differences in the homogeneity of the contacts. The image force corrected homogeneous barrier height, Φ_B^{hom*}, for the '50 mTorr O_2' iridium oxide diodes on the Zn-polar and O-polar faces were found to be 1.16 eV and 0.91 eV respectively.

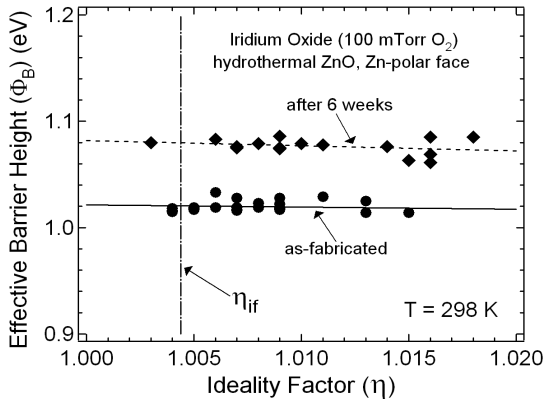

Figure 5.27: Φ_B versus η plots, for '100 mTorr O_2' iridium oxide diodes on the Zn-polar face of a hydrothermal c-axis wafer.

Figure 5.27 shows a Φ_B versus η plot for the '100 mTorr O_2' iridium oxide diodes on the Zn-polar face of an additional hydrothermal wafer. After fabrication, these diodes again had very low ideality factors close to the image force limit η_{if}. However, the barrier heights of these diodes were significantly less than those of the '50 mTorr O_2' iridium oxide diodes on the same polar face. The Φ_B^{hom*} for the as-fabricated '100 mTorr O_2' iridium oxide diodes in Figure 5.27 is 1.05 eV compared to 1.16 eV for the '50 mTorr O_2' diodes. This is probably a consequence of the lower O/Ir fraction of the '100 mTorr O_2' iridium oxide contacts which from electronegativity arguments should result in a lower work function compared to the more oxygen rich '50 mTorr O_2' contacts. The very low ideality factors of these diodes indicates the formation of a very homogeneous Schottky barrier. Consequently, the lower barrier height of the '100 mTorr O_2' diodes can only be a result of a lower work function or alternatively a decreased electric dipole contribution from Ir–O chemical bonding at the Schottky interface.

The *I–V* characteristics of the '100 mTorr O_2' iridium oxide diodes were re-measured after 6 weeks storage at room temperature. The 're-measured' Φ_B versus η plot (Figure 5.27) shows an age-related barrier height increase of ~ 60 meV, and a corresponding increase in Φ_B^{hom*} to 1.11 eV. The *I–V* characteristics were re-measured again after a further 10 week storage period, and while most diodes showed no further change, the barrier height of a few diodes had increased by another 30 – 40 meV, bringing them close to the barrier height of the '50 mTorr O_2' diodes. This increase in barrier height for almost ideal contacts must be due to either (a) further oxidation of the film resulting in an increased O/Ir fraction and therefore an increased work function, or (b) an increase in chemical bonding, involving Ir–O bonds, at the Schottky interface.

5.8 PLATINUM OXIDE

Platinum oxide is another high work function metal oxide with interesting electrical properties, including the metallic-like conduction of certain oxide phases. These properties make platinum oxide another promising candidate for producing Schottky contacts to ZnO.

5.8.1 Platinum Oxide Review

The catalytic properties of platinum oxide have been widely used for over 100 years [123] and currently play an important role in fuel cells [124]. Platinum oxide thin films are used as electrodes in memory capacitors and in super-resolution near field optical recording [126].

Platinum oxide films can be produced by the reactive sputtering of a platinum target in Ar/O_2 atmospheres [125–129]. Thermally stable PtO and PtO_2 phases have been reported with

electrical properties which vary with composition and structure. Abe *et al.* [129] reported PtO to be a metallic conductor with a resistivity of 1–2 mΩcm. The same authors found that α-PtO_2 films showed semiconductor-like behaviour with a higher resistivity (~1 Ωcm) and a negative temperature coefficient. Neff *et al.* [125] observed a conductor to insulator transition of PtO_x films at $x \geq 2$. Platinum oxide films have been reported to be thermally stable in air up to 500 ^{o}C after which decomposition to Pt occurs [127, 129]. There are no literature reports of the use of deliberately fabricated platinum oxide films in the production of Schottky contacts.

5.8.2 Growth and Characterisation

For Schottky contact fabrication, platinum oxide films were grown using the same eclipse-PLD technique used for the growth of iridium oxide. Apart from the use of a high purity platinum target and an ambient oxygen pressure of 100 mTorr, all growth conditions and parameters were the same as previously described in Section 5.7.2. Figure 5.28 shows an AFM surface plot of the 100 mTorr O_2 platinum oxide film, showing a r.m.s. surface roughness of 2.5 – 3.0 m. This film was grown for 1 hour and had a thickness (from AFM step-height analysis) of 240 nm.

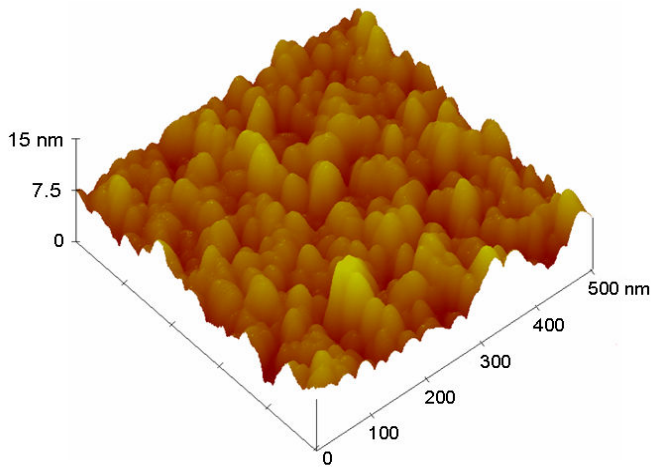

Figure 5.28: Tapping mode AFM image of the surface of a 240 nm thick '100 mTorr O_2' platinum oxide film, grown by eclipse PLD on a bulk ZnO substrate.

The composition of this film was again determined from an XPS survey scan taken after a 4 minute Ar ion sputter clean. The O/Pt fraction was ~ 0.17 indicating a Pt rich film. The valence band spectrum (Figure 5.29) taken from the sputter cleaned film showed a high density of states near the Fermi level, which is characteristic of strong catalysts [125] and indicates a metallic rather than semiconducting nature.

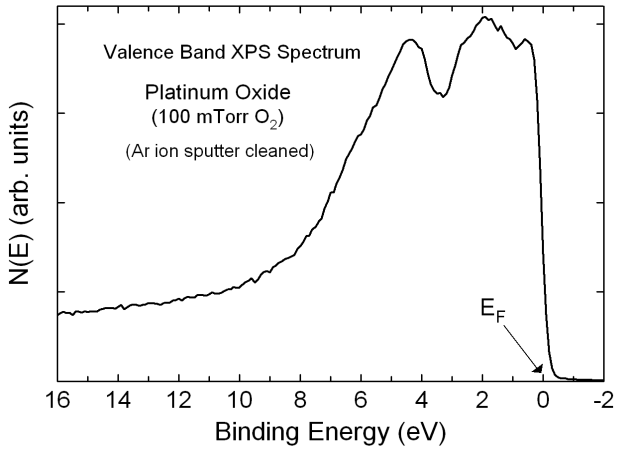

Figure 5.29: Valence band XPS spectrum (90^{o} take off angle) taken, after a 5 minute 2.4 keV Ar ion sputter clean, from a platinum oxide film, grown by eclipse-PLD for 1 hour with an O_2 pressure of 100 mTorr on a bulk ZnO substrate.

5.8.3 Schottky Contact Performance

Arrays of vertical geometry diodes with 300 μm diameter, 240 nm thick, '100 mTorr O_2' platinum oxide Schottky contacts were fabricated on the Zn-polar and O-polar faces of the same hydrothermal, bulk, c-axis ZnO wafer. The platinum oxide film had poor lateral conductivity and a ~ 30 nm thick Pt capping layer was added to improve the current flow through the contacts. Figure 5.30(a) shows Φ_B versus η plots for the diodes on each polar face, taken 4 weeks after fabrication. During that time the barrier heights of the diodes on the Zn-polar face had increased by ~ 60 meV. The barrier heights of the '100 mTorr O_2' platinum oxide diodes on the Zn-polar and O-polar face of hydrothermal ZnO were remarkably similar to those previously observed for silver oxide Schottky contacts on the same material. The Φ_B^{hom*} values for the platinum oxide diodes on the Zn-polar and O-polar faces are 1.23 eV and 1.01 eV respectively, from Figure 5.30(a), compared to 1.21 eV and 1.01 eV for vertical geometry silver oxide diodes on similar hydrothermal ZnO material.

Figure 5.30(b) shows the typical room temperature *C–V* characteristics for the '100 mTorr O_2' platinum oxide diodes. These show a polarity difference of 0.18 eV in the built-in voltage V_{bi}, similar to the 0.22 eV difference in Φ_B^{hom*} extracted from the *I–V* characteristics in Figure 5.30(a). However, the values of the $\Phi_{B,C\text{-}V}$, determined from $\Phi_{B,C\text{-}V} = V_{bi} + \xi$, were only 0.98 eV and 0.80 eV for the Zn-polar and O-polar faces respectively, a deficit once again of approximately 0.20 eV for vertical geometry diodes.

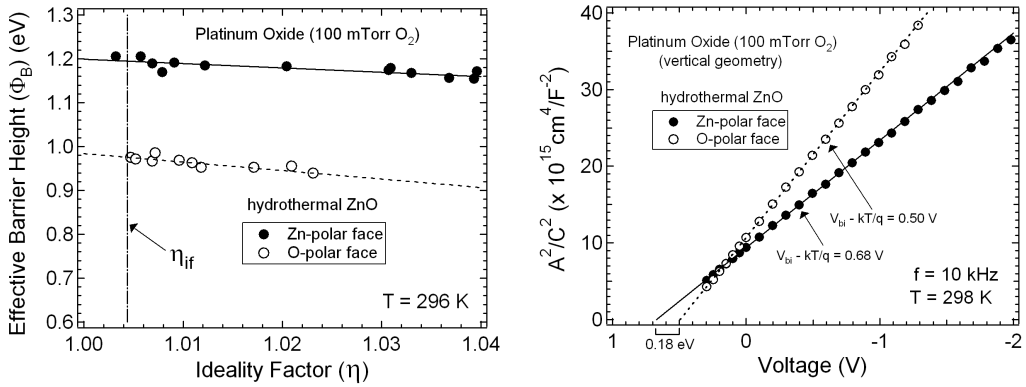

Figure 5.30: Φ_B versus η plots, for '100 mTorr O_2' platinum oxide diodes on the Zn-polar and O-polar faces of the same hydrothermal c-axis wafer.

5.9 COPPER OXIDE

Series connected copper / copper oxide disks were commonly used as small signal diodes and power rectifiers in the 1920s and 30s. Copper oxidises to brown/red cuprous oxide (Cu_2O) and black cupric oxide (CuO). Both are *p*-type semiconductors (band gap of Cu_2O = 2.0 eV) due to copper vacancies which form acceptor levels ~ 0.4 eV above the valence band.

5.9.1 Growth and Characterisation

Copper oxide films were fabricated by the reactive r.f. sputtering of a high purity copper target in an O_2/Ar atmosphere, similar to the method used for silver oxide. Oxygen/argon gas flow rates of 2.0 sccm/10 sccm were used, at a processing pressure of 5 x 10^{-3} mbar. Growth was carried out at an r.f. power of 100 r.m.s for 5 minutes resulting in a brown film of 160 nm thickness, which was subsequently capped with 30 nm of Pt. An XPS survey scan, taken from the film after Ar ion sputter cleaning (~ 4 minutes), gave an atomic O/Cu fraction of 0.316 close to the stoichiometric value of 0.33 for CuO_2. An AFM surface plot of the film (Figure 5.31) showed a slightly rougher surface (r.m.s. roughness ~ 3.5 nm) with larger feature sizes in comparison to the metal oxide films grown by eclipse-PLD.

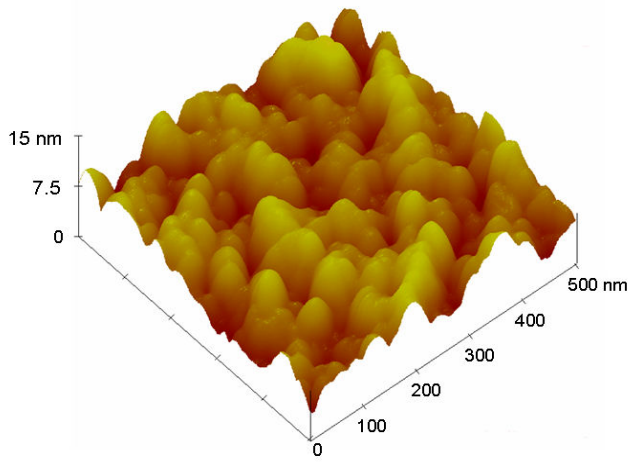

Figure 5.31: Tapping mode AFM image of the surface of a 160 nm thick reactively sputtered copper oxide on a bulk ZnO substrate.

Figure 5.32 shows the valance band XPS spectrum of the sputter cleaned copper oxide film compared to that of a sputter cleaned copper reference sample. The valence band spectrum of the copper oxide film shows no evidence of the expected band gap of 2.0 eV for Cu_2O, but neither does it have the flat 'de-localised' density of states near the Fermi level observed in the Cu reference sample. The XPS spectra suggests that the film is likely to contain degenerate charge carriers and possibly more metallic than semiconducting in nature.

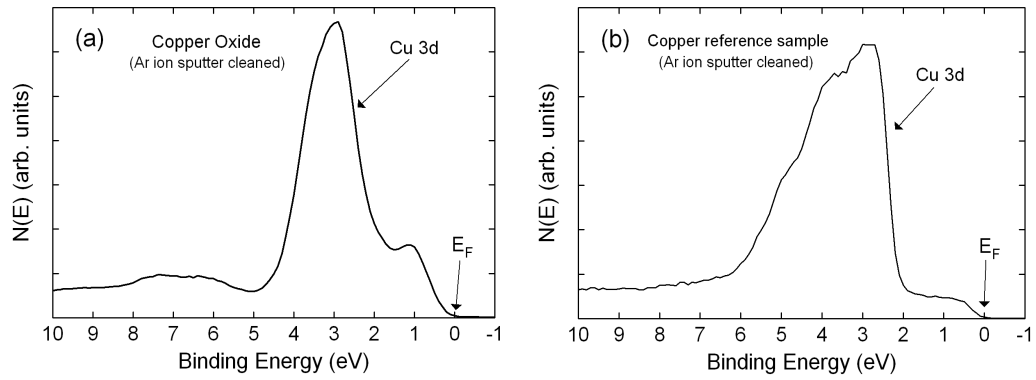

Figure 5.32: Valence band XPS spectrum (90^o take off angle) taken from (a) a reactively r.f. sputtered copper oxide film, and (b) a pure copper reference sample. Both samples were sputter cleaned with 2.4 keV Ar ions to remove the more heavily oxidised surface layers and surface carbon contamination.

5.9.2 Schottky Contact Performance

Arrays of vertical geometry diodes with 300 μm diameter, 100 nm thick, copper oxide Schottky contacts were fabricated on the Zn-polar face of a hydrothermal ZnO wafer. A 30 nm thick Pt capping layer was added to improve current flow through the contacts. For comparison, a separate array of plain copper contacts was fabricated separately alongside the copper oxide contacts. Figure 5.33(a) shows the typical *I–V* characteristics of the copper and copper oxide diodes. The rectifying performance of the copper oxide diodes were significantly better than their plain copper counterparts, with rectifying ratios (at ± 1 V) of 3×10^7 compared to 3×10^2 respectively. Figure 5.33(b) shows a Φ_B versus η plot for multiple copper oxide diodes giving a Φ_B^{hom*} value of 0.94 eV. The ideality factors of the copper oxide diodes, while good by literature standards, were significantly higher than those for silver, iridium, and platinum oxide.

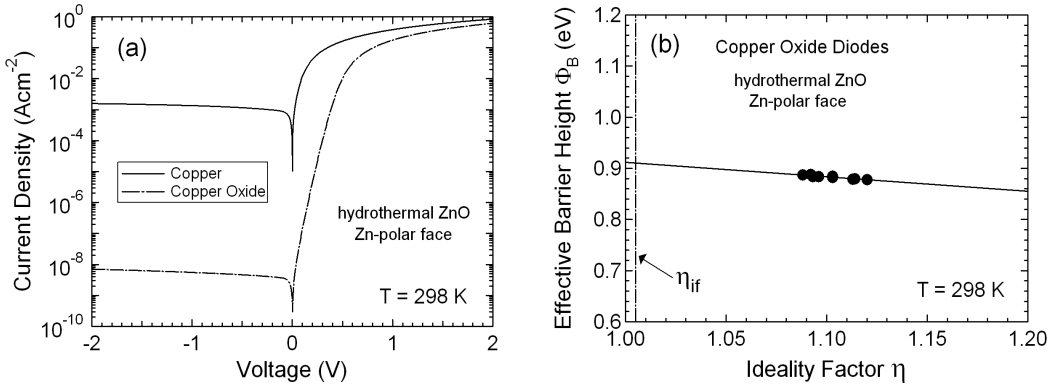

Figure 5.33: (a) Typical *I–V* characteristics for vertical geometry copper and copper oxide Schottky contacts on the Zn-polar face of the same hydrothermal, bulk, c-axis ZnO wafer; and (b) a Φ_B versus η plot for multiple copper oxide diodes.

5.10 SUMMARY

Silver, copper, iridium and platinum oxide films fabricated in reactive oxygen ambients, using either r.f. sputtering or pulsed laser ablation of metal targets, consistently produce high performance Schottky contacts to bulk ZnO. Figure 5.34 shows the effective barrier heights (Φ_B) and ideality factors (η) of the best Schottky diodes fabricated using these metal oxide films, compared to the best reported results using plain metal contacts.

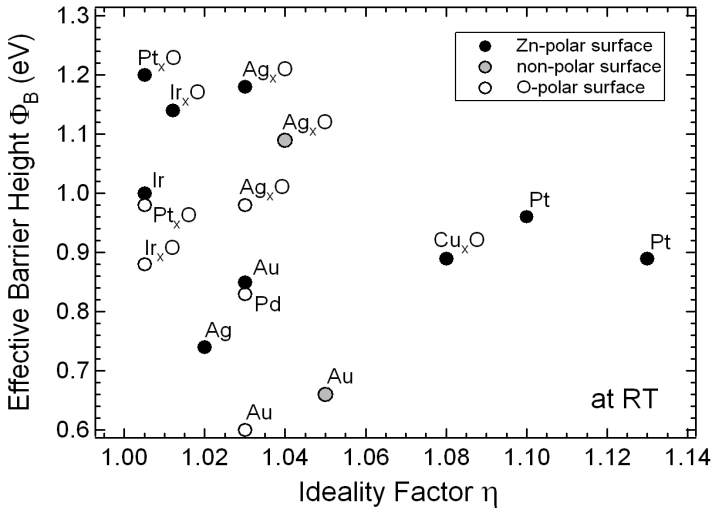

Figure 5.34: Best reported Schottky contacts to *n*-type ZnO showing the superior rectifying performance of metal oxides.

It is clear that the silver, iridium, and platinum oxide Schottky contacts significantly outperform their plain metal counterparts. In addition, the superior rectifying properties of these metal oxide contacts can be consistently reproduced and with high yields, something that has proved difficult to achieve with plain metals. Investigations of the properties of these metal oxide contacts resulted in the following key findings:

1) The metal oxide contacts (with the exception of copper oxide) were metal rich with significantly lower oxygen fractions than those expected for stoichiometric oxide films.

2) The metal oxide contacts all had a continuous valence band density of states near the Fermi level, indicating a metallic-like nature.

3) Most metal oxide films, with the exception of iridium oxide, had low lateral conductivity requiring the use of a metal capping layer (usually platinum) to achieve good current flow through the contacts.

4) The barrier height of metal oxide contacts often showed significant age-related improvements, even for contacts which initially had very low ideality factors close to the image force controlled limit, η_{if}.

5) A significant surface polarity effect was evident for all metal oxide contacts, especially those on hydrothermal ZnO, with the barrier height of contacts on the Zn-polar face consistently higher, by 200 – 250 meV, than those on the O-polar face.

The are several possible factors for the success of metal oxides in consistently producing high performance Schottky contacts with reproducible rectifying properties. These are:

1) The r.f. sputtering / eclipse-PLD techniques generate a plasma / plume containing reactive oxygen species, e.g. charged oxygen ions, oxygen radicals, and excited molecular and atomic oxygen. These reactive oxygen species are likely to be efficient scavengers of hydrogen from the hydroxide layers which terminate the ZnO surface in vacuum conditions. In Chapter 2, this hydroxide termination was linked to a surface accumulation layer which must be removed prior to Schottky contact formation.

2) Oxygen vacancies are intrinsic donors which can increase the conductivity of the surface and pin the near surface ZnO Fermi level [159]. Kunat *et al.* [49] showed that thermal de-hydrogenation (at 600 K) of the O-polar ZnO surface results in a 1 x 3 reconstruction with a significant number of oxygen vacancies. The use of reactive oxygen ambients to remove hydrogen from the ZnO surface may avoid the creation of oxygen vacancies. The reactive oxygen species may even neutralise intrinsic near surface oxygen vacancies and oxygen vacancies introduced by the metalisation process [159]. In Chapter 7, oxygen vacancies will be identified as a likely candidate for the Fermi level of pinning of the barrier height of ZnO Schottky contacts at 0.6 – 0.8 eV.

3) The age-related improvement in the barrier height of almost ideal (i.e. $\eta \approx \eta_{if}$) metal oxide Schottky contacts may be due to further oxidation of the metal oxide film increasing either (a) its bulk oxygen content and as a consequence its work function, or (b) the number of metal–oxygen bonds at the Schottky interface and as a result their electric dipole contribution to the barrier height.

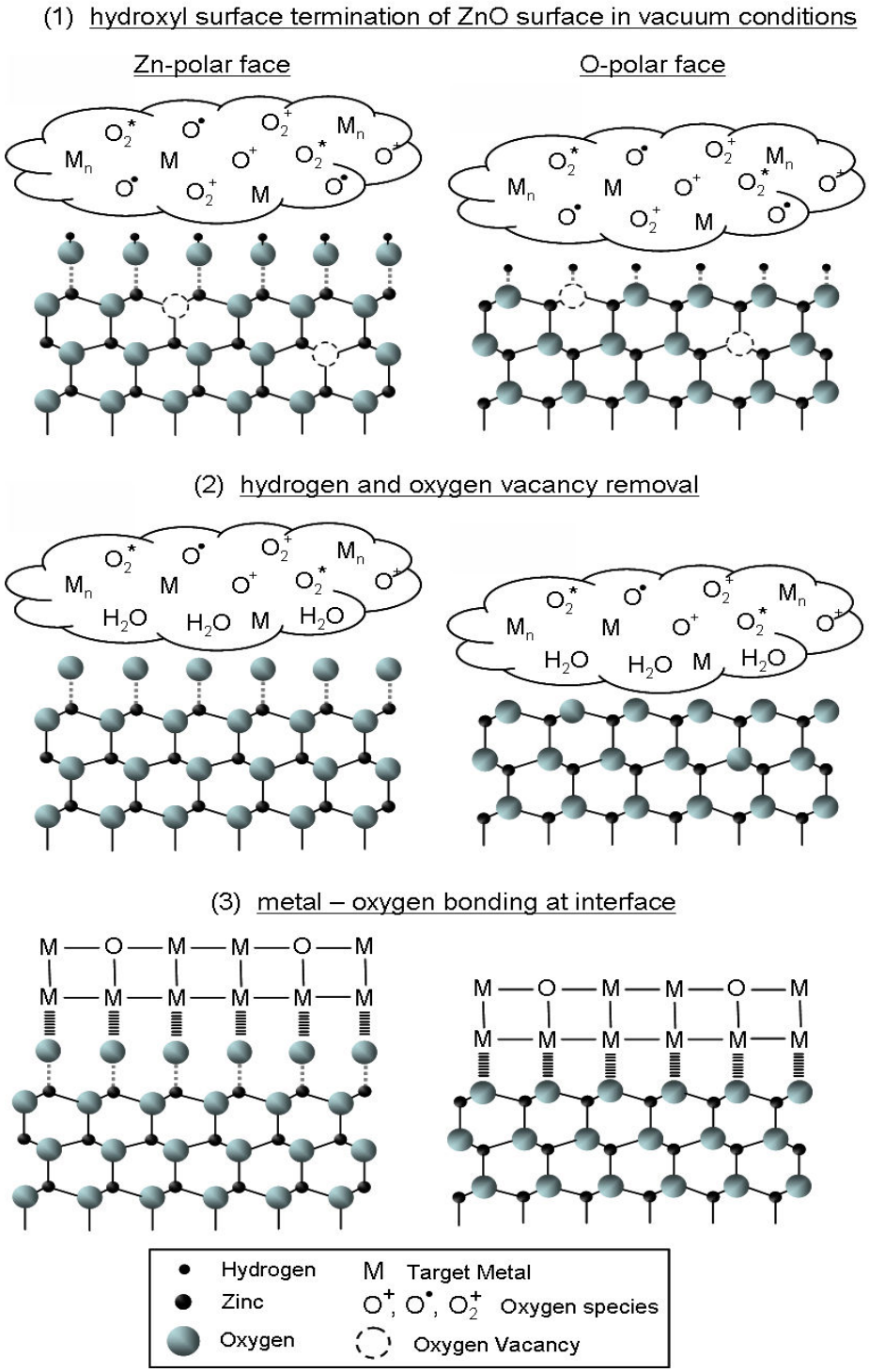

Figure 5.35: Possible Schottky contact formation mechanism during the fabrication of metal oxide contacts, using reactive oxygen ambients.

Possible mechanisms for 1) and 2) are illustrated in Figure 5.35. The main assumptions are (a) that only hydrogen is removed, by reactive oxygen species, from the hydroxyl groups which terminate the ZnO surface in vacuum conditions, and (b) the dominant chemical bonding at the Schottky interface is between metal and oxygen atoms. The first assumption is very plausible for the O-polar surface, as the hydrogen is attached to oxygen atoms which are threefold coordinated to Zn atoms, and it seems unlikely that three O–Zn bonds would be easily broken by the reactive oxygen species. On the Zn-polar face, the hydrogen is attached to oxygen atoms which have a single O–Zn bond, and so individual H atoms or whole OH groups can be removed by the breaking of just a single bond. However, the removal of OH groups would leave behind an outermost plane of Zn atoms which would readily recombine with the reactive oxygen, so it seems more likely that only the hydrogen atoms would be detached. The second assumption follows from that the larger bond energy and electronegativity difference of metal–oxygen bonds compared to metal–zinc bonds. Dong and Brillson [89] theoretically modelled the influence of metal–oxygen and metal–zinc bonding on Schottky barrier formation and concluded that the former was much more likely to be associated with Schottky-like behaviour.

Chapter 6

Surface Polarity Effects

In Chapters 3, 4, and 5, significant surface polarity related effects were observed in the structural and electrical properties of the ZnO surface. These are now discussed together with additional effects which have been observed in photoluminescence, reflectivity, and surface Kelvin probe microscopy measurements.The strength of these polarity related effects appear to be linked to bulk carrier density of the ZnO material, and are significantly stronger for the hydrothermal bulk ZnO, which is several orders of magnitude more resistive than melt or seeded chemical vapour deposition, bulk ZnO.

6.1 BOND IONICITY MODELS

The electrical asymmetry of the different crystallographic faces of ZnO is related to the substantial ionic character of the Zn–O bond and the lack of inversion symmetry of the wurtzite structure along the c-axis. Historically, ZnO sits on the borderline of classification as a covalently bonded semiconductor and an ionic solid [9]. This has resulted in the development of two, quite different, models both of which seek to explain the influence of the bond ionicity of ZnO on its surface properties. These are the spontaneous polarisation and the ionic models.

6.1.1 Spontaneous Polarisation Model

According to the spontaneous polarisation model [130, 149], large fixed surface charges of opposite sign occur on the Zn-polar and O-polar faces. These fixed charges affect the carrier distribution, near-surface band bending, and the electrical and optical properties of bulk crystals, epilayers, and nanostructures.

ZnO crystallises into the wurtzite structure with a c:a ratio lower than that for perfectly, hexagonally close-packed atoms; c:a=1.6020 for ZnO and 1.6333 for hcp. Each elementary ZnO_4 tetrahedron is distorted from the 'ideal' T_d symmetry [12] as shown in Figure 6.1. This, together with the heteropolar nature of the Zn–O bond, creates a permanent net dipole moment along the c-axis of each unit cell. These dipole moments cancel in the bulk but cause equal and opposite bound polarisation charges on the Zn-polar and O-polar faces.

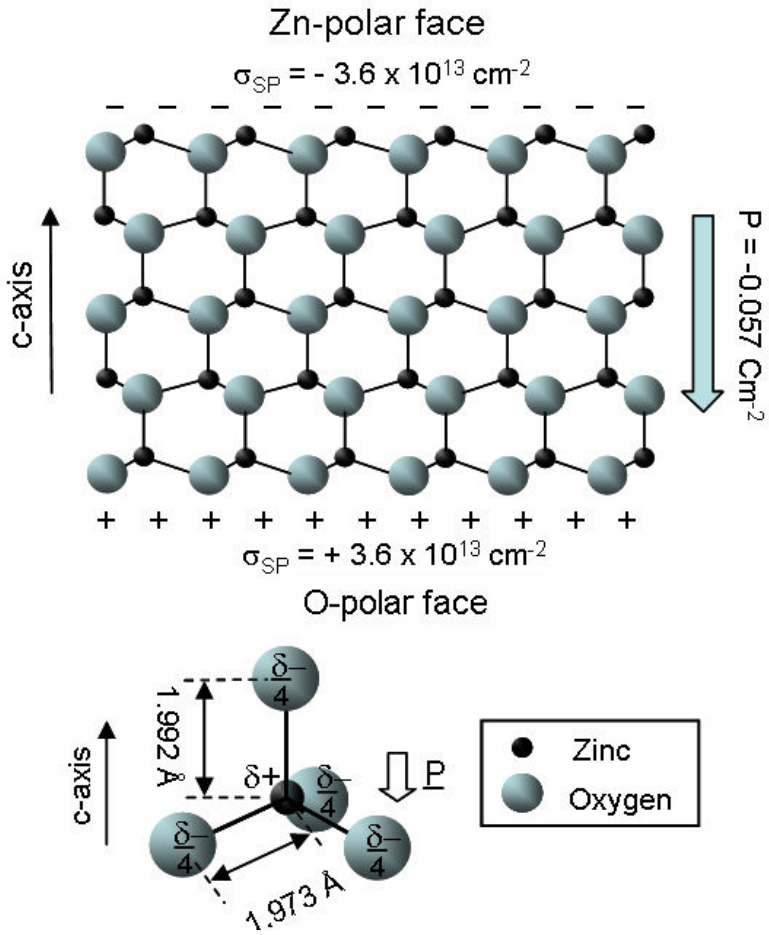

Figure 6.1: Spontaneous polarisation model showing the fixed 2-dimensional sheet charges induced on the Zn-polar and O-polar faces and the distortion of the ZnO_4 tetrahedron.

The theoretical spontaneous polarisation of ZnO, i.e. the polarisation at zero strain, has been theoretically calculated by Nann *et al.* [12] and Bernardini *et al.* [13] to be $\mathbf{P}_{SP}$ = -0.048 and -0.057 Cm^{-2} respectively. This is large compared to most binary semiconductors — for example, GaN (-0.029 Cm^{-2}), InN (-0.032 Cm^{-2}), SiC (-0.007 Cm^{-2} for 4H-SiC). Electrostatically, the spontaneous polarisation is equivalent to a fixed, two-dimensional, negative sheet carrier concentration of -3.6 x 10^{13} cm^{-2} (using the $\mathbf{P}_{SP}$ value of Bernardini *et al.)* at the Zn-polar face and a fixed positive sheet carrier concentration of the same magnitude at the O-polar face. The resulting internal electric field is given by,

$$\underline{E} = \frac{\underline{P}}{\varepsilon_0(\varepsilon_s - 1)} \tag{6.9}$$

which for ZnO is ~ 8 MVcm^{-1} [131]. Harris *et al.* [130] have modeled the implications of spontaneous polarization on the electrical properties of GaN and their analysis has been used here.

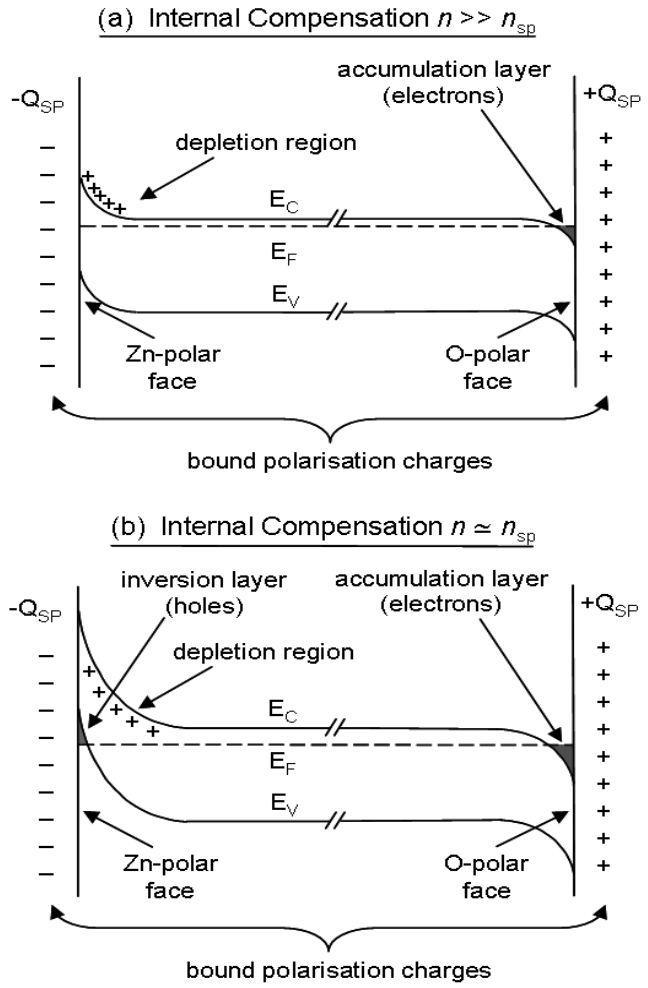

Figure 6.2: Near surface band bending on the Zn-polar and O-polar faces of *n*-type wurtzite ZnO in response to spontaneous polarisation induced, fixed surface charges for (a) high, and (b) low bulk carrier concentrations.

Figure 6.2 illustrates the effect of spontaneous polarisation on the energy bands of *n*-type ZnO. Free electrons will move in an attempt to compensate the fixed spontaneous polarisation charges $+Q_{SP}$, $-Q_{SP}$ and reduce the internal electric field. Electrons will accumulate near the O-polar face and a depletion region will form adjacent to the Zn-polar face. In ZnO material with a high free carrier concentration, the fixed spontaneous polarisation charges are efficiently screened and only a modest amount of surface band bending occurs, as shown in Figure 6.2(a). In the case of low free carrier concentration ZnO [Figure 6.2(b)], the number of ionised donors in the depletion region on the Zn-polar face will be insufficient to compensate the negative

spontaneous polarisation charge and the energy bands will bend strongly upward. If this bending is strong enough so that the Fermi level moves into the valence band, a sheet of holes will be generated in a "strong" inversion layer close to the Zn-polar surface.

Figure 6.3(a) shows the fraction of 'bulk carriers /fixed spontaneous polarisation charges' for 500 μm thick *n*-ZnO wafers with bulk carrier concentrations in the range $10^{13} - 10^{19}$ cm^{-3}. This shows that for 500 μm thick hydrothermal ZnO wafers, the number of bulk carriers is actually less than the theoretical number of fixed spontaneous polarisation charges, indicating the need for strong surface band bending. For 500 μm thick melt ZnO wafers, the number of bulk carriers is 1 – 3 orders of magnitude higher than the number of fixed spontaneous polarisation charges and so less surface band bending is required. Figure 6.3(b) shows the width of the depletion region at the Zn-polar face estimated using the theory of metal-oxide-semiconductor devices [22],

$$W_{depl} = \sqrt{\frac{2\varepsilon\varepsilon_o E_g}{qN_D}} \tag{6.10}$$

where E_g is the band gap (3.35 eV) and N_D is the effective doping density.

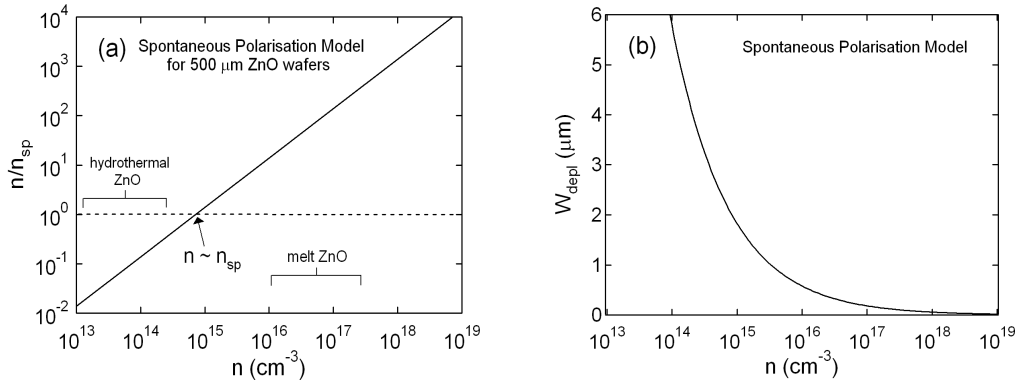

Figure 6.3: (a) Fraction of 'bulk carriers/fixed spontaneous polarisation charges' for 500 μm thick *n*-ZnO wafers with bulk carrier concentrations (*n*) in the range $10^{13} - 10^{19}$ cm^{-3}; and (b) width of the spontaneous polarisation induced, depletion layer at the Zn-polar face of *n*-ZnO versus bulk carrier concentration.

This analysis of the influence of the large spontaneous polarisation of ZnO neglects the role of external adsorbates in neutralising fixed spontaneous polarisation charges and represents an ideal case for atomically clean surfaces. It will almost certainly be an over estimate due to structural defects in the crystal structure and the hydroxyl termination of the

Zn-polar and O-polar surfaces. Despite this, the following general predictions follow from the spontaneous polarisation model for ZnO:

1) Spontaneous polarisation induced surface band bending will tend to increase the effective barrier height of Schottky contacts fabricated on the Zn-polar face and decrease those on the O-polar face. The Φ_B of Schottky contacts on a non-polar face should be unaffected.

2) An internal electric field will be created. The field will be directed along the c-axis towards the Zn-polar face and away from the O-polar face. This internal electric field may affect the optical properties of the polar ZnO surfaces, e.g. by separating photogenerated electron – hole pairs.

3) Spontaneous polarisation effects will be greater for ZnO material with low carrier concentration due to incomplete screening of the fixed surface charges at the Zn-polar and O-polar faces. For the same reason, compensating surface adsorbates may be more strongly attached to low carrier concentration ZnO material.

6.1.2 Ionic Model

In the ionic model, the ZnO crystal structure is considered to be formed from alternate double layers of oppositely charged Zn and O ions, stacked along the c-axis. This is illustrated in Figure 6.4. Each double layer has a dipole moment density $\mu = \sigma R_1$, where σ is the magnitude of the ionic sheet charge density on each layer, creating a total dipole moment density $\mathbf{M} = N\sigma R_1$ in the +c direction, where N is the number of double layers [132]. The associated electrostatic energy diverges with increasing N making the polar surfaces unstable [133]. As a result, ionic crystals generally facet or undergo dramatic surface reconstructions [134]. ZnO is somewhat unique, in that unreconstructed polar surfaces are very common in nature, suggesting some other form of stabilisation mechanism. Noguera [132] showed that the electrostatic instability can be lifted by a charge re-arrangement on the outer layers of the polar ZnO surfaces. Specifically the Zn-polar face needs to be made less positive and O-polar face less negative by an amount $\sigma R_2/(R_1 + R_2) \sim 0.75\sigma$, where R_1 and R_2 are defined in Figure 6.4. This can occur via three possible stabilisation mechanisms: (a) a fractional negative charge transfer from the O-polar to Zn-polar face, (b) reconstruction of the Zn-polar (O-polar) surface which removes ¼ of the Zn (O) atoms, or (c) a coverage of (½ monolayer) hydroxyl groups on both polar faces [135, 136].

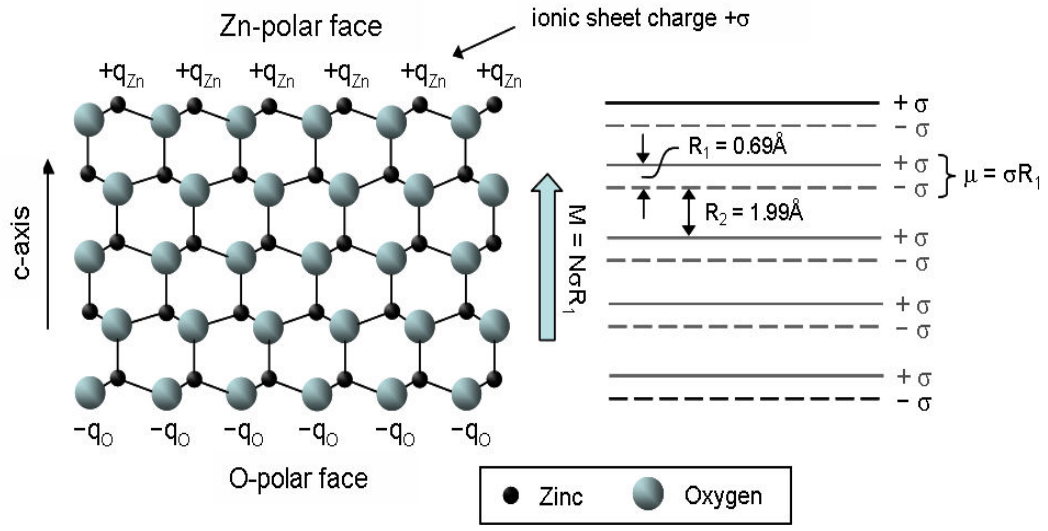

Figure 6.4: Ionic model describing the wurtzite ZnO structure a series of alternating double layers of oppositely charged Zn and O ions, with partial ionic charges of $+q_{Zn}$ and $-q_O$ respectively.

Mechanism (a) leads to the prediction of two-dimensional metallic-like surface states [137, 138] on the polar faces which have not been observed. Therefore, it appears that mechanisms (b) and (c) are more likely, although their relative contributions are still unknown. Dulub *et al.* [134] used scanning tunneling microscopy to reveal the presence of triangular shaped, single layer pits and islands, with O-terminated step edges, on the Zn-polar face of hydrothermally grown ZnO surfaces. In Chapter 3, similar triangular shaped features were seen in Figure 3.1, which showed an AFM image taken on the Zn-polar face of a hydrothermal, bulk ZnO wafer, from Tokyo Denpa Co. Ltd. However, XPS measurements also showed a hydroxide termination on the Zn-polar and O-polar faces (and m-plane face) of the same hydrothermal ZnO material and also on melt bulk ZnO.

There appears to be evidence in the literature of a competition between surface reconstruction and hydroxyl coverage on the Zn-polar and O-polar faces; Kresse *et al*. [135] used first-principles, density fluctuation calculations to show that the formation of large scale triangular reconstructions are energetically more favourable than isolated Zn vacancies on the Zn-polar ZnO surface. They also showed that the presence of OH groups lifts this reconstruction and stabilises an unreconstructed Zn-polar surface. Valtiner *et al.* [139] prepared and characterised hydroxide stabilised, unreconstructed single crystal Zn-polar ZnO surfaces by wet NaOH etching and also etching followed by thermal treatment in a humid oxygen atmosphere. Interestingly, the tetramethyl ammonium hydroxide (TMAH) developer, used in

the photolithographic Schottky contact fabrication technique in this thesis, is a hydroxide containing base. Kunat *et al.* [49, 140] used low energy electron diffraction (LEED) and He atom scattering (HAS) to show that the clean and hydrogen free O-polar ZnO surface was characterised by a (1 x 3) reconstruction with large scale oxygen vacancies, and that this was lifted by the presence of atomic hydrogen to form an unreconstructed H(1 x 1) adlayer. Staemmler *et al.* [141] also used the binding energy of a CO probe molecule to conclude that the O-polar ZnO surface is either H terminated or reconstructed.

The following key findings follow from the ionic model for ZnO:

1) Unreconstructed atomically clean Zn-polar [O-polar] ZnO surfaces are electrostatically unstable and will reconstruct with a loss of ~ 1/4 of the Zn [O] atoms from the outermost surface layer. These reconstructions are readily lifted by the hydroxylation of the surface.
2) The electric dipole associated with the ionic charge density of the Zn and O atomic planes is opposite to the direction to the spontaneous polarisation dipole.

6.1.3 Comparison of the Spontaneous Polarisation and Ionic Models

The spontaneous polarisation model predicts the presence of fixed negative [positive] two-dimensional sheet charges on the Zn-polar [O-polar] faces while the ionic model predicts fixed charges of the opposite sign on the same faces. The obvious question is whether the spontaneous polarisation of ZnO in some way compensates the electrostatic instability predicted by the ionic model. However, the spontaneous polarisation model only predicts a negative [positive] bound charge of 0.033|e| per surface atom at the Zn-polar [O-polar] face. Duffy [14] calculated the ionicity of the Zn–O bond to be 39% with a charge of 0.61|e| residing on the Zn atom, which makes any compensation provided by the spontaneous polarisation charges negligible. On face value, it doesn't appear that these models can both correctly predict the electrical and optical properties of the polar faces of ZnO. These properties are now reviewed.

6.2 ELECTRICAL SURFACE POLARITY EFFECTS

6.2.1 Enhanced Schottky Barriers on the Zn-polar Face

In Chapter 5, high quality metal oxide Schottky contacts, with ideality factors close to the image force controlled limit, were fabricated on the Zn-polar and O-polar faces of hydrothermal bulk ZnO (from Tokyo Denpa Co. Ltd.). The results are summarised in Table 6.1, which gives the image force corrected, homogeneous barrier height, Φ_B^{hom*}, and the barrier height, $\Phi_{B,C\text{-}V}$, determined from *C–V* measurements at frequencies from 5 – 20 kHz. A comparison of the results for both planar and vertical geometry diodes is provided for the silver oxide Schottky contacts, while the data for iridium oxide and platinum oxide were obtained from vertical geometry diodes only. For each metal oxide contact, Φ_B^{hom*} is consistently higher by 200 – 250 meV on the Zn-polar face compared to the O-polar face. Similarly, the value of $\Phi_{B,C\text{-}V}$ is also higher by 150 – 220 meV on the Zn-polar face. This polarity related effect is consistent with the spontaneous polarisation model which predicts an additional upwards [downwards] contribution to the band banding at the Schottky interface on the Zn-polar [O-polar] faces. The same model predicts that any polarity related effects will be greater for hydrothermal ZnO compared to melt ZnO, due to the 2 – 3 orders of magnitude lower carrier concentration of the former.

Figure 6.5(a) shows a comparison of the effective barrier height (Φ_B) versus ideality factor (η) plots for planar silver oxide Schottky diodes on the Zn-polar and O-polar faces of hydrothermal and melt grown bulk ZnO wafers. As expected, the polarity related difference in Φ_B is much smaller for the higher carrier concentration melt ZnO. However, the apparent similarity between the barrier heights of the silver oxide contacts on the O-polar face of both hydrothermal and melt ZnO is somewhat misleading. The image force lowering effect, which reduces the effective barrier height, is a function of carrier concentration; typically lowering Φ_B by ~ 20 meV for hydrothermal ZnO and by ~ 80 – 90 meV for melt ZnO. Figure 6.5(b) shows the Φ_B versus η data from Figure 6.5(a) corrected for the image force lowering effect, using Equations (2.20) and (2.21). This shows that the corrected Φ_B versus η plots for the Zn-polar and O-polar faces of melt ZnO now lie between those for hydrothermal ZnO, which is a more accurate reflection of the anticipated spontaneous polarisation-induced, band bending shown in Figure 6.2.

Furthermore, the image force corrected Φ_B versus η plots for planar silver oxide contacts on the non-polar faces of hydrothermal and melt ZnO, shown in Figure 6.5(c), are very similar. These plots represent the barrier height of silver oxide Schottky contacts on hydrothermal and melt ZnO in the absence of spontaneous polarisation effects. Significantly, these non-polar plots lie between those for the Zn-polar and O-polar faces of both the hydrothermal and melt

ZnO material [Figure 6.5(d)], which is again consistent with the spontaneous polarisation model. In the case of melt ZnO, the image force corrected Φ_B versus η plot for the non-polar (a-plane) face is close to the corresponding plot for the O-polar face [Figure 6.5(d)]. This is another anticipated effect: for high carrier concentration *n*-type material, the downward band bending on the O-polar face is expected to be small, as there are sufficient bulk carriers (i.e. free electrons) to compensate the fixed positive spontaneous polarisation charges. The upward band bending on the Zn-polar face is expected to be larger, due to the lack of intrinsic free holes to compensate the fixed negative spontaneous polarisation charges, leaving only incomplete screening provided by ionised donors [142].

In the case of hydrothermal ZnO, the image force corrected Φ_B versus η plot for the non-polar (m-plane) face lies approximately half way between the corresponding plots for the Zn-polar and O-polar faces [Figure 6.5(d)]. This difference can be explained by the fact that in hydrothermal ZnO, there is also a lack of free electrons to compensate the fixed positive spontaneous polarisation charges on the O-polar face, due to the much lower bulk carrier concentration of this material.

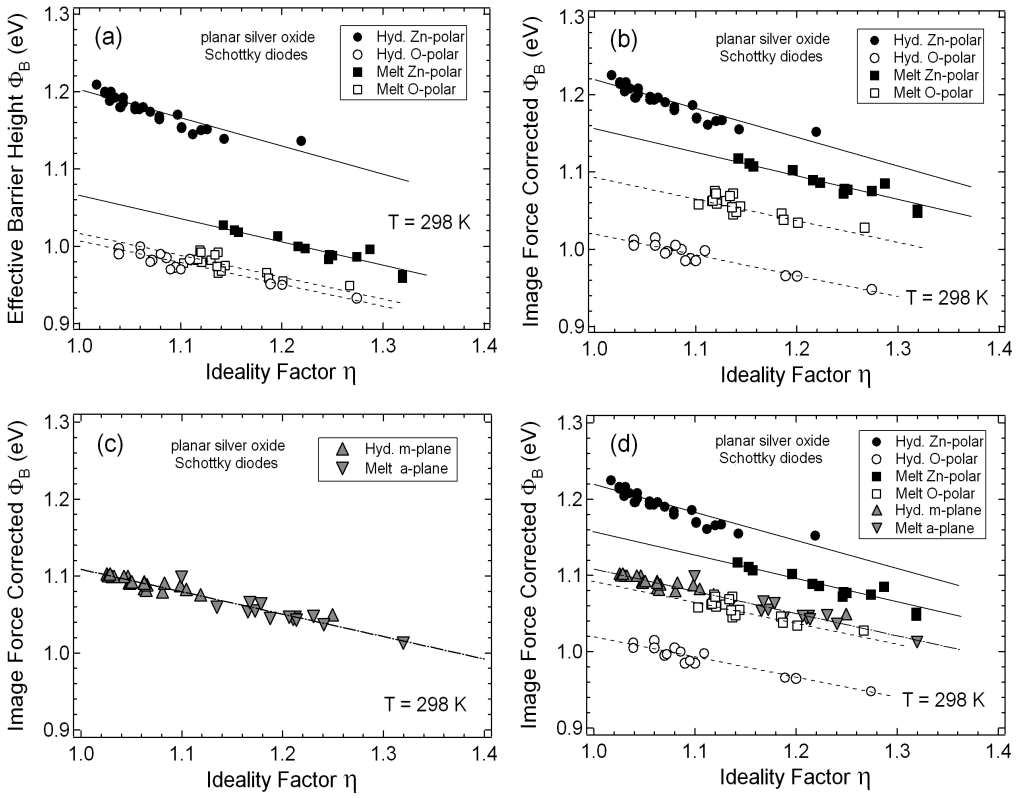

Figure 6.5: Comparison of surface polarity-related effects in the barrier heights of planar silver oxide Schottky diodes on hydrothermal and melt bulk ZnO: (a) effective barrier height Φ_B versus η; (b), (c), (d) image force corrected effective barrier height versus η.

Table 6.1: Comparisons of the image force corrected, homogeneous barrier height (Φ_B^{hom*}) and the barrier height determined from *C–V* measurements ($\Phi_{B,C\text{-}V}$) for planar and vertical geometry silver oxide Schottky diodes. The polarity, Zn-polar or O-polar, refers to the ZnO face on which the Schottky contact is fabricated.

Schottky Contact	Diode Polarity	Φ_B^{hom*} (eV)			$\Phi_{B,C\text{-}V}$ (eV)		
		Zn-polar	O-polar	Δ	Zn-polar	O-polar	Δ
Ag_xO	planar	1.23	1.03	0.20	1.19	1.04	0.15
	vertical	1.21	1.01	0.20	0.96	0.80	0.16
Ir_xO	vertical	1.16	0.91	0.25	0.78	0.56	0.22
PtxO	vertical	1.23	1.01	0.22	0.98	0.80	0.18

Schottky Contact	Diode Polarity	$(\Phi_B^{hom*} - \Phi_{B,C\text{-}V})$	
		Zn-polar	O-polar
Ag_xO	planar	0.04	-0.01
	vertical	0.25	0.21
Ir_xO	vertical	0.38	0.35
Pt_xO	vertical	0.26	0.21

Similar polarity-related effects in Schottky barrier height been reported for GaN which adopts a similar wurtzite structure to that of ZnO. Karrier *et al.* [142] observed that the mean barrier height of planar Pt Schottky diodes on MBE grown *n*-GaN films ($n = \sim 8 \times 10^{17}$ cm^{-3}) were 1.1 eV on the Ga-polar face, compared to 0.9 eV on the N-polar face. Jang *et al.* [143, 144] reported a similar effect, i.e. a 320 meV higher barrier height on the Ga-polar face, for planar Pt Schottky contacts on MOCVD grown *n*-GaN films ($n = 3 \times 10^{16} - 1 \times 10^{17}$ cm^{-3}). They also investigated the surface band bending of the GaN films using synchrotron radiation photoemission spectroscopy, observing a larger upwards band bending of 1.4 eV on the Ga-polar face, which they concluded was due to spontaneous polarisation effects.

6.2.2 $\Phi_{B,C\text{-}V}$ Deficit in Vertical Geometry Metal Oxide Schottky diodes

Another significant effect can be seen from a comparison of Φ_B^{hom*} versus $\Phi_{B,C\text{-}V}$ for planar and vertical silver geometry oxide diodes in Table 6.1. For planar geometry devices, Φ_B^{hom*} and $\Phi_{B,C\text{-}V}$ are almost the same, but for vertical geometry diodes there is a significant deficit in the value of $\Phi_{B,C\text{-}V}$. This deficit is similar, 250 meV and 210 meV respectively, on the Zn-polar and O-polar faces. Table 6.1 also shows almost identical deficits in the values of $\Phi_{B,C\text{-}V}$ compared to Φ_B^{hom*} for vertical geometry platinum oxide diodes and an even larger deficit 380 meV [350 meV] for vertical geometry iridium oxide diodes with the Schottky contact on the Zn-polar [O-polar] face.

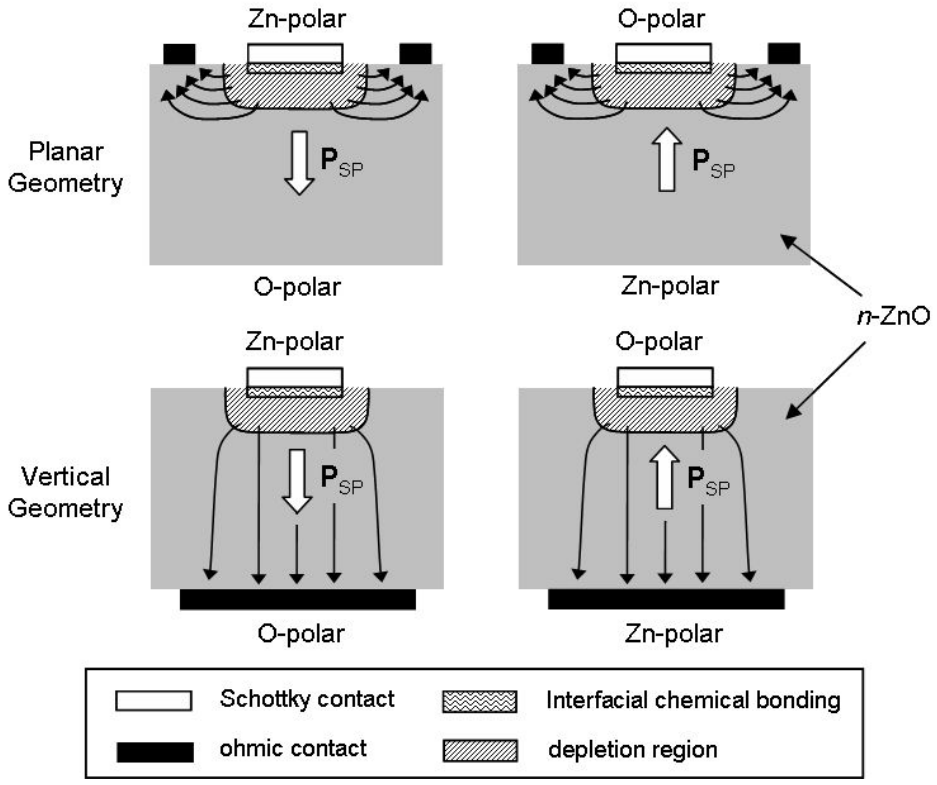

Figure 6.6: Comparison of the structure of planar and vertical geometry ZnO Schottky diodes with reference to (i) current flow, (ii) spontaneous polarisation dipole, and (iii) the chemical bond polarisation layer.

These deficits are examined with reference to Figure 6.6 which shows the direction of the current flow and the spontaneous polarisation dipole for planar and vertical geometry ZnO Schottky diodes. Φ_B^{hom*} is determined from *I–V* measurements which involve d.c. current flow between the Schottky and ohmic contacts, while $\Phi_{B,C\text{-}V}$ measurements involve the a.c. displacement current ($dE/dt = j\omega C$) which originates from changes in the width of the depletion region with an applied low frequency (ω) test voltage [28]. As already discussed, the

spontaneous polarisation dipole $\mathbf{P}_{SP}$ is the probable cause of the higher values of Φ_B^{hom*} and $\Phi_{B,C\text{-}V}$ for Schottky contacts on the Zn-polar face compared to the O-polar face. However, it is unlikely to be the cause of the difference between Φ_B^{hom*} and $\Phi_{B,C\text{-}V}$ for a vertical diode geometry, since the difference is a consistent deficit which does not change sign as the diode polarity changes.

A more probable cause of the $\Phi_{B,C\text{-}V}$ deficit is the interface dipole due to the polarisation of chemical bonds at the metal oxide – ZnO interface. Figure 6.7 shows the likely chemical bonding for metal oxide Schottky contacts on the Zn-polar and O-polar faces of ZnO. As discussed in Chapter 5, the Zn-polar and O-polar faces are both terminated by a persistent hydroxide layer. Successful Schottky contact formation is likely to involve the de-hydrogenisation of this hydroxide layer and the formation of an interfacial layer of metal – oxygen bonds on both the Zn-polar and O-polar faces. The polarisation of these metal – oxygen bonds creates an interface dipole μ_{CB} directed away from the ZnO surface, on both the Zn-polar and O-polar faces.

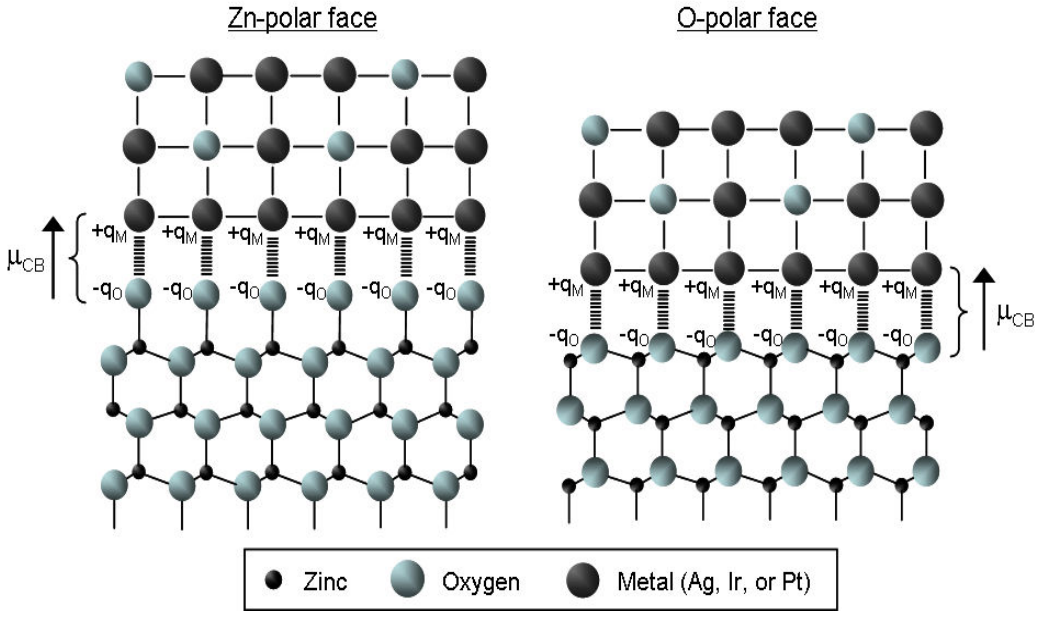

Figure 6.7: Electric dipoles due to polarised chemical bonds at the interface layers of metal oxide Schottky contacts on the Zn-polar and O-polar face of ZnO.

This interface dipole will cause a contribution to the barrier height of the Schottky contact which can be written as [148],

$$\Delta\Phi_{CB} = \frac{N_B \mu_{CB}}{\varepsilon_{int}\varepsilon_o} \tag{6.11}$$

where N_B is the interfacial bond density and $\mu_{CB} \sim q_M d_{MO}$ where d_{MO} is the separation of the metal and oxygen atoms at the interface. Since the dipole is localised at the interface, $\Delta\Phi_{CB}$ does not appear in $\Phi_{B,C\text{-}V}$ as it is only related to the band bending in the semiconductor. Futhermore, since the direction of μ_{CB} is the same on both the Zn-polar and O-polar faces, the sign of $\Delta\Phi_{CB}$ will also be the same. Figure 6.8 shows how such a chemical bonding-induced interface dipole could affect the band bending at the metal oxide – ZnO Schottky junction and cause the deficit in $\Phi_{B,C\text{-}V}$ compared to Φ_B^{hom*}.

Equation (6.11) can be used to estimate the size of μ_{CB}. Assuming N_B to be ~ 1/2 the atomic density on the polar ZnO face, $\varepsilon_{int} = \varepsilon_{ZnO}$, and $\Delta\Phi_{CB} = 0.25$ eV, then $\mu_{CB} \sim 1.1$ Debye (1 Debye = 3.34×10^{-28} Ccm). Although the presence of a chemical bonding-induced interface dipole may explain the $\Delta\Phi_{CB}$ deficit for vertical geometry diodes, it is still unclear why the deficit disappears when the diode geometry is planar. Another geometry related factor is the Schottky – ohmic contact separation, which is much larger for the vertical (500 μm) compared to the planar (25 μm) geometry diodes. However, this only seems to cause a small increase in the series resistance of the vertical diodes and is not expected to significantly affect the *C–V* measurements.

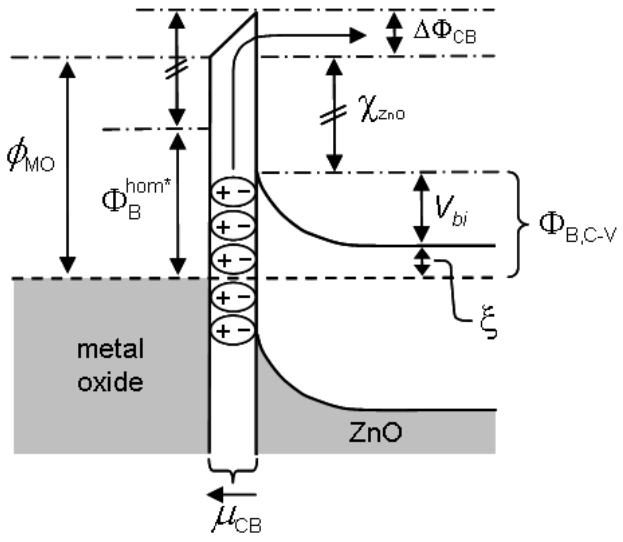

Figure 6.8: Band diagram of a metal oxide Schottky contact showing a dipole contribution, Φ_{CB}, due to metal – oxygen bonding at the interface and its effect on $\Phi_{B,C\text{-}V}$ compared to Φ_B^{hom*}.

Nakano *et al.* [88] observed a similar deficit of 200 meV in the '*C–V* determined' versus '*I–V* determined' barrier heights of PEDOT:PSS/ZnO Schottky contacts ($\eta = 1.2$) fabricated on the Zn-polar face of hydrothermal ZnO (from Tokyo Denpa Co. Ltd), using a vertical mesa geometry with Ti/Au ohmic contacts at the bottom of each mesa. This was attributed to an interface dipole layer between the Zn-polar surface and the anionic PSS molecules. In a subsequent comment to their work, Lin [145] derived a band diagram similar to Figure 6.8.

The use of thin interfacial films of polar molecules to modify the barrier height of metal contacts to organic semiconductors is well established [146]. For example, Hong *et al.* [147] used a very thin C_{60} buckminsterfullerene film to create an interfacial dipole layer to modify the energy barrier between an indium tin oxide contact and the N,N'-diphenyl-N,N'-bis (1,1'-biphenyl)-4,4'-diamine organic semiconductor. Nuesch *et al.* [148] grafted molecules with different dipole moments onto indium tin oxide contacts to tris-(8-hydroxylquinoline) aluminium (Alq) and showed that the resulting shift in barrier energy was related to the direction of the surface dipole.

6.3 OPTICAL SURFACE POLARITY EFFECTS

In addition to the structural and electrical polarity effects discussed so far, a number of significant optical surface polarity related effects were observed in the 4 K photoluminescence (PL) spectra and room temperature reflectance spectra of hydrothermal ZnO. The results are presented here and discussed in terms of the spontaneous polarisation model.

6.3.1 4 K Photoluminescence Spectra

A systematic study was carried out into the influence of surface polarity on the PL of unintentionally doped hydrothermal and melt ZnO [149]. Three double-sided polished, c-axis wafers, which will be referred to as A1, A2, and A3, were cut to provide Zn-polar and O-polar samples from each wafer. These were also compared with samples from the Zn-polar and O-polar faces of melt grown, c-axis wafers from Cermet Inc. All wafers were 10 mm x 10 mm x 500 μm. The carrier concentration of the hydrothermal wafers were ~ 3×10^{14} cm^{-3} compared to $(3 - 7) \times 10^{16}$ cm^{-3} for the melt wafers.

PL spectra were measured at 4 K and a vacuum pressure of ~ 1 mTorr, using a liquid helium cooled, cold finger cryostat and the 325 nm line of a He-Cd laser. The penetration depth of the He-Cd laser is approximately 40 nm. The measurements were performed by doctoral student Paul Miller in the Department of Physics and Astronomy, University of Canterbury,

N.Z. Figure 6.9(a) shows a comparison of non-normalised PL from the Zn-polar and O-polar faces of wafer A1, using the same laser excitation intensity (30 mW) on both faces.

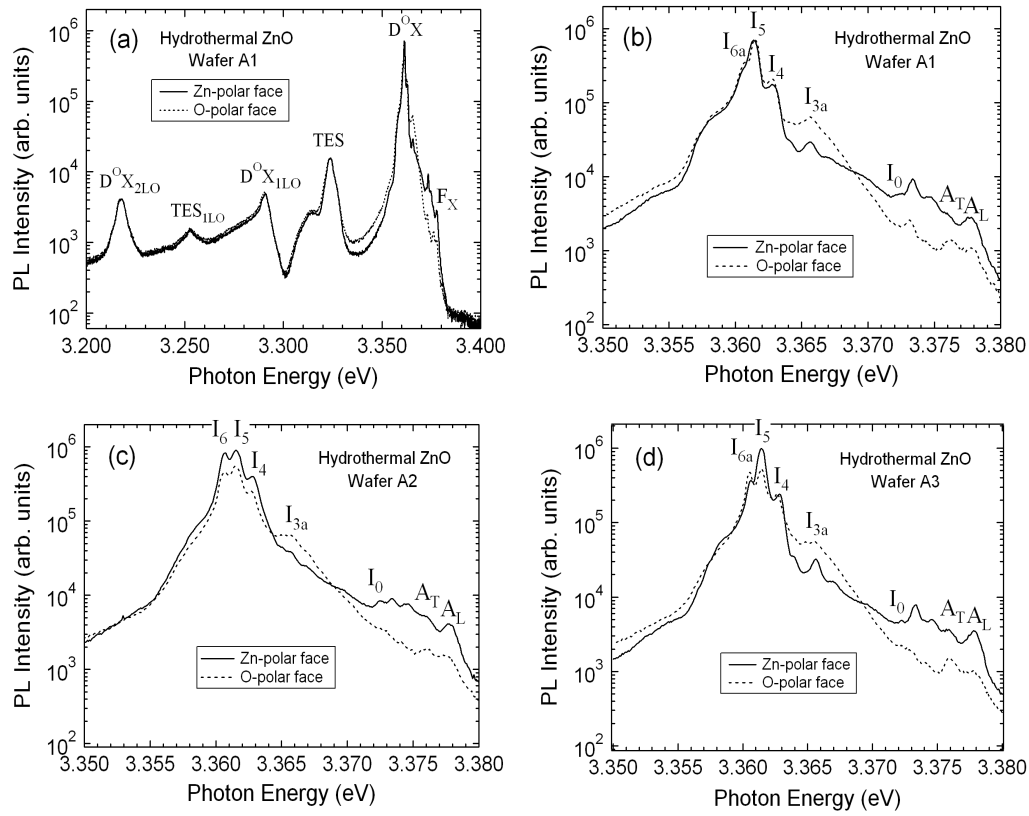

Figure 6.9: Non-normalised, 4 K photoluminescence spectra taken from the Zn-polar and O-polar faces of unintentionally doped hydrothermal, bulk, c-axis ZnO wafers.

The dominant emission is from neutral donor bound excitons (denoted D^OX) between 3.3600 – 3.3628 eV, their two-electron satellites (TES), and longitudinal phonon replicas (energy separation ~ 72 meV). The PL from the two polar faces was very similar except for specific regions on either side of the D^OX emission. Figure 6.9(b) shows the bound and free exciton PL of wafer A1 in more detail, with the most prominent features labeled using the line positions published by Meyer *et al.* [150]. Figures 6.9(c) and (d) show the corresponding PL spectra of wafers A2 and A3.

The dominant emissions in Figure 6.9(b), (c) and (d) are from neutral donor bound excitons I_6 (3.3608 eV), I_5 (3.3614), and I_4 (3.3628 eV). I_6 and I_4 are due to Al and H donor impurities respectively, while I_5 is as yet unassigned [150]. The relative strength of these emissions varies between wafers, perhaps due to variations in impurity concentration. More significantly, several consistent polarity dependent differences can be seen between 3.3640 eV and the band edge. In particular, emissions from both longitudinal and transverse free A–excitons, A_T (3.3759 eV) and A_L (3.3772 eV), are significantly stronger from the Zn-polar

face, as are emissions from a triplet of recombination lines between 3.3725 and 3.3750 eV. The low binding energy line of this triplet is very close to I_0 (3.3725 eV). In a recent publication, Meyer *et al*. [151] unambiguously (from magneto-optical behaviour) assigned I_0 to an ionised donor bound exciton related to the I_6/I_{6a} (neutral Al donor) line. In Figures 6.9 (b), (c) and (d), there appears to be a correlation between the shape of the I_6, I_5, and I_4 lines and the shape of this triplet (this is even more apparent in 4 K PL spectra taken on hydrothermal wafers annealed at 400 ^oC in O_2 , not shown here). Therefore it is reasonable to assign the whole of the triplet between 3.3725 and 3.3750 eV as ionised donor bound exciton replicas of the neutral donor bound I_6, I_5, and I_4 lines.

The presence of an increased number of ionised donors near the Zn-polar face is consistent with the spontaneous polarisation model (Figure 6.2), which requires extra positive charge from ionised donors to compensate the fixed, negative, spontaneous polarization charge on the Zn-polar face. The spontaneous polarisation model also predicts an inversion layer near the Zn-polar face of 'low carrier concentration' ZnO and it is tempting to suppose that this is the cause of the increased free exciton PL emission from the Zn-polar face of hydrothermal ZnO. Such an inversion layer is expected to contain a high density of holes which could form extra free excitons with electrons generated by the HeCd laser. However, this is much more speculative as no direct evidence of free holes near the Zn-polar surface has been found by variable field Hall effect measurements or by any other technique. Furthermore, since the PL measurements were carried out in medium vacuum conditions (~ 1 mbar), the ZnO surface (both Zn- and O-polar) will be hydroxyl terminated (Chapter 3) which will cause the near surface band bending to deviate from that predicted by the spontaneous polarisation model (Figure 6.2). In addition, it is not known whether atmospheric adsorbates (such as O_2 and H_2O) will be present at this pressure to further affect the near surface band bending.

Conversely, PL emission between 3.3640 and 3.3680 eV is significantly more intense on the O-polar face. Sasaki *et al.* [152] also reported increased emission from the O-polar face of hydrothermal, bulk ZnO over a similar range. No definite assignment has yet been made for emissions, such as the I_{3a} line, that occur in this range. According to the spontaneous polarisation model, increased emission from the O-polar face could be due to excitons bound to ionised acceptors as these would help compensate the fixed positive charge expected on the O-polar face.

Figure 6.10 shows the PL from the Zn-polar and O-polar faces of melt ZnO wafers. These spectra have much weaker I_5 and I_4 lines and the appearance of donor bound emissions I_9 (3.3567 eV) and I_8 (3.3598 eV) which are assigned to In and Ga, respectively [150]. The strong polarity related effects observed in the hydrothermal wafers are either absent or much

smaller here. This is again consistent with the spontaneous polarisation model, which predicts smaller polarity related effects for higher carrier concentration ZnO material.

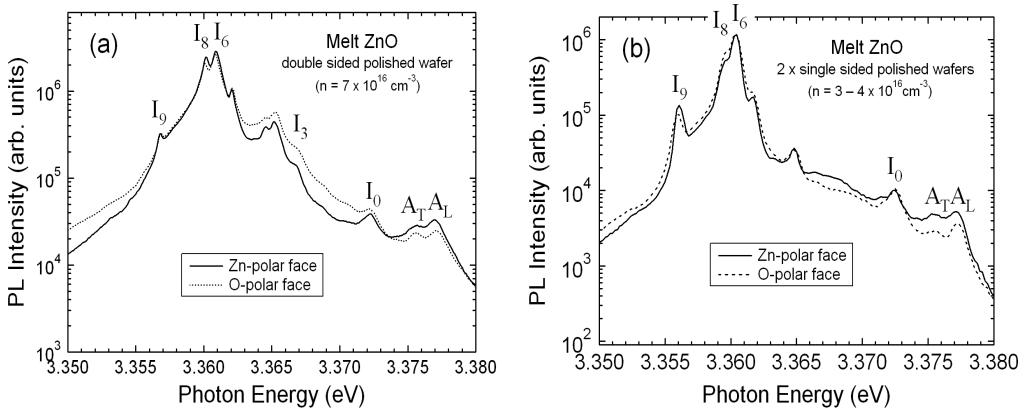

Figure 6.10: Non-normalised, 4 K photoluminescence spectra taken from the Zn-polar and O-polar faces of an unintentionally doped melt, bulk, c-axis ZnO wafer.

6.3.2 Reflectivity Spectra

Room temperature reflectivity spectra were measured, in atmospheric conditions, on Zn-polar and O-polar samples cut from the same double-sided polished hydrothermal, bulk, c-axis ZnO wafer, and compared to measurements made on the Zn-polar and O-polar faces of similar melt, single-sided polished, bulk, c-axis ZnO wafers. The measurements were made by doctoral student Martin Henseler in the Department of Physics and Astronomy, University of Canterbury, N.Z., using a 300 W Cermex UV Xenon-arc lamp and a Spec500 monochrometer. The Zn-polar and O-polar face samples were mounted together and alongside a silver reference mirror in a 45 degree geometry, reflecting the incoming light (modulated using a chopper wheel) into a vertically mounted Si-diode detector equipped with a lock-in amplifier. The reflectivity spectra are shown in Figure 6.11. A significant surface polarity effect was observed for hydrothermal ZnO, in that the reflectivity of the O-polar face at photon energies below ~ 3.15 eV was significantly higher than that of the Zn-polar face. This same effect was not apparent in melt ZnO where the reflectivity spectra from the Zn-polar and O-polar faces were very similar. The fact that the polarity effect was only observed in the low carrier concentration, hydrothermal material suggests a possible spontaneous polarisation origin. It could be argued that the electron accumulation layer predicted by the spontaneous polarisation model on the O-polar face would be more reflective than the inversion region / depletion layer predicted for the Zn-polar face. However, this is speculative especially due to the fact that the measurements were performed in atmospheric conditions in which the ZnO surface is likely to be affected by atmospheric adsorbates.

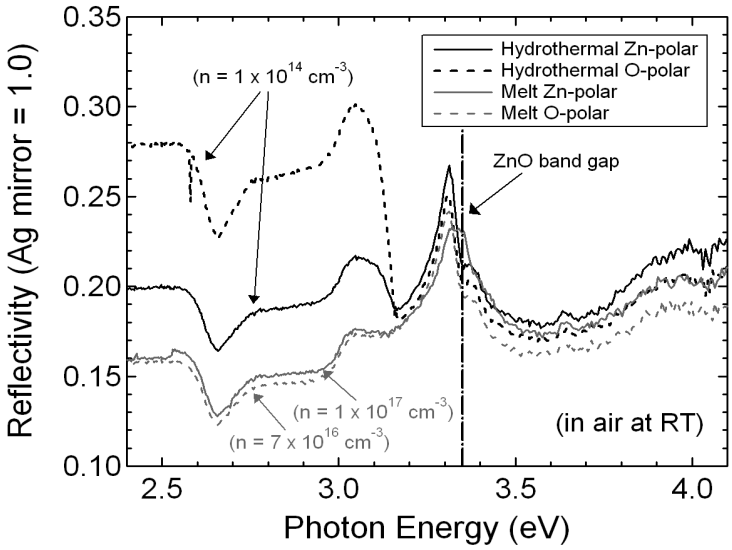

Figure 6.11: Reflectivity spectra measured, at room temperature, from the Zn-polar and O-polar faces of hydrothermal and melt, bulk, c-axis ZnO wafers.

6.4 SURFACE KELVIN PROBE MICROSCOPY (SKPM)

Surface Kelvin probe microscopy was used to determine the work function of the Zn-polar and O-polar surfaces of the same hydrothermal, bulk, c-axis ZnO wafer ($n = 1 \times 10^{14}$ cm^{-3}). These measurements were made using a Digital Instruments 3100 Atomic Force Microscope, in dark conditions (with the exception of scattered light from the red AFM laser), at room temperature, and with the samples exposed to air.

SKPM is used to image the surface contact potential V_S between a conducting AFM cantilever tip (in this case Au coated silicon) and the sample being studied. V_S is defined as,

$$V_S = (\phi_{Au} - \phi_{ZnO}) / q \tag{6.12}$$

where ϕ_{Au} (5.10eV) and ϕ_{ZnO} (to be determined) are the work functions of the cantilever tip and the ZnO surface respectively. A topographic trace is first obtained with the cantilever tip in tapping AFM mode. The cantilever tip is then retraced in feedback mode at a constant height above the sample surface with which it forms a capacitor. During this retrace, a d.c. and a.c. bias voltage $V_{bias} = V_{dc} + V_{ac} \sin\omega_o t$, is applied to the sample, where ω_o is the resonant frequency of the cantilever. The cantilever is grounded and the a.c. voltage causes it to oscillate at the resonant frequency ω_o and the second harmonic $2\omega_o$. The force at ω_o is given by,

$$F(\omega_o) = -\frac{dC}{dz}[(|V_{dc}| - V_s)V_{ac}sin\omega_o t] \quad (6.13)$$

where C is the capacitance between the cantilever tip and the sample, and z is the tip – surface separation. The d.c. voltage is automatically adjusted and recorded, so as to minimise the oscillation of the cantilever. Provided z is held constant, this directly measures the surface contact potential V_S.

In practice, there is a constant system dependent offset potential, ϕ_{offset}, which can be determined by measuring V_S on a clean Au calibration sample. In this case Equation (6.12) becomes,

$$V_S = (\phi_{Au} - \phi_{ZnO} + \phi_{offset})/q \quad (6.14)$$

which can be rearranged to give the work function of the ZnO surface,

$$\phi_{ZnO} = (\phi_{Au} - qV_s + \phi_{offset}) \ . \quad (6.15)$$

The surface band bending ($\Delta\phi$) at the ZnO surface can be calculated using,

$$\Delta\phi = (\phi_{ZnO} - \chi_{ZnO} - \xi) \quad (6.16)$$

where χ_{ZnO} is the electron affinity (~ 4.25 eV for ZnO) and ξ is the energy difference between the Fermi level and the conduction band minimum, which was ~ 0.27 eV for the hydrothermal wafer investigated.

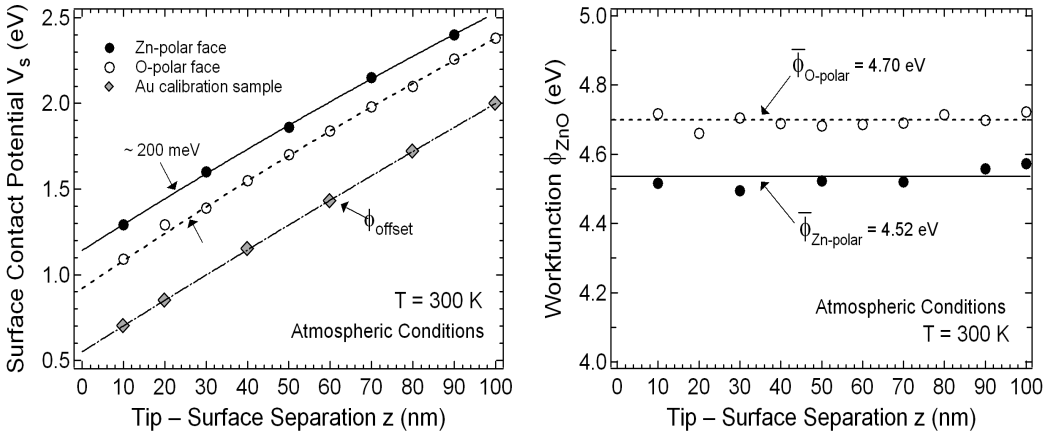

Figure 6.12: (a) Surface contact potentials at different 'cantilever tip – sample surface' separations (z) measured using SKPM, in atmospheric conditions, on the Zn-polar and O-polar faces of the same double-sided polished, hydrothermal c-axis, bulk ZnO wafer (n = 1 x 10^{14} cm^{-3}); and (b) calculated work functions for the Zn-polar and O-polar faces of the same hydrothermal wafer assuming a work function of 5.10 eV for a Au calibration sample.

Figure 6.12(a) shows the surface contact potential V_S measured from SKPM images on the Zn-polar and O-polar faces of the hydrothermal, bulk, c-axis ZnO wafer for a range of cantilever tip – surface separations, z. The SKPM images were all uniform with no discernible features. Figure 6.12(a) also shows the offset potential ϕ_{offset} from a thermally evaporated Au calibration sample, which was imaged before and after the ZnO measurements. Equation (6.15) was used to calculate the work function of the Zn-polar and O-polar surface for each z and this is shown in Figure 6.12(b). The mean work function was 4.52 [4.70] eV on the Zn-polar [O-polar] surfaces with little dependence on z. These work function values lie in between those published by Moormann *et al.* [57] using the vibrating gold wire (Kelvin) method on the Zn-polar (4.25 eV) and O-polar (4.95 eV) faces of ultra high vacuum cleaved, hexagonal vapour phase grown ZnO crystals. The same authors published a value of 4.64 eV for the m-plane face. The work function measured on the Zn-polar face is significantly lower than that on the O-polar face.

A similar hydrothermal wafer was also sent to collaborators at Tel-Aviv University, Israel who used SKPM measurements in a nitrogen atmosphere to determine a similar 200 meV difference in work function between the Zn-polar (4.12 eV) and O-polar (4.32 eV) faces. The difference in the work function values for the Zn-polar and O-polar faces of hydrothermal ZnO measured here and at Tel-Aviv University may be a result of the different ambients used or due to a systematic error in the offset correction. Chevtchenko *et al*. [154] used SKPM to determine a work function difference of 110 meV between the Zn-polar and O-polar faces on melt ZnO ($n = 4.5 \times 10^{16}$ cm^{-3}) from Cermet Inc., but interestingly they reported a higher work function on the Zn-polar face compared to the O-polar face.

A lower work function on the Zn-polar face is consistent with the lower Pauling electronegativity of zinc (1.65) compared to oxygen (3.44), but also indicates stronger downward band bending on the Zn-polar face which is not consistent with the predictions of the spontaneous polarisation model. However, it is consistent with the valence band XPS measurements described in Chapter 3 and analysed further here.

6.5 VALENCE BAND XPS MEASUREMENTS

In Chapter 3, a polarity effect was observed in the valence band maximum (VBM) – Fermi level (E_F) separations determined by XPS measurements at a pressure of 1×10^{-8} mbar. Table 6.2 provides a summary of the valence band XPS measurements for hydrothermal and melt ZnO. The VBM – E_F separation was systematically larger on the Zn-polar face compared to the O-polar face. This is equivalent to ~ 190 [120] meV stronger downward band bending on the Zn-polar face relative to the O-polar face for hydrothermal [melt] ZnO. The stronger downward band bending on the Zn-polar face is opposite to that predicted by the spontaneous

polarisation model (Figure 6.2), however it is important to remember that this model is based on the assumption of atomically clean, adsorbate free surfaces, whereas it has been established (Chapter 3) that both the Zn-polar and O-polar faces are terminated by a hydroxide layer which is not fully detached under high vacuum conditions. The presence of a stronger accumulation layer on the Zn-polar face is also contrary to the significantly higher barrier heights achieved for metal oxide Schottky contacts on the Zn-polar face compared to the O-polar face. However, as discussed in Chpater 4, it is likely that the hydroxide termination is removed in the formation of high quality Schottky contacts to ZnO.

Table 6.2: Valence band maximum (VBM) – Fermi level (E_F) separations determined from valence band XPS spectra and downward (negative) surface band bending assuming a ZnO band gap of 3.35 eV (at RT) for hydrothermal and melt bulk ZnO. CBM – Fermi level energy differences of 0.27 eV and 0.11 eV were assumed for the hydrothermal and melt ZnO material respectively.

ZnO Bulk Material	Surface Polarity	VBM – E_F (eV)	surface band bending (eV)
Hydrothermal	Zn -polar	3.69	- 0.61
	O - polar	3.50	- 0.42
	m-plane	3.60	-0.52
Melt	Zn -polar	3.60	- 0.36
	O - polar	3.48	- 0.24

Another significant surface polarity related effect occurs in the valence band XPS spectra of hydrothermal and melt ZnO, shown in Figure 6.13. The dominant emission in the valence band region is from peaks I (4.9 eV) and II (7.8 eV). The relative intensity of peaks I and II varies as a function of surface polarity. For valence band emission from the Zn-polar face, peak I is significantly more intense than peak II, while for the O-polar face peak II is marginally higher than peak I. Furthermore, the size of this polarity effect is very similar for hydrothermal and melt ZnO, which suggests that it may not be related to the spontaneous polarisation of ZnO. Significantly, the effect almost completely vanishes when the take-off angle of the analysed x-rays is changed from 90^o to 30^o with respect to the surface plane. X-rays with take-off angles of 30^o originate from a near surface region approximately half as deep as that for 90^o x-rays although, in this case, it may be more significant that the 90^o x-rays are emitted parallel to any surface electric fields generated by either spontaneous polarisation, ionic, or chemical bonding dipoles. An almost identical effect was reported by Veal *et al.* [153] for the In-polar (0001) and N-polar ($000\bar{1}$) faces of wurtzite InN grown by molecular beam epitaxy.

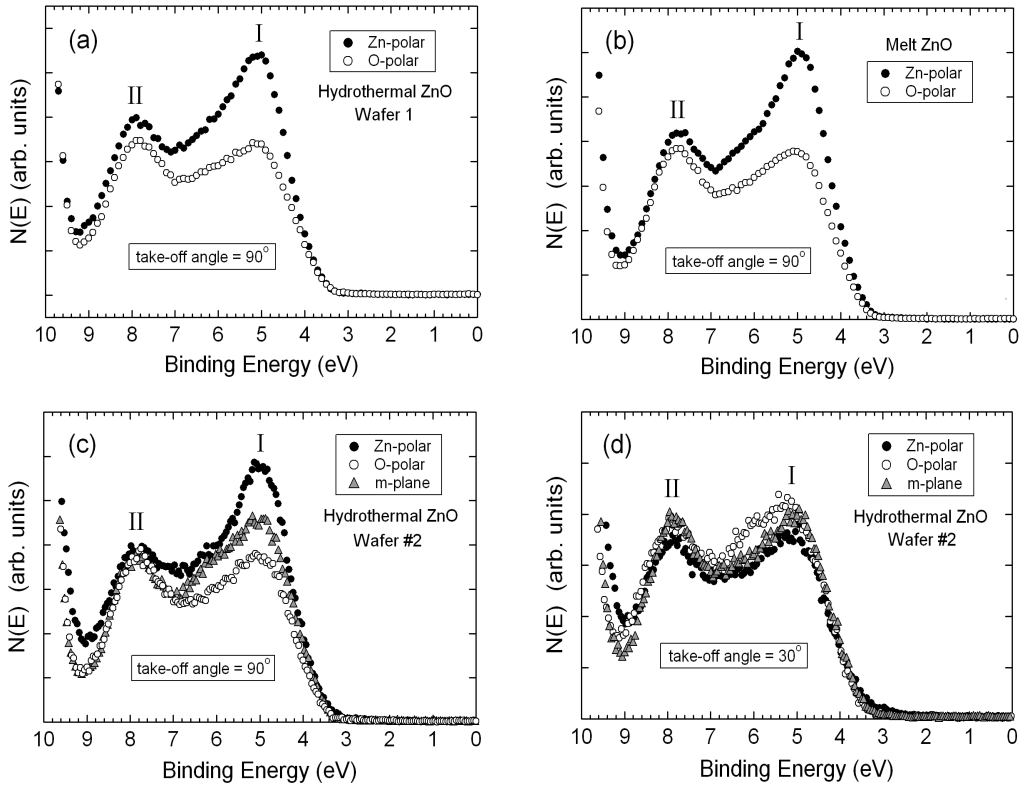

Figure 6.13: Valence band XPS spectra of the Zn-polar, O-polar, and m-plane faces of hydrothermal and melt bulk ZnO wafers. Spectra (a), (b), and (c) were obtained from photoelectrons with a 90^{o} take-off angle with respect to the surface while spectra (d) was obtained room photoelectrons with a 30^{o} take-off angle.

6.6 SUMMARY

Significant surface polarity effects appear to be commonplace in the structural, electrical, and optical properties of ZnO, particularly in the case of hydrothermal material as a consequence of its low bulk carrier concentration. On first impression, the polarity effects observed in Schottky contact barrier height and 4 K photoluminescence measurements appear to be in good agreement with the predictions of the spontaneous polarisation model, while other effects in surface morphology (from AFM), work function (from SKPM), and valence band maximum – Fermi level separation (from VBXPS) appear to be more difficult to explain using the same model. However, any comparison of these effects needs to be done with reference to the surface sensitivity of the measurement technique and also the surface conditions involved, particularly with regard to the presence or absence of surface adsorbates. Heiland and Kunstmann [11], as early as 1969, showed that depletion and accumulation layers could be induced on the Zn-polar and O-polar surfaces of vapour phase bulk ZnO crystals by

the adsorption of molecular oxygen and atomic hydrogen respectively. In Chapter 5, it was shown that a surface conduction layer could be activated when planar silver oxide Schottky diodes were taken from atmospheric to high vacuum conditions.

In light of this, the polarity effects observed in hydrothermal ZnO are summarised in Table 6.3 with particular emphasis on sampling depth and surface conditions.

Table 6.3: Summary of polarity-related effects observed between the Zn-polar and O-polar faces of hydrothermal, bulk, c-axis ZnO wafers.

Measurement	Surface Sensitivity	Surface Conditions	Observed Polarity Effect	Proposed Explanation
Schottky contact barrier height from *I-V* and *C-V* measurements	depletion region ~ 1 μm	atmospheric conditions but surface underneath Schottky contact expected to be hydroxide free	~ 200 meV higher image-force-corrected homogeneous barrier heights on the Zn-polar face	additional surface band bending due to spontaneous polarisation induced dipole
4K PL (Photoluminescence)	~ 40 nm	medium vacuum, ~ 1 mbar, presence of surface hydroxide termination, and possible presence of atmospheric adsorbates	significantly higher PL emission from free excitons and excitons bound to positively ionised donor impurities on the Zn-polar face.	presence of inversion layer and depletion region in response to fixed negative spontaneous polarisation charges on Zn-polar face.
Scanning Kelvin Probe Microscopy (SKPM)	immediate surface plane	atmospheric conditions, i.e. hydroxide termination + H_2O and O_2 atmospheric adsorbates.	work function ~ 200 meV lower on Zn-polar face compared to O-polar face.	lower electronegativity of Zn-polar surface due to fixed negative spontaneous polarisation charges
Valance band x-ray photoemission spectroscopy (VBXPS)	0.5 – 5 nm	high vacuum, ~10^{-8} mbar, presence of surface hydroxide termination but removal of atmospheric adsorbates	accumulation layers on Zn-polar and O-polar face, downward band bending ~ 200 meV stronger on Zn-polar face.	heavier hydroxide induced accumulation layer on Zn-polar face?

Chapter 7

Oxygen Vacancy Model

In this Chapter, the influence of oxygen vacancies on the formation of ZnO Schottky contacts is investigated. A defect model of Schottky barrier formation is proposed, in which the density of oxygen vacancies near the Schottky interface determines the degree of Fermi level pinning of the resulting Schottky contact. The Fermi level of a Schottky contact with a high density of interfacial oxygen vacancies (V_O) is likely to be pinned close to the V_O (+2, 0) defect level, at approximately 0.7 eV below the conduction band minimum. This may explain why the majority of reported ZnO Schottky barrier heights have been in the 0.6 – 0.8 eV range, regardless of the Schottky metal used [5, 8, 176].

7.1 INTRODUCTION

In Chapter 3, oxygen core-level and valence band XPS measurements showed that, in high vacuum conditions similar to those used in Schottky contact fabrication, the Zn-polar, O-polar, and m-plane faces of hydrothermal and melt ZnO are chemically terminated with a hydroxide layer, and at the same time are electrically characterised by an electron accumulation layer, which is strongest on the Zn-polar face. The removal of this hydroxide termination / accumulation layer is mandatory for Schottky barrier formation. Several theoretical and experimental studies have indicated that de-hydrogenation of the Zn-polar [O-polar] surface causes large scale reconstructions with the formation of a significant number of Zn [O] vacancies [40, 48]. Oxygen vacancies are also likely to be created by the deposition of metals onto the ZnO surface via metal oxidation reactions.

The creation of oxygen vacancies is thought to play an important role in the fabrication of ohmic contacts to ZnO, for which the readily oxidised metals Ti [155] and Al [156] are commonly used. Kim *et al.* observed the formation of TiO, using XPS and XRD spectroscopy, in low resistance Ti/Al ohmic contacts, whose excellent ohmic properties were attributed to the creation of oxygen vacancies which caused a local increase in carrier concentration at the contact interface [155]. Although most Schottky contacts are made with noble metals of low reactivity, the observed improvement in metal Schottky contact performance with age and

annealing (especially in oxygen ambients) suggests that chemical reactions at the Schottky interface may play an important role. Schaeffer *et al.* [158] reported that the effective work function of platinum on hafnium dioxide (HfO_2) can be reversibly modified by annealing in oxygen deficient or oxygen rich conditions, which is thought to be due to the creation or annihilation of interfacial oxygen vacancies. Robertson *et al.* [159] argued that the creation of positively charged oxygen vacancies were responsible for pinning of the effective Fermi level of high work function metals in HfO_2 – metal gate contacts to Si FETs. The question here is whether a similar model can be applied to formation of Schottky contacts to ZnO.

7.2 OXYGEN VACANCY EXPERIMENT

As with any investigation into Schottky barrier formation, a useful starting point is the fabrication of a range of high work function metal contacts, preferably using the same deposition technique, onto the same semiconductor surface. In this experiment, Ni, Ir, Pd, and Pt Schottky contacts were fabricated by electron beam evaporation on the Zn-polar face of hydrothermal ZnO. The potential reactivity of these contact metals towards ZnO can be gauged from their metal oxide formation energy. Figure 7.1 shows the experimental free energy of metal oxide formation per oxygen atom (at 298 K) versus the metal work function for a number of common contact metals to ZnO [159]. (Note the low oxide formation energy for Ti and Al which are used in ohmic contacts to ZnO).

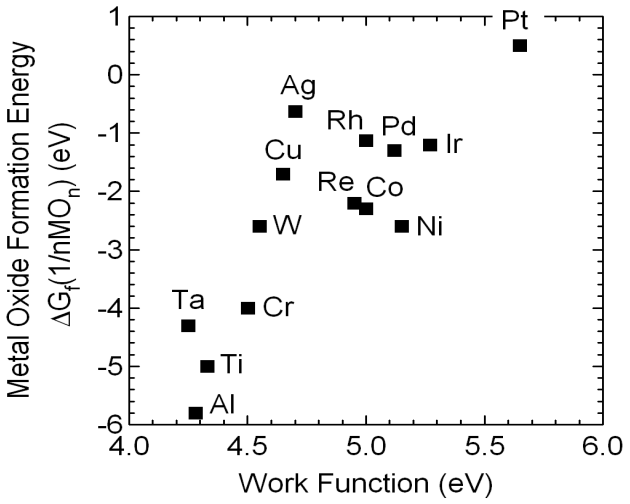

Figure 7.1: Standard free energy of metal oxide formation per oxygen atom versus metal work function for common contact metals to ZnO.

7.2.1 Schottky Contact Fabrication

Arrays of planar Ni, Ir, Pt, and silver oxide Schottky diodes were fabricated on the Zn-polar surface of a single hydrothermal, bulk, c-axis ZnO wafer (from Tokyo Denpa Co. Ltd). The room temperature carrier concentration (n) and mobility of this wafer were 1 x 10^{13} cm^{-3} and 210 cm^2 V^{-1} s^{-1} respectively, from single field 0.51 T Hall effect measurements, using the van der Pauw technique. A separate array of planar Pd Schottky diodes was fabricated on the Zn-polar face of a similar hydrothermal wafer (n = 3 x 10^{14} cm^{-3}) from the same manufacturer.

The Schottky contact fabrication technique was similar to that used for the metal Schottky contacts in Chapter 4: prior to contact deposition the as-received wafers were cleaned in ultrasonically agitated acetone followed by rinses in methanol and isopropyl alcohol. The cleaned Zn-polar ZnO surface was photolithographically patterned with circular contacts of diameter 300 μm. These were developed using tetramethyl ammonium hydroxide, rinsed in de-ionised water, and dried using N_2 gas. The Ni, Ir, Pd, and Pt Schottky contacts were deposited by electron beam evaporation in a vacuum chamber at a base pressure of 10^{-5} mbar. The silver oxide Schottky contacts were deposited using the reactive r.f. sputtering technique described in Chapter 5 – with an r.f. power of 50 W r.m.s., Ar/O_2 gas flow rates of 10.00 sccm and 1.70 sccm respectively, and a processing pressure of 4 x 10^{-3} mbar. Annular Ti/Al/Pt Ohmic contacts (50/100/30 nm) were fabricated around each Schottky contact at a separation of 25 μm, using e-beam evaporation.

7.2.2 *I–V* and *C–V* Characterisation

Figure 7.2(a) shows the typical *I–V* characteristics for the Ni, Ir, Pt, and silver oxide Schottky diodes, obtained in dark conditions and at room temperature (RT). A clear progression in rectifying behaviour was observed, from the Ni diodes which were ohmic in nature through to the silver oxide diodes which had greater than 7 orders of magnitude rectification at ± 2 V. Figure 7.2(c) shows the typical *I–V* characteristics for the Pd Schottky diodes, which had similar rectifying behaviour to the Ir diodes in Figure 7.2(a). The typical *C–V* characteristics of the Pt and silver oxide diodes, measured at a frequency of 20 kHz, are shown in Figure 7.2(b) and the corresponding *C–V* characteristics of the Pd diodes are shown in Figure 7.2(d). The *I–V* characteristics were used to extract the ideality factor (η) and effective barrier height ($\Phi_{B,I\text{-}V}$), while the built-in voltage (V_{bi}), and flat band barrier height ($\Phi_{B,C\text{-}V}$) were obtained from the *C–V* characteristics. The results for each Schottky 'metal' are shown in Table 7.1. Note: the values of $\Phi_{B,I\text{-}V}$ have not been corrected for the image force lowering effect, but this would only result in an increase of ~ 10 meV in each case.

Only the silver oxide contacts formed low η barriers for which the barrier height determined from *I–V* and *C–V* measurements were in reasonable agreement. The Ir, Pd, and Pt contacts had $\eta \geq 2$ indicating that thermionic emission is no longer the dominant transport mechanism. High ideality factors are often attributed to laterally inhomogeneous contacts caused by non-uniformities in the Schottky interface, such as structural defects, surface contamination and variations in interface composition.

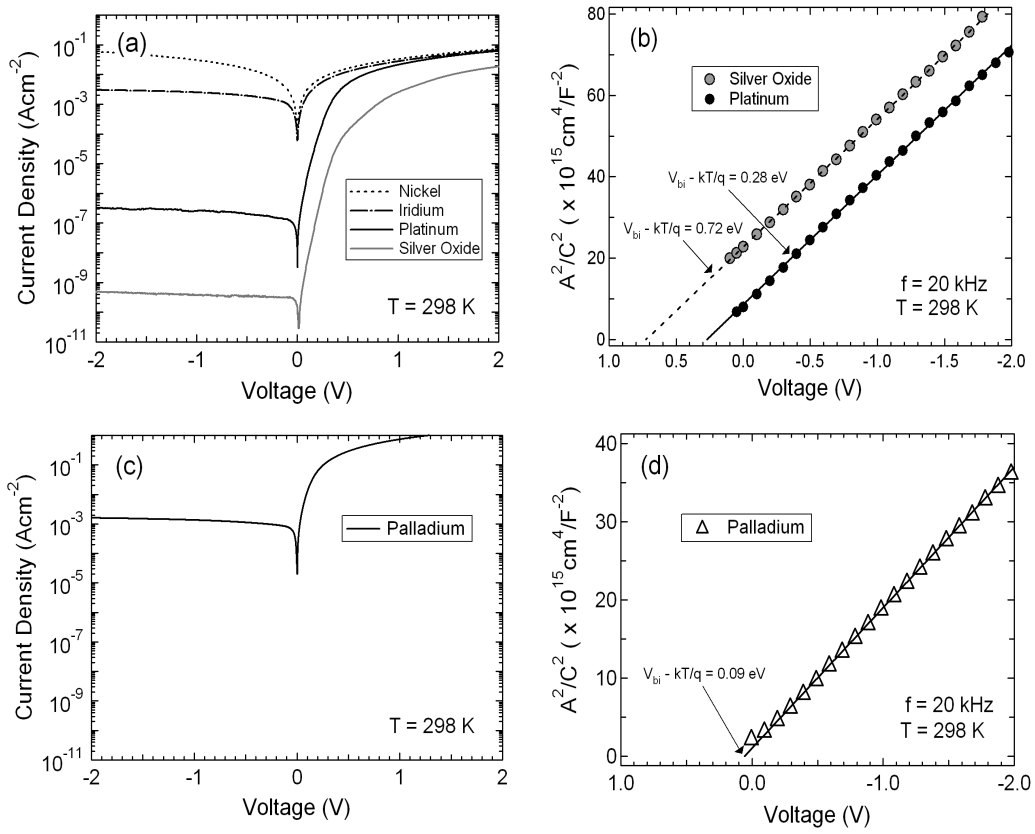

Figure 7.2: (a) Typical *I–V* characteristics, at RT, for Ni, Ir, Pt, and silver oxide Schottky diodes on the Zn-polar face of the same hydrothermally grown bulk ZnO wafer; (b) typical *C–V* characteristics, at RT, of the Pt and silver oxide diodes in (a); (c) typical *I–V* characteristics, at RT, for Pd Schottky diodes on the Zn-polar face of a similar wafer; and (d) typical *C–V* characteristics, at RT, of the Pd diode in (c).

Table 7.1: Schottky diode characteristics, at RT, for various Schottky 'metals' on the Zn-polar surface of hydrothermally grown, bulk ZnO [ideality factor (η) and barrier height ($\Phi_{B,I\text{-}V}$) from *I–V* measurements; built-in potential ($V_{bi,C\text{-}V}$), barrier height ($\Phi_{B,C\text{-}V}$) and effective donor density ($N_{D,C\text{-}V}$) from *C–V* measurements]. Uncertainties in $\Phi_{B,I\text{-}V}$ and $\Phi_{B,C\text{-}V}$ were ± 0.03 eV, averaged over 10 – 12 devices.

Schottky Metal	η	$\Phi_{B,I\text{-}V}$ (eV)	$V_{bi,C\text{-}V}$ (V)	$\Phi_{B,C\text{-}V}$ (eV)	$N_{D,C\text{-}V}$ (cm^{-3})
Ni	–	–	–	–	–
Ir	3.5	0.57	–	–	–
Pd	2.0	0.57	0.09	0.33	9×10^{14}
Pt	2.0	0.72	0.28	0.61	5×10^{14}
Silver Oxide	1.06	1.00	0.72	1.05	5×10^{14}

However, it is expected that $\Phi_{B,I\text{-}V} < \Phi_{B,C\text{-}V}$ for inhomogeneous contacts, since the d.c. *I–V* measurements are more sensitive to the lower barrier height 'patches' while the a.c. *C–V* measurements 'see' the average barrier height of the contact [28]. This is clearly not the case here, where the barrier height of the Pd and Pt contacts from *I–V* measurements were approximately 200 meV higher than those from *C–V* measurements. However, it is possible that the non-ideality is due to some form of more homogeneous defect distribution, such as that due to crystallographic point defects. Furthermore, the $\Phi_{B,I\text{-}V}$ value of 0.57 eV for the Ir contacts here was much lower than the value of 1.00 eV obtained for 'almost ideal' ($\eta < 1.01$) Ir contacts in Chapter 4, indicating some form of strong Fermi level pinning. Klein *et al.* [157] proposed that the Schottky barrier heights of polar bonded, wide band gap semiconductors, such as II-VI compounds, were more likely to experience Fermi level pinning from point defects than from MIGS, due to their relatively low defect formation energies and short MIGS decay lengths, compared to more covalent semiconductors.

7.2.3 Relationship Between Φ_B and Metal Oxide Formation Energy

A comparison of the experimentally determined $\Phi_{B,I\text{-}V}$ for the Ni, Ir, Pd, and Pt Schottky contacts in Table 7.1 and the free energy of metal oxide formation in Figure 7.1 shows a clear correlation, in that the Schottky barrier height of the metal contact increases with the free energy of formation of its metal oxide. Significantly, Ir, Pd, and Ni have similar work functions but Ni has a much lower metal oxide formation energy, which may be the cause of its ohmic behaviour. Metal oxide forming chemical reactions are likely to increase the density of oxygen vacancies (V_O) at the Schottky interface. The intrinsic defects of ZnO have been the subject of

a number of recent first-principles studies; oxygen vacancies have been shown to have the lowest formation energy in the Zn-rich conditions often found during ZnO growth [160–167]. These studies have yielded values for the formation energy of a neutral oxygen vacancy, $\Delta G_f(V_O^X)$, in the 1.7 - 3.5 eV range, with respect to molecular oxygen.

This formation energy is too high to generate a large number (N) of oxygen vacancies using the standard expression,

$$N = N_o exp(-\Delta G / kT) \tag{7.1}$$

where ΔG is the formation energy and N_o is the bulk oxygen atomic density in ZnO. However, Robertson *et al.* [159] have described various mechanisms for the lowering of ΔG near HfO_2 – metal electrodes, which can be adapted to Schottky contacts to ZnO. Specifically, the creation of oxygen vacancies becomes energetically more favorable near a metal – ZnO interface via the chemical reaction (using Kröger-Vink notation),

$$O_O^X + \frac{1}{n}M \rightarrow V_O^X + \frac{1}{n}MO_n \tag{7.2}$$

which has a reaction energy of,

$$G_1 = \Delta G_f(V_O^X) + \Delta G_f\left(\frac{1}{n}MO_n\right) . \tag{7.3}$$

G_1 can be considered to be the 'effective' formation energy of a neutral oxygen vacancy near the Schottky interface. The neutral oxygen vacancy is an F-centre, filled with two electrons which occupy a hydrogenic-like state in the band gap [166]. A number of first-principles studies [3, 162, 167] have shown the oxygen vacancy to be a negative-U defect, in which ionisation to the doubly charged +2 state is energetically more favourable than to the +1 state. It is likely that neutral oxygen vacancies near the Schottky interface will be readily ionised, as the two electrons in the neutral vacancy level can gain an energy G_2 by falling to the metal Fermi level,

$$V_O^X \rightarrow V_O^{\circ\circ} + 2e^{/} \tag{7.4}$$

which provides an energy gain,

$$G_2 = qE[V_O(-2, 0)] - E_F \tag{7.5}$$

where $E[V_O(+2,0)]$ is the energy level of the $V_O(+2,0)$ transition. The total energy for the formation of doubly ionised oxygen vacancies near the Schottky interface is $G_{total} = G_1 + G_2$, and if $G_{total} < 0$ then oxygen vacancy formation will be exothermic. In addition, it has been

suggested that a charged vacancy will be attracted by its image charge in the metal contact, further lowering G_{total} [159].

The position of E[V_O(+2,0)] relative to the conduction band minimum (CBM) has been theoretically calculated as part of the ongoing debate into the source of the intrinsic *n*-type conductivity of ZnO. However, interpretation of the results of these first-principles studies, which are based on density functional theory (DFT) is not straightforward due to underestimation of the ZnO band gap, meaning that some form of correction has to be applied in order to calculate the position of defect states. Figure 7.3 shows recently published positions of the V_O(+2,0) transition. It would appear that, despite the limitations of the DFT analysis, the consensus is that oxygen vacancies are deep, rather than shallow, donors with the energy level of the V_O(+2,0) transition at approximately 0.7 ± 0.2 eV below the CBM [3, 161, 162, 164, 168]. This is too deep to contribute significantly to the unintentional *n*-type conductivity of ZnO, but it is shallow enough to cause Fermi level pinning at ZnO interfaces. Significantly, most ZnO Schottky barrier heights reported in the literature are in the 0.6 – 0.8 eV range, with relatively high ideality factors.

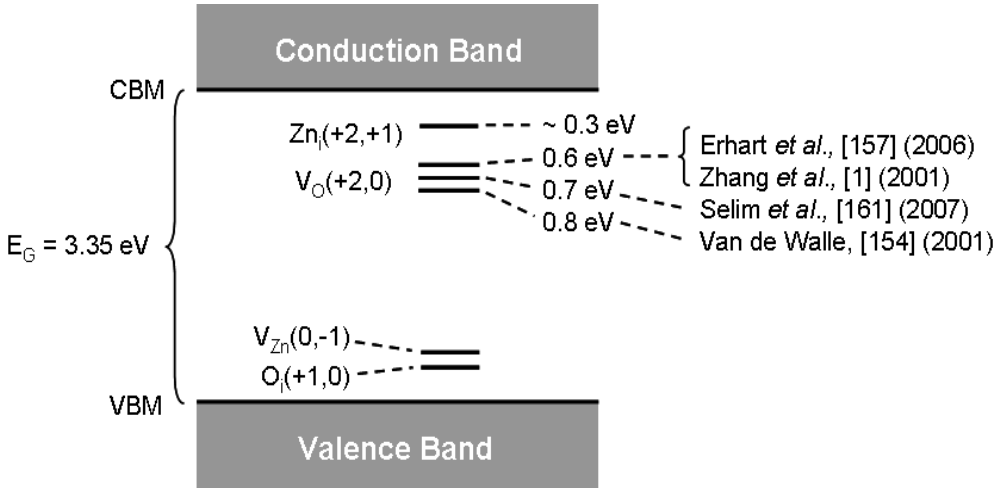

Figure 7.3: Reported energy levels for the V_O(+2,0) transition.

7.2.4 Influence of Oxygen Vacancies on Schottky Contact Formation

Figure 7.4 shows a model of the influence of oxygen vacancies on Schottky contact formation to ZnO. Prior to contact formation, the bulk ZnO Fermi level E_F lies at $E_C - \xi$ (ξ is typically ~ 0.3 eV for hydrothermal bulk ZnO) and the V_O (+2,0) defect level is assumed to be at E_C – 0.7 eV. The Fermi level of the metal is determined by its work function. On contact,

electrons will flow from the semiconductor to the metal until both Fermi levels line up. In the case of ZnO, this electron flow can occur via three mechanisms:

1. from the ZnO conduction band as in conventional Schottky-Mott theory;
2. from the ionisation of intrinsic near surface oxygen vacancies; or
3. from the creation and ionisation of extrinsic oxygen vacancies near the metal – ZnO interface, provided G_{total} is small or < 0.

If the density of oxygen vacancies is sufficiently high, the ZnO Fermi level will be pinned close to the V_O (+2,0) defect level and the depletion region will contain two distinct regions of positive space charge: region I – a narrow region of positively ionised oxygen vacancies close to the Schottky interface, and region II – the conventional space charge region due to shallow ionised donors. Region I is only likely to be a few atomic layers thick making it susceptible to electron tunneling which increases η. The total barrier height of the contact will be $\Phi_B = qV_{bi} + \xi + \gamma$, where γ is the band bending associated with region I. Due to the narrow width of region I and its close proximity to the Schottky metal, γ does not appear in the *C–V* measurements, explaining why $\Phi_{B,I\text{-}V} > \Phi_{B,C\text{-}V}$ for the Pd and Pt contacts.

Silver oxide Schottky contacts have η < 1.1 and $\Phi_{B,I\text{-}V} \sim \Phi_{B,C\text{-}V}$ indicating that the ZnO Fermi level is unpinned. Silver oxide, already in an oxidised state, is unlikely to introduce extrinsic oxygen vacancies and the use of an Ar/O_2 plasma in its fabrication may help passivate intrinsic vacancies near the Schottky interface. This may explain the success of silver oxide and other metal oxides in consistently producing high quality Schottky contacts to bulk ZnO.

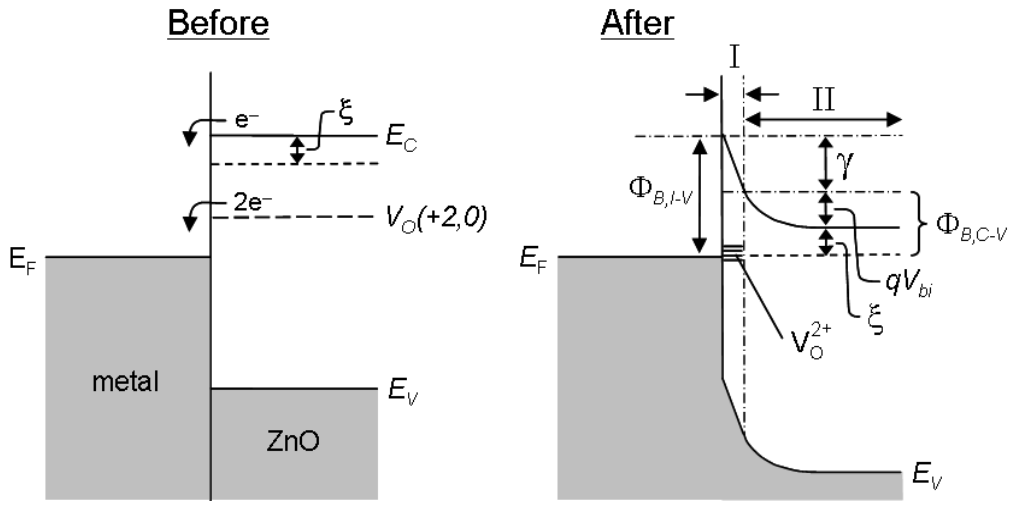

Figure 7.4: Band diagrams showing the influence of oxygen vacancies on Schottky barrier formation to ZnO.

7.3 SUMMARY

A relationship between the barrier height of Ni, Ir, Pd, and Pt Schottky contacts and the free energy of formation of the metal oxide has been found. This suggests that oxygen vacancies have a significant influence on the formation of Schottky contacts to ZnO. An 'oxygen vacancy model' is proposed in which the density of oxygen vacancies near the Schottky interface determines the extent to which the ZnO Fermi level is pinned by the V_O (+2,0) defect level. The density of oxygen vacancies is a combination of the intrinsic V_O density of the ZnO material and additional vacancies created or removed by chemical reactions at the interface. A high interfacial V_O density will cause the ZnO Fermi level to be pinned close to the V_O (+2,0) defect level at ~ 0.7 eV below the conduction band minimum and create a narrow region of positive space charge close to the interface, increasing the non-ideality of the contact. This may explain why most reported ZnO barriers heights have been in the 0.6 – 0.8 eV range with relatively high values of η and only a weak dependence on the metal used.

In Chapter 4 significant improvements in the rectifying performance of Ag and Ir contacts with age or post-fabrication annealing were observed and these may, in part, be due to the diffusion of ambient oxygen to the Schottky interface and subsequent V_O annihilation. The literature reports of improvements in ZnO Schottky contact performance with pre-contact oxidation treatments, such as remote oxygen plasmas, ozone, and hydrogen peroxide, have been mainly attributed to the removal of surface carbon and hydroxide contamination, but the passivation of near surface intrinsic oxygen vacancies may also be important.

Finally, the oxygen vacancy model provides an explanation for the success of metal oxide Schottky contacts in consistently producing 'almost ideal' Schottky contacts to bulk ZnO. These are fabricated in reactive oxygen ambients which will naturally inhibit the formation of extrinsic oxygen vacancies while passivating intrinsic vacancies and those introduced by the removal of the surface hydroxide layer during the Schottky contact formation process.

Chapter 8

Conclusions and Future Work

8.1 BACKGROUND

The aim of this thesis was to advance the understanding of Schottky contact formation to ZnO. Despite the fact that ZnO Schottky contacts have been studied since 1965 and are critical for many ZnO applications (e.g. UV photodiodes, high temperature power diodes, MESFETs), little is known about the mechanisms involved. Indeed, the fabrication of high quality Schottky contacts with reproducible figures of merit (i.e. effective barrier height Φ_B and ideality factor η) has proved challenging with most historical reports of Φ_B restricted to the 0.6 – 0.8 eV range, and relatively high (> 1.3) values of η.

In recent years, bulk single crystal ZnO wafers, grown by the hydrothermal and melt techniques, have become readily available from commercial suppliers. This provides consistent, high quality, baseline material which allows systematic studies of Schottky contact formation to be carried out, and results published by different authors to be meaningfully compared. In particular, hydrothermal ZnO is characterised by a low bulk carrier concentration (10^{13} – 10^{14} cm^{-3}) which is theoretically advantageous for Schottky contact formation. However, even the use of hydrothermal ZnO with its high crystallinity, low surface roughness and low carrier concentration, has not lead to consistent reports of high quality Schottky contacts, and anecdotal evidence from other researchers suggests that Schottky contact fabrication on hydrothermal ZnO is more difficult than on less resistive ZnO material.

8.2 EXPERIMENTAL

In this thesis, hydrothermal bulk ZnO wafers from Tokyo Denpa Co. Ltd. (Japan) and melt bulk ZnO wafers from Cermet Inc. (U.S.A.) were used to investigate the influence of contact composition, fabrication techniques, and surface polarity on the performance of Schottky contacts to ZnO.

At an early stage, it was discovered that the polarity of the ZnO surface has a significant influence on the properties of the resulting Schottky contacts [178, 179] and that the surface

polarity must be treated as an additional variable in any comparison of experimental results with theoretical models. Generally speaking, Schottky diodes fabricated on Zn-polar faces outperformed those on non-polar (m- and a-plane) and O-polar faces of the same wafer. It was also confirmed, using x-ray photoemission spectroscopy (XPS), that the polar and non-polar surfaces of hydrothermal and melt ZnO are naturally terminated by hydroxyl groups which generate a strong surface electron accumulation layer [173, 180]. Accumulation layers inhibit the formation of rectifying barriers, and literature reports of the effect of oxidation treatments on ZnO Schottky contact performance [45, 77, 83] have linked conversions from ohmic to Schottky behaviour to a reduction/removal of this surface hydroxide layer.

Literature reports of Schottky contacts to ZnO have involved the publication of single barrier height (Φ_B) and ideality factor (η) results, often using different ZnO material and surface preparation methods. This makes it difficult to meaningfully compare the results of different authors, even for the same Schottky metal. The strategy employed in this thesis was to fabricate and characterise arrays of Schottky diodes for each type of Schottky contact studied. This allows a relationship between Φ_B and η to be determined, from which the image-force-corrected barrier height for an ideal, homogeneous contact, Φ_B^{hom*}, can be found and compared to theoretical predictions [26]. However, this still requires the fabrication of high quality contacts ($\eta < \sim 1.2$), otherwise the extrapolation of the Φ_B versus η relationship to the image-force-controlled ideality factor (η_{if}) introduces a large uncertainty in the value of Φ_B^{hom*}.

Previously, the barrier heights of non-ideal Schottky contacts have been compared to the theoretical predictions of the Schottky – Mott, metal induced gap states (MIGS), and chemical bond polarisation (CBP) models [29, 170, 171]. This approach is not strictly valid as Schottky contacts with values of η greater than η_{if} are generally influenced by some form of barrier inhomogeneity or defect level pinning, whereas these theoretical models all assume ideal, defect free, and laterally homogeneous interfaces.

8.3 KEY FINDINGS

Values of Φ_B^{hom*} for Ag (0.74 eV), Au (0.85 eV), and Ir (1.00 eV) Schottky metals were determined from arrays of low ideality factor diodes on the Zn-polar face of hydrothermal bulk ZnO. These values can be meaningfully compared with theoretical models as they are representative of the fundamental rectifying properties of the metal–semiconductor contact, free of non-ideal processes and inhomogeneities which can artificially reduce the measured barrier height [26]. Unfortunately, values of Φ_B^{hom*} are only available for a few Schottky metals, which is a reflection on the difficultly in reproducibly fabricating high quality ZnO Schottky contacts using plain metals and conventional deposition techniques.

Although good agreement between the Schottky – Mott model and the experimental Φ_B^{hom*} values for Au and Ir can be obtained, by assuming an electron affinity for ZnO of 4.25 eV, this is far from conclusive as the same model predicts a Φ_B^{hom*} value for Pt of ~ 1.4 eV which is much higher than the literature reports for low ideality factor Pt Schottky contacts to ZnO [94].

The CBP model proposed by Tung [29, 30] does not provide a good fit to the experimental Φ_B^{hom*} results for any value of S_Φ significantly below unity. The problem with the CBP model is that any Fermi level pinning at the Schottky interface is directed towards the middle of the band gap. For wide band gap semiconductors, such as ZnO and GaN, this is likely to result in predicted Φ_B^{hom*} values that are much higher than those experimentally observed [33].

Good agreement can be obtained with the MIGS model, by assuming that the charge neutrality level (or branch point energy) for ZnO is significantly lower in the band gap than the only available experimental value [0.3 eV below the conduction band minimum (CBM)], published by Mönch [35]. Theorerical branch point energies for other II-VI semiconductors have been calculated using the empirical tight binding approach [33, 34] and are 1.2 – 1.6 eV below the respective CBM. No theoretical value for the branch point energy of ZnO is presently available.

In the seminal achievement of this thesis, a metal oxide fabrication technique was developed for the consistent production of high quality Schottky contacts with reproducibly high barrier heights and low ideality factors. This technique involves the deposition of metal oxide films in a reactive oxygen ambient and has been successfully demonstrated for silver and copper oxides using reactive r.f. sputtering, and for iridium and platinum oxides using reactive eclipse pulsed laser deposition. The success of this technique is thought to be due to the presence of active oxygen species during the deposition process which results in a combination of the following beneficial effects:

1) removal of the hydroxide termination from the ZnO surface and the associated accumulation layer which inhibits the formation of rectifying barriers;

2) passivation of intrinsic near surface oxygen vacancies and prevention of extrinsic oxygen vacancy formation during the contact deposition process, which would otherwise tend to pin the ZnO Fermi level near the $V_O(+2,0)$ defect level at ~ 0.7 eV;

3) promotion of polarised metal – oxygen bonds at the Schottky interface which provides an additional electric dipole contribution to the height of the Schottky barrier; and

4) production of metal oxide species which increase the work function of the Schottky contact.

In general, these metal oxide Schottky contacts were found to be metal rich with atomic oxygen contents, from XPS measurements, significantly lower than those expected for stoichiometric oxides. Valence band XPS measurements also showed a continuous density of states up to the Fermi level indicating that these metal oxides all have a metallic-like nature.

Values of Φ_B^{hom*} for vertical geometry iridium oxide (1.16 eV), silver oxide (1.21 eV), and platinum oxide (1.23 eV) Schottky diodes were determined for the Zn-polar face of hydrothermal ZnO, which are significantly higher than their plain metal counterparts; Ir (1.00 eV) and Ag (0.74 eV). This is thought to be due to a combination of the effects of 3) and 4) in the above list. Significantly, these high quality metal oxide Schottky contacts could be consistently reproduced on many additional hydrothermal wafers, often with close to 100% device yields, something that has not been achieved with plain metals.

The significantly lower reproducibility of plain metal Schottky contacts is thought to be linked to either a failure to completely remove the surface hydroxide termination and/or the creation of interfacial oxygen vacancies during the metal deposition. The most dramatic example of this lack of reproducibility came from the fabrication of Au Schottky contacts (by thermal evaporation in high vacuum conditions) on the Zn-polar face of hydrothermal bulk ZnO wafers. Most attempts yielded contacts with pure ohmic behaviour, while in one instance a high yield of almost ideal Schottky diodes ($\eta < 1.04$) was obtained. Since Au has the highest oxide formation energy of any known metal (all forms of gold oxide are energetically unstable), it is unlikely that the creation of oxygen vacancies is responsible for this pure ohmic behaviour. It is more likely that for the ohmic Au contacts, the hydroxide termination remained intact and the local increase in carrier concentration from the associated accumulation layer allows current to tunnel directly across the interface.

Evidence for the influence of oxygen vacancies was found for metals such as Ni, Ir, Pd, and Pt which have lower metal oxide formation energies than Au. A relationship between the barrier heights of diodes fabricated using these Schottky metals and the free energy of formation of their metal oxide was found, suggesting that the creation of oxygen vacancies during contact deposition has a significant influence on Schottky barrier formation.

8.4 SCHOTTKY CONTACT FORMATION

Two key prerequisites have emerged, from the findings in this thesis, for the formation of high quality Schottky contacts to ZnO. These are:

1) removal of the hydroxide termination / accumulation layer which naturally occurs on the ZnO surface; and
2) minimisation of the density of oxygen vacancy defects (V_O) near the Schottky interface: this is a sum of the intrinsic defects present in the ZnO material and additional vacancies introduced by the contact fabrication process.

Schottky contacts in which the hydroxide termination / accumulation layer is not removed are likely to be ohmic in nature, while partial removal will result in poor rectifying performance [45, 77, 83]. A high density of oxygen vacancies near the Schottky interface will tend to pin the ZnO Fermi level close to the $V_O(+2,0)$ defect level at approximately 0.7 eV below the CBM [172]. This will restrict the barrier height of the resulting contacts to the 0.6 – 0.8 eV range commonly observed in the literature and cause a significant increase in ideality factor. The success of metal oxide fabrication techniques in consistently producing high quality Schottky contacts can be explained by the presence of reactive oxygen species which are efficient hydrogen scavengers [prerequisite (1)] and which may cause a reduction in both intrinsic and extrinsic oxygen vacancies [prerequisite (2)]. Schottky contact fabrication using plain metals relies on the kinetic energy of the incident metal particles to remove the hydroxide layer and the creation of extrinsic oxygen vacancies is much more likely due to metal oxidation reactions at the Schottky interface.

8.5 SURFACE POLARITY EFFECTS

Surface polarity related effects were observed in the structural, electrical, and optical properties of bulk ZnO. In general, these effects were significantly larger for hydrothermal ZnO. This is thought to be a result of the low carrier concentration of this material, in which the number of mobile charge carriers is insufficient to screen the large internal electric fields created by either (a) the large spontaneous polarisation of ZnO, or (b) the highly ionic nature of the Zn–O bond.

In particular, previously unreported polarity related effects were observed in the low temperature (4 K) photoluminescence (PL) [149] and the valence band x-ray photoemission spectra, which provide new non-destructive methods of polarity determination.

Low ideality factor Schottky contacts were obtained on the Zn-polar, O-polar and non-polar faces of hydrothermal and melt ZnO using the metal oxide fabrication technique. However, the resulting values of Φ_B^{hom*} were consistently higher on the Zn-polar face compared to the O-polar face, with intermediate values obtained on the non-polar faces. The polarity effect was largest for hydrothermal ZnO with 200 – 250 meV higher values of Φ_B^{hom*} on the Zn-polar face relative to the O-polar face for silver oxide, iridium oxide, and platinum oxide Schottky contacts.

The PL and Schottky barrier height effects are consistent with the large spontaneous polarisation of ZnO, which is predicted to produce fixed negative [positive] spontaneous polarisation charges on the Zn-polar [O-polar] face. The Schottky barrier height effect is thought to be due to the additional upward [downward] band bending on the Zn-polar [O-polar] face, in response to these fixed spontaneous polarisation charges. The PL effect – increased emission from free excitons and excitons bound to positively ionised donors on the Zn-polar face of hydrothermal ZnO – may be due to strong, spontaneous polarisation induced, inversion and depletion regions [149].

8.6 FUTURE WORK

8.6.1 Experimental

Valence band XPS was used in Chapter 2 to quantify the band bending associated with the accumulation layers on the hydroxyl covered Zn-polar, O-polar and m-plane faces of hydrothermal and melt ZnO. These measurements should be repeated after removal of the hydroxide layer, e.g. by *in-situ* oxygen plasma treatment, to determine the Fermi levels of the hydroxyl free Zn-polar, O-polar and m-plane surfaces.

There is a need for experimental values of Φ_B^{hom*} for additional Schottky metals, such as Pt, Pd, Ge, Cu etc., especially on the Zn-polar face of hydrothermal ZnO, so that a stronger comparison with the Schottky – Mott and MIGS models can be made. Similarly, although values of Φ_B^{hom*} were experimentally determined for silver oxide, iridium oxide, and platinum oxide contacts, on both the Zn-polar and O-polar faces of hydrothermal ZnO, the work function of these ‘metal rich’ metal oxide films is not known. Work function measurements could be made, for example using scanning probe Kelvin microscopy, which would allow these values of Φ_B^{hom*} to be included in the comparison with theory.

The metal oxide fabrication technique presented in this thesis represents a significant step towards a reliable contact technology for the development of ZnO based devices. Researchers at the University of Leipzig, Germany, have recently used the published technique for the

fabrication of silver oxide Schottky contacts [173], to produce ZnO MESFETs with the *n*-type channel conductivity tunable over 8 orders of magnitude [174]. However, transmission electron microscopy images of silver oxide contacts [175] revealed the presence of a significant density of voids. The metal oxide Schottky contacts presented in this thesis were fabricated on unheated ZnO wafers and *in-situ* substrate heating during contact deposition is likely to result in improved film morphology and consequently improved device performance, particularly in the area of reverse breakdown voltage.

The metal oxide Schottky contact fabrication technology should also allow the realisation of high performance ZnO based UV photodetectors, power diodes, and MESFETs capable of operation in high temperature environments.

8.6.2 Theoretical

There is an obvious need for a theoretical value for the branch point energy of ZnO, which would significantly improve the predictions of the MIGS model for ZnO. First principles calculations of the valence band density of states for the Zn-polar and O-polar faces would also be useful in explaining the observed polarity related effects in the valence band XPS spectra of ZnO. Finally, the spontaneous polarisation model for ZnO presented in Chapter 6 could be usefully extended by application of the Poisson equation and/or the Poisson–Schrödinger equation to quantify the extent of the induced band bending and surface states on the Zn-polar and O-polar faces.

References

[1] Umicore Group (Belgium), http://zincoxide.umicore.com.

[2] Nano-Infinity Nanotech Ltd. (Taiwan), http://www.b2bnano.com/about-nano-zno.htm.

[3] S. B. Zhang, S. H. Wei, and A. Zunger, "Intrinsic n-type versus p-type doping asymmetry and the defect physics of ZnO," Physical Review B **63**, 075205 (2001).

[4] Y. Yanfa, L. Jingbo, W. Su-Huai, and M. M. Al-Jassim, "Possible approach to overcome the doping asymmetry in wideband gap semiconductors," Physical Review Letters **98**, 135506 (2007).

[5] Ü. Özgür, Y.I. Alivov, C. Liu, A. Teke, M. A. Reshchikov, S. Dogan, V. Avrutin, S. J. Cho, and H. Morkoç, "A comprehensive review of ZnO materials and devices," Journal of Applied Physics **98**, 041301 (2005).

[6] S. J. Pearton, D. P. Norton, K. Ip, Y. W. Heo, and T. Steiner, "Recent progress in processing and properties of ZnO," Superlattices and Microstructures **34**, 3 (2004).

[7] D. C. Look, "Progress in ZnO materials and devices," Journal of Electronic Materials, **35**, 1299 (2006).

[8] C. Jagadish and S.J. Pearton (Editors), Zinc oxide bulk, thin films and nanostructures – processing, properties and applications, Elsevier Ltd., Oxford, 2006.

[9] C. Klingshirn, "ZnO: From basics towards applications," Physica Status Solidi B-Basic Solid State Physics **244**, 3027 (2007).

[10] N. Izyumskaya, V. Avrutin, U. Oz, Y. I. Alivov, and H. Morkoç, "Preparation and properties of ZnO and devices," Physica Status Solidi B-Basic Solid State Physics **244**, 1439 (2007).

[11] G. Heiland and P. Kunstman, "Polar surfaces of zinc oxide crystals," Surface Science **13**, 72 (1969).

[12] T. Nann and J. Schneider, "Origin of permanent electric dipole moments in wurtzite nanocrystals," Chemical Physics Letters **384**, 150 (2004).

[13] F. Bernardini, V. Fiorentini, and D. Vanderbilt, "Spontaneous polarization and piezoelectric constants of III-V nitrides," Physical Review B **56**, R10 024, (1997).

[14] J.A. Duffy, "Ionic–covalent character of metal and nonmetal oxides," Journal of Chemical Physics A. **110**, 13245 (2006).

[15] Z. Hua-Wei, S. Er-Wei, C. Zhi-Zhan, Y. Cheng-Feng, and C. Bo-Yuan, "Characteristics of ZnO single crystal grown by seeded chemical chemical vapor transport method," Journal of Inorganic Materials **22**, 907 (2007).

[16] J. Nause and B. Nemeth, "Pressurized melt growth of ZnO boules," Semiconductor Science and Technology **20**, S45, (2005).

[17] E. Ohshima. H. Ogino, I. Niikura, K. Maeda, M. Sato, M. Ito, and T. Fukuda, "Growth of the 2-in-size bulk ZnO single crystals by the hydrothermal method," Journal of Crystal Growth **260**, 166 (2004).

[18] F. Braun, "Uber die Stromleitung durch Schwefelmetalic," Annalen der Physik and Chemie, **153**, 556 (1874) reprinted in English as "On the current conduction in metal sulphides," in S. M. Sze, *Semiconductor Devices*:*Pioneering Papers* (World Scientific, Singapore) pp. 337 (1991).

[19] W. Schottky, "Semi-conductor theory in barrier layers," Naturwissenschaften **26**, 843 (1938).

[20] N. F. Mott, "Note on the contact between a metal and an insulator or semi-conductor," Proceedings of the Cambridge Philosophical Society **34**, 568 (1938).

[21] M. Grundmann, The physics of semiconductors, Springer-Verlag, Berlin Heidelberg, 2006.

[22] S. M. Sze and K. K. Ng, Physics of semiconductor devices, third edition, John Wiley & Sons, Inc., Hoboken, New Jersey, 2007.

[23] D. K. Schroder, Semiconductor material and device characteristion, Third Edition, John Wiley & Sons, Inc., Hoboken, New Jersey, 2006.

[24] H. A. Bethe, "Theory of the boundary layer of crystal rectifiers," MIT Radiation Laboratory Report, 43-12 (1942).

[25] R. T. Tung, "Recent advances in Schottky barrier concepts," Materials Science & Engineering R-Reports **35**, 1-138 (2001).

[26] W. Mönch, "Barrier heights of real Schottky contacts explained by metal-induced gap states and lateral inhomogeneities," Journal of Vacuum Science & Technology B **17**, 1867 (1999).

[27] H. Henisch, S. Rahimi, Y. Moreau, and L. Szepessy, "Schottky barrier ideality, real and imagined," Solid-State Electronics **27**, 1033 (1984)

[28] J. H. Werner, and H. H. Guttler, "Barrier inhomogeneities at Schottky contacts," Journal of Applied Physics **69**, 1522 (1991).

[29] R. T. Tung, "Formation of an electric dipole at metal-semiconductor interfaces," Physical Review B **64,** 205310, (2001).

[30] R. T. Tung, "Chemical bonding and Fermi level pinning at metal-semiconductor interfaces," Physical Review Letters **84**, 6078 (2000).

[31] J. Bardeen, "Surface states and rectification at a metal semi-conductor contact," Physical Review **71**, 717 (1947).

[32] V. Heine, "Theory of surface states," Physical Review **138**, 1689 (1965).

[33] W. Mönch, Electronic properties of semiconductor interfaces, Springer Series in Surface Science, Springer-Verlag, Berlin Heidelberg, (2004).

[34] W. Mönch, "Elementary calculation of the branch-point energy in the continuum of interface-induced gap states," Applied Surface Science **117**, 380 (1997).

[35] W. Mönch, "On the band structure lineup of ZnO heterostructures," Applied Physics Letters **86**, 162101 (2005).

[36] P. N. First, J. A. Stroscio, R. A. Dragoset, D. T. Pierce, and R. J. Celotta, "Metallicity and gap states in tunneling to Fe clusters in GaAs(110)," Physical Review Letters **63**, 1416 (1989).

[37] T. C. G. Reusch, M. Wenderoth, L. Winking, N. Quaas, and R. G. Ulbrich, "Origin of Schottky barriers in gold contacts on GaAs(110)," Physical Review Letters **93**, 206801 (2004).

[38] W. E. Spicer, I. Lindau, P. Skeath, and C.Y. Su, "Unified defect model and beyond," Journal of Vacuum Science & Technology **17**, 1019 (1980).

[39] W. E. Spicer, Z. Lilientalweber, E. Weber, N. Newman, T. Kendelewicz, R. Cao, C. McCants, P. Mahowald, K. Miyano, and I. Lindau, "The advanced unified defect model for Schottky-barrier formation," Journal of Vacuum Science & Technology B **6**, 1245 (1988).

[40] O. Dulub, U. Diebold, and G. Kresse, "Novel stabilization mechanism on polar surfaces: ZnO(0001)-Zn," Physical Review Letters **90**, 016102 (2003).

[41] O. Dulub, L. A. Boatner, and U. Diebold, "STM study of the geometric and electronic structure of ZnO(0001)-Zn, (000$\bar{1}$)-O, (10$\bar{1}$0), and (11$\bar{2}$0) surfaces," Surface Science **519**, 201 (2002).

[42] C. Woll, "The chemistry and physics of zinc oxide surfaces," Progress in Surface Science **82**, 55 (2007).

[43] U. Diebold, L. V. Koplitz, and O. Dulub, "Atomic-scale properties of low-index ZnO surfaces," Applied Surface Science **237**, 336-342 (2004).

[44] A. Einstein, "Generation and conversion of light with regard to a heuristic point of view ," Annalen der Physik **17**, 132 (1905).

[45] B. J. Coppa, C. C. Fulton, S. M. Kiesel, R. F. Davis, C. Pandarinath, J. E. Burnette, R. J. Nemanich, and D. J. Smith, "Structural, microstructural, and electrical properties of gold films and Schottky contacts on remote plasma-cleaned, n-type ZnO{0001} surfaces," Journal of Applied Physics **97**, 103517 (2005).

[46] M. Valtiner, S. Borodin, and G. Grundmeier, "Preparation and characterisation of hydroxide stabilised ZnO(0001)-Zn-OH surfaces," Physical Chemistry Chemical Physics **9**, 2406 (2007).

[47] S. Spruytte, C. Coldren, J. Harris, D. Pantelidis, H. J. Lee, J. Bravman, and M. Kelly, "Use of angle resolved x-ray photoelectron spectroscopy for determination of depth and thickness of compound layer structures," Journal of Vacuum Science & Technology A **19**, 603 (2001).

[48] M. Kunat, S. Gil Girol, T. Becker, U. Burghaus, and C. Woll, "Stability of the polar surfaces of ZnO: A reinvestigation using He-atom scattering," Physical Review B **66**, 081402 (2002).

[49] M. Kunat, S. G. Girol, U. Burghaus, and C. Woll, "The interaction of water with the oxygen-terminated, polar surface of ZnO," Journal of Physical Chemistry B **107**, 14350 (2003).

[50] S. A. Chambers, T. Droubay, T. C. Kaspar, and M. Gutowski, "Experimental determination of valence band maxima for SrTiO[sub 3], TiO[sub 2], and SrO and the associated valence band offsets with Si(001)," Journal of Vacuum Science & Technology B: Microelectronics and Nanometer Structures **22**, 2205 (2004).

[51] L. F. J. Piper, T. D. Veal, P. H. Jefferson, C. F. McConville, F. Fuchs, J. Furthmuller, F. Bechstedt, H. Lu, and W. J. Schaff, "Valence-band structure of InN from x-ray photoemission spectroscopy," Physical Review B **72**, 245319 (2005).

[52] T. D. Veal, P. H. Jefferson, L. F. J. Piper, C. F. McConville, T. B. Joyce, P. R. Chalker, L. Considine, H. Lu, and W. J. Schaff, "Transition from electron accumulation to depletion at InGaN surfaces," Applied Physics Letters **89**, 202110 (2006).

[53] G. Mercedes, G. Susana, R.-B. Jose Ramon, S. Miguel, T. B. Nicholas, A. Jose, and S. Maurizio, "Unraveling the conduction mechanism of Al-doped ZnO films by valence band soft x-ray photoemission spectroscopy," Applied Physics Letters **86**, 042104 (2005).

[54] E. I. Solomon, P. M. Jones, and J. A. May, "Electronic-Structures of Active-Sites on Metal-Oxide Surfaces - Definition of the Cu/Zno Methanol Synthesis Catalyst by Photoelectron-Spectroscopy," Chemical Reviews **93**, 2623 (1993).

[55] M. Schiek, K. Al-Shamery, M. Kunat, F. Traeger, and C. Woll, "Water adsorption on the hydroxylated H-(1x1) O-ZnO(0001) surface," Physical Chemistry Chemical Physics **8**, 1505 (2006).

[56] V.E. Henrich and P.A. Cox, The surface science of metal oxides, Cambridge University Press, Cambridge, 1994, p. 297.

[57] H. Moormann, D. Kohl, and G. Heiland, "Work function and band bending on clean cleaved zinc-oxide surfaces," Surface Science **80**, 261 (1979).

[58] M. Nakagawa, and H. Mitsudo, "Anomalous temperature-dependence of the electrical-conductivity of zinc-oxide thin-films," Surface Science **175**, 157 (1986).

[59] G. Brauer, W. Anwand, W. Skorupa, J. Kuriplach, O. Melikhova, J. Cizek, I. Prochazka, C. Moisson, H. von Wenckstern, H. Schmidt, M. Lorenz, and M. Grundmann, "Comparative characterization of differently grown ZnO single crystals

by positron annihilation and Hall effect," Superlattices and Microstructures **42**, 259 (2007).

[60] D. C. Look, "Unusual electrical properties of hydrothermally grown ZnO," Superlattices and Microstructures **42**, 284 (2007).

[61] C. H. Swartz, R. P. Tompkins, N. C. Giles, T. H. Myers, H. Lu, W. J. Schaff, and L. F. Eastman, "Investigation of multiple carrier effects in InN epilayers using variable magnetic field Hall measurements," Journal of Crystal Growth **269**, 29 (2004).

[62] C. H. Swartz, R. P. Tompkins, T. H. Myers, D. C. Look, and J. R. Sizelove, "Characterization of multiple carriers in GaN using variable magnetic-field Hall measurements," Journal of Electronic Materials **33**, 412 (2004).

[63] J. Antoszewski, and L. Faraone, "Quantitative mobility spectrum analysis (QMSA) in multi-laver semiconductor structures," Opto-Electronics Review **12**, 347 (2004).

[64] I. Vurgaftman, J. R. Meyer, C. A. Hoffman, D. Redfern, J. Antoszewski, L. Faraone, and J. R. Lindemuth, "Improved quantitative mobility spectrum analysis for Hall characterization," Journal of Applied Physics **84**, 4966 (1998).

[65] T. M. Borseth, B. G. Svensson, and A. Y. Kuznetsov, "Annealing study of hydrothermally grown ZnO wafers," Physica Scripta **T126**, 10 (2006).

[66] T. M. Borseth, B. G. Svensson, A. Y. Kuznetsov, P. Klason, Q. X. Zhao, and M. Willander, "Identification of oxygen and zinc vacancy optical signals in ZnO," Applied Physics Letters **89**, 262112 (2006).

[67] L. J. Brillson, H. L. Mosbacker, M. J. Hetzer, Y. Strzhemechny, and G. H. Jessen, "Dominant effect of near-interface native point defects on ZnO Schottky barriers," Applied Physics Letters **90**, 102116 (2007).

[68] R. Dingle, "Luminescent transitions associated with divalent copper impurities and green emission from semiconducting zinc oxide," Physical Review Letters **23**, 579 (1969).

[69] O. Schmidt, A. Geis, P. Kiesel, C. G. Van de Walle, N. M. Johnson, A. Bakin, A. Waag, and G. H. Döhler, "Analysis of a conducting channel at the native zinc oxide surface," Superlattices and Microstructures **39**, 8 (2006).

[70] C. A. Mead, "Surface barriers on ZnSe and ZnO," Physics Letters **18**, 218 (1965).

[71] C. A. Mead, "Metal-semiconductor surface barriers," Solid-State Electronics **9**, 1023 (1966).

[72] R. C. Neville and C. A. Mead, "Surface barriers on zinc oxide," Journal of Applied Physics, **41**, 3795 (1970).

[73] B. J. Coppa, R. F. Davis, and R. J. Nemanich, "Gold Schottky contacts on oxygen plasma-treated, n-type ZnO($000\bar{1}$)," Applied Physics Letters **82**, 400 (2003).

[74] H. Sheng, S. Muthukumar, N. W. Emanetoglu, and Y. Lu, "Schottky diode with Ag on (11$\bar{2}$0) epitaxial ZnO film," Applied Physics Letters **80**, 2132 (2002).

[75] S. Liang, H. Sheng, Y. Liu, Z. Huo, Y. Lu, and H. Shen, "ZnO Schottky ultraviolet photodetectors," Journal of Crystal Growth **225**, 110 (2001).

[76] A. Y. Polyakov, N. B. Smirnov, E. A. Kozhukhova, V. I. Vdovin, K. Ip, Y. W. Heo, D. P. Norton, and S. J. Pearton, "Electrical characteristics of Au and Ag Schottky contacts on n-ZnO," Applied Physics Letters **83**, 1575 (2003).

[77] H. L. Mosbacker, Y. M. Strzhemechny, B. D. White, P. E. Smith, D. C. Look, D. C. Reynolds, C. W. Litton, and L. J. Brillson, "Role of near-surface states in ohmic-Schottky conversion of Au contacts to ZnO," Applied Physics Letters **87**, 012102 (2005).

[78] H. L. Mosbacker, S. E. Hage, M. Gonzalez, S. A. Ringel, M. Hetzer, D. C. Look, G. Cantwell, J. Zhang, J. J. Song, and L. J. Brillson, "Role of subsurface defects in metal-ZnO(0001) Schottky barrier formation," Journal of Vacuum Science & Technology B **25**, 1405 (2007).

[79] H. L. Mosbacker, C. Zgrabik, M. Hetzer, A. Swain, D. C. Look, G. Cantwell, J. Zhang, J. J. Song, and L. J. Brillson, "Thermally driven defect formation and blocking layers at metal-ZnO interfaces," Applied Physics Letters **91**, 072102 (2007).

[80] S. H. Kim, H. K. Kim, and T. Y. Seong, "Effect of hydrogen peroxide treatment on the characteristics of Pt Schottky contact on n-type ZnO," Applied Physics Letters **86**, 112101 (2005).

[81] S. H. Kim, H. K. Kim, S. W. Jeong, and T. Y. Seong, "Characteristics of Pt Schottky contacts on hydrogen peroxide-treated n-type ZnO(0001) layers," Superlattices and Microstructures **39**, 211 (2006).

[82] S. H. Kim, H. K. Kim, and T. Y. Seong, "Electrical characteristics of Pt Schottky contacts on sulfide-treated n-type ZnO," Applied Physics Letters **86**, 022101 (2005).

[83] Q. L. Gu, C. C. Ling, X. D. Chen, C. K. Cheng, A. M. C. Ng, C. D. Beling, S. Fung, A. B. Djurisic, L. W. Lu, G. Brauer, and H. C. Ong, "Hydrogen peroxide treatment induced rectifying behavior of Au/n-ZnO contact," Applied Physics Letters **90**, 122101 (2007).

[84] R. Schifano, E. V. Monakhov, U. Grossner, and B. G. Svensson, "Electrical characteristics of palladium Schottky contacts to hydrogen peroxide treated hydrothermally grown ZnO," Applied Physics Letters **91**, 193507 (2007).

[85] K. Ip, B. P. Gila, A. H. Onstine, E. S. Lambers, Y. W. Heo, K. H. Baik, D. P. Norton, S. J. Pearton, S. Kim, J. R. LaRoche, and F. Ren, "Improved Pt/Au and W/Pt/Au Schottky contacts on n-type ZnO using ozone cleaning," Applied Physics Letters **84**, 5133 (2004).

[86] V. A. Coleman, Ph.D thesis, Australian National University, 2006.

[87] K. Ip, B. P. Gila, A. H. Onstine, E. S. Lambers, Y. W. Heo, K. H. Baik, D. P. Norton, S. J. Pearton, S. Kim, J. R. LaRoche, and F. Ren, "Effect of ozone cleaning on Pt/Au and W/Pt/Au Schottky contacts to n-type ZnO," Applied Surface Science **236**, 387 (2004).

[88] M. Nakano, A. Tsukazaki, R. Y. Gunji, K. Ueno, A. Ohtomo, T. Fukumura, and M. Kawasaki, "Schottky contact on a ZnO (0001) single crystal with conducting polymer," Applied Physics Letters **91**, 142113 (2007).

[89] Y. F. Dong, and L. J. Brillson, "First-principles studies of metal (111)/ZnO{0001} interfaces," Journal of Electronic Materials **37**, 743 (2008).

[90] M. S. Oh, D. K. Hwang, J. H. Lim, Y. S. Choi, and S. J. Park, "Improvement of Pt Schottky contacts to n-type ZnO by KrF excimer laser irradiation," Applied Physics Letters **91**, 042109 (2007).

[91] K. Fukutani, H. Iwai, Y. Murata, and H. Yamashita, "Hydrogen at the surface and interface of metals on Si(111)," Physical Review B **59**, 13020 (1999).

[92] U. Grossner, S. Gabrielsen, T. M. Borseth, J. Grillenberger, A. Y. Kuznetsov, and B. G. Svensson, "Palladium Schottky barrier contacts to hydrothermally grown n-ZnO and shallow electron states," Applied Physics Letters **85**, 2259 (2004).

[93] H. von Wenckstern, G. Biehne, R. A. Rahman, H. Hochmuth, M. Lorenz, and M. Grundmann, "Mean barrier height of Pd Schottky contacts on ZnO thin films," Applied Physics Letters **88**, 092102 (2006).

[94] H. Endo, M. Sugibuchi, K. Takahashi, S. Goto, S. Sugimura, K. Hane, and Y. Kashiwaba, "Schottky ultraviolet photodiode using a ZnO hydrothermally grown single crystal substrate," Applied Physics Letters **90**, 121906 (2007).

[95] H. Kobayashi, H. Mori, T. Ishida, and Y. Nakato, "Zinc oxide/n-Si junction solar cells produced by spray-pyrolysis method," Journal of Applied Physics **77**, 1301 (1995).

[96] J. A. Aranovich, D. Golmayo, A. L. Fahrenbruch, and R. H. Bube, "Photo-voltaic properties of ZnO-CdTe heterojunctions prepared by spray pyrolysis," Journal of Applied Physics **51**, 4260 (1980).

[97] M. Gajdos, A. Eichler, and J. Hafner, "Ab initio density functional study of O on the Ag (001) surface," Surface Science **513**, 272 (2003).

[98] W. X. Li, C. Stampfl, and M. Scheffler, "Insights into the function of silver as an oxidation catalyst by ab initio atomistic thermodynamics," Physical Review B **68**, 165412 (2003).

[99] H. von Wenckstern, H. Schmidt, M. Grundmann, M. W. Allen, P. Miller, R. J. Reeves, and S. M. Durbin, "Defects in hydrothermally grown bulk ZnO," Applied Physics Letters **91**, 022913 (2007).

[100] K. Sang-Ho, K. Han-Ki, and S. Tae-Yeon, "Effect of hydrogen peroxide treatment on the characteristics of Pt Schottky contact on n-type ZnO," Applied Physics Letters **86**, 112101 (2005).

[101] E. Gur, S. Tuzemen, B. Kilic, and C. Coskun, "High-temperature Schottky diode characteristics of bulk ZnO," Journal of Physics-Condensed Matter **19**, 196206 (2007).

[102] B. Angadi, H. C. Park, H. W. Choi, J. W. Choi, and W. K. Choi, "Oxygen plasma treated epitaxial ZnO thin films for Schottky ultraviolet detection," Journal of Physics D-Applied Physics **40**, 1422 (2007).

[103] D. C. Oh, J. J. Kim, H. Makino, T. Hanada, M. W. Cho, T. Yao, and H. J. Ko, "Characteristics of Schottky contacts to ZnO : N layers grown by molecular-beam epitaxy," Applied Physics Letters **86**, 042110 (2005).

[104] G. D. Yuan, Z. Z. Ye, L. P. Zhu, J. Y. Huang, Q. Qian, and B. H. Zhao, "Gold schottky contacts on n-type ZnO thin films with an Al/Si(100) substrates," Journal of Crystal Growth **268**, 169 (2004).

[105] K. Ip, Y. W. Heo, K. H. Baik, D. P. Norton, S. J. Pearton, S. Kim, J. R. LaRoche, and F. Ren, "Temperature-dependent characteristics of Pt Schottky contacts on n-type ZnO," Applied Physics Letters **84**, 2835 (2004).

[106] H. von Wenckstern, E. M. Kaidashev, M. Lorenz, H. Hochmuth, G. Biehne, J. Lenzner, V. Gottschalch, R. Pickenhain, and M. Grundmann, "Lateral homogeneity of Schottky contacts on n-type ZnO," Applied Physics Letters **84**, 79 (2004).

[107] J. C. Simpson, and J. F. Cordaro, "Characterization of deep levels in zinc oxide," Journal of Applied Physics **63**, 1781 (1988).

[108] W. Gopel, L. J. Brillson, and C. F. Brucker, "Surface point-defects and Schottky-barrier formation on ZnO ($10\bar{1}0$)," Journal of Vacuum Science & Technology **17**, 894 (1980).

[109] N. Y. Garces, L. Wang, L. Bai, N. C. Giles, L. E. Halliburton, and G. Cantwell, "Role of copper in the green luminescence from ZnO crystals," Applied Physics Letters **81**, 622 (2002).

[110] G. I. N. Waterhouse, G. A. Bowmaker, and J. B. Metson, "Interaction of a polycrystalline silver powder with ozone," Surface and Interface Analysis **33**, 401 (2002).

[111] G. I. N. Waterhouse, G. A. Bowmaker, and J. B. Metson, "Oxidation of a polycrystalline silver foil by reaction with ozone," Applied Surface Science **183**, 191 (2001).

[112] T. Hatakeyama, and T. Shinohe, "Reverse characteristics of a 4H-SiC Schottky barrier diode," in *Silicon Carbide and Related Materials 2001*, Materials Science Forum **389**, 1169 (2002).

[113] F. A. Padovani, and R. Stratton, "Field and thermionic-field emission in Schottky Barriers," Solid-State Electronics **9**, 695 (1966).

[114] S. Y. Han, and J. L. Lee, "Characteristics of Schottky contacts on n-type 4H-SiC using IrO_2 and RuO_2," Journal of Applied Physics **94**, 6159 (2003).

[115] L. M. Zhang, Y. S. Gong, C. B. Wang, Q. Shen, and M. X. Xia, "Substrate temperature dependent morphology and resistivity of pulsed laser deposited iridium oxide thin films," Thin Solid Films **496**, 371 (2006).

[116] R. C. Babu, W. Yi, H. R. Robert, A. Sanjeev, E. G. Bruce, R. Ramesh, M. B. John, D. S. Edward, and E. G. David, "Effect of growth conditions on surface morphology and photoelectric work function characteristics of iridium oxide thin films," Applied Physics Letters **74**, 1394 (1999).

[117] R. S. Chen, Y. S. Chen, Y. S. Huang, Y. L. Chen, Y. Chi, C. S. Liu, K. K. Tiong, and A. J. Carty, "Growth of IrO2 films and nanorods by means of CVD: An example of compositional and morphological control of nanostructures," Chemical Vapor Deposition **9**, 301 (2003).

[118] C. U. Pinnow, I. Kasko, C. Dehm, B. Jobst, M. Seibt, and U. Geyer, "Preparation and properties of dc-sputtered IrO_2 and Ir thin films for oxygen barrier applications in advanced memory technology," Journal of Vacuum Science & Technology B **19**, 1857 (2001).

[119] J. K. Kim, H. W. Jang, C. M. Jeon, and J. L. Lee, "GaN metal-semiconductor-metal ultraviolet photodetector with IrO_2 Schottky contact," Applied Physics Letters **81**, 4655 (2002).

[120] J. K. Kim, and J. L. Lee, "GaN MSM ultraviolet photodetectors with transparent and thermally stable RuO_2 and IrO_2 Schottky contacts," Journal of the Electrochemical Society **151**, G190 (2004).

[121] C. M. Jeon, and J. L. Lee, "Investigation of IrO_2 and RuO_2 Schottky contacts on AlGaN/GaN heterostructure," Journal of Applied Physics **95**, 698 (2004).

[122] M. Tachiki, and T. Kobayashi, "An improved laser ablation method using a shadow mask (eclipse method)," Electrical Engineering in Japan **130**, 88 (2000).

[123] N. Seriani, Z. Jin, W. Pompe, and L. C. Ciacchi, "Density functional theory study of platinum oxides: From infinite crystals to nanoscopic particles," Physical Review B **76**, 155421 (2007).

[124] J. Uddin, J. E. Peralta, and G. E. Scuseria, "Density functional theory study of bulk platinum monoxide," Physical Review B **71**, 155112 (2005).

[125] H. Neff, S. Henkel, E. Hartmannsgruber, E. Steinbeiss, W. Michalke, K. Steenbeck, and H. G. Schmidt, "Structural, optical, and electronic properties of magnetron-sputtered platinum oxide films," Journal of Applied Physics **79**, 7672 (1996).

[126] K. Kuribayashi, and S. Kitamura, "Preparation of Pt-PtO_x thin films as electrode for memory capacitors," Thin Solid Films **400**, 160 (2001).

[127] W. D. Westwood, and Bennewit.Cd, "Formation of PtO Films by Reactive Sputtering," Journal of Applied Physics **45**, 2313 (1974).

[128] J. R. McBride, G. W. Graham, C. R. Peters, and W. H. Weber, "Growth and characterization of reactively sputtered thin-film platinum oxides," Journal of Applied Physics **69**, 1596 (1991).

[129] Y. Abe, M. Kawamura, and K. Sasaki, "Preparation of PtO and alpha-PtO_2 thin films by reactive sputtering and their electrical properties," Japanese Journal of Applied Physics Part 1-Regular Papers Short Notes & Review Papers **38**, 2092 (1999).

[130] J. J. Harris, K. J. Lee, J. B. Webb, H. Tang, I. Harrison, L. B. Flannery, T. S. Cheng, and C. T. Foxon, "The implications of spontaneous polarization effects for carrier transport measurements in GaN," Semiconductor Science and Technology **15**, 413 (2000).

[131] M. Stutzmann, O. Ambacher, M. Eickhoff, U. Karrer, A. L. Pimenta, R. Neuberger, J. Schalwig, R. Dimitrov, P. J. Schuck, and R. D. Grober, "Playing with polarity," Physica Status Solidi B-Basic Research **228**, 505 (2001).

[132] C. Noguera, "Polar oxide surfaces," Journal of Physics-Condensed Matter **12**, R367 (2000).

[133] P. W. Tasker, "Stability of ionic-crystal surfaces," Journal of Physics C-Solid State Physics **12**, 4977 (1979).

[134] O. Dulub, U. Diebold, and G. Kresse, "Novel stabilization mechanism on polar surfaces: ZnO(0001)-Zn," Physical Review Letters **90**, 016102 (2003).

[135] G. Kresse, O.Dulub, and U. Diebold, "Competing stabilization mechanism for the polar ZnO(0001)-Zn surface," Physical Review B. **68**, 245409 (2003).

[136] B. Domenichini, G. Pataut, and S. Bourgeois, "Stabilization of polar solid oxide surfaces: competition between adsorption and reconstruction," Surface and Interface Analysis **34**, 540 (2002).

[137] A. Wander and N. M. Harrison, "The stability of polar oxide surfaces: The interaction of H_2O with ZnO(0001) and ZnO(000$\bar{1}$)," Journal of Chemical Physics **115**, 2312 (2001).

[138] J. M. Carlsson, "Electronic structure of the polar ZnO{0001}-surfaces," Computational Materials Science **22**, 24 (2001).

[139] M. Valtiner, S. Borodin, and G. Grundmeier, "Preparation and characterisation of hydroxide stabilised ZnO(0001)-Zn-OH surfaces," Physical Chemistry Chemical Physics **9**, 2406 (2007).

[140] M. Kunat, U. Burghausy, and Ch. Wöll, "Adsorption of hydrogen on the polar O–ZnO surface: a molecular beam study," Physical Chemistry Chemical Physics, **5**, 4962 (2003).

[141] V. Staemmler, K. Fink, B. Meyer, D. Marx, M. Kunat, S.Gil Girol, U. Burghaus, and Ch. Wöll, "Stabilization of polar ZnO-surfaces:Validating microscopic models by using CO as a probe molecule," Physical Review Letters **90,** 106102 (2003).

[142] U. Karrer, O. Ambacher, and M. Stutzmann, "Influence of crystal polarity on the properties of Pt/GaN Schottky diodes," Applied Physics Letters **77**, 2012 (2000).

[143] H. W. Jang, J. H. Lee, and J. L. Lee, "Characterization of band bendings on Ga-face and N-face GaN films grown by metalorganic chemical-vapor deposition," Applied Physics Letters **80**, 3955 (2002).

[144] H. W. Jang, K. W. Ihm, T. H. Kang, J. H. Lee, and J. L. Lee, "Polarization-induced surface band bendings of GaN films studied by synchrotron radiation photoemission spectroscopy," Physica Status Solidi B-Basic Research **240**, 451 (2003).

[145] Y. J. Lin, "Comment on "Schottky contact on a ZnO(0001) single crystal with conducting polymer" [Appl. Phys. Lett. 91, 142113 (2007)]," Applied Physics Letters **92**, 046101 (2008).

[146] H. Ishii, K. Sugiyama, E. Ito, and K. Seki, "Energy level alignment and interfacial electronic structures at organic metal and organic organic interfaces," Advanced Materials **11**, 605 (1999).

[147] I. H. Hong, M. W. Lee, Y. M. Koo, H. Jeong, T. S. Kim, and O. K. Song, "Effective hole injection of organic light-emitting diodes by introducing buckminsterfullerene on the indium tin oxide anode," Applied Physics Letters **87**, 063502 (2005).

[148] F. Nuesch, F. Rotzinger, L. Si-Ahmed, and L. Zuppiroli, "Chemical potential shifts at organic device electrodes induced by grafted monolayers," Chemical Physics Letters **288**, 861 (1998).

[149] M. W. Allen, P. Miller, R. J. Reeves, and S. M. Durbin, "Influence of spontaneous polarization on the electrical and optical properties of bulk, single crystal ZnO," Applied Physics Letters **90**, 062104 (2007).

[150] B. K. Meyer, H. Alves, D. M. Hofmann, W. Kriegseis, D. Forster, F. Bertram, J. Christen, A. Hoffmann, M. Strassburg, M. Dworzak, U. Haboeck, and A. V. Rodina, "Bound exciton and donor-acceptor pair recombinations in ZnO," Physica Status Solidi B-Basic Research **241**, 231 (2004).

[151] B. K. Meyer, J. Sann, S. Lautenschlager, M. R. Wagner, and A. Hoffmann, "Ionized and neutral donor-bound excitons in ZnO," Physical Review B **76**, 184120 (2007).

[152] H. Sasaki, H. Kato, F. Izumida, H. Endo, K. Maeda, M. Ikeda, Y. Kashiwaba, I. Niikura, and Y. Kashiwaba, Phys. Status Solidi C **3**, 1034 (2006).

[153] T. D. Veal, P. D. C. King, P. H. Jefferson, L. F. J. Piper, C. F. McConville, H. Lu, W. J. Schaff, P. A. Anderson, S. M. Durbin, D. Muto, H. Naoi, and Y. Nanishi, "In adlayers on *c*-plane InN surfaces: A polarity-dependent study by x-ray photoemission spectroscopy," Physical Review B **76**, 075313 (2007).

[154] S. A. Chevtchenko, J. C. Moore, Ü. Özgür, X. Gu, A. A. Baski, H. Morkoç, B. Nemeth and J. E. Nause, "Comparative study of the (0001) and (000$\bar{1}$) surfaces of ZnO," Applied Physics Letters **89**, 182111 (2006).

[155] S. Y. Kim, H. W. Jang, S.K. Kim, C. M. Jeon, W.I. Park, G.C. Yi, and J.L. Lee, "Low-resistance Ti/AI ohmic contact on undoped ZnO," Journal of Electronic Materials **31**, 868 (2002).

[156] H. K. Kim, K. K. Kim, S.J. Park, T. Y. Seong, and I. Adesida, "Formation of low resistance nonalloyed Al/Pt ohmic contacts on n-type ZnO epitaxial layer," Journal of Appied Physics **94**, 4225 (2003).

[157] A. Klein, F. Sauberlich, B. Spath, T. Schulmeyer, and D. Kraft, "Non-stoichiometry and electronic properties of interfaces," Journal of Materials Science **42**, 1890 (2007).

[158] J. K. Schaeffer, L. R. C. Fonseca, S. B. Samavedam, Y. Liang, P. J. Tobin, and B. E. White, "Contributions to the effective work function of platinum on hafnium dioxide," Applied Physics Letters **85**, 1826 (2004).

[159] J. Robertson, O. Sharia, and A.A. Demkov, "Fermi level pinning by defects in HfO_2-metal gate stacks," Applied Physics Letters **91**, 132912 (2007).

[160] A. F. Kohan, G. Ceder, D. Morgan, and C. G. Van de Walle, "First-principles study of native point defects in ZnO," Physical Review B **61**, 15019 (2000).

[161] C. G. Van de Walle, "Defect analysis and engineering in ZnO," Physica B-Condensed Matter **308**, 899 (2001).

[162] F. Oba, S. R. Nishitani, S. Isotani, H. Adachi, and I. Tanaka, "Energetics of native defects in ZnO," Journal of Applied Physics **90**, 824 (2001).

[163] A. Janotti, and C. G. Van de Walle, "Oxygen vacancies in ZnO," Applied Physics Letters **87**, 122102 (2005).

[164] P. Erhart, K. Albe, and A. Klein, "First-principles study of intrinsic point defects in ZnO: Role of band structure, volume relaxation, and finite-size effects," Physical Review B **73**, 205203 (2006).

[165] A. Janotti, and C. G. Van de Walle, "New insights into the role of native point defects in ZnO," Journal of Crystal Growth **287**, 58 (2006).

[166] A. A. Sokol, S. A. French, S. T. Bromley, C. Richard, A. Catlow, H. J. J. van Dam, and P. Sherwood, "Point defects in ZnO," Faraday Discussions **134**, 267 (2007).

[167] A. Janotti and C. G. Van de Walle, "Native point defects in ZnO," Physical Review B **76**, 165202 (2007).

[168] F. A. Selim, M. H. Weber, D. Solodovnikov, and K. G. Lynn, "Nature of native defects in ZnO," Physical Review Letters **99**, 085502 (2007).

[169] S. Kurtin, T. C. McGill, and C. A. Mead, "Fundamental transition in electronic nature of solids," Physical Review Letters **22**, 1433 (1969).

[170] M. Schluter, "Chemical trends in metal-semiconductorbarrier heights," Physical Review B **17**, 5044 (1978).

[171] M. Schluter, "Theoretical-models of Schottky barriers," Thin Solid Films **93**, 3 (1982).

[172] M. W. Allen and S. M. Durbin, "Influence of oxygen vacancies on Schottky contacts to ZnO," Applied Physics Letters **92**, 122110 (2008).

[173] M. W. Allen, S. M. Durbin, and J. B. Metson, "Silver oxide Schottky contacts on n-type ZnO," Applied Physics Letters **91**, (2007).

[174] H. Frenzel, A. Lajn, M. Brandt, H. von Wenckstern, G. Biehne, H. Hochmuth, M. Lorenz, and M. Grundmann, "ZnO metal-semiconductor field-effect transistors with Ag-Schottky gates," Applied Physics Letters **92**, 192108 (2008).

[175] M. W. Allen, S. M. Durbin, X. Weng, J. M. Redwing , H. von Wenckstern, and M. Grundman, "Structural and temperature dependent properties of silver oxide Schottky contacts to n-type ZnO," unpublished (2008).

[176] K. Ip, G. T. Thaler, H. S. Yang, S. Y. Han, Y. J. Li, D. P. Norton, S. J. Pearton, S. W. Jang, and F. Ren, "Contacts to ZnO," Journal of Crystal Growth **287**, 149 (2006).

[177] O. Schmidt, A. Geis, P. Kiesel, C. G. Van de Walle, N. M. Johnson, A. Bakin, A. Waag, and G. H. Dohler, "Analysis of a conducting channel at the native zinc oxide surface," Superlattices and Microstructures **39**, 8-16 (2006).

[178] M. W. Allen, M. M. Alkaisi, and S. M. Durbin, "Metal Schottky diodes on Zn-polar and O-polar bulk ZnO," Applied Physics Letters **89**, 103520 (2006).

[179] M. W. Allen, P. Miller, J. B. Metson, R. J. Reeves, M. M. Alkaisi, and S. M. Durbin, Material Research Society Symposium Proceedings **0957**, K09–03 (2006).

[180] M. W. Allen, H. von Wenckstern, M. Grundmann, P. D. C. King, S. A. Hatfield, P. H. Jefferson, T. D. Veal, C. F. McConville, and S. M Durbin, Material Research Society Symposium Proceedings **1035**, L10-06 (2007).